Xuelin Lei
Vsevolod V. Koryanov   *Editors*

Proceedings of 5th International Conference on Mechanical, System and Control Engineering

ICMSC 2021

Springer

Lecture Notes in Mechanical Engineering

Series Editors

Francisco Cavas-Martínez ⓘ, Departamento de Estructuras, Construcción y Expresión Gráfica Universidad Politécnica de Cartagena, Cartagena, Murcia, Spain

Fakher Chaari, National School of Engineers, University of Sfax, Sfax, Tunisia

Francesca di Mare, Institute of Energy Technology, Ruhr-Universität Bochum, Bochum, Nordrhein-Westfalen, Germany

Francesco Gherardini ⓘ, Dipartimento di Ingegneria "Enzo Ferrari", Università di Modena e Reggio Emilia, Modena, Italy

Mohamed Haddar, National School of Engineers of Sfax (ENIS), Sfax, Tunisia

Vitalii Ivanov, Department of Manufacturing Engineering, Machines and Tools, Sumy State University, Sumy, Ukraine

Young W. Kwon, Department of Manufacturing Engineering and Aerospace Engineering, Graduate School of Engineering and Applied Science, Monterey, CA, USA

Justyna Trojanowska, Poznan University of Technology, Poznan, Poland

Xuelin Lei · Vsevolod V. Koryanov
Editors

Proceedings of 5th International Conference on Mechanical, System and Control Engineering

ICMSC 2021

Springer

Editors
Xuelin Lei
East China University of Science
and Technology
Shanghai, China

Vsevolod V. Koryanov
Bauman Moscow State Technical
University
Moscow, Russia

Contents

About the Editors

Dr. Xuelin Lei holds a Ph.D. in Mechanical Engineering from Shanghai Jiaotong University in 2015. He has worked in the School of Mechanical and Power Engineering of East China University of Science and Technology. Dr. Lei also presided over a series of research projects such as Youth Program of National Natural Science Foundation of China, sub-project of National Science and Technology Major Project, Chinese Postdoctoral Science Foundation and Open Fund of State Key Laboratory of Tribology at Tsinghua University.

Dr. Vsevolod V. Koryanov is the first deputy head of the Department of Dynamics and Flight Control of Rockets and Spacecraft's at Bauman Moscow State Technical University, Russia. He has authored over 160 published scientific papers and 3 textbooks. He has published papers in journals of national and international repute. He has mentored several scholars for their master's and Ph.D. theses. He teaches courses such as theory of space flight, ballistics of rockets and space vehicles, and theory of space vehicles flight. In 2013, he was awarded Yu. A. Gagarin medal of the Russian Federation of Cosmonautics.

Materials Science and Engineering

Effect of Fibre Treatment on Tensile Properties in Bamboo Fibre Extraction: A Review Paper

Moviyndiran Muniandy, Sukri Mustapa, Nurdin Ali, Waluyo Adi Siswanto, Azrin Hani Abdul Rashid, and Mohd Idrus Mohd Masirin

1 Introduction

Synthetic fibres such as glass fibres have many uses varying from healthcare, aerospace, electronics and automotive [1]. Despite the many uses of synthetic fibres, it has high production and the material cost is expensive which limits the development of the synthetic fibres into those sectors [1]. Natural fibres such as bamboo fibres possess good qualities which are lightweight, sustainability, biodegradability and a lower cost [1]. Other benefits of natural fibres over synthetic fibres are good thermal insulation, high specific strength and low density characteristics [2]. Besides that natural fibre composites are also environmentally superior to glass fibres [3] and this makes them as one of the best replacements for synthetic fibres. Bamboo fibres are cellulosic fibres produced from bamboo plants and is widely available throughout the world and has been used as a replacement for wood in the production of furniture

M. Muniandy · S. Mustapa (✉)
Structure Integrity Monitoring Research Group (SIMReG), Faculty of Mechanical And Manufacturing Engineering, Universiti Tun Hussein Onn Malaysia (UTHM), Johor, Malaysia
e-mail: sukri@uthm.edu.my

N. Ali
Department of Mechanical and Industrial Engineering, Universitas Syiah Kuala (UNSYIAH), Banda Aceh, Indonesia

W. A. Siswanto
Universitas Muhammadiyah Surakarta (UMS), Jawa Tengah, Indonesia

A. H. A. Rashid
Faculty of Engineering Technology, Universiti Tun Hussein Onn Malaysia (UTHM), Johor, Malaysia

M. I. M. Masirin
Faculty of Civil Engineering and Built Environment, Universiti Tun Hussein Onn Malaysia (UTHM), Johor, Malaysia
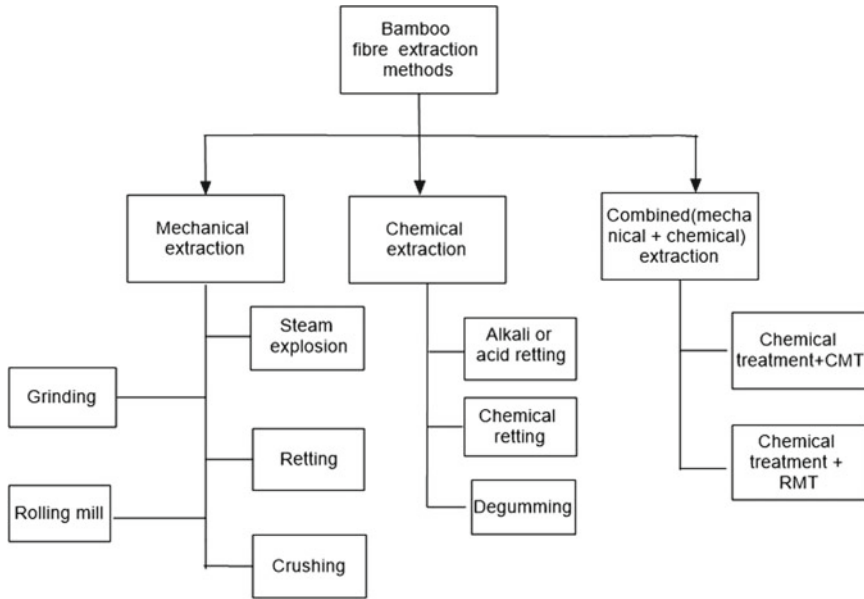
Fig. 1 Bamboo fibre extraction methods (Drawn by referring Zakikhani et al. [12]). CMT: Compression Moulding Technique, RMT: Roller Mill Technique

and low-cost housing [3]. Bamboo has greater renewability as well and since with high calorific values, they can be incinerated for energy recovery at the end of their lifetime [4]. It has been estimated that more than 2.5 billion people depend on the use of bamboo [4]. Compared to other natural fibres, bamboo is eco-friendly with a high growth rate and atmospheric carbon dioxide fixation, making it the most effective plant fibre. More than 1000 bamboo species and about 70 genera are found to grow naturally in diverse climates, especially in Asia and South America [4, 5]. Even though natural fibres has more advantages over synthetic fibres the interest in growing bamboo as reinforcement materials for composites has only grown in recent years. This is because it is technically complex and difficult to extract long and straight bamboo fibres [6]. Besides that, there are several water-absorbing hydroxyl groups in natural fibres made from cellulose fibres [7]. The fibres are hydrophilic, which means they draw water, while the matrix materials are normally hydrophobic, which means they repel it [8]. This distinction in hydrophility makes it difficult to achieve good wetting of fibres by the polymer matrix during production. Consequently, weak interphase properties between fibres and the matrix result in poor. Also, Bamboo culm contains approximately 10.15% amorphous lignin and 73.83% cellulose which is a high percentage of amorphous lignin. Such amounts, however, differ between bamboo species [8, 9–10]. In comparison to other natural plants, this high lignin content makes bamboo fibre brittle. The hydrophilic properties of natural composite fibres make it easy to draw water, which then plays a major role in degrading the

physical and mechanical properties of the resulting composites [11]. The mechanical properties can be improved by choosing the best fibre treatment methods during bamboo fibre extraction. Figure 1 shows the type of bamboo fibre extraction methods.

2 Methodology

Combined chemical and mechanical extraction: The compression moulding technique (CMT) and the roller milling technique (RMT) are normally used to extract fibres after alkali and chemical treatment. In one research study, a bed of alkaline treated bamboo strips was pressurised between two flat plates under a load of 10 tonnes using the CMT technique. The starting bed thickness and compression time are important factors for the separation of high quality fibres in this technique. The treated bamboo strips were forced between two rollers in the RMT technique, with one fixed and the other rotating. The bamboo strips were flattened in both methods and the combined alkaline and mechanical processing made it possible to easily separate strips into individual fibres [11]. In addition, the compression mould size and the roller diameter are two factors that in both techniques limit the ability to extract fibres with smaller strip sizes. In another study, only a roller was used for fibre extraction. The nodes of the bamboo culm were removed in this procedure and the slicer sliced the internodes in the longitudinal direction to create strips. With concentrations of 1%, 2% and 3% at 70 °C for 10 h, the bamboo strips were immersed in NaOH solution. The mechanical properties of fibres that are immersed in 1% NaOH are greater than those of fibres that are immersed in other concentrations. The alkali-treated strips were rolled to extract fibre by a roller looser, and finally the small fibres obtained in this way were washed with water and dried for 24 h at 105 °C in an oven [13].

3 Discussion

Table 1 shows that Chemical + Compression method has the highest tensile strength which is 1000 MPa. Alkaline treatment is preferred as the chemical treatment. According to Mohanty et al. [14], alkaline treatment is one of the most widely used and least expensive chemical treatments for natural fibres. This treatment removes a certain amount of lignin, wax and oil from the outer surface of the fibre cell wall, causing the amount of cellulose exposed to the surface of the fibre to increase. The alkaline treatment also reduces the fibre aggregation in the matrix and increases the roughness of the surface, improving the interconnection between the fibre and the matrix [15, 16]. The experimental results from Phong et al. [13] showed that the alkaline-treatment was better for extracting bamboo fibres than the steam-explosion process. The result of the test method is shown in the bar graph below.

Table 1 Comparison of the mechanical and physical properties of bamboo fibres based on the extraction procedures with fibre glass [9, 16–18]

Fibre	Extraction procedure	Tensile strength (MPa)
Bamboo	*Mechanical methods*	
	Steam explosion	441 ± 220
	Crushing	420 ± 170
	Grinding	450–800
	Rolling mill	270
	Retting	503
	Chemical methods	
	Chemical	450
	Alkaline	395 ± 155
	Combined chemical and mechanical methods	
	Chemical + Compression	645 Max:1000
	Chemical + Roller mill	370 Max:480
E-Glass	-	1200–1500
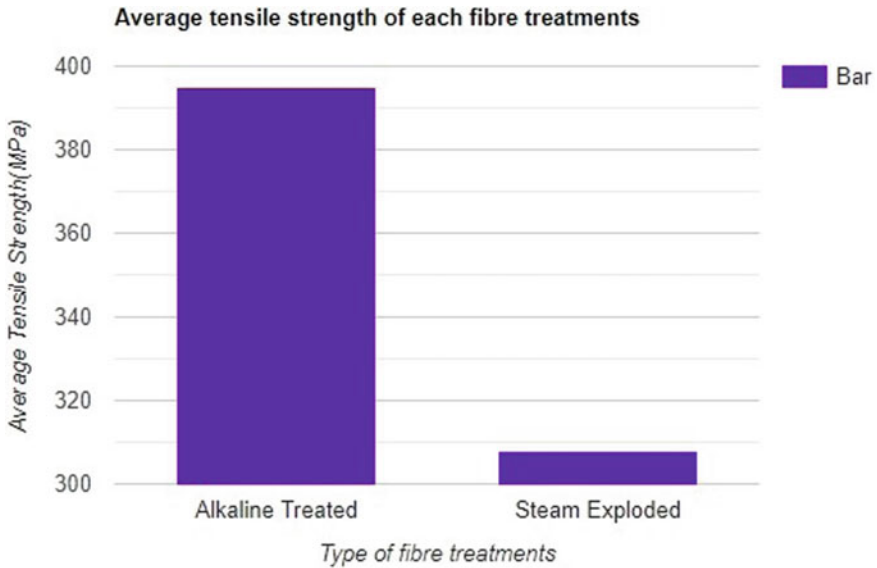
Fig. 2 Average tensile strength of each fibre treatments (drawn by referring Phong et al. [8])

Based on Fig. 2, the tensile strength of alkaline treatment (395 MPa) is higher than the tensile strength of steam explosion (308 MPa). The amount of lignin content in alkaline treatment (22.6%) is less than the steam exploded treatment (23.3%) [13]. Lignin is hydrophilic and always tend to absorb moisture. When it loses or gains
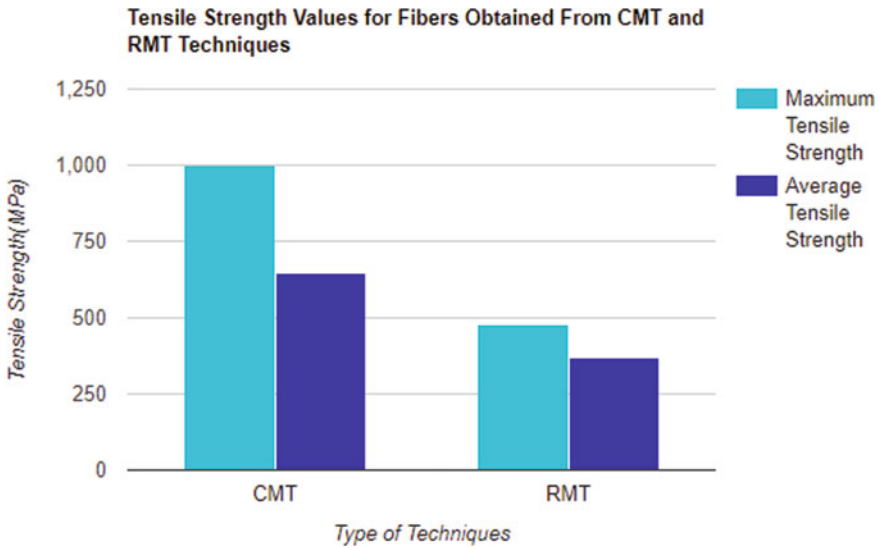
Fig. 3 Tensile strength distributions for fibres obtained from CMT and RMT techniques [28]

moisture, bamboo alters its dimension. Moisture is bamboo's number one enemy and prolonged exposure will ultimately weaken the material [9]. This explains why Alkaline treated bamboo fibers has higher mechanical properties such as tensile strength and young modulus compared to steam exploded fibre treatment. Furthermore, Deshpande et al. [11] used the combination of chemical and mechanical techniques to extract bamboo fibres. For mechanical separation, conventional methods of compression moulding technique (CMT) and roller mill technique (RMT) were explored. The results is as shown below.

From Fig. 3, the maximum and average strengths were found to be 1000 and 645 MPa respectively, for CMT bamboo fibres. However with maximum and average tensile strengths of 480 and 370 MPa respectively, the tensile strength of fibres obtained from RMT was considerably lower. Compared to the fibres obtained from CMT, the fibres from RMT have lower tensile strength as well as less variation in tensile strength. It is observed that higher diameter fibres (obtained from CMT) have greater strength compared to lower diameter fibres (obtained from RMT). In fibres of larger diameters, the probability of interaction between fibrils is higher than in fibres of lower diameters. A fibre with a larger diameter is expected to have greater strength. Thus the CMT isolated fibres with higher diameters had higher average strengths than the RMT isolated fibres with lower diameters [11]. As a conclusion, Alkaline treatment with CMT as a mechanical separation has the highest tensile strength which is 1000 MPa compared to other treatment methods.

4   Conclusion

Natural fibres and biocomposites from natural sources incorporate sustainable, eco-friendly and well-designed industrial products that can replace the future dominance of petroleum-based products. In terms of fast growth and better mechanical properties, bamboo fibre is obtained from a source known for its renewability. The use of bamboo fibre for the production of biocomposites transforms the future of the coming generation by using advanced technology. Well-designed and engineered bamboo fibre products can help make new uprisings to sustain our natural resources. In order to improve the adhesion between hydrophobic polymers and hydrophilic bamboo fibres, fibre surface treatments are applied before composite processing. Resistance to humidity as well as mechanical properties such as tensile strength are improved by methods of chemical and physical modification. The hydrophilic nature of bamboo fibres was altered by the treatment method, which subsequently led to improved adhesion between the fibres and the polymer matrices. It has been found out that alkaline treatment is a cheap and efficient way to remove lignin which plays a huge role in moisture absorption. High moisture absorption degrades the mechanical properties of the bamboo fibre. Combining alkaline treatment with compression moulding technique (CMT) produces high tensile strength value (1000 MPa) which is higher than other treatment methods.

References

1. Porras A, Maranon A (2012) Development and characterization of a laminate composite material from polylactic acid (PLA) and woven bamboo fabric. Compos B Eng 43(7):2782–2788. https://doi.org/10.1016/j.compositesb.2012.04.039
2. Joshi S, Drzal L, Mohanty A, Arora S (2004) Are natural fiber composites environmentally superior to glass fiber reinforced composites? Compos A Appl Sci Manuf 35(3):371–376. https://doi.org/10.1016/j.compositesa.2003.09.016
3. Widiastuti I, Solikhun M, Cahyo DN, Pratiwi YR, Juwantono H (2018) Treatment of bamboo fibres in improving mechanical performance of polymer composites—a review. https://doi.org/10.1063/1.5042966
4. Manalo A, Karunasena W, Lau K (2012) Mechanical properties of bamboo fiber-polyester composites. From Mater Struct: Adv Through Innov 519–524. https://doi.org/10.1201/b15320-90
5. Gratani L, Crescente MF, Varone L, Fabrini G, Digiulio E (2008) Growth pattern and photosynthetic activity of different bamboo species growing in the botanical garden of Rome. Flora—Morphol Distribution Functional Ecol Plants 203(1):77–84. https://doi.org/10.1016/j.flora.2007.11.002
6. Abdul Khalil H, Bhat I, Jawaid M, Zaidon A, Hermawan D, Hadi Y (2012) Bamboo fibre reinforced biocomposites: a review. Mater Des 42:353–368. https://doi.org/10.1016/j.matdes.2012.06.015
7. Chaowana P (2013) Bamboo: an alternative raw material for wood and wood-based composites. J Mater Sci Res 2(2). https://doi.org/10.5539/jmsr.v2n2p90
8. Osorio L, Trujillo E, Van Vuure A, Verpoest I (2011) Morphological aspects and mechanical properties of single bamboo fibers and flexural characterization of bamboo/ epoxy composites. J Reinf Plast Compos 30(5):396–408. https://doi.org/10.1177/0731684410397683

9. Zhu J, Zhu H, Abhyankar H, Njuguna J (2013) Effect of fibre treatment on water absorption and tensile properties of flax/tanin composites. In: The 19th international conference on composite materials (ICCM19), JEC Group, Montreal, Canada
10. Bledzki A (1999) Composites reinforced with cellulose based fibres. Prog Polym Sci 24(2):221–274. https://doi.org/10.1016/s0079-6700(98)00018-5
11. Deshpande AP, Bhaskar Rao M, Lakshmana Rao C (1999) Extraction of bamboo fibers and their use as reinforcement in polymeric composites. J Appl Polym Sci 76:83–92
12. Zakikhani P, Zahari R, Sultan M, Majid D (2014) Extraction and preparation of bamboo fibre-reinforced composites. Mater Des 63:820–828. https://doi.org/10.1016/j.matdes.2014.06.058
13. Phong NT, Fujii T, Chuong B, Okubo K (2011) Study on how to effectively extract bamboo fibers from raw bamboo and wastewater treatment. J Mater Sci Res 1(1). https://doi.org/10.5539/jmsr.v1n1p144
14. Mohanty A, Misra M, Hinrichsen GB (2000) Biofibres, biodegradable polymers and biocomposites: an overview. Macromol Mater Eng 2000:276–277
15. Gomes A, Matsuo T, Goda K, Ohgi J (2007) Development and effect of alkali treatment on tensile properties of curaua fiber green composites. Compos A Appl Sci Manuf 38(8):1811–1820. https://doi.org/10.1016/j.compositesa.2007.04.010
16. Aziz SH, Ansell MP (2004) The effect of alkalization and fibre alignment on the mechanical and thermal properties of kenaf and hemp bast fibre composites: Part 1—polyester resin matrix. Compos Sci Technol 64(9):1219–1230. https://doi.org/10.1016/j.compscitech.2003.10.001
17. Shi Z, Xiao L, Jia-Deng Xu F, Sun R (2012) Physicochemical characterization of lignin fractions sequentially isolated from bamboo (*Dendrocalamus brandisii*) with hot water and alkaline ethanol solution. J Appl Polym Sci 125(4):3290–3301. https://doi.org/10.1002/app.36580
18. Yueping W, Ge W, Haitao C et al (2010) Structures of bamboo fiber for textiles. Textile Res J 80(4):334–343. https://doi.org/10.1177/0040517509337633
19. Ogawa K, Hirogaki T, Aoyama E, Imamura H (2008) Bamboo fiber extraction method using a machining center. J Adv Mech Des Syst Manuf 2(4):550–559. https://doi.org/10.1299/jamdsm.2.550

Spray Solution Combustion Synthesis of NiCu Hollow Spheres

Zhanna Yermekova [iD]**, German Trusov** [iD]**, and Sergey I. Roslyakov** [iD]

1 Introduction

Both Ni and Cu are catalytically active metals for a wide range of chemical reactions. It has been experimentally confirmed that mixing these elements into single phase component might significantly improve the stability and general performance of the catalyst. For example, during CO_2 reforming of methane, the Ni catalyst stability could be greatly improved by the addition of the Cu element into the structure. In this case, Cu changes the carbon deposition mechanism and protects the active Ni sites [1]. Besides that, the implementation of the NiCu alloy in the catalysis changes the H_2 decomposition mechanism compared to the one on the pure Ni catalyst, which in its turn affects a broad spectrum of catalytical reactions [2–4].

The catalytic properties depend not only on the composition but also the morphology of the material which is another approach for catalyst stabilization. Spray solution combustion synthesis (SSCS) [5] is one of the new directions of the traditional solution combustion synthesis (SCS) [6]. This method allows synthesizing the hollow nanoparticles as the opposite of the sponge-like morphology of the materials obtained by the classical SCS [7, 8] or of needle-like structures supported on the surface of inert bulk spheres, which forms after slow and prolonged temperature treatment [9].

In this work, we have synthesized pure hollow spheres of NiCu alloy through spray solution combustion synthesis. The correlation between the synthesis parameters such as the preset temperature of the reactor (tubular furnace, T_{furn}), rate of the

Z. Yermekova (✉) · G. Trusov · S. I. Roslyakov
Center of Functional Nano-Ceramics, National University of Science and Technology "MISiS", Moscow 119049, Russia

S. I. Roslyakov
e-mail: roslyakov.si@misis.ru

11

carrier gas flow (U_g), nature of the carrier gas (Ar or N_2), nature of the fuel (HMTA or Glycine) and final phase composition of the product is shown.

2   Experimental Procedures

$Ni(NO_3)_2 \cdot 6H_2O$ (Chimmed, 98%, Russia) and $Cu(NO_3)_2 \cdot 3H_2O$ (Sigma-Aldrich, 99.99%, USA) were used as metal-containing precursors as well as oxidizer. Glycine and Hexamethylenetetramine (HMTA) (Chimmed, 98%, Russia) were used as a fuel/reducer agent. 1 M aqueous solutions of the metal nitrates were mixed with each other in a ceramic beaker. Then, 1 M fuel solution was added into the beaker and the resulting composition was mixed thoroughly for 30 min with the magnetic stirrer until a homogeneous solution was formed. The mass fractions of the components in the precursor mixture depending on the source of fuel used were calculated according to the stoichiometric reactions 1 and 2.

$$Ni(NO_3)_2 \cdot 6H_2O + Cu(NO_3)_2 \cdot 3H_2O + 2.7C_2H_5NO_2$$
$$= NiCu + 5.3CO_2 + 3.3N_2 + 5.6H_2O \tag{1}$$

$$1.5Ni(NO_3)_2 \cdot 6H_2O + 1.5Cu(NO_3)_2 \cdot 3H_2O + C_6H_{12}N_4$$
$$= NiCu + 6CO_2 + 5N_2 + 19.5H_2O \tag{2}$$

As-prepared precursor solutions were divided on the individual reactive micro drops inside of the ultrasonic nebulizer, then were carried into the ceramic reactor (tubular furnace) using carrier gas flow (N_2 or Ar). As soon as a drop of the solution entered the hot zone of the furnace, a rapid exothermic combustion reaction occurred. The resulting combustion product was collected by a Schott filter located at the end of the furnace. The detailed technical information with a schematic representation of the SSCS experimental setup can be found elsewhere [5]. The phase composition of the obtained powder was studied by X-ray diffraction (XRD) analysis. Analysis was conducted at room temperature on a DIFREY-401 diffractometer operated at 25 kV and 40 mA, using Cr-Kα radiation source with the Bragg-Brentano focusing geometry. The morphology of the product was investigated by JSM 7600F (JEOL, Japan) field-emission scanning electron microscope (FESEM) with spatial resolution of ~1 nm. Combustion products were also imaged using a transmission electron microscope (TEM) (FEI TITAN 80–300), with a point-to-point resolution of 0.19 nm and resolution limit below 0.1 nm. The particles size distribution was measured by the aerodynamic particle sizer (APS) spectrometer (SKU: 3321) which measures the aerodynamic size of particles from 0.5 to 20 microns. The specific surface area (SSA) values of the products were measured by the Brunauer-Emmett-Teller (BET) method, using a NOVA 1200 setup (Quantachrome Instruments, USA). Prior to this analysis, the samples were degassed at 200 °C for 15 h.

3 Result and Discussion

The typical morphology of the as-synthesized NiCu powders is shown in Fig. 1. The SEM image reveals that the powder particles possess the form of independent spheres with complete surface. The surface of alloy particles is smooth without any visible holes or cracks (Fig. 1a). Further TEM investigation shows that all the particles are hollow (Fig. 1b) with a wall thickness less than ~50 nm which is close to the size of the crystallites (~30 nm) calculated from the Scherrer equation. The size of the particles varies significantly in the range from several microns to less 100 nm. The average size of the spheres is around 1.5 μm (Fig. 2) which is comparable with the size of the droplets generated by the nebulizer [5].
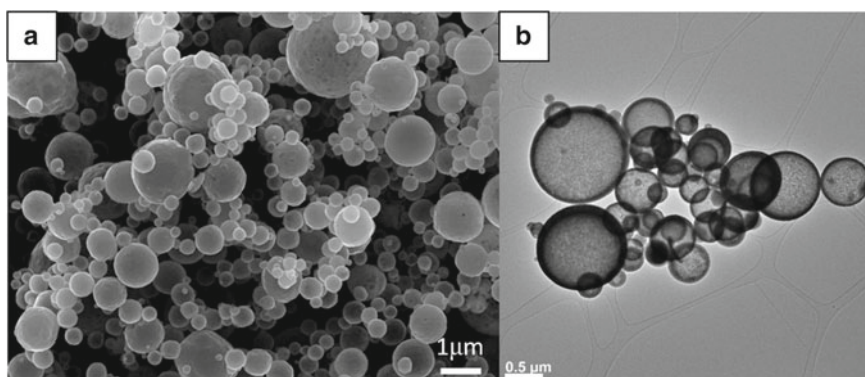
Fig. 1 NiCu alloy powder **a** SEM and **b** TEM images

Fig. 2 NiCu alloy particle size distribution
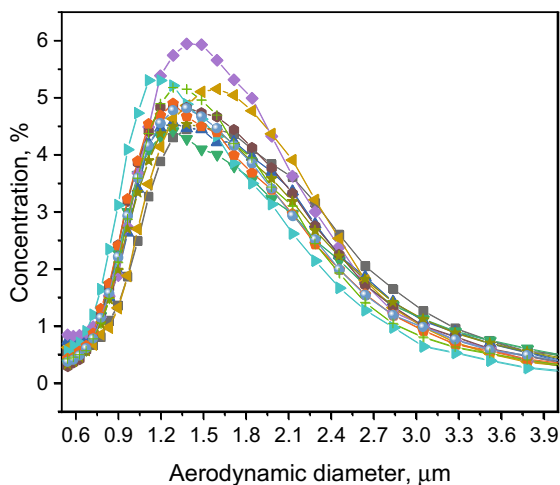
For the spherical hollow particles, the high ratio between the surface and bulk part of the synthesized material makes the synthesis product very sensitive to the ambient (T_a) and reaction (T_r) temperatures change, as well as exposure time under external heating [5], which in its turn can be affected by such SSCS parameters as the preset temperature of the reactor (tubular furnace, T_{furn}), rate of the carrier gas flow (U_g), nature of the carrier gas (Ar or N_2), the ratio between the fuel and oxidizer (φ) and nature of the fuel (HMTA or Glycine). Within the framework of the current work, the influence of four of the main parameters is considered at a constant fuel-to-oxidizer ratio equal 2.

An influence of the T_{furn} and the U_g on the phase composition of the combustion products is shown in Fig. 3. For the $Ni(NO_3)_2$-$Cu(NO_3)_2$-$C_6H_{12}N_4$ chemical system a pure NiCu alloy can be synthesized at two different conditions: $T_{furn} = 1000\,°C$, $U_g = 4$ L/min and $T_{furn} = 900°C$, $U_g = 2$ L/min. As one can see from Fig. 3 decreasing the furnace temperature on 100 from 1000 to 900 °C at the same gas flow rate changes the reaction path. In that case, some new intense peaks appear. Those peaks are corresponding to the well-known class of the material called antiperovskite nitrides [10]. These nitrides are thermally unstable and can be synthesized in a narrow interval of the temperatures (300–700 °C) under the appropriate NH_3/H_2 gases ratio [11]. In the case of SSCS, the fuel is the general source of those gases, which form during the fuel decomposition. The SSCS reactive gas mixture typically consists not only of the NH_3 and H_2 but also comprises some quantity of the N_2O and NO gases, which are formed during the decomposition of the metal nitrate precursors. All the gas components eventually become combined into an active hyperbolic gas mixture, exothermic combustion of which promotes a self-sustained mode of the synthesis. A typical sol–gel combustion synthesis temperature is around 1000–2000 °C.

On the other side, a surplus amount of the NH_3 и H_2 can be produced under the fuel excess (φ ratio higher 1) and create a reductive atmosphere suited for the production of nonoxide components [12]. At such a case, an occurrence of the nitrides

Fig. 3 XRD patterns of SSCS products obtained from $Ni(NO_3)_2$-$Cu(NO_3)_2$-$C_6H_{12}N_4$ (HMTA) reaction mixture at inert Ar gas and different reactor temperatures (T_{furn}) and carrier gas flow rates (U_g)
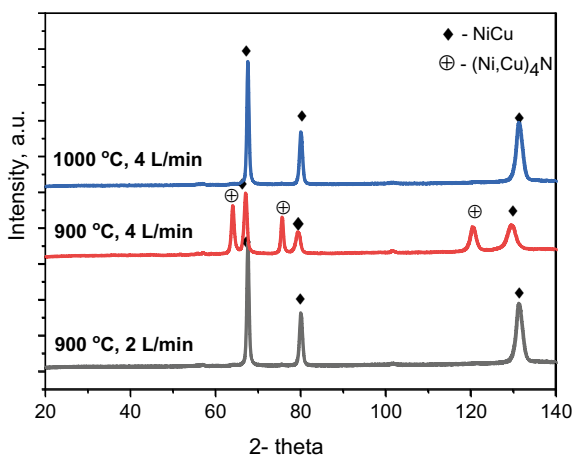
at the $T_{furn} = 900$ °C and $U_g = 4$ L/min conditions implies that at the end of the exothermal reaction the actual ambient temperature around the single drop of the reactive $Ni(NO_3)_2$-$Cu(NO_3)_2$-$C_6H_{12}N_4$ mixture is lower than the one of the preset furnace temperature. In its turn, an absence of the same nitride phase at the $T_{furn} = 900$ °C and $U_g = 2$ L/min conditions shows an important role of the carrier gas flow rate. With the slower gas rate, each particle spends a longer time inside of the hot zone of the reactor where the temperature is generally higher than that of the temperature of the nitride decomposition. Thus, the condition of the alloy formation is fulfilled. From the other side under the higher $U_g = 4$ L/min the newly formed nitride phase is quickly moving to the cooler part of the reactor or outside of it at all where the nitride could be quenched and preserved.

As an additional parameter for mild regulation of the ambient temperature inside the tubular reactor a carrier gas with the lower specific heat capacity could also be changed to the gas with the higher one. For example, if argon ($C_p = 0.52$ J/gK) carrier gas is substituted by the nitrogen ($C_p = 1.04$ J/gK) the nitride phase peak intensity increases and becomes higher than that for the alloy peak, as it is shown in Fig. 4. Due to the great strength of the nitrogen N≡N bonding [13] this gas is relatively inert under conditions of the SSCS but it can lower down the T_{furn} and hence the T_a of the process which might affect the phase composition, crystallinity and particles size of the final SSCS products.

Fuel nature is the last parameter considered in this work, depending on the fuel under equal other conditions the intensity of the alloy peak was significantly increased. HMTA ($C_6H_{12}N_4$) fuel provides more active combustions due to the higher energy capacity and reductive strength [14, 15] which brings more favorable conditions for the alloy formation. In its turn, lower combustion temperature of the glycine provides the better atmosphere for the metal nitride synthesis Fig. 4.

Fig. 4 XRD patterns of the SSCS products obtained at constant $U_g = 4$ L/min and $T_{furn} = 900$ °C at various nature of carrier gas, and fuels
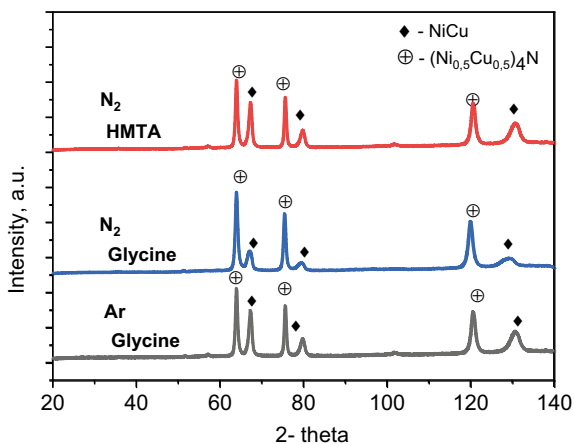
4 Conclusions

In this work, we demonstrate the spray solution combustion synthesis of the NiCu alloy in the form of hollow spheres. During the parametrization of the synthesis, we have shown that the major factor for the alloy formation is the ambient temperature around the droplet of the precursor. Some synthesis parameters such as preset temperature of the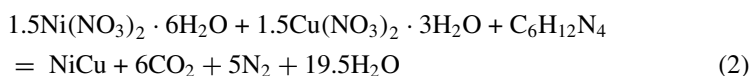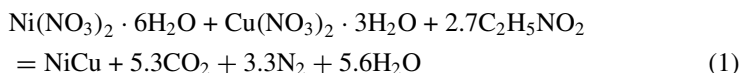 reactor (tubular furnace, T_{furn}), rate of the carrier gas flow (U_g), nature of the carrier gas (Ar or N_2) and nature of the fuel (HMTA or Glycine) might affect the ambient temperature and should be considered simultaneously for successful synthesis. For the $\varphi = 2$ mixture of the HMTA fuel and metal salts, and the carrier gas flow rate 4 L/min the preset temperature within the reactor should not be less than 1000 °C otherwise the significant part of the Me_4N, Me=Cu, Ni, is formed. Investigation of the mechanism of the alloy nitridation is one of the directions for our future work, as the conditions of the synthesis are very different from the traditional nitridation approaches, and the synthesis time of the Me_4N nitride phase is significantly shorter. Eventually, sintering of initially hollow particles might result in a specter of the materials with a wide range of porosity. Considering the catalytical activity of both constituents of the alloy the further investigation of the material properties is a compelling topic for study.

References

1. Lee JH, Lee EG, Joo OS, Jung KD (2004) Stabilization of Ni/Al$_2$O$_3$ catalyst by Cu addition for CO$_2$ reforming of methane. Appl Catal A Gen 269(1–2):1–6
2. Miao C, Zhou G, Chen S, Xie H, Zhang X (2020) Synergistic effects between Cu and Ni species in NiCu/γ-Al$_2$O$_3$ catalysts for hydrodeoxygenation of methyl laurate. Renew Energy 153:1439–1454
3. Tang F, Wang L, Dessie Walle M, Mustapha A, Liu YN (2020) An alloy chemistry strategy to tailoring the d-band center of Ni by Cu for efficient and selective catalytic hydrogenation of furfural. J Catal 383:172–218
4. Zhang J, He L, Yao Y, Zhou XJ, Yu LP, Lu XZ et al (2020) Catalytic effect and mechanism of NiCu solid solutions on hydrogen storage properties of MgH$_2$. Renew Energy 154:1229–1239
5. Trusov GV, Tarasov AB, Goodilin EA, Rogachev AS, Roslyakov SI, Rouvimov S et al (2016) Spray solution combustion synthesis of metallic hollow microspheres. J Phys Chem C 120(13):7165–7171
6. Varma A, Mukasyan AS, Rogachev AS, Manukyan KV (2016) Solution combustion synthesis of nanoscale materials. Chem Rev 116(23):14493–14586
7. Khort A, Roslyakov S, Loginov P (2021) Solution combustion synthesis of single-phase bimetallic nanomaterials. Nano-Struct Nano-Objects 26:10727
8. Kang W, Guo H, Varma A (2019) Noble-metal-free NiCu/CeO$_2$ catalysts for H$_2$ generation from hydrous hydrazine. Appl Catal B Environ 249:54–62

9. Ghiat I, Saadi A, Bachari K, Coville NJ, Boudjemaa A (2020) Spherical NiCu phyllosilicate photocatalysts for hydrogen generation. Int J Hydrogen Energy. https://doi.org/10.1016/j.ijhydene.2020.10.203

10. Hui Z, Tang X, Shao D, Lei H, Yang J, Song W et al (2014) Epitaxial antiperovskite superconducting $CuNNi_3$ thin films synthesized by chemical solution deposition. Chem Commun 50(84):12734–12737

11. Scholz T, Görne AL, Dronskowski R (2018) Itinerant nitrides and salt-like guanidinates—the diversity of solid-state nitrogen chemistry. Prog Solid State Chem 51:1–18

12. Manukyan KV, Cross A, Roslyakov S, Rouvimov S, Rogachev AS, Wolf EE, Mukasyan AS (2013) Solution combustion synthesis of nano-crystalline metallic materials: mechanistic studies. J Phys Chem C 117(46):24417–24427

13. Craig PJ (1998) Book review: chemistry of the elements, 2nd edn. Greenwood, NN Earnshaw A Butterworth-Heinemann, Oxford, 1997. 340p

14. Carlos E, Martins R, Fortunato E, Branquinho R (2020) Solution combustion synthesis: towards a sustainable approach for metal oxides. Chem Eur J 26(42):9099–9125

15. Novitskaya E, Kelly JP, Bhaduri S, Graeve OA (2021) A review of solution combustion synthesis: an analysis of parameters controlling powder characteristics. Int Mater Rev 66(3):188–214

Approach to the Selection of Classification Features for Integrated and Combined Technological Processes of Metal Ware Manufacturing

Marina Polyakova ⓘ **, Ekaterina Lopatina, and Aleksandr Gulin** ⓘ

1 Introduction

Increase of technological flexibility and cost effectiveness, improving the quality of finished metal products are the urgent tasks in metallurgical sphere in the market conditions. With further solution of these tasks the overall competitiveness of metal products increases. From this point of view design of integrated and combined technological processes is the perspective way to improve the manufacturing processes efficiency.

Design of integrated and combined processes in metal ware manufacturing is based on combination of two or more basic processes. Basic process is a process during which both applied stress and external force as well as their direction in deformation zone do not change. As for metals the basic processes are the following: casting, rolling, pressing, and drawing. Based on this definition of basic process the integrated process consists in a combining more than two basic processes during which integral imposition of stresses occurs in one deformation zone. Combined process is characterized by differentiation of basic processes in time or space (place).

When speaking about methods based on plastic deformation it is necessary to take into consideration the evident change of microstructure of the processed metal. In several works [1–7] it is shown that integrated methods are used to obtain the ultra-fine grained structure in the processed material. Sometimes integrated and combined processes are also considered to be methods of severe plastic deformation. At the same time there are metals which do not respond well to plastic deformation due to their specific structural features of the crystal lattice [8]. The change of mechanical

M. Polyakova (✉) · E. Lopatina · A. Gulin
Nosov Magnitogorsk State Technical University, 38 Lenin Avenue, Magnitogorsk 455000, Russia
e-mail: m.polyakova@magtu.ru

A. Gulin
e-mail: a.gulin@magtu.ru

properties of such metals occurs only during integrated and combined processing. It is evident that such classification features as structure or properties of the processed materials can be applied for integrated and combined processes. It is necessary to mention that not all integrated and combined processes can be classified using to the above mentioned criteria. In some cases mathematical modeling is used. Mathematical modeling determines the specific criteria of integrated process more accurately [9].

At present time there are different kinds of integrated and combined methods which are implemented in the industrial conditions for metal ware manufacturing. When creating new classification features it is obligatory to take into consideration the specific technical characteristics of any method and its affect on the change of properties and microstructure in the processed material. That is why there is no unique classification of integrated and combined methods which are used for metal ware manufacturing. The aim of this study is to analyze the existing approaches of classification of the integrated and combined processes.

2   Theoretical Part

The approach for classification of integrated and combined methods based on their principle schemes is proposed in [10]. As it is shown in Fig. 1 integral metal processing methods can be divided into three groups: integrated processes, combined processes, and combined-and-integrated processes. It is necessary to mention that group of integrated processes consists of methods based on plastic deformation of processing metals in solid state. As for combined processes they combine casting with different deformational methods of metal processing.
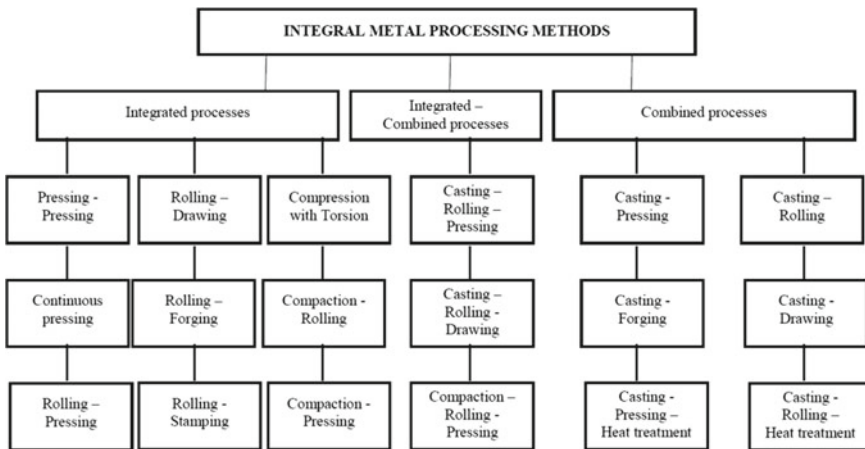
Fig. 1 Classification of integral metal processing methods [10]

It is evident that every method can be characterized by its peculiar advantages and disadvantages. On the other hand, limits of metal processing methods such as rolling, drawing, forging etc. can be neglected when they are integrated with each other. That is why integration of different methods of metal processing based on plastic deformation is one of the perspective ways for the development of new metal ware manufacturing processes. When analyzing integrated processes the following classification features can be proposed for classification: kind of deformation, stress–strain state, friction coefficient, deformation degree, process temperature, processed metal, change of metal structure and properties, and others [11]. For example, the feature "deformation degree" can be applied to processes where such basic processes as rolling, drawing or pressing are integrated. In integrated process "rolling-pressing" the deformation of the strip remains constant when rolling parameters (tension, strip properties, difference in thickness before and after the processing, etc.) change in a sufficiently wide range. In this process deformation degree depends on the ratio of the circumferential speeds of the rolls. Hence, the deformation degree is constant that is why it can be used as the peculiar feature of this process.

The deformation zone in the above mentioned integrated process of "rolling-pressing" (Fig. 2) is divided into three areas (longitudinal rolling, prepressing zone, and pressing zone).
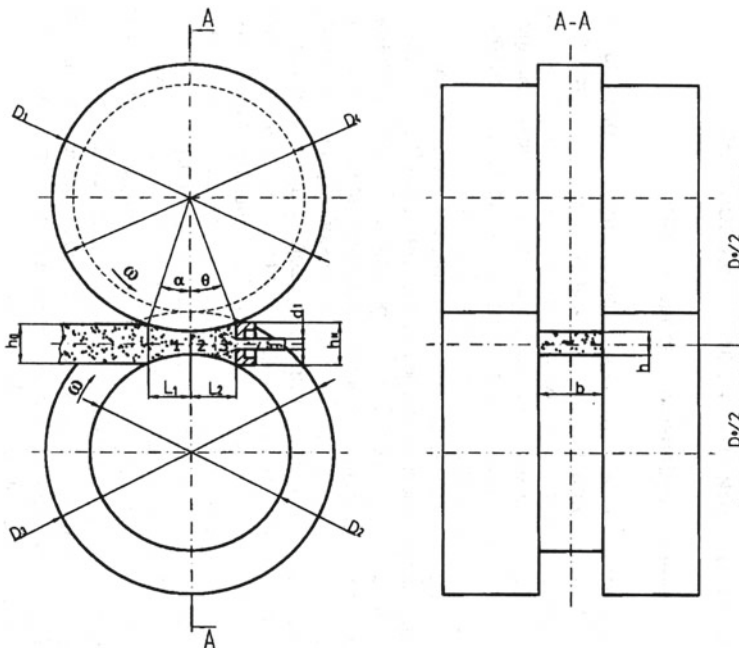
Fig. 2 Principal scheme of the integrated process "rolling-pressing"
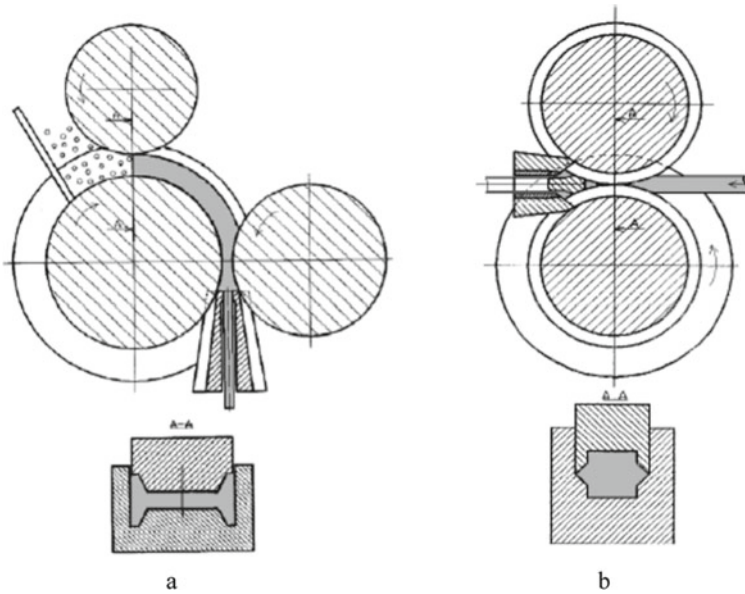
Fig. 3 Manufacturing of metal long length products by integrated process "rolling-pressing": **a** from metal powder; **b** from bulk workpiece [10]

Integration rolling with pressing allows to achieve the uniformity of stress–strain state across the deformation zone. That is why this integrated method can be used to manufacture metal items of complicated shape as it is shown in Fig. 3.

Hence, when choosing classification features, the number of deformation zones should be also taken into consideration.

3   Results and Discussion

As it was mentioned above, there is no single approach to select the classification features for integral methods of metal forming. The choice of parameters should be carried out in accordance with scientific validity. A hypothetical example of the classification of integrated methods based on plastic deformation according to the metal structure and the quantity of deformation zones is presented in Fig. 4.

From this point of view the grain size of a metal after any kind of processing can be considered as the dimensional parameter. The metals structure after processing can be denoted as coarse grained, fine grained, and ultra-fine grained one. One of the tasks of theoretical research is to search and justify classification features for integrated and combined processes. For this purpose it is necessary to find such feature that distinguishes one process from another one. It will become the basis to
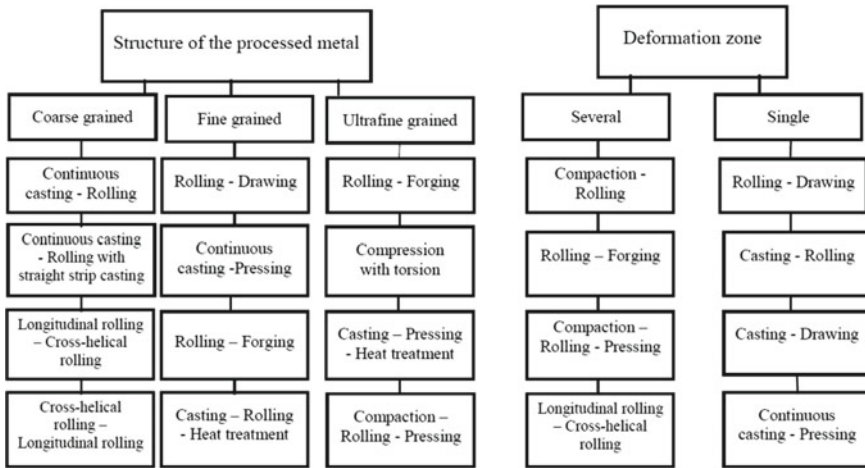
Fig. 4 Classification of integrated and combined processes based on microstructure change and quantity of deformation zones

create classification of integral methods. The question of scientific justification of the classification features currently remains open.

4   Conclusions

Different approaches for selection of the classification features of integrated processes based on plastic deformation of metals are presented in the paper. The relevance of this topic is confirmed by the demand for further development of integrated and combined processes for metal processing. Traditional approach for classification is based on using deformation scheme as the classification feature. It is proposed to enhance classification scheme using kind of metal structure after processing and quantity of deformation zones as features of integrated and combined processes. The use of integrated and combined processes in manufacturing processes of metal and hardware industries is one of the priority tendencies of their development. Hence, classification of integrated and combined processes using new classification features is the basics to design new methods of metal processing.

References

1. Ivanov AM (2019) Combining methods of severe plastic deformation as an effective way to increase the strength of metallic materials. IOP Conf Ser Mater Sci Eng 672:1–4
2. Khandani ST, Faraji G, Torabi H (2020) Development of a new integrated severe plastic deformation method. Mater Sci Technol 36(5):1–9

3. Pourbashiri M, Sedighi M, Poletti C, Sommitsch C (2017) Enhancing mechanical properties of wires by a novel continuous severe plastic deformation method. Int J Mater Res 108(9):741–749
4. Hu H, Qin X, Zhang D, Ma X (2018) A novel severe plastic deformation method for manufacturing AZ31 magnesium alloy tube. Int J Adv Manuf Technol 98(9–12):1–7
5. Dobatkin S, Zrnik J, Mamuzi I (2010) Development of SPD continuous processes for strip and rod production. Metallurgia 49(4):343–347
6. Polyakova MA, Calliari I, Pivovarova KG, Gulin AE (2018) Approach to obtaining medium carbon steel wire with a specified set of mechanical properties after combined deformational processing. Mater Phys Mech 36:53–59
7. Usanov MYu, Kharitonov VA (2016) Effectiveness to apply torsion deformation in manufacturing methods of nanostructured wire. Vestnik Nosov Magnitogorsk State Tech Univ 14(4):66–71 (in Russian)
8. Miyahara Y, Horita Z, Langdon TG (2006) Exceptional superplasticity in an AZ61 magnesium alloy processed by extrusion and ECAP. Mater Sci Eng 420:240–244
9. Taysaev KK, Petrova LG (2020) Mathematical models analysis of combined processing methods of parts. Mater Sci Forum 992:901–906
10. Sidelnikov SB, Dovzhenko NN, Zagirov NN (2005) Integrated and combined methods of processing non-ferrous metals and alloys. MAKS Press, Moscow (in Russian)
11. Lopatina EV, Polyakova MA (2020) Features of classification of combined processes of metal processing by pressure. In: 5th International youth scientific conference "Magnitogorsk rolling practice 2020", 24–27 Nov 2020. http://mrp.magtu.ru/en. Last assessed 18 Aug 2021

Synthesis and Characterization of PSf-CQD Nanocomposite Membrane via Non-solvent Induced Phase Separation Technique

Persia Ada N. de Yro, Dianne Y. Amor, Sweetheart Meryl G. Navarro, Gerald Mari O. Quiachon, and Sharyjel R. Cayabyab

1 Introduction

Non-solvent induced phase separation (NIPS) is a membrane fabrication technique that involves thermodynamic and kinetic processes by the dissolution of a polymer in a solvent then, inducing the polymeric component to coagulate or precipitate in the non-solvent bath [1, 2]. Membranes of varying pore sizes and morphology can be produced by NIPS via changing the polymer and its concentration, the type and additive or filler loading, the precipitation medium and temperature [3].

Polysulfone (PSf), a thermoplastic film forming material, has been a research interest of membrane manufacturers for a long time due to its high thermal strength, excellent heat resistance, solubility in a variety of aprotic polar solvents, and chemical resistance over a wide pH range [4, 5]. PSf is used for the preparation of microfiltration and ultrafiltration membranes, as well as support material for fabrication of composite nanofiltration and reverse osmosis membranes [4]. Nevertheless, applications of the PSf membranes in the filtration of aqueous solutions are often limited because of their hydrophobic nature which results in a low permeate flux and membrane fouling.

The majority of carbon quantum dots (CQD) are rich in oxygen-containing groups which endows them with feasibility in hydrogen and covalent bonding [6]. Other

P. A. N. de Yro (✉) · G. M. O. Quiachon
Materials Science Division, Industrial Technology Development Institute, Department of Science and Technology, DOST Compound, Bicutan, 1631 Taguig City, Philippines

P. A. N. de Yro · D. Y. Amor · S. M. G. Navarro · S. R. Cayabyab (✉)
School of Chemical, Biological, and Materials Engineering and Sciences, Mapúa University, 658 Muralla St, 1002 Intramuros Manila, Philippines

S. R. Cayabyab
National Graduate School of Engineering, University of the Philippines, Diliman, 1101 Quezon City, Philippines

advantages of CQDs are high hydrophilicity, high biocompatibility, excellent photo-chemical stability, low toxicity, and excellent mechanical properties. Together with other advantages such as low cost and ease of synthesis, CQDs are in a favorable position for achieving unprecedented performance [7, 8].

The general objective of this study is to fabricate a PSf/CQD membrane with varying PSf concentration in dope solution and CQD loading via NIPS method. The specific objectives are (a) to study the effect of varying concentrations of CQD on PSf membrane, (b) to study the effect of varying concentration of PSf, (c) to char-acterize the membrane using SEM and ImageJ to analyze the surface morphology and pore size, (d) to characterize the membrane using contact angle measurement for hydrophilicity, (e) to characterize the membrane using FTIR for chemical compo-sition, and (f) to characterize the membrane using UTM for mechanical property analysis.

2 Methodology

2.1 Materials

The materials and chemicals utilized are polysulfone (PSf, average $M_{W \sim 35,000 \text{ g}}$/mol and average $M_n \sim 16,000$ g/mol) from Sigma Aldrich, N-methyl-2-pyrrolidone (NMP, MW = 99.13 g/mol, 99%) from Sigma Aldrich, and carbon quantum dots (CQD) prepared by the Materials Science Division of Department of Science and Technology—Industrial Technology Development Institute (DOST-ITDI).

2.2 Membrane Fabrication

Two sets of PSf membranes were prepared. One set of membrane, PCA, was prepared using 15 wt% PSf with 85 wt% NMP. The other set of membranes, PCB, comprised 18 wt% PSf with 82 wt% NMP. CQD of different concentrations (0.50, 1.0, and 2.0%) was added to the predetermined amount of NMP. The solution was mixed in a vacuum mixer (Planetary Centrifugal Vacuum Mixer, ARV-310/ARV-310LED) for 30 min under room temperature. Then, PSf was added gradually to the CQD/NMP solution and vacuum mixed for 2 h. The PSf/CQD solution was casted using Porometer MEMCAST^{TM} (Plus) at room temperature. The casted solution was submerged in distilled water. The membrane formed was left for 24 h in the non-solvent (distilled water) to complete phase separation, and the membrane is air-dried for 3 h (Table 1).

Table 1 Concentrations of PSf, NMP, and CQD in the dope solution

CuZ loading [wt%]	PSf [wt%]	NMP [wt%]	CQD [wt% based on PSf]
PCA-1	15	85	–
PCA-2	15	85	0.1
PCA-3	15	85	1.0
PCA-4	15	85	2.0
PCB-1	18	82	–
PCB-2	18	82	0.1
PCB-3	18	82	1.0
PCB-4	18	82	2.0

2.3 Membrane Characterization

Hitachi Scanning Electron Microscope SU3500 was used in capturing the surface morphology of the prepared membranes. ImageJ software was used to determine pore size distribution. Shimadzu FT-IR Spectrometer in De La Salle University, Philippines was used in determining the chemical composition and functional groups that are present in the prepared membranes. In characterizing the hydrophilicity of membranes, the contact angle between the water and the membrane surface was measured using a goniometer. Contact angle measurements were carried out through sessile drop method. Image analysis system at three different locations for each of the prepared sample was examined. Shimadzu Autograph AGS-X Mini Universal Testing Machine was used in mechanical analysis of the membrane.

3 Results and Discussion

3.1 FTIR Analysis

The chemical composition and functional groups present in the membrane were identified using FTIR analysis. Moreover, the interaction between bonds present in PSf and CQD in the resulting membrane was also observed. For PCA, a broad absorption band was observed at 3100–3650 cm^{-1} which is attributed to the O-H bond and N-H (amide or amine) group of CQD as shown in Fig. 1a [9]. A decrease in intensities of the absorption bands between 2870 and 3100 cm^{-1} and broadening of the peak was observed as the concentration of the additive increased. The broadening peak of PSf might suggest further interaction and the formation of hydrogen bonding between surface functional groups of CQD and available functional groups of PSf membrane [9, 10]. The IR spectra of PCB show the same result as the PCA for the concentrations of 0%, 0.50%, and 1.0% CQD. PCB-4 show a similar IR spectrum with PCB-1 which indicate that the CQD did not form significant bonds with PSf and
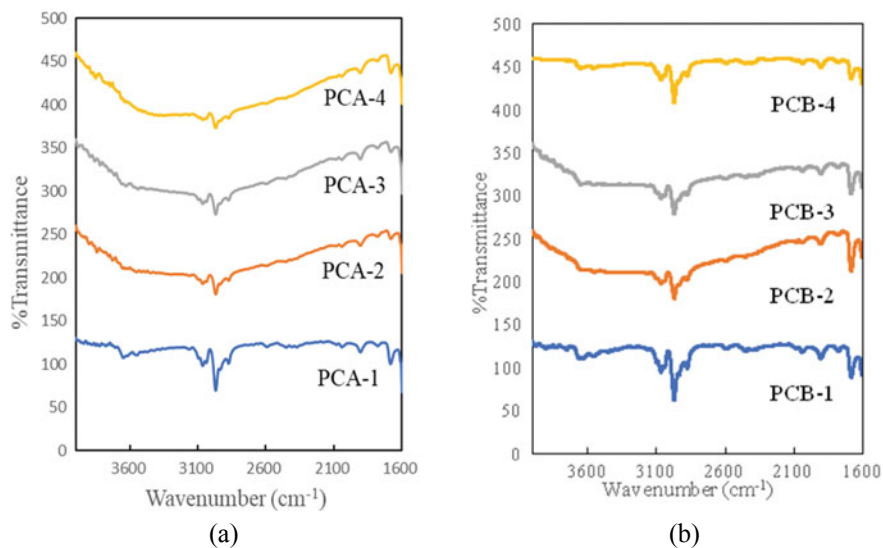
Fig. 1 FTIR spectra for **a** PCA membranes and **b** PCB membranes

Table 2 Observed peaks in the IR spectra of PCA and PCB membranes

Positions (cm^{-1})	Functional group assignments
3100–3600	O-H and N-H (amine or amine) stretching
2870–3100	C-H (alkyl or alkenyl) stretching

was not fully incorporated into the polymer matrix [10]. Moreover, incorporation of CQD did not alter the chemical composition of the polymer matrix (Table 2).

3.2 SEM Imaging Analysis

The surface morphologies of the membranes were observed using SEM, and pore sizes were measured using ImageJ software. Figures 2 and 3 for PCA and PCB membranes, respectively. Table 3 presents the pore size measurements gathered from the SEM images.

For PCA membranes, it is observed that the addition of 0.50% CQD minimally increased the porosity of the membrane. Conversely, addition of 1.0 and 2.0% CQD led to the slight decrease of porosity of the membrane. This could suggest that at 0.50, 1.0, and 2.0% CQD loading, CQD particles act as hindering sites for pore growth. However, pore size increases again at 2.0% loading.

For PCB membranes, it showed a significant drop in porosity with 0.50 and 1.0% CQD loading then a large increase at the addition of 2% CQD. Upon the addition of high amount of CQD, the porosity of the composite membrane significantly
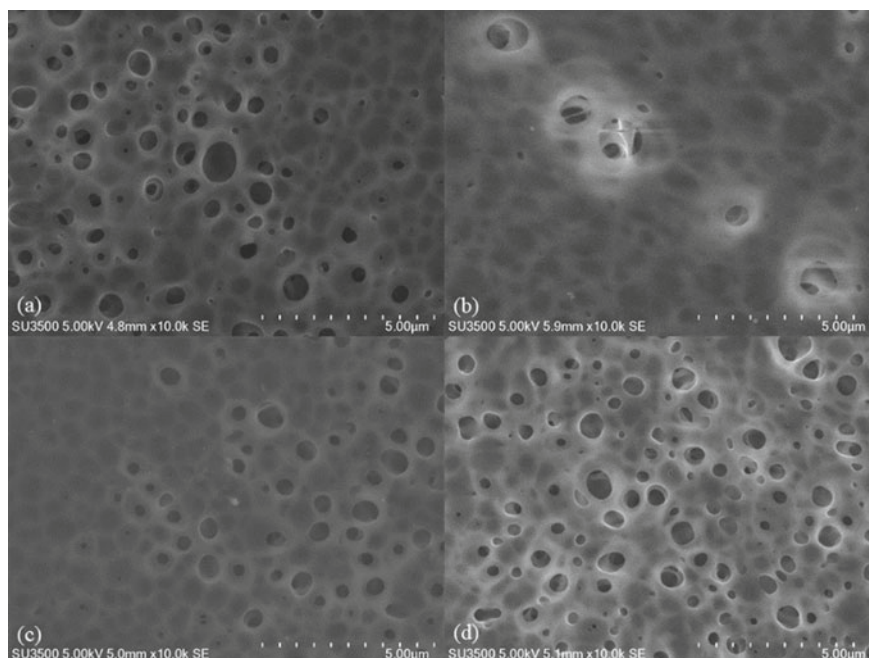
Fig. 2 SEM images of **a** PCA-1, **b** PCA-2, **c** PCA-3, and **d** PCA-4

increased. This could suggest ineffective incorporation or intrusion into the polymeric matrix at high CQD loading. The sudden pore diameter increase of PCB-4 is the result of the agglomeration of the CQD particles possible disrupting the formation of pore structure during membrane fabrication.

In terms of PSf concentrations, PCB-1 has almost the same porosity with PCA-1. The same trend is observed for both 15% and 18% PSf as a function of CQD loading. For both sets, pore sizes dropped up to 1.0% CQD loading and pore size started to increase again at 2.0% CQD loading. This could mean that at 2.0% CQD loading, the particles begin to agglomerate. However, at higher CQD loading changes on the pore structure is more visible with higher PSf concentrations.

3.3 Contact Angle Measurement

Contact angle measurements were carried out using sessile drop method to determine the hydrophilicity and surface properties of PSf/CQD nanocomposites. Membranes with contact angle greater than 90° are considered hydrophobic while membranes with contact angle less than 90° are hydrophilic materials which means it has a tendency to permit the flow of liquid into the membrane through the pores [11].
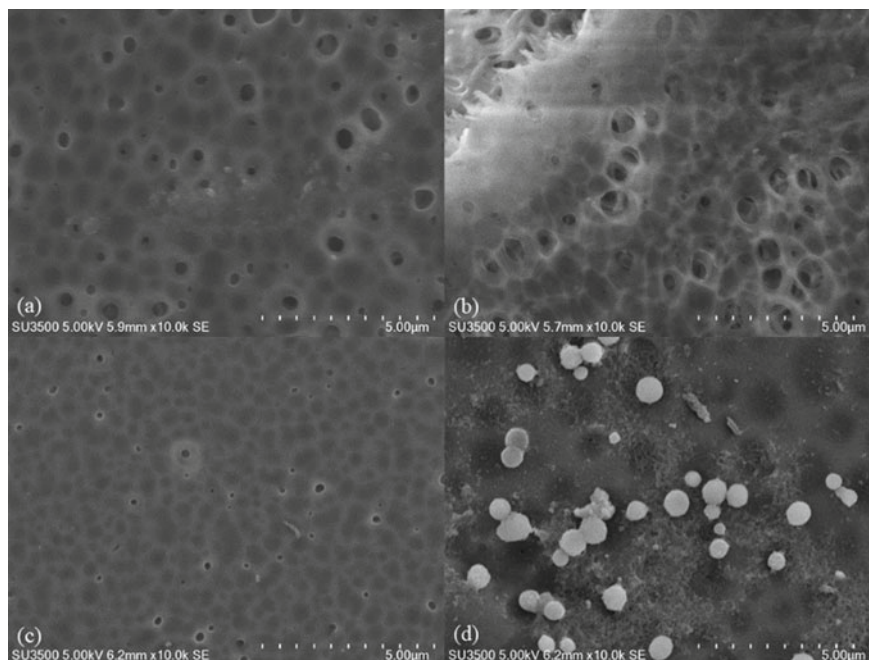
Fig. 3 SEM images of **a** PCB-1, **b** PCB-2, **c** PCB-3, and **d** PCB-4

Table 3 Pore size measurements

Membrane ID	Mean pore diameter (µm)	Pore size range (µm)
PCA-1	0.75	0.48–1.20
PCA-2	0.76	0.46–1.34
PCA-3	0.66	0.45–0.91
PCA-4	0.70	0.58–0.88
PCB-1	0.78	0.59–0.98
PCB-2	0.73	0.56–0.96
PCB-3	0.60	0.25–0.79
PCB-4	0.94	0.58–1.24

Figure 4 presents the plot of contact angle measurements for PCA and PCB membranes, respectively. PCA membranes show that as the CQD loading increases up to 2.0%, contact angles of the membranes decrease. This means that CQD significantly imparts hydrophilicity in the membranes. The presence of oxygen-rich groups added by CQD [11], as seen in the IR spectra, improves the hydrophilicity and stability of PSf in aqueous media. Furthermore, this increase of hydrophilic property maybe useful in filtration and sterilization applications.
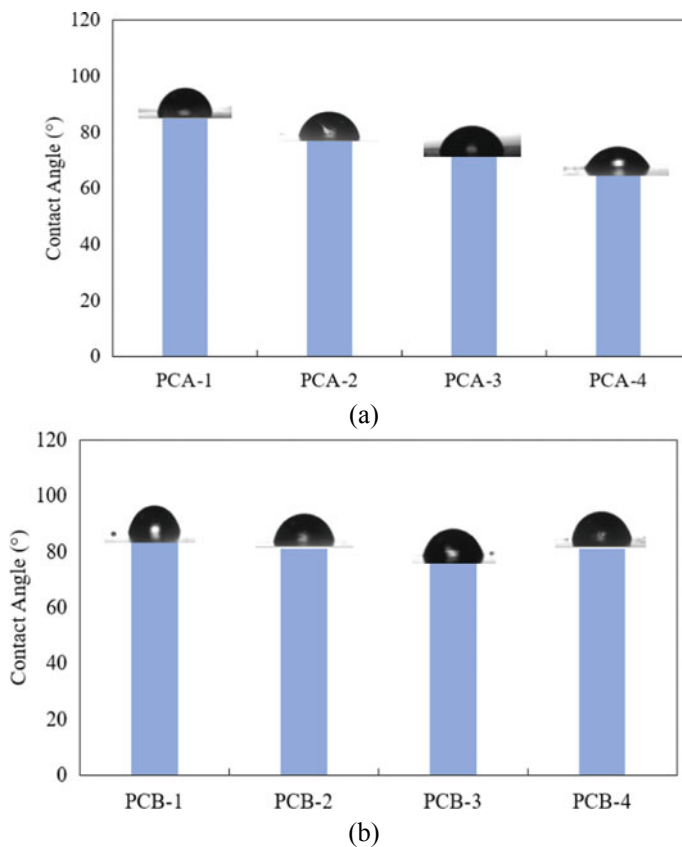
Fig. 4 Plot of contact angle measurements against CQD loading for **a** PCA membranes and **b** PCB membranes

For PCB membranes, there is a slight decrease at 1.0% CQD loading. However, at 0.50 and 2.0% CQD loading contact angles have almost equal magnitude with membrane without CQD (PCB-1). At high PSf concentrations, hydrophobicity of PSf is maintained even with addition of high amount of CQD. This could be due to the inability of CQD to combine with the matrix of PSf and agglomeration of CQD in certain areas within the membrane (Table 4).

Table 4 Contact angle measurements

Membrane ID	Mean contact angle [°]	Membrane ID	Mean contact angle [°]
PCA-1	84.6	PCB-1	83.3
PCA-2	76.9	PCB-2	81.1
PCA-3	71.4	PCB-3	75.9
PCA-4	64.8	PCB-4	81.1

3.4 Mechanical Properties

Figure 5 shows the young's modulus of PCA and PCB membranes, respectively. For PCA membranes, Young's modulus decreased when the concentration of 0.50% CQD was added. Then, at 1.0 and 2.0% CQD, the stiffness increased significantly. The stiffness of PCA membrane also continuously increased at the addition of 2% CQD. As the concentration of the additive increases the number of hydrogen and covalent bonds also increase, consequently increasing the stiffness of the membrane [12, 13].

For PCB membranes, same trend was observed at 0.50% CQD loading. At 1.0% CQD, the Young's modulus of the membrane was equal in magnitude as PCB-1.

(a)

(b)
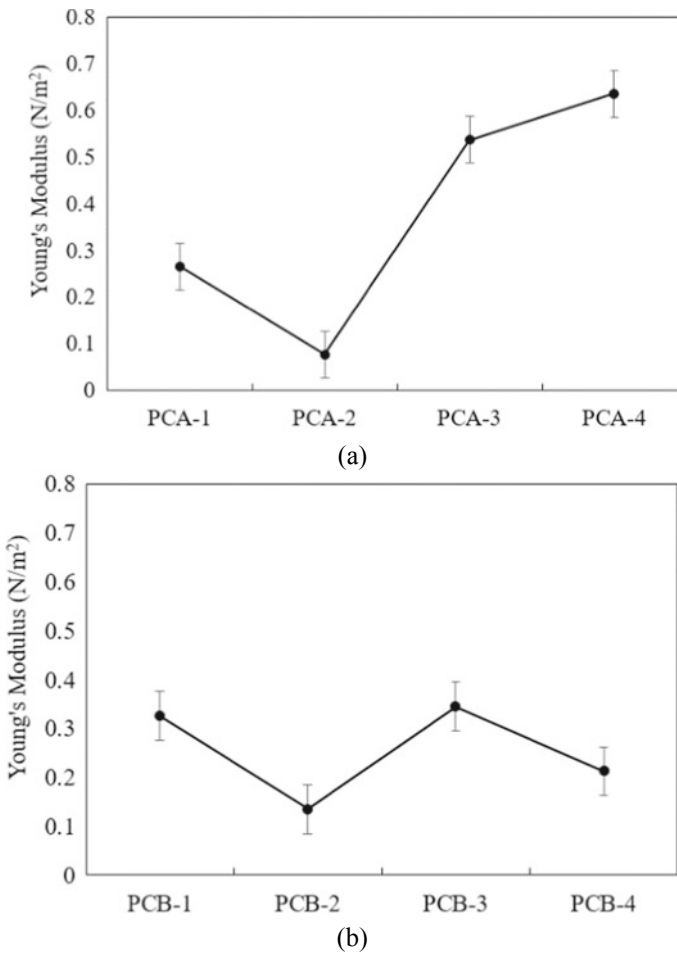
Fig. 5 Plot of Young's modulus against CQD loading for **a** PCA and **b** PCB membranes

At this loading, addition of CQD did not affect the mechanical integrity of the membrane nor did it impart any reinforcing effect. Moreover, at 2.0% CQD the stiffness decreased marginally because the CQD nanoparticles were not able to bond properly with the polymer matrix [12]. Concerning filtration applications, 2.0% CQD with 15% PSf is the preferred concentration as it may be able to withstand a larger range of fluid flow rate compared to other concentrations of CQD.

4   Conclusion

PSf/CQD membranes with varying concentrations of PSf and CQD via casting method were successfully fabricated. Determination of chemical composition through FTIR showed that the CQD was successfully incorporated in the 15% and 18% PSf membrane with the broadening of the peaks at 3100–3600 cm^{-1} which are responsible for the O-H and N-H groups of CQD. Moreover, the chemical composition of PSf was not altered with the addition of CQD. SEM images showed that there is no significant effect of the addition of CQD up to 2.0% loading on the pore size of the PCA membranes. However, SEM images showed the increase of porosity on the surface of the PCB membranes as the concentration of CQD increases. Furthermore, it showed the agglomeration of CQD incorporated in 18% PSf polymer matrix at 2.0% loading. Contact angle measurement revealed the hydrophilic character of the membranes and showed that CQD had some effect on the hydrophilicity of the membrane. UTM testing showed that PCB-1 has a higher mechanical property than PCA-1. The addition of CQD greatly increased the stiffness of the membrane for PCA membranes and marginally decreased for PCB membranes. The results show that PSf/CQD membrane may be useful in filtration or sterilization applications.

References

1. Ma Y, Shi F et al (2011) Effect of PEG additive on the morphology and performance of polysulfone ultrafiltration membranes. Desalination 272(1):51–58
2. Basilia B, Cayabyab S et al (2020) Development of nanocomposite polysulfone-nanoclay membrane with enhanced hydrophilicity. J Environ Sci Manag SI-1:29–36
3. Padilha LF, Borges CP (2019) PVC membranes prepared via non-solvent induced phase separation process. Braz J Chem Eng 36
4. Khalid A, Al-Juhani AA et al (2015) Preparation and properties of nanocomposite polysulfone/multi-walled carbon nanotubes membranes for desalination. Desalination 367:134–144
5. Arahman N, Maimun T et al (2017) The study of membrane formation via phase inversion method by cloud point and light scattering experiment. In: International conference on engineering science and nanotechnology, Solo, Indonesia. AIP Conf Proc 1788
6. Wang Y, Hu A (2014) Carbon quantum dots: synthesis, properties and applications. J Mater Chem C 2:6921
7. Baptista FR, Belhout SA, Giordani S, Quinn SJ (2015) Recent developments in carbon nanomaterial sensors. Chem Soc Rev 44:4433–4453

8. Cayuela A, Benitez-Martinez S, Soriano ML (2016) Carbon nanotools as sorbents and sensors of nanosized objects: the third way of analytical nanoscience and nanotechnology. TrAC Trends Anal Chem 84:172–180
9. Lee C, Pant B, Alam AM et al (2016) Biocompatible and photoluminescent keratin/poly(vinyl alcohol)/carbon quantum dot nanofiber: a novel multipurpose electrospun mat. Macromol Res 24:924–930
10. Lee C, Pant B et al (2017) Carbon quantum dots incorporated keratin/polyvinyl alcohol hydrogels: preparation and photoluminescent assessment. Mater Lett 207:57–61
11. Feng X, Zhao Y et al (2015) Low-temperature hydrothermal synthesis of green luminescent carbon quantum dots (CQD), and optical properties of blends of the CQD with poly(3-hexylthiophene). J Electron Mater 44:3436–3442
12. Zhang C, Du L et al (2016) Photostable epoxy polymerized carbon quantum dots luminescent thin films and the performance study. Results Phys 6:767–771
13. Aziz SB, Hassan AQ et al (2018) Structural and optical characteristics of PVA:C-dot composites: tuning the absorption of ultraviolet (UV) region. Nanomaterials (Basel) 9

Study of the Movement of the Descent Vehicle with an Inflatable Device Made of a Special Material Taking into Account the Arising Asymmetry

Vsevolod V. Koryanov, Andrey S. Kukharenko, Lang Shuobin, and Danhe Chen

1 Introduction

1.1 A Subsection Sample

One of the stages of some space research is the landing of a spacecraft on the surface of the planet. Some of the planets are covered by the atmosphere, due to which the spacecraft is exposed to thermal effects during its descent. To protect the payload from thermal effects, the spacecraft must be equipped with thermal protection. With a stable motion of the spacecraft relative to the center of mass, it is possible to apply thermal protection to only the part of the spacecraft surface that will be most exposed to high temperatures. Consequently, the stable motion of a spacecraft in the planet's atmosphere will reduce the mass of thermal protection, which serves as an important criterion for the effectiveness of space technology applications. Currently, such space technology is implemented in some space programs. Examples of such space programs are ExoMars [1], InSight, Perseverance, and Mars Science Laboratory [2]. This article is part of a series of articles by the author Vsevolod Koryanov, devoted to the study of the landing of descent vehicles and the use of special inflatable devices made of special materials [3, 4]. Investigations of inflatable braking devices in various

V. V. Koryanov (✉) · A. S. Kukharenko · L. Shuobin
Bauman Moscow State Technical University, 2-nd Baumanskaya str., 5, build 1, Moscow, Russian Federation
e-mail: vkoryanov@bmstu.ru

A. S. Kukharenko
e-mail: kafsm3@bmstu.ru

D. Chen
School of Mechanical Engineering, Nanjing University of Science and Technology (NJUST), Nanjing, China

© The Author(s), under exclusive license to Springer Nature Singapore Pte Ltd. 2022
X. Lei and V. V. Koryanov (eds.), *Proceedings of 5th International Conference on Mechanical, System and Control Engineering*, Lecture Notes in Mechanical Engineering, https://doi.org/10.1007/978-981-16-9632-9_5

versions were carried out by the authors [5–8] within the framework of the MetNet project.

The purpose of this work is to study the stability of the descent vehicle motion in the incoming flow, which has constant parameters (speed, density), and in the incoming flow, the parameters of which change during the movement.

2 Description of the Shape of the Descent Vehicle

The descent vehicle is a conical body with a half-opening angle of 60 [9]. The cone has a spherical bluntness. The external view is shown in Fig. 1. The center of pressure (C.P.) of this descent vehicle is displaced by l perpendicular to the longitudinal axis passing through the center of mass (C.M.) (see Fig. 2). This bias may be due to inaccuracy in its production. The center of pressure also changes its position during movement due to uneven burning of the heat-protective coating.

Motion in a stationary incoming flow. Let us write down a system of differential equations of rotational motion relative to the center of mass. The equation for conservation of angular momentum is as follows:

$$\frac{d^2\alpha}{dt^2} = \frac{1}{J_z} \sum M_z, \tag{1}$$

Fig. 1 External view of the descent vehicle
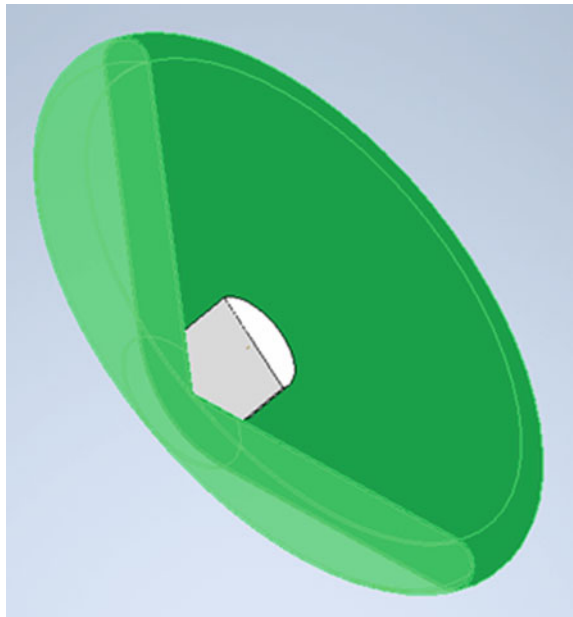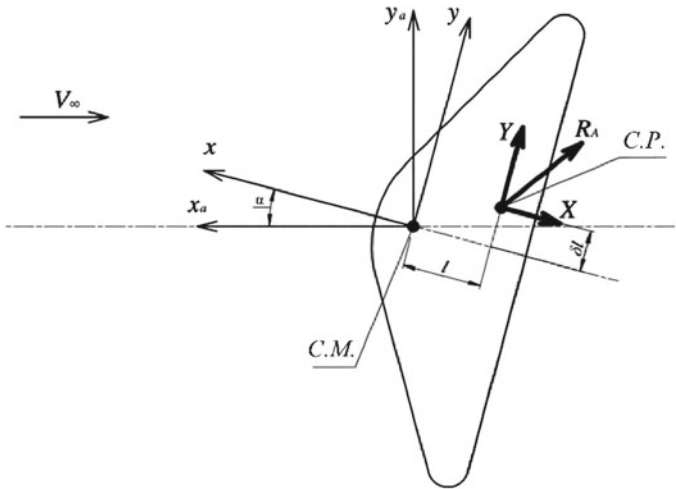
Fig. 2 Scheme for drawing up the equations of rotational motion relative to the center of mass

where α—angle of attack (Fig. 2); J_z—moment of inertia about the z-axis passing through the center of mass and perpendicular to the plane of the figure; $\sum M_z$—sum of the moments of external forces about the axis z.

The sum $\sum M_z$ includes the moments created by external forces, in this case this is the aerodynamic force.

We decompose the aerodynamic force into components:

(1) drag force X;

(2) lifting force Y.

Let's write down the moments that create these components.

Moment from drag force

$$M_x = -\delta l \cdot X;$$

where $X = C_x(\alpha) \cdot q \cdot S_M$

Lift moment

$$M_y = l \cdot Y;$$

where $Y = C_y(\alpha) \cdot q \cdot S_M$

where q—velocity head $q = \rho V^2/2$ S_M—midship area, $S_M = \pi d_m^2/4$.

As a result, the sum of the moments

$$\sum M_z = \delta l \cdot X - l \cdot Y. \tag{2}$$

Substituting expression (2) into expression (1), we obtain
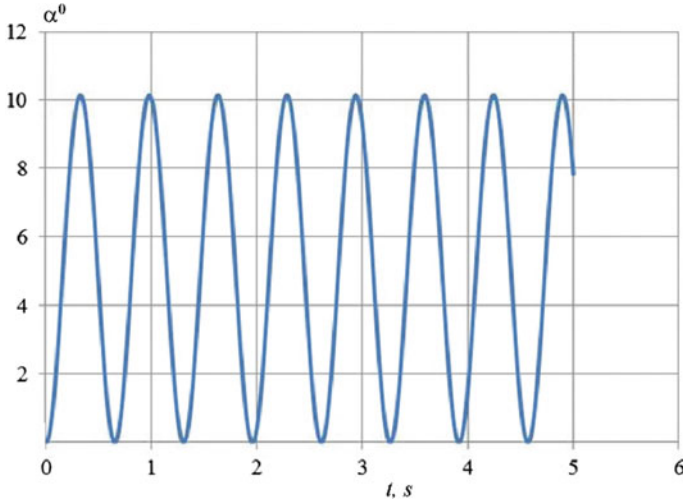
Fig. 3 Dependence of the angle of attack on time for a stationary flow

$$\frac{\mathrm{d}^2\alpha}{\mathrm{d}t^2} = \frac{1}{J_z}(\delta l \cdot X - l \cdot Y). \tag{3}$$

Having solved the differential Eq. (3) by the Runge–Kutta method of the 4th order with the initial conditions $V = 1000$ m/s; $\rho = 1225$ kg/m^3; $\alpha = 0$, we get the result shown in Fig. 3.

When integrating by the Runge–Kutta method of the 4th order, the oscillations do not change their amplitude, i.e., are harmonic. In further calculations, the Runge–Kutta method was used.

Since the descent vehicle oscillates about the center of mass, let us take into account damping in order to obtain damped oscillations.

The calculation of the damping moment coefficient was carried out according to the formula given in the literature [10]:

$$\frac{-2m_z^{\dot{\alpha}}}{k \cos \alpha} = \bar{r}^2 \cos^4 \theta \cdot \left(\frac{\bar{r}}{2} - \frac{x_{\mathrm{T}}}{D}\right) + \frac{1 - \bar{r}^4 \cos^4 \theta}{4 \sin^2 \theta}$$
$$- \frac{4}{3} \frac{\cos \theta (1 - \bar{r}^3 \cos^3 \theta)}{\sin \theta}\left[\frac{x_{\mathrm{T}}}{D} + \frac{\bar{r}(1 - \sin \theta)}{2 \sin \theta}\right]$$
$$+ 2 \cos^2 \theta (1 - \bar{r}^2 \cos^2 \theta)\left[\frac{x_{\mathrm{T}}}{D} + \frac{\bar{r}(1 - \sin \theta)}{2 \sin \theta}\right]^2,$$

where θ—cone half-opening angle; x_{T}—coordinate of the point from the nose of the cone, relative to which the damping moment coefficient is calculated; $k = 2$; $\bar{r}$—the ratio of the radius of spherical bluntness to the radius of the midsection; D—midsection diameter; α—attack angle.

This formula is applicable for calculating the damping coefficient of a conical aircraft with a spherical bluntness in a supersonic incoming flow.

Having calculated the damping moment coefficient, we calculate the damping moment by the formula

$$M_{\text{д}} = qS_M lm_z^{\dot{\alpha}} \dot{\alpha}.$$

Then the sum of the moments will be equal to

$$\sum M_z = \delta l \cdot X - l \cdot Y + M_{\text{д}}. \tag{4}$$

Having solved the differential Eq. (1) taking into account (4) under the same initial conditions as for the case without damping, we obtain the result in the form of a graph of the angle of attack versus time, which is shown in Fig. 4.

From the analysis of Fig. 4, we conclude that in the presence of damping, the oscillatory process is damped. Thus, in the presence of damping, the movement of the descent vehicle is stable.

The movement of the descent vehicle in the Earth's atmosphere. Now, let us consider the behavior of the descent vehicle during its descent in the Earth's atmosphere. In this case, changes in the parameters of the incident flow will be taken into account: the speed and direction, as well as the density. To solve this problem, a system of differential equations of motion of the center of mass of the descent vehicle has been compiled (see Fig. 5).

Let us compose the system of differential equations for the case of the descent vehicle moving in the central gravitational field of the Earth with the parameters
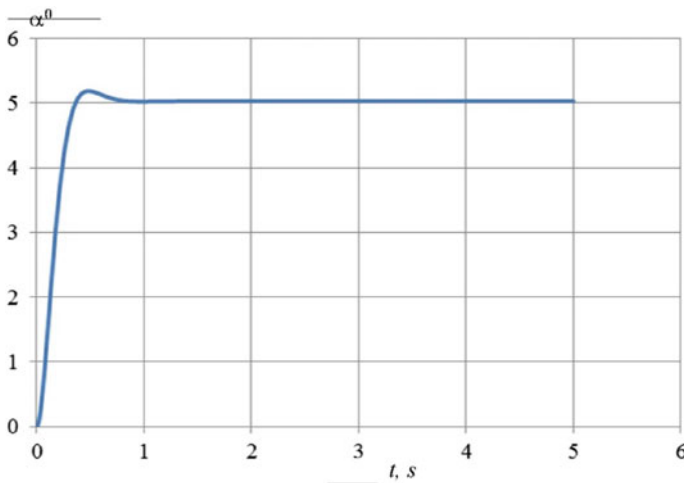
Fig. 4 Dependence of the angle of attack on time for a stationary flow taking into account damping

The position of the descent vehicle at different points in time

Conditional boundary of the atmosphere

Surface of the planet
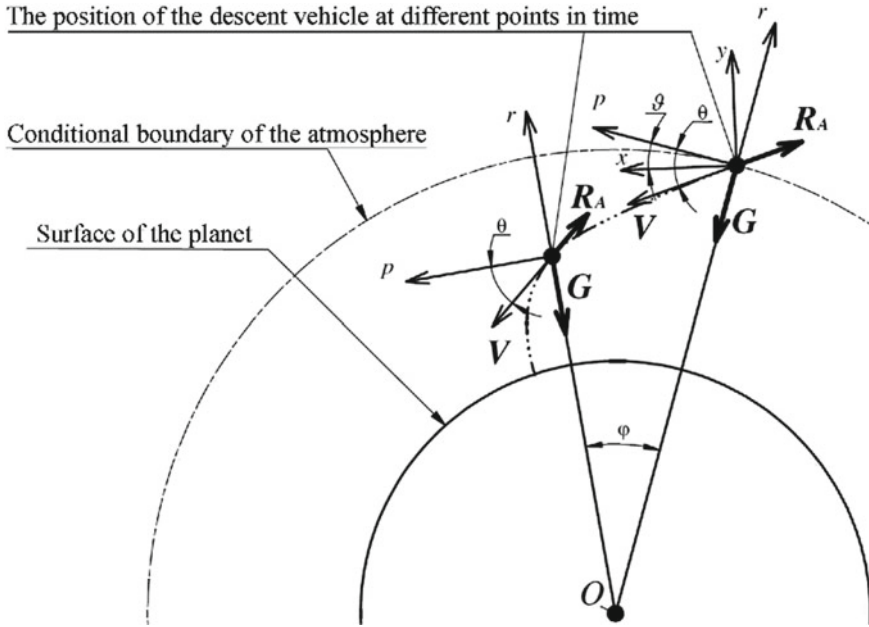
Fig. 5 Scheme of movement of the descent vehicle

of the atmosphere in the polar coordinate system. The polar coordinate system was chosen due to the fact that the movement occurs around the attracting center, which is taken as the origin of the given coordinate system, thus, the gravitational force will be directed along one of the axes of this coordinate system.

The equations of motion of a material point in polar coordinates are as follows:

$$\begin{cases} m(\ddot{\rho} - \rho\dot{\varphi}^2) = F_\rho; \\ m(\rho\ddot{\varphi} + 2\dot{\rho}\dot{\varphi}) = F_p, \end{cases} \tag{5}$$

where F_ρ, F_p—the projection of the vector of the resultant on the axis of the local coordinate basis [11].

Figure 6 shows a diagram of the movement of the descent vehicle. The following notation is introduced here:

φ the angle of rotation of the r axis relative to its initial position, which corresponds to the moment of entry into the atmosphere;

$\dot{\varphi} = \omega$ angular velocity of the axis r;

R_A full aerodynamic force;

G acceleration due to the action of the planet's gravitational field;

θ the angle of inclination of the velocity vector to the local horizon (angle of inclination of the trajectory);
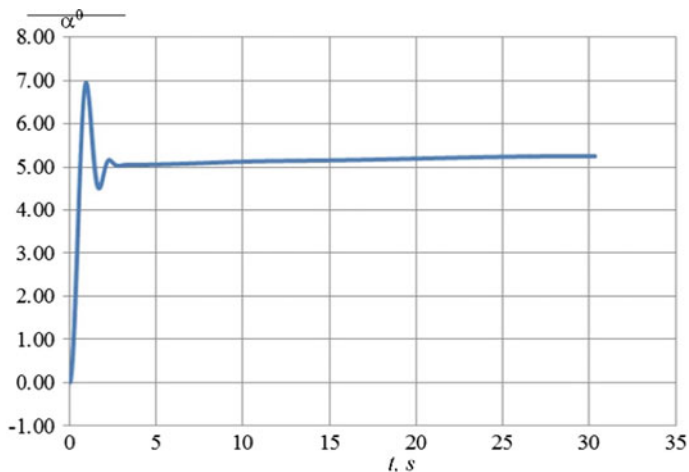
Fig. 6 Dependence of the angle of attack on time in a flow with changing parameters

Let us rewrite the system of differential Eq. (5) for those introduced in Fig. 4 designations:

$\rho = R$ radius connecting the center of mass of the Earth and the center of mass of the descent vehicle;

$\dot{\rho} = V_r$ the velocity along the axis r;

m the mass of the descent vehicle.

After substituting the introduced designations into the system of Eq. (5) and some transformations, we obtain a system of differential equations of the descent vehicle motion:

$$
\begin{cases}
\dot{V}_r = R\omega^2 - \left(G + \frac{X_a \sin\theta}{m} - \frac{Y_a \cos\theta}{m}\right) \\
\dot{\omega} = -\frac{X_a \cos\theta + Y_a \sin\theta}{mR} - \frac{2V_r\omega}{R}; \\
\dot{R} = V_r; \\
\dot{\varphi} = \frac{V\cos\theta}{R},
\end{cases}
\tag{6}
$$

where $V = \frac{V_r}{\sin\theta}; \theta = \text{arctg}\frac{V_r}{R\dot{\varphi}}$.

The position of the axes of the polar coordinate system changes over time; therefore, we write down the equation of rotational motion relative to the position of the axes corresponding to the moment the descent vehicle enters the atmosphere. To do this, we introduce the pitch angle ϑ (see Fig. 6), then we rewrite the equation of rotational motion as follows:

$$
\begin{cases}
\dot{\omega}_z = \frac{1}{J_z}\sum M_c, \\
\dot{\vartheta} = \omega_z;
\end{cases}
\tag{7}
$$

The angle of attack can be found from the relation $\alpha = \vartheta - (\theta - \varphi)$.

Let us solve the system of differential Eq. (6), together with the system of Eq. (7) in the presence of a damping moment and the following initial conditions: $V_0 = 7000$ m/s; $\theta_0 = -40°$; $H_0 = 80{,}000$ m; $\alpha_0 = 0$ rad. We get the result in the form of a graph of the change in the angle of attack versus time, which is shown in Fig. 6.

As you can see in the graph, the device vibrates the longitudinal axis with a maximum deviation of 7°. After the transient mode (in the steady state), the vehicle continues to move steadily at an angle of attack to the incoming flow of 5°. This type of movement allows you to limit the area of heat exposure. For uniform heating of the heat-shielding coating, it is assumed that the descent vehicle rotates around the longitudinal axis with an angular velocity of 30°/s.

To ensure the rotation of the descent vehicle, we will move its center of pressure in a direction perpendicular to the longitudinal axis, according to a sinusoidal law $\delta l \sin \omega_{\text{B}p}$.

Thus, the instantaneous value of the deviation of the center of pressure relative to the longitudinal axis will have the following value:

$$\Delta l = \delta l \cdot \sin \omega_{\text{B}p}. \tag{8}$$

Substituting Eq. (8) into the equation for finding the moment instead of and solving the differential equation of rotational motion relative to the center of mass together with the system of differential equations of motion of the center of mass, we obtain a graph of the angle of attack versus time, shown in Fig. 7.

The graph shows that the spinning of the descent vehicle around the longitudinal axis led to a slight decrease in the range of variation of the angle of attack.
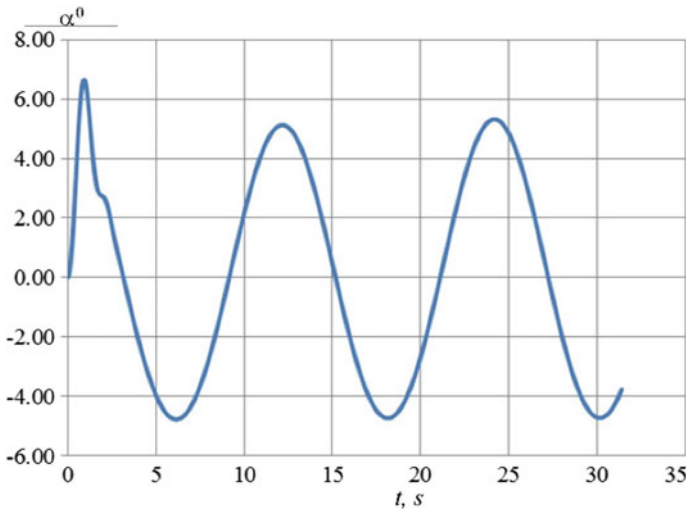
Fig. 7 Dependence of the angle of attack on time when the descent vehicle is twisted

3 Conclusions

This work investigates the stability of the descent vehicle motion at various parameters of the incoming flow. As a result of the study, the following results were obtained:

- in a stationary incoming flow, the descent vehicle performs harmonic oscillations (with an amplitude of 10°) relative to the center of mass without taking into account damping and damping taking into account it;
- when moving in a stream with changing parameters, the descent vehicle is stable in the presence of damping (the range of change in the angle of attack was 7°);
- twisting of the descent vehicle around the longitudinal axis with an angular velocity of 30°/s gives a slight decrease in the range of variation of the angle of attack.

Thus, it is shown in the work that the descent vehicle of the considered design will move steadily in the atmosphere provided there is damping.

References

1. Information on—https://exploration.esa.int/
2. Information on—https://mars.nasa.gov/
3. Koryanov V, Kazakovtsev V (2018) Dynamics of angular motion of landing vehicle in Martian atmosphere with allowance for small asymmetries. Int J Mech Eng Robot Res 7:385–391. https://doi.org/10.18178/ijmerr.7.4.385-391
4. Koryanov VV, Chen D, Wei X (2020) Research of using inflatable braking devices in the orbital service system application. J Phys: Conf Ser 1510(1):012005
5. Harri A-M, Pellinen R, Uspensky M, Siili T, Linkin V, Lipatov A, Savijärvi H, Vorontsov V, Ivankov A (2006) Metnet atmospheric science network for Mars
6. Harri A-M, Leinonen J, Merikallio S, Paton M, Haukka H, Polkko J, Linkin V, Lipatov V, Pichkadze K, Polyakov A, Uspensky M, Vasquez L, Guerrero H, Crisp D, Haberle R, Calcutt S, Wilson C, Taylor P, Lange C, Zarnecki J (2007) MetNet: in situ observational network and orbital platform to investigate the Martian environment
7. Heilimo J, Harri A-M, Aleksashkin S, Koryanov V, Arruego I, Schmidt W, Haukka H, Finchenko V, Martynov M, Ostresko B, Ponomarenko A, Kazakovtsev V, Martin S (2015) RITD—adapting mars entry, descent and landing system for earth
8. Marraffa L, Vennemann D, Anschuetz U, Walther S, Stelter C, Pitchkhadze K, Finchenko V (2003) RITD—inflatable re-entry and descent technology. 521:19
9. Finchenko VS, Pichkhadze KM, Efanov VV (2019) Inflatable elements in spacecraft structures—breakthrough technology in rocket and space technology. In: Kolmykova VA, Karchaev HJ (eds) Khimki. Publishing house of JSC "NPO Lavochkina", 488p
10. Lipnitsky YM, Krasilnikov AV, Pokrovsky AN, Shmanenkov VN (2003) Non-stationary aerodynamics of ballistic flight. Yu MM (ed) Doctor of technical sciences prof. Lipnitskiy. FIZMATLIT, 176p
11. Kilchevsky NA (1972) Course of theoretical mechanics, vol 1 (kinematics, statics, dynamics of a point). Main edition of physical and mathematical literature of the publishing house "Nauka", Moscow, 456pp

Electrode Shape Design and Current Density Distribution for Stable Plasma Beam Incinerator

Grich Kongphet, Tanakorn Wongwuttanasatian, and Amnart Suksri

1 Introduction

Nowadays, there are plenty of waste resulting from fast growing industries and more recently, hospital-borne waste. During the past year of 2020, an epidemic illness that led to a COVID-19 outbreak. Among other infectious waste, high temperature burner must be used for destroying the hazzardous waste so as not to affect the environment [1]. There were various methods of waste destruction using heat from hydrocarbon fuel burners that were widely used [2]. Apart from that, there is another method for generating extreme heat by converting electric energy into heat energy, namely the Plasma technology method [3].

Plasma has high energy and high temperature as the fourth state of matter [4]. The plasma technology method is an efficient method of generating high heat by arc process between positive and negative electrodes [5]. At the arcing time, there was an inert gas as an intermediate of ionization, where a vital parameter of the plasma torch was the design of the electrode used in the experiment.

Recently, researchers have designed various electrodes shapes. Zhang [6] introduces a single cathode and three cathode structures to investigate on the impact of plasma spraying. Patel [3] using pen shape plasma electrode design by longitudinal

G. Kongphet
Department of Electrical Engineering, Faculty of Engineering, Khon Kaen University, Khon Kaen, Thailand
e-mail: kogrich@kkumail.com

T. Wongwuttanasatian · A. Suksri (✉)
Center of Alternative Energy Research and Development, Faculty of Engineering, Khon Kaen University, Khon Kaen, Thailand
e-mail: samnar@kku.ac.th

T. Wongwuttanasatian
e-mail: tanwon@kku.ac.th

cylindrical to investigate the generated plasma for various application of surface modification. The proposed electrode in this research is implemented by simulating the computer program for a plasma tip generator. The comparison of current density and testing of plasma torch for three types of materials were studied.

2   Material and Method

The electrode materials selected for the plasma burners in this study were tungsten, copper, and graphite. The electrode material should have high electrical conductivity properties and high heat resistance [4]. Tungsten has a highest heat resistance than other materials when comparing on the melting point properties with other materials. Comparison of the three electrode materials from the actual test for the material's wear durability will be investigated from [2, 5]. Plasma Beam Size [7] and Plasma Beam Stability [8]. The Scanning electron microscope: SEM (D8 Advance, Bruker, United States) will be used for a comparison on surface deterioration.

   To compare the maximum current density at the electrode distribution of current density at electrodes and average of surface current density electrodes, a computer program (COMSOL®) simulates these four electrodes shapes using electrical parameters of the voltage DC 240 V, the current 40 A. The air gap between electrode is 1 mm and the feed gas is using compressed air. Based on previous studies, researchers have found some fundamental findings on the plasma formation process. Perambadur [9] has found that the current density at the tip of the electrode and the density of the current depends on the design shape and sharp edges at the electrode's tip. Wen [10, 11] investigated the plasma beam's optimal shape and a continuity of the stable plasma beam. Simulation of selected electrode shapes was performed under the same configuration condition. Each design of the proposed shape of electrode is shown in Fig. 1. Shape A electrode has been referenced from previous researcher (Zhang) [6], with the shape of the electrode having a sharp spherical shape as shown the Fig. 1. The shape B electrode evolved from shape A with a pyramid shape with a 3-sided base cut off the pointed top. The shape C electrode was similar to shape B but differs from a four-sided pyramid shape and cut off at the pointed top. The shape D electrode has evolved from shape A, but the top end cut was performed and grooved on the electrode's side [12].
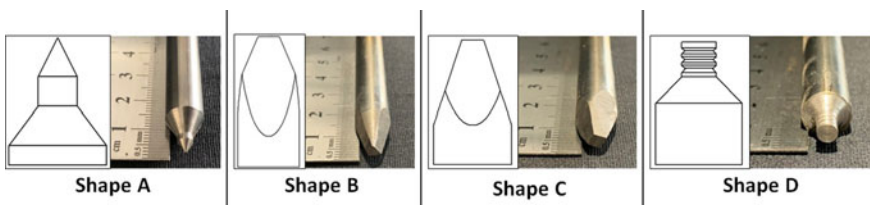
Fig. 1 Electrodes design shapes
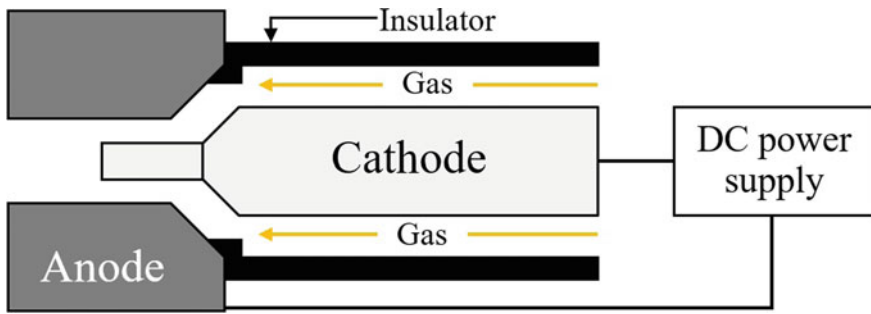
Fig. 2 Plasma generator

2.1 The Component of the Plasma Generator

The plasma generator is divided into three sections: a DC power supply, a gas feeder, and a proposed electrode, as shown in Fig. 2. The power supply voltage was DC 240 V at 40 A. The gas use can be a compress air or argon at 0.5 bar with an air gap of 1 mm between electrodes. Copper, graphite, and tungsten-based materials were fabricated for the tested electrodes. After testing, the electrodes will be examined by scanning electron microscope (SEM) for the material's durability against thermal erosion.

3 Result and Discussion

3.1 Current Density

From the COMSOL computer simulation program, the maximum value of the current density, the mean value of current density was obtained and shown in the Table 1. The electrode with the highest current density value was shape A with the value at 25.7×10^6 A/m^2. The highest average surface current density (359,055 A/m^2) of electrodes was shape A. Finally, the distribution of the current density topology around the electrode was observed from Fig. 3. It was found that the shape A electrode has the most uniform current density distribution and follow by electrode shape B, C, and D. Based on simulation results, it was expected that, the A-shape is most suitable

Table 1 Current density value

	Shape A	Shape B	Shape C	Shape D
Current density maximum ($\times 10^6$ A/m^2)	25.7	2.99	2.05	1.48
Average surface current density (A/m^2)	359,055	355,342	353,397	312,226
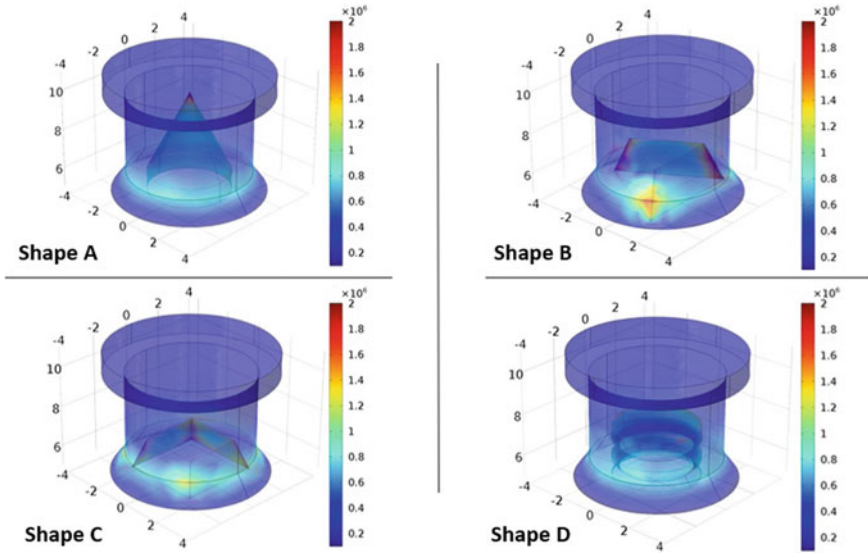
Fig. 3 Simulation results of current density distribution

for plasma beam generation when the maximum value of current density at the electrode is considered. Although the shape A electrode was suitable for producing a plasma beam, the shape B electrode had better current density distribution at the area between the electrodes than the A-shape. Furthermore, researcher have observed that the resulting plasma beam produced was stable from the actual test for the B type shape.

3.2 Surface Topology

The durability of the tested material resulting from the test was found that the tungsten electrode surface was not damaged nor eroded at the tip of the electrode. Followed by the graphite at the tip of the electrode was slightly worn. Furthermore, copper electrode had a tremendous erosion at the electrode end tip from the imaging of SEM as shown in Fig. 4.

The shape A electrode had slightly thermal erosion at the tip of the electrode head as shown in Fig. 5. Electrodes type B and C were found to have cracked at the contact surface of the electrode end cross-section. It was also observed that the square edge was more thermally corroded. Finally, the D type electrode was found to have more thermal erosion at the spherical cross-sectional area and at the rounded edge.
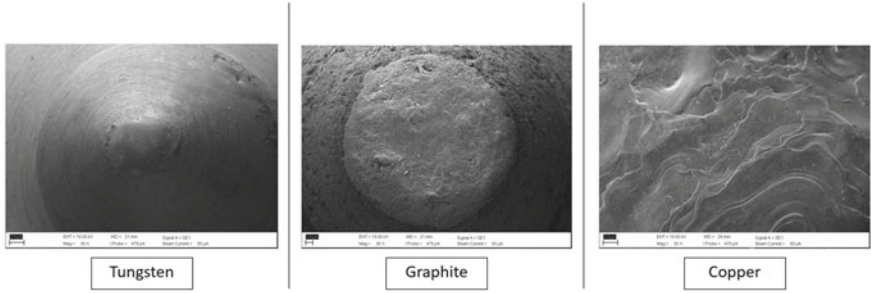
Fig. 4 SEM image of electrode tip for each type of material
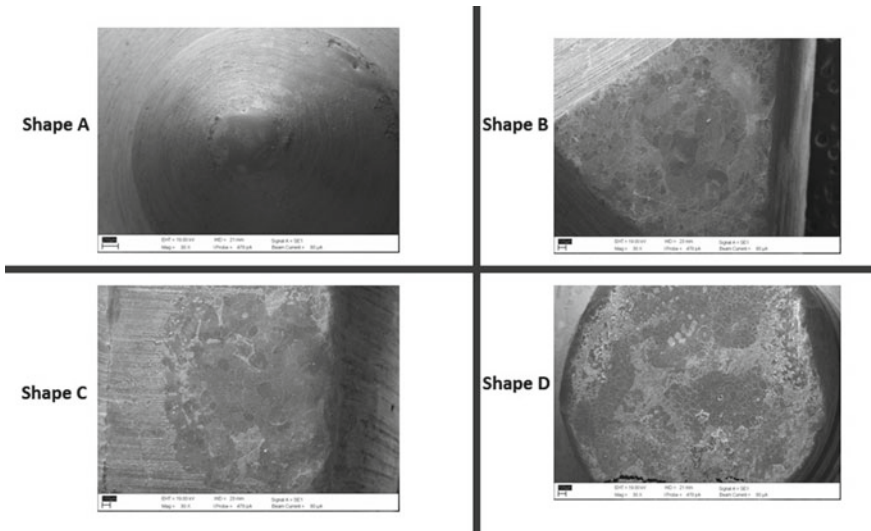
Fig. 5 SEM image of each electrode type

3.3 Plasma Torch

Plasma torch size observation was found that the maximum length of 31 mm with a width of 6 mm was obtained from a shape B as shown in Fig. 6. Also, the materials that produce the longest and widest plasma beam dimensions are tungsten. The plasma beam's stability showed that the shape B electrode had the continuous plasma beam stability. The most continuous and stable electrode material for the merit order was tungsten, graphite, and copper, respectively. Each plasma flame shape of the designed electrode type was taken with digital camera as shown in Fig. 6.
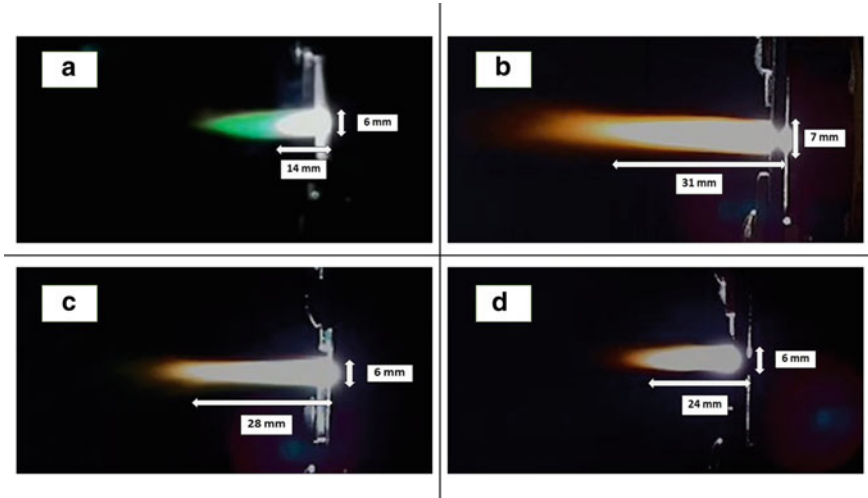
Fig. 6 Plasma length and size for each designed electrode shape

4 Conclusion

Based on computer simulations comparing the current density distribution at the electrode, the proposed electrode designed was based on current density distribution values with the constructed electrodes tip design. The actual test results and simulations with computer programs found that Shape B electrodes are most suitable for plasma beam formation. The longest plasma beam produced a flame length of 31 mm, and a width of 7 mm was obtained from type B shape. The electrode tip of shape B at the edge and the triangular cross-sectional area has major contribution for the plasma to initiate after the electrode material was energized by the power supply. Although the average surface current density values were found to have relatively close to each other, shape A has the highest current density. Each designed electrode tip was then examined by Scanning Electron Microscope for the surface deterioration after it has been tested. Tungsten electrode has found to perform well against corrosion resistance and producing largest plasma beam in size as well as stable plasma flame. As a result of testing, tungsten has the best corrosion resistance, largest plasma beam size, and the best plasma beam uniformity, suitable for use as a plasma incinerator for waste disposal.

References

1. Vecten S, Wilkinson M, Bimbo N, Dawson R, Herbert BMJ (2021) Experimental investigation of the temperature distribution in a microwave-induced plasma reactor. Fuel Process Technol 212:106631
2. Surov AV et al (2017) Multi-gas AC plasma torches for gasification of organic substances. Fuel 203:1007–1014
3. Patel AR, Shukla AN (2018) Design and experiments on pen-shaped plasma torch for surface modification. Alexandria Eng J 57(4):3199–3203
4. Yamamoto Y, Tachibana T (2016) Feasibility study of water plasma jets for combustion promotion. Fuel 186:846–852
5. Voltolina S et al (2016) Assessment of plasma torches as innovative tool for cleaning of historical stone materials. J Cult Herit 22:940–950
6. Zhang D, Zheng L, Hu X, Zhang H (2016) Numerical studies of arc plasma generation in single cathode and three-cathode plasma torch and its impact on plasma spraying. Int J Heat Mass Transf 98:508–522
7. Mašláni A, Sember V, Hrabovský M (2017) Spectroscopic determination of temperatures in plasmas generated by arc torches. Spectrochim Acta—Part B At Spectrosc 133:14–20
8. Pan W, Chen L, Meng X, Zhang Y, Wu C (2016) Sufficiently diffused attachment of nitrogen arc by gasdynamic action. Theor Appl Mech Lett 6(6):293–296
9. Perambadur J, Klimenko AY, Rudolph V, Shukla P (2020) The investigation of arc fluctuations in thermal plasma torch using 3D modeling approach. Int J Heat Mass Transf 165:120666
10. Wen K et al (2019) Numerical simulation and experimental study of Ar-H2 DC atmospheric plasma spraying. Surf Coatings Technol 371(April):312–321
11. Wen K et al. (2019) 3D time-dependent numerical simulation for atmospheric plasma spraying. Surf Coatings Technol 371:344–354
12. Kuzmin V, Gulyaev I, Sergachev D, Vashchenko S, Lysakov A, Palagushkin B (2020) Supersonic air-plasma spraying of carbide ceramic coatings. Mater Today Proc xxxx

Influence of Materials and Their Constitutive Laws on the Stress Fields Produced in the Residual Limb of a Transfemoral Amputation

Armando Ramalho, Miguel Ferraz, Marcelo Gaspar, and Carlos Capela

1 Introduction

The friction coefficient between the various components of a prosthesis and the contacting biological tissues has a significant influence on the intensity of the shear stresses generated at the interfaces of the biological materials of lower limb osteotomized patients [1, 2]. Furthermore, the distribution of shear stresses at the interface between the liner and the soft tissues is referred to as one of the leading causes of pressure ulcers in patients with transfemoral amputation [3].

Even though it is widely recognized that the materials' constitutive laws have a significant influence on the stress fields generated at the residual limb (when interacting with the combined socket prosthesis), most simulations of these biomechanical systems using the finite element method (FEM) still use linear elastic models [4–7]. Thus, such linear elastic models are mostly suitable for simulating most rigid materials, *e.g.*, cortical bone and the vast majority of hard sockets prosthesis.

A. Ramalho (✉)
Polytechnic Institute of Castelo Branco, Castelo Branco, Portugal
e-mail: aramalho@ipcb.pt

M. Ferraz · M. Gaspar · C. Capela
Polytechnic Institute of Leiria, Leiria, Portugal
e-mail: marcelo.gaspar@ipleiria.pt

C. Capela
e-mail: carlos.capela@ipleiria.pt

A. Ramalho · C. Capela
Centre for Mechanical Engineering, Materials and Processes (CEMMPRE), Univ Coimbra, Coimbra, Portugal

M. Gaspar
Centre for Rapid and Sustainable Product Development (CDRSP), Leiria, Portugal

However, this model is not suitable for more flexible materials when subjected to large deformations, namely the liners and the soft tissues [8–10].

In most simulations using FEM, the soft tissues are generally approached as homogeneous and isotropic materials. Nonetheless, the use of software that allows generating geometries with various components collected from medical images (*e.g.*, Materialize) provide for the simulation of these materials in a more realistic way, thus separating the soft tissues into their main components—skin, fat, muscle, blood vessels, fascia—and allowing for considering the anisotropy of their properties [9].

The mechanical characterization of biomaterials that allows the definition of its constitutive law is widely available in the current literature [8, 10]. However, this characterization is limited when considering biological materials. This is mainly due to the fact that these materials' characterization is strongly endogenous. In most simulations using the FEM of biomechanical systems, soft tissues are characterized by a linear elastic model. Nonetheless, this approach does not seem adequate when these biological materials are subject to large deformations. Thus, according to the literature, hyperelastic models are the most used for nonlinear soft tissue mechanical characterization [9, 11, 12]. The main hyperelastic models used in the simulation of soft tissues' constitutive law are the Mooney-Rivlin model (in their Mooney second and third-order variants) and the Neo-Hookean model, the Yeoh model and the Ogden model.

In this study, the stress field at the prosthesis interfaces (of a patient with transfemoral amputation) is assessed using FEM numerical simulation. The influence of the constitutive law applied in modelling the mechanical behaviour of the liner material, and the soft tissues, are analyzed and discussed. Additionally, the friction coefficient between the prosthesis and the liner, the liner and the skin and between the soft tissues and the femur are also analyzed and discussed. The model previously presented by the authors in Ramalho et al. [1] is improved in terms of the geometry and the materials characterization. For the manufacturing of the prosthesis, propylene thermoplastic is compared with the use of an epoxy resin in which the majority of the molecular structure is of vegetable origin (SR GreenPoxi 56) produced by Sicomin. In most of the simulations presented, a composite material is used for prosthesis manufacturing in which the GreenPoxi resin is reinforced with natural jute fibres. This composite is modelled as a linear elastic material with anisotropic behaviour.

2 Finite Element Model

2.1 Geometry

The two-dimensional finite element model previously presented by the authors in Ramalho et al. [1] has been improved in terms of geometry definition. Several points were collected from the femur and limb profiles presented in Hoellwarth et al. [13]. These points allowed for modelling the profiles of these organic components using
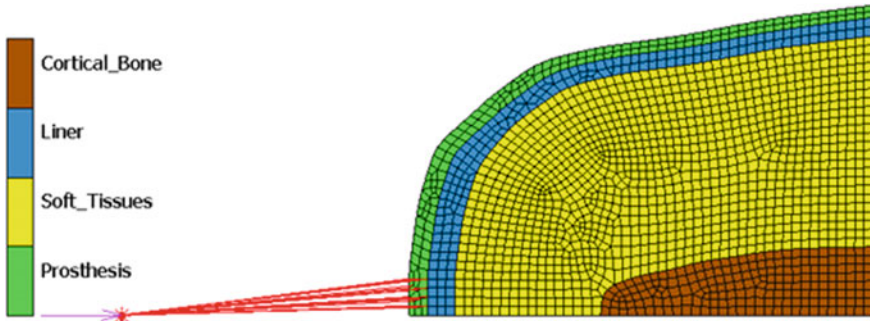
Fig. 1 Geometry, mesh and deformable bodies of the numerical model

cubic spline interpolation. The previous 2D axisymmetric formulation was maintained. An elastic foundation is used to support the patient's limb. To increase the damping effect, the liner's thickness was reinforced in the distal part of the stem [4, 7]. The connection between the socket and the pylon, taking into account its rigidity, is modelled through a REB2 type connection [14].

Three materials were considered to build the socket type prosthesis model: the thermoplastic previously used in Ramalho et al. [1], propylene, the SR GreenPoxi 56 resin produced by Sicomin and a composite in which the SR GreenPoxi 56 is reinforced with natural jute fibres. Considering the mechanical properties of these materials, the prosthesis's thickness was increased in the distal part of the stump, where the stresses in the prosthesis are higher.

The geometry, finite element mesh, and the model's various components are presented in Fig. 1.

2.2 Mechanical Properties of the Materials—Constitutive Laws

Biologic Materials. The femur is modelled as an isotropic, homogeneous and linear elastic material. The cortical bone properties are considered along the longitudinal direction [15], with an elastic modulus, $E = 11.5$ GPa, and Poisson's ratio, $\nu = 0.31$.

For the soft tissues, two different models were used: the Neo-Hookean model (presented in Portnoy et al. [12]) for the muscle, with $C_{10} = 4.25$ kPa and the volumetric behaviour obtained only with the first term of the series, $D1 = 24.34$ MPa^{-1}; the first order Ogden model (presented in Kallin et al. [9]) for the muscle, with the ground state shear modulus $\mu = 1907$ kPa, strain hardening $\alpha = 4.6$ and volumetric behaviour obtained only with the first term of the series, $D1 = 10.5$ MPa^{-1}.

To compare the results using the hyperelastic model with those of the linear elastic model (after acquiring the stress field in the soft tissues), the properties of an equivalent elastic material were computed. The volume deformation energy was equivalent

to that absorbed in both simulated hyperelastic models for the equivalent elastic material. In this process, the Poisson's ratio was fixed at $\nu = 0.45$, corresponding to an approximately incompressible situation. The equivalent elasticity coefficients' values were $E_{equNH} = 0.0534$ MPa (Neo-Hookean model) and $E_{equO} = 0.0196$ MPa (Ogden model).

Liner. When modelling the liner, the experimental results presented in Sanders et al. [10] were used. Four different liners were chosen from each presented stiffness classes, ordered from C_1 to C_4 by increasing stiffness value. For the more rigid class, C_1, an elastomer was selected, the Fillauer Silicone liner, produced by Fillauer, Inc., Chattanooga, Tennessee; for the next class, C_2 a polyurethane, TEC Pro 18, produced by TEC Interface Systems, Waite Park, Minnesota; for class C_3 an elastomer, Iceross Comfort, produced by Ossur USA, Inc., Columbia, Maryland was chosen; for the most flexible class, a gel was selected, the Super Stretch, made by ALPS, St. Petersberg, Florida. The selection of these materials was based not only on their stiffness value but also considering the corresponding friction coefficient between that material and human skin. These friction coefficient values were also ordered in different classes (F_1 to F_4), from the highest to the lowest.

The experimental results were approximated fitting time-independent data by differential evolution, using the finite element software MSC Marc 2018 [14]. In the approximation, the results available in Sanders et al. [10], corresponding to the tensile, compression and pure shear tests, were taken into account. Among the hyperelastic models (H M) available, the best approximations for the selected liners corresponded to the second-order Mooney-Rivlin (M-R) and Yeoh models, shown in Table 1. The friction coefficient (FC) shown in the table refers to the friction between the liner and the skin. Also is defined a stiffness class (S C) and a friction class (Fr C) for the liners.

On an initial exploratory study, the constitutive equations presented in Łagan and Liber-Kneć [16] were used on the liner, for a Neo-Hookean model, with $C_{10} = 23$ kPa and the bulk modulus of 230 MPa.

Prothesis. For the socket type prosthesis composition, three different materials were analyzed: propylene thermoplastic; an epoxy resin in which most of the molecular structure is of vegetable origin (SR GreenPoxi 56 produced by Sicomin) and a composite material in which an SR GreenPoxi 56 resin matrix is reinforced with jute fibres.

The propylene thermoplastic is modelled as homogeneous, isotropic and linear elastic, based on the mechanical properties presented in Silver-Thorn and Childress [17], with an elastic modulus (E) of 1000 *MPa* and the Poisson's ratio $\nu = 0.30$.

SR GreenPoxi 56 resin is also modelled as homogeneous, isotropic and linear elastic, based on the properties presented in Perrier [18] with an elastic modulus (E) of 3000 *MPa*, a Poisson's ratio $\nu = 0.39$ and the specific mass $\rho = 1180$ kg/m^3.

The jute fibre is modelled as homogeneous, 2D orthotropic and linear elastic, based on the properties presented in Suthenthiraveerappa and Gopalan [19], with elastic modulus $E_1 = 23,949$ MPa and $E_2 = 978$ MPa, the Poisson's ratio $\nu_{12} =$

0.374 and $\nu_{21} = 0.014$, the shear modulus $G_{12} = 411$ MPa and the specific mass $\rho = 1440$ kg/m^3.

Based on the Halpin–Tsai model for discontinuous fibres, the composite material's elastic properties (SR GreenPoxi 56 resin matrix reinforced with jute fibres) were computed in the MSC Patran 2019 software [20] considering a 60/40% for the resin/fibre volume ratio. A 10 to 1 ratio was considered for the fibres' length vs diameter.

The fibre of this composite was later dispersed using a 2D short fibre model implemented in the MSC Patran 2019 software [20], with angles $\alpha = 0°$ and $\phi = 45°$, a standard deviation of 10° through a random process, with zero correlation, using 1000 Monte Carlo iterations. The elasticity matrix of this composite is represented in Eq. (1). The composite was oriented so that axis 1 has, at each point, the direction of the tangent to the prosthesis profile shown in Fig. 1. Axis 2 has the direction of thickness and axis 3, the radial direction [14].

$$[C_{ij}] = \begin{bmatrix} 1.30 \times 10^5 & 1.39 \times 10^5 & 1.26 \times 10^5 & 3.07 \times 10^1 \\ 1.39 \times 10^5 & 1.59 \times 10^5 & 1.40 \times 10^5 & 5.04 \times 10^1 \\ 1.26 \times 10^5 & 1.40 \times 10^5 & 1.31 \times 10^5 & 5.32 \times 10^1 \\ 3.07 \times 10^1 & 5.04 \times 10^1 & 5.32 \times 10^1 & 2.10 \times 10^3 \end{bmatrix} \text{(MPa)}. \qquad (1)$$

Table 1 Hyperelastic models used for various liners

Liner	S C	FC/Fr C	H M	Parameters and coefficients
Fillauer silicone	C_1	$\mu_f = 0.6$	Yeoh	$C_{10} = 0.923252$ kPa
		F3		$C_{20} = 2.18386e\text{-}05$ kPa
				$C_{30} = 44.9592$ kPa
TEC Pro 18	C2	$\mu_f = 1$	M-R	$C_{10} = 1.5152e\text{-}06$ kPa
		F1		$C_{01} = 41.365$ kPa
TEC Pro 18 L	C2	$\mu_f = 0.65$		$C_{11} = 9.4846e\text{-}7$ kPa
		F1		Bulk Modulus = 413,650 kPa
Iceross comfort	C3	$\mu_f = 0.4$	M-R	$C_{10} = 2.19397e\text{-}05$ kPa
		F4		$C_{01} = 20.775$ kPa
				$C_{11} = 1.28457e\text{-}05$ kPa
				Bulk Modulus = 207,750 kPa
Super stretch gel	C4	$\mu_f = 0.65$	M-R	$C_{10} = 1.23146e\text{-}04$ kPa
		F2		$C_{01} = 10.5949$ kPa
				$C_{11} = 2.89243e\text{-}9$ kPa
				Bulk Modulus = 105,905 kPa

2.3 Friction Model

In the contact between the system's various components, a Coulomb's bilinear friction model was used, with an average friction coefficient between the cortical bone and the soft tissues of $\mu = 0.3$ [21]. A friction coefficient of $\mu = 0.5$ was considered for the contact between the socket type prosthesis made of SR GreenPoxi 56 and the liner [22]. When the prosthesis is made of propylene, a friction coefficient of $\mu = 0.6$ between the prosthesis and the liner was kept [1]. On the contact between the liner and the soft tissues, the friction coefficient varies, considering each of the liners, the values shown in Table 1. In the numerical model, the contact between deformable bodies is modelled by the finite sliding segment-to-segment contact algorithm. The separation criteria are based upon stresses (Lagrange multipliers): separation threshold is treated as residual stress of negligible magnitude (0.9e-06 MPa).

2.4 Finite Element Analysis

Given the symmetry of the model, a 2D axisymmetric analysis was performed. The simulations with this model were made using the implicit module of MSC Marc Mentat 2018 [14]. A multifrontal direct sparse solver, the Paradiso solver, is used with a Newton–Raphson iterative procedure. For convergence testing, a relative force tolerance of 10% is used. An adaptative multicriteria stepping procedure is used for load increment—was used the initial time step (load increment) of 1e-06. The numerical constrictions associated with the implicit method were overcome using a mesh adaptivity algorithm, the advancing front quadrilateral. An automatic algorithm was used for meshing, and linear quadrilateral axisymmetric solid elements with four nodes (Quad 10) were used. The initial mesh dimensions of the elements were 3 mm. This value was established in a previous iterative process and is considered an objective in the adaptive mesh algorithm. In this process, the mesh size may be reduced to a quarter of its initial value, depending on the strain change and the distortion that may take place in each element [1]. In the structural analysis, large strain nonlinear procedures were used. Based on an automatic algorithm depending on the constitutive law, the Multiplicative Updated Lagrange procedure is preferential for hyperelastic materials.

2.5 Loading

The prosthesis is considered to support the patient's total weight (70 kgf) during the static stance. Loading is imposed in quasi-static conditions [1], as illustrated in Fig. 1.

3   Numerical Simulations Planning

A preliminary simulation was carried out to compare the effect of the constitutive low on the stress field produced at the prosthesis's different components. Model 3, presented in Ramalho et al. [1], was simulated varying only the liner and soft tissues' constitutive law. The geometry and all of the remaining parameters were maintained. For the soft tissues, the Neo-Hookean model presented in Portnoy et al. [12] was used, whereas, for the liner, a Neo-Hookean behaviour with the parameters of in Łagan and Liber-Kneć [16] was considered. The constitutive law used for soft tissues has a much less rigid behaviour than that of the previously used linear elastic model. In addition, the volumetric compressibility is also much lower in the constitutive low. Thus, much higher deformation and normal (80%) and shear stresses (40%) were observed for the same loading. However, it appears that this variation is much smaller in terms of biological tissues. The resulting normal and shear stress fields (MPa) are shown in Fig. 2.

This pilot simulation allowed outlining a set of simulations to be carried out with the geometry presented in Fig. 1. In addition to the influence of the constitutive low, the simulations focused on the effect of friction. When comparing models, it was essential to take into account the stiffness and the volumetric compressiveness. Considering that the study presented in Sanders et al. [10] provides the required data for the range of liners available in the market, it was decided to use that data for the parameters of current work, according to Table 1.

The first simulations led to the rupture of the propylene-based prosthesis. Thus, considering the more sustainable nature of the bio epoxy and the improved mechanical properties, the GreenPoxi 56 resin was selected for current research with and without the reinforcement of natural jute fibres. Thus, to study the influence of friction and the constitutive law of materials in the stress fields produced in the biological tissues of a patient with a transfemoral amputation, the simulations presented in Table 2 were carried out.

4   Results and Discussion

The biological tissues use most of the volume of the numerical model. This verifies that the constitutive law used in its modelling has a significant effect on the results.

Figure 3 shows the stress distribution (MPa) in the biological tissues of the $A5$ model, which is considered representative of the generic distribution that occurred in the various simulations in which the soft tissues were characterized with the Neo-Hookean model.

On what concerns the normal stresses, it can be observed that at the biological tissues level, the highest stresses take place at the interface between the femur and the soft tissues (on the distal part of the femur at the osteotomized section).
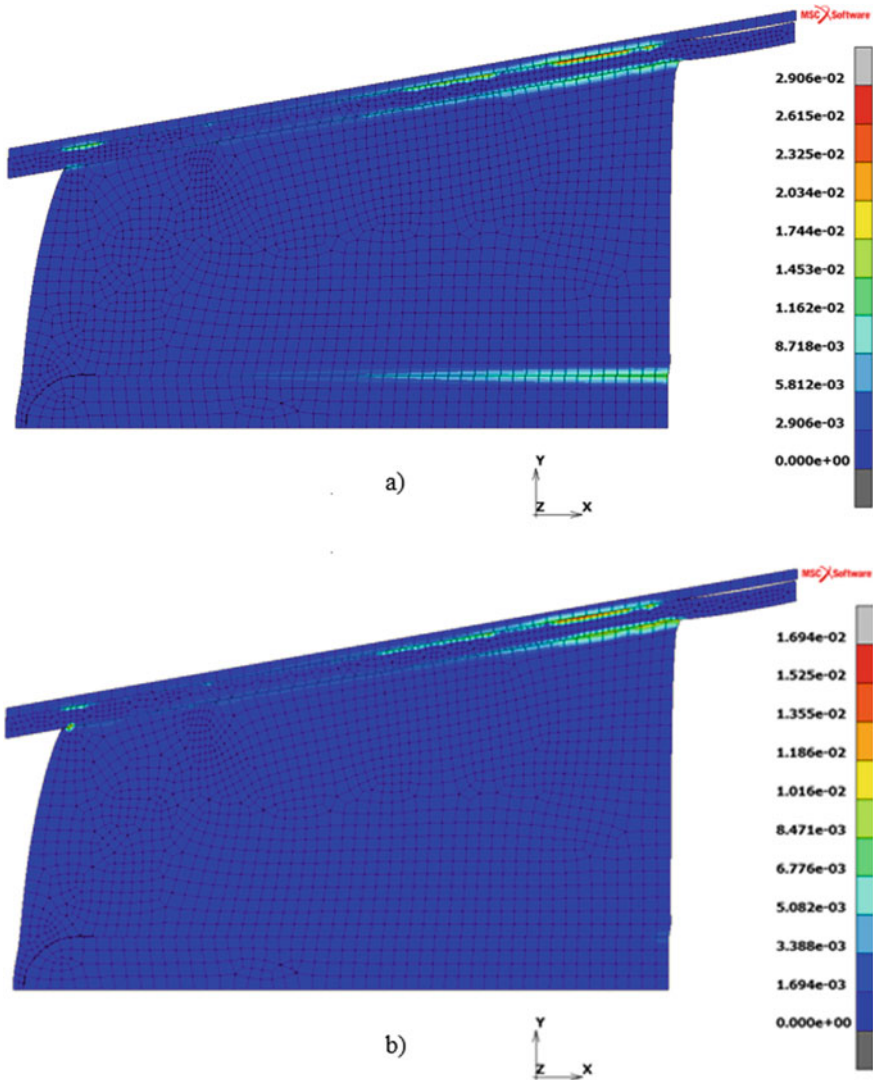
Fig. 2 Preliminary study. **a** Normal contact stresses. **b** Shear contact stresses

On what refers to the shear stresses, it can also be observed that the higher stresses occur either at the interface between the liner and the soft tissues (in the proximal part of the liner), or close to the femur (in the region adjacent to that in which the maximum normal tensions take place). This distribution varies significantly in intensity for the various simulations.

Figure 4 shows the stress distribution (MPa) in the biological tissues of the A8 simulation, which is considered representative of the generic distribution that

Table 2 Characterization of the performed simulations

Simulation	Soft tissues constitutive law	Prosthesis material	Liner
A1	Neo-Hookean	Propylene	TEC Pro 18
A2	Neo-Hookean	GreenPoxi 56	TEC Pro 18
A3	Neo-Hookean	GreenPoxi 56	TEC Pro 18L
A4	Neo-Hookean	Composite	Fillauer Silicone
A5	Neo-Hookean	Composite	TEC Pro 18
A6	Neo-Hookean	Composite	Iceross Comfort
A7	Neo-Hookean	Composite	Super Stretch Gel
A8	Ogden	Composite	TEC Pro 18
A9	Elastic equivalent Neo-Hookean	Composite	ElasEqTEC Pro 18
A10	Elastic equivalent Ogden	Composite	ElasEqTEC Pro 18
A11	Neo-Hookean	Composite	TEC Pro 18L
A12	Elastic equivalent Neo-Hookean	Composite	TEC Pro 18L

occurred in the various models in which the soft tissues were characterized with the Ogden model.

This figure shows that at the biological tissues' level, the maximum normal stress occurs at the interface between the liner and the soft tissues (on the distal part of the stump).

On what concerns the shear stresses, the highest stresses occur at the interface between the liner and the soft tissues (in the proximal part of the liner). This distribution varies significantly in intensity for the various simulations.

Finally, it can be observed that in the area where the normal contact stresses are highest, the shear stresses are neglectable, as there is no slip.

The highest values of normal and shear contact stresses that take place at the interfaces of the various components of the prosthesis (σ and τ) and the biological tissues (σ_B and τ_B) are shown in Table 3, as well as the equivalent Von Mises (σ_{VM}) stress that occurs in the prosthesis (hard socket).

In the initial simulations (*A1-A3*), it can be observed that the stiffness increase of the prosthesis material leads to a slight decrease in contact stresses, as well as in the equivalent Von Mises stress that occurs in the prosthesis. The significant material stiffness increase does not lead to a very substantial change in the maximum stresses
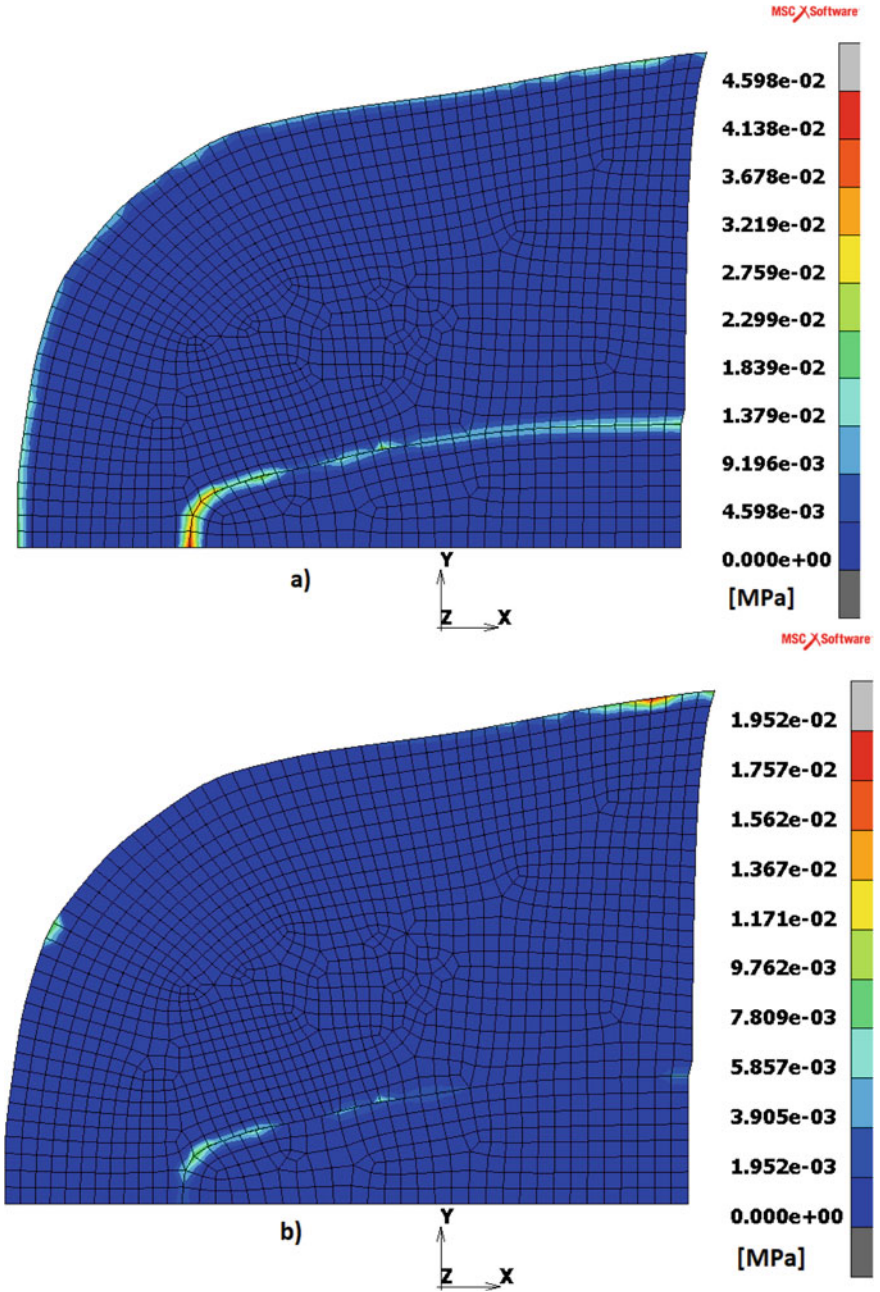
Fig. 3 Contact stresses at biological tissues, *A*5 model. **a** Normal stresses. **b** Shear stresses
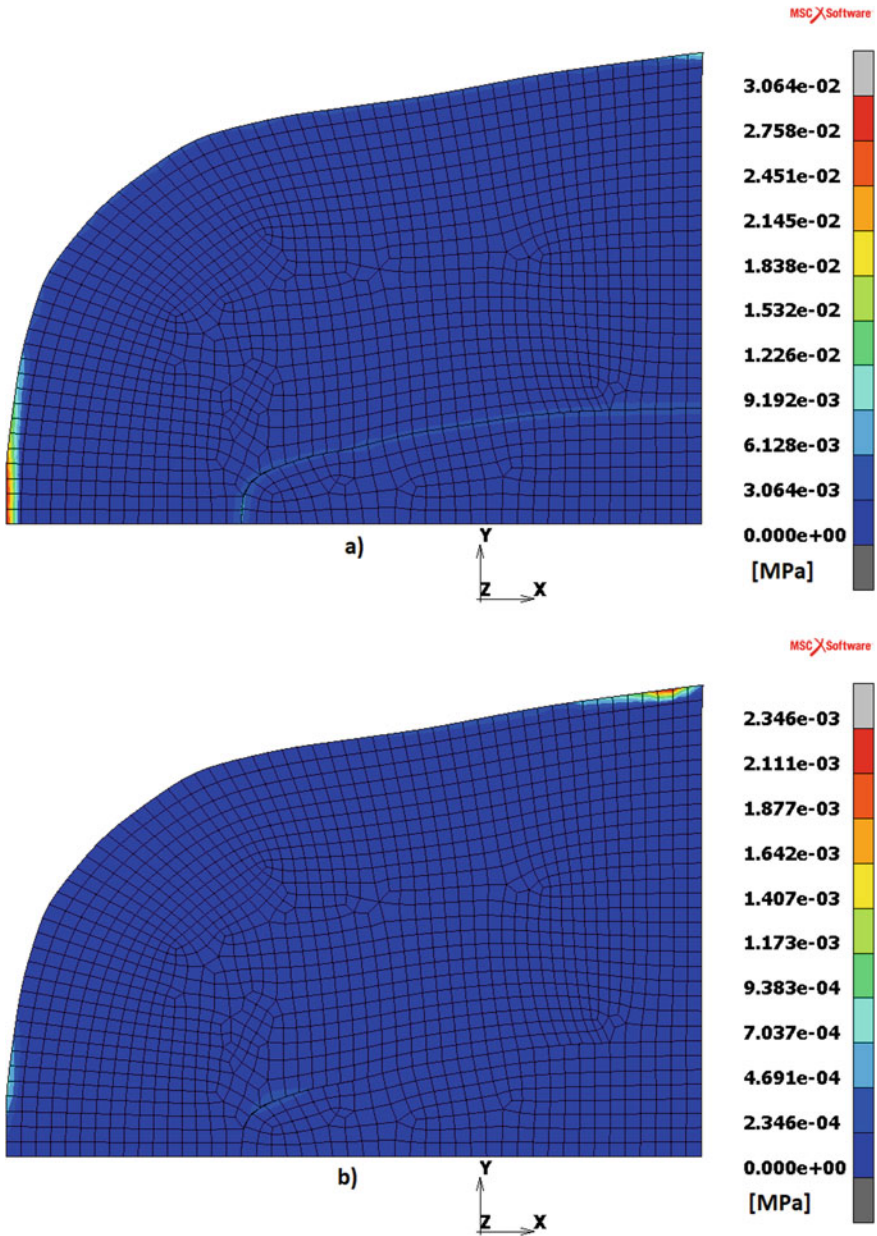
Fig. 4 Contact stresses at biological tissues, *A*8 model. **a** Normal stresses. **b** Shear stresses

Table 3 Summary of the simulation results

Simulation	σ (kPa)	τ (kPa)	σ_B (kPa)	τ_B (kPa)	σ_{VM} (MPa)
A1	68.24	17.94	68.24	17.94	63.84
A2	56.27	14.43	56.27	14.43	55.45
A3	44.86	3.09	14.53	3.09	54.81
A4	46.45	13.67	46.45	13.37	14.78
A5	67.84	19.52	45.98	19.52	13.77
A6	51.57	9.40	51.57	7.38	14.87
A7	68.57	19.50	36.29	10.37	13.59
A8	21.86	4.04	30.64	2.35	10.16
A9	60.47	18.88	60.47	17.93	14.99
A10	33.17	5.58	11.35	5.58	13.10
A11	50.06	14.52	50.06	14.52	14.34
A12	45.12	18.11	45.12	16.52	14.98

due to the influence of the prosthesis's small thickness on the overall stiffness of the structure. In the case of A3 simulation, reducing the friction coefficient between the liner and the soft tissues leads to a significant decrease in the normal and shear stresses at the interfaces. It is observed that the stresses that take place in the prosthesis exceed the resistance stresses of the materials [16, 20]. The use of a short fibre composite has the particularity of increasing the stiffness of the material and also of the whole prosthesis. According to Eq. (1), this occurs by decreasing the membrane effect with the significant increase in stiffness in the direction of thickness, resulting from the short fibres' orientation. The substantial increase in normal stresses observed along direction 2 (alongside the thickness) leads to a significant decrease in the equivalent Von Mises stress that occurs in the prosthesis, also leading to some changes in the distribution in the contact stress field (A2 and A5).

The decrease in friction between the liner and the soft tissues seems to lower, with some consistency, the shear stresses. When comparing the evolution of these shear stresses in simulations A5, A7, A4 and A6, the inconsistency between the results of A7 and A4 can be explained due to the Yoeh model used in A4. This effect is more evident when comparing the results of simulations A5 and A11, in which the only change observed is for the friction coefficient between the liner and the soft tissues, which changes from 1 to 0.65. The friction decrease leads to an increase in the normal contact stress and a reduction in the shear contact stress. These results, focusing on the friction coefficient variation, are consistent with those presented in Zhang et al. [23].

The effect of the constitutive law used in the characterization of soft tissues, and the liner, can be observed when comparing the use of hyperelastic models in simulations A11, A5 and A8 with the equivalent linear elastic simulations A12, A9 and A10. Thus, at the biological tissues level, one can observe a significant decrease in the normal contact stresses and a slight increase in the shear contact stresses.

5 Conclusions

The developed Finite Element Model reveals to be effective when assessing the effects of friction on the residual limb of a transfemoral amputee.

The results obtained allow evaluating the influence of the friction coefficient between the prosthesis, the liner and the soft tissues on the whole biomechanical system's stress distribution.

The stiffness and the anisotropy of the prosthesis material effectively influence the contact stresses field developed in the residual limb of a transfemoral amputation.

The friction between the liner and the soft tissues has an effective influence on the field of contact stresses developed in the residual limb of a transfemoral amputation.

The constitutive laws used to characterize liner and soft-tissue materials effectively influences the fields of contact stresses developed in the residual limb of a transfemoral amputation.

References

1. Ramalho A, Ferraz M, Gaspar M, Capela C (2020) Development of a preliminary finite element model to assess the effects of friction on the residual limb of a transfemoral amputee. Mater Today Proc 33:1859–1863
2. Ramírez JF, Vélez JA (2012) Incidence of the boundary condition between bone and soft tissue in a finite element model of a transfemoral amputee. Prosthet Orthot Int 36(4):405–414
3. Sanders JE, Daly CH, Burgess EM (1992) Interface shear stresses during ambulation with a below-knee prosthetic limb. J Rehabil Res Dev 29(4):1–8
4. Zhang M, Mak AFT, Roberts VC (1998) Finite element modelling of a residual lower-limb in a prosthetic socket: a survey of the development in the first decade. Med Eng Phys 20(5):360–373
5. Misra S, Ramesh KT, Okamura AM (2008) Modeling of tool-tissue interactions for computer-based surgical simulation: a literature review. Presence (Camb) 17(5):463
6. Mackerle J (2006) Finite element modeling and simulations in orthopedics: a bibliography 1998–2005. Comput Methods Biomech Biomed Engin 9(3):149–199
7. Gholizadeh H, Abu Osman NA, Eshraghi A, Ali S, Razak NA (2014) Transtibial prosthesis suspension systems: systematic review of literature. Clin Biomech 29(1):87–97
8. Cagle JC, Hafner BJ, Taflin N, Sanders JE (2018) Characterization of prosthetic liner products for people with transtibial amputation. J Prosthetics Orthot 30(4):187–199
9. Kallin S, Rashid A, Salomonsson K, Hansbo P (2019) Comparison of mechanical conditions in a lower leg model with 5 or 6 tissue types while exposed to prosthetic sockets applying finite element analysis. ArXiv, 1–27
10. Sanders JE, Nicholson BS, Zachariah SG, Cassisi DV, Karchin A, Fergason JR (2004) Testing of elastomeric liners used in limb prosthetics: classification of 15 products by mechanical performance. J Rehabil Res Dev 41(2):175–185
11. Misra S, Reed KB, Schafer BW, Ramesh KT, Okamura AM (2010) Mechanics of flexible needles robotically steered through soft tissue. Int J Rob Res 29(13):1640–1660
12. Portnoy S, Siev-Ner I, Shabshin N, Gefen A (2011) Effects of sitting postures on risks for deep tissue injury in the residuum of a transtibial prosthetic-user: a biomechanical case study. Comput Meth Biomech Biomed Engin 14(11):1009–1019

13. Hoellwarth JS, Al Muderis M, Rozbruch SR (2020) Cementing Osseointegration implants results in loosening: case report and review of literature. Cureus 12(2)
14. MSC Software Corporation (2018) Marc 2018.0 Theory and User Information. Newport Beach, CA 92660 USA
15. Ivarsson BJ, Crandall JR, Hall GW, Pilkey WD (2004) Biomechanics. In: Kreith F (ed) Handbook of mechanical engineering, 2nd edn. CRC Press, Boca Raton
16. Łagan S, Liber-Kneć A (2018) The determination of mechanical properties of prosthetic liners through experimental and constitutive modelling approaches. Czas Tech 3:197–209
17. Silver-Thorn DS, Childress MB (1996) Parametric analysis using the finite element method to investigate prosthetic interface stresses for persons with trans-tibial amputation. J Rehabil Res Dev 33(3):227–238
18. Perrier A (2016) Influence du Vieillissement Hydrique Sur le Comportement Mécanique de l'Interface Fil/Matrice Dans des Composites Chanvre/Époxy. L'École Nationale Supérieure de Mécanique et D'Aérotechnique
19. Suthenthiraveerappa V, Gopalan V (2017) Elastic constants of tapered laminated woven jute/epoxy and woven aloe/epoxy composites under the influence of porosity. J Reinf Plast Compos 36(19):1453–1469
20. MSC.Software Corporation (2008) Materials application—theory—composite materials, in Patran 2008 r1, Reference Manual Part 4: Functional Assignments, 88–160, Santa Ana, CA 92707 USA
21. Shacham S, Castel D, Gefen A (2010) Measurements of the static friction coefficient between bone and muscle tissues. J Biomech Eng 132(8):1–4
22. Persson BNJ (2016) Silicone rubber adhesion and sliding friction. Tribol Lett 62(2):1–5
23. Zhang M, Lord M, Turner-Smith AR, Roberts VC (1995) Development of a non-linear finite element modelling of the below-knee prosthetic socket interface. Med Eng Phys 17(8):559–566

Study of the Elastic Field of a Plane Strain Orthotropic Composite Plate Subjected to Uniform Tension

S K Deb Nath

1 Introduction

There are several analytical studies of the elastic field of orthotropic and composite materials using Fourier series were reported earlier [1–8]. The boundary conditions of the problem are simplified satisfying the governing equation of orthotropic and composite materials satisfying the physical characteristics of the problem by the Fourier series, which give simultaneous linear algebraic equations that are solved to evaluate the unknown constants, and these unknown constants are used to estimate the elastic field throughout the whole domain of orthotropic and composite materials. Details of the theoretical formulations of the plane strain composite using displacement potential formulations are explained in the reference [5]. Stress and strains of a loaded notched finite graphite/epoxy laminated composite [11], shear stress–strain for composites in all three principal material planes [12], the elastic field of duralumin plate for the case of plane stress and plane strain conditions using displacement potential formulation [13] were obtained. In the present study the displacement and stress components of a stressed thick orthotropic T 300/5208 carbon/epoxy plate under tension are obtained analytically and finite difference method.

2 Displacement Potential Formulation of Orthotropic Composite Materials for the Case of Plane Strain Condition [5]

The displacement components are.

S K Deb Nath (✉)

Sendaishi Aoba Ku Komegafukuro 2 chome 1-3, Sendai, Japan

$$u_x(x, y) = \frac{\partial^2 \psi}{\partial x \partial y} \tag{1a}$$

$$u_y(x, y) = -\frac{1}{M_2}\left[M_1 \frac{\partial^2 \psi}{\partial x^2} + G_{12} \frac{\partial^2 \psi}{\partial y^2}\right] \tag{1b}$$

The governing equation is as follows:

$$G_{12} M_1 \frac{\partial^4 \psi}{\partial x^4} + \left(G_{12}^2 - M_2 M_3 + M_1 M_4\right)\frac{\partial^4 \psi}{\partial x^2 \partial y^2} + G_{12} M_4 \frac{\partial^4 \psi}{\partial y^4} = 0 \tag{2}$$

The expressions of four stress components in terms of the potential function ψ are obtained as.

$$\sigma_{xx}(x, y) = \frac{1}{M_2(K_1 K_4 - K_3 K_2)}\left[(K_4 M_2 + K_2 M_1)\frac{\partial^3 \psi}{\partial x^2 \partial y} + K_2 G_{12}\frac{\partial^3 \psi}{\partial y^3}\right] \tag{3a}$$

$$\sigma_{yy}(x, y) = \frac{1}{M_2(K_2 K_3 - K_1 K_4)}\left[(K_3 M_2 + K_1 M_1)\frac{\partial^3 \psi}{\partial x^2 \partial y} + K_1 G_{12}\frac{\partial^3 \psi}{\partial y^3}\right] \tag{3b}$$

$$\sigma_{xy}(x, y) = \frac{1}{M_2}\left[(G_{12} M_2 - G_{12}^2)\frac{\partial^3 \psi}{\partial x \partial y^2} - M_1 G_{12}\frac{\partial^3 \psi}{\partial x^3}\right] \tag{3c}$$

$$\sigma_{zz}(x, y) = \frac{E_3}{E_1 E_2(K_1 K_4 - K_2 K_3)M_2}\left[\begin{array}{c}(\nu_{13} K_4 E_2 - \nu_{23} K_3 E_1)M_2 \\ -M_1(\nu_{23} K_1 E_1 - \nu_{13} K_2 E_2)\end{array}\right]\frac{\partial^3 \psi}{\partial x^2 \partial y}$$
$$+ \frac{E_3 G_{12}(\nu_{13} K_2 E_2 - \nu_{23} K_1 E_1)}{E_1 E_2(K_1 K_4 - K_2 K_3)M_2}\frac{\partial^3 \psi}{\partial y^3} \tag{3d}$$

3   Solution of the Problems

A stiffened T 300/5208 carbon/epoxy plate is considered for the case of plane strain condition. All of the mechanical properties of T 300/5208 carbon/epoxy used in this study was available in the Table 1 [5, 10]. Management of the boundary conditions to solve the problem is considered using the similar procedure as mentioned in the reference [5]. For the present problem as shown in Fig. 1, the potential function, ψ is assumed as

Table 1 Elastic properties of T 300/5208 carbon/epoxy orthotropic composite

$E_1(10^3)$ MPa	$E_2(10^3)$ MPa	$E_3(10^3)$ MPa	$G_{12}(10^3)$ MPa	$G_{23}(10^3)$ MPa	$G_{13}(10^3)$ MPa	ν_{12}	ν_{23}	ν_{13}
132	10.8	10.8	5.65	3.38	5.65	0.24	0.59	0.24

Fig. 1 Deformed shape of
an orthotropic thick plate
with its original shape
(displacements are magnified
by 20 times) describing all
boundary conditions
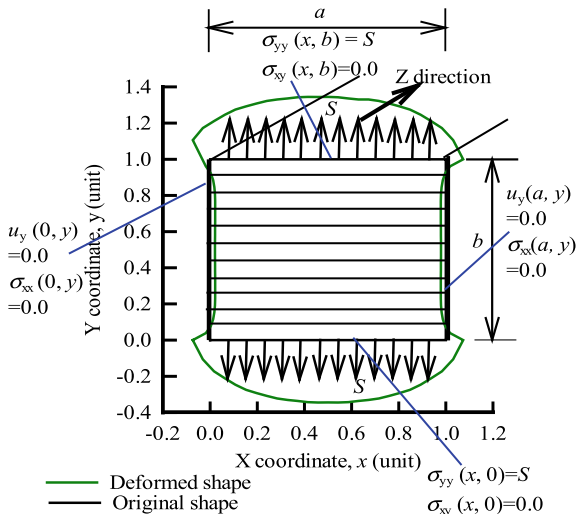
$$\psi(x, y) = \sum_{n=1}^{\infty} Y_n \sin \beta x \tag{4}$$

where Y_n is a function of y only, and $\beta = n\pi/a$, then Y_n has to satisfy the ordinary differential equation. After substituting the above expressions of ψ in the Eq. (2), the following ordinary differential equation is obtained.

$$\frac{d^4 Y_n}{dy^4} - P_{11}\beta^2 \frac{d^2 Y_n}{dy^2} + \frac{M_1}{M_4}\beta^4 Y_n = 0 \tag{5}$$

where $P_{11} = \frac{G_{12}^2 - M_2 M_3 + M_1 M_4}{G_{12} M_4}$.

The general solution of the Eq. (5) can be given by

$$Y_n = P_n e^{n_1 y} + Q_n e^{n_2 y} + R_n e^{n_3 y} + S_n e^{n_4 y}$$

where n_1, n_2 $=$ $\frac{\beta}{\sqrt{2}}\left[\left(P_{11} \pm \sqrt{P_{11}^2 - \frac{4M_1}{M_4}}\right)\right]^{1/2}$; n_3, n_4 $=$
$-\frac{\beta}{\sqrt{2}}\left[\left(P_{11} \pm \sqrt{P_{11}^2 - \frac{4M_1}{M_4}}\right)\right]^{\frac{1}{2}}$

where P_n, Q_n, R_n, and S_n are arbitrary constants.

After substituting the expression of ψ as given by the Eq. (4) into the Eqs. (1) and (3), the following expressions of the displacement and stress components are obtained.

$$u_x(x, y) = \beta \sum_{n=1}^{\infty} Y_n' \cos \beta x \tag{6a}$$

$$u_y(x, y) = \sum_{n=1}^{\infty} \left(\frac{M_1}{M_2} Y_n \beta^2 - \frac{G_{12}}{M_2} Y_n'' \right) \sin \beta x \tag{6b}$$

$$\sigma_{xx}(x, y) = \frac{1}{M_2(K_1 K_4 - K_3 K_2)} \sum_{n=1}^{\infty} \left[-(K_4 M_2 + K_2 M_1) Y_n' \beta^2 + K_2 G_{12} Y_n''' \right] \sin \beta x \tag{7a}$$

$$\sigma_{yy}(x, y) = \frac{1}{M_2(K_2 K_3 - K_1 K_4)} \sum_{n=1}^{\infty} \left[-(K_3 M_2 + K_1 M_1) Y_n' \beta^2 + K_1 G_{12} Y_n''' \right] \sin \beta x \tag{7b}$$

$$\sigma_{xy}(x, y) = \frac{1}{M_2} \sum_{n=1}^{\infty} \left[\left(G_{12} M_2 - G_{12}^2 \right) \beta Y_n'' + M_1 G_{12} \beta^3 Y_n \right] \cos \beta x \tag{7c}$$

$$\sigma_{zz}(x, y) = \frac{E_3}{E_1 E_2 (K_1 K_4 - K_2 K_3) M_2}$$
$$\sum_{n=1}^{\infty} \left[\begin{array}{c} \left\{ \begin{array}{c} M_1(-v_{13} K_2 E_2 + v_{23} K_1 E_1) \\ - (v_{13} K_4 E_2 - v_{23} K_3 E_1) M_2 \end{array} \right\} \\ Y_n' \beta^2 + (v_{13} K_2 E_2 - v_{23} K_1 E_1) G_{12} Y_n''' \end{array} \right] \times \sin \beta x \tag{7d}$$

where $M_1 = \frac{K_4}{K_1 K_4 - K_3 K_2}$; $M_2 = G_{12} - \frac{K_2}{K_1 K_4 - K_3 K_2}$; $M_3 = \frac{K_3}{K_2 K_3 - K_1 K_4} + G_{12}$; $M_4 = -\frac{K_1}{K_2 K_3 - K_1 K_4}$; $K_1 = \frac{1}{E_1} - \frac{E_3 v_{13}^2}{E_1^2}$ $K_2 = -\left(\frac{v_{12}}{E_1} + \frac{v_{13} v_{23} E_3}{E_1 E_2} \right)$; $K_3 = -\left(\frac{v_{12}}{E_1} + \frac{v_{13} v_{23} E_3}{E_1 E_2} \right)$; $K_4 = \frac{1}{E_2} - \frac{v_{23}^2 E_3}{E_2^2}$.

4 Finite Difference Method

$$\psi(x + 2h, y) = \psi(x, y) + 2h\psi_x'(x, y) + 2h^2 \psi_x''(x, y) + \frac{4}{3} h^3 \psi_x'''(x, y) + \ldots \tag{8a}$$

h and *k* are the mesh lengths between two successive grids along *x* and *y* directions respectively.

$$\psi(x + h, y) = \psi(x, y) + h\psi_x'(x, y) + \frac{h^2}{2} \psi_x''(x, y) + \frac{1}{6} h^3 \psi_x'''(x, y) + \ldots \tag{8b}$$

8(a)–(b) $\times 4 \rightarrow$ $\frac{\partial \psi(x, y)}{\partial x} = \frac{4\psi(x+h, y) - \psi(x+2h, y) - 3\psi(x, y)}{2h} + O\left(h^2 \right).$

Similarly $\frac{\partial \psi(x,y)}{\partial y} = \frac{4\psi(x,y+k)-\psi(x,y+2k)-3\psi(x,y)}{2k} + O(k^2)$

$$\frac{\partial^2 \psi}{\partial x \partial y} = \frac{1}{4kh} \begin{bmatrix} 16\psi(x+h,\,y+k) - 4\psi(x+h,\,y+2k) - 12\psi(x+h,\,y) \\ -\,4\psi(x+2h,\,y+k) + \psi(x+2h,\,y+2k) + 3\psi(x+2h,\,y) \\ -\,12\psi(x,\,y+k) + 3\psi(x,\,y+2k) + 9\psi(x,\,y) \end{bmatrix}$$

$$
\begin{aligned}
u_x(x,\,y) = \frac{1}{4kh}\big[&16\psi\big(i+i_0,\,j+j_0\big) - 4\psi\big(i+i_0,\,j+2j_0\big) - 12\psi\big(i+i_0,\,j\big) \\
&-\,4\psi(i+2i_0,\,j+j_0) + \psi(i+2i_0,\,j+2j_0) \\
&+\,3\psi(i+2i_0,\,j) - 12\psi(i,\,j+j_0) \\
&+\,3\psi(i,\,j+2j_0) + 9\psi(i,\,j)
\end{aligned}
\tag{9}
$$

The governing equation in finite difference form as shown in equation (2) is

$$
\begin{aligned}
&\frac{G_{12}M_1}{h^4}\{\psi(i+2i_0,\,j+\psi(i-2i_0,\,j) \\
&+6\psi(i,\,j) - 4\psi(i+i_0,\,j) - 4\psi(i-i_0,\,j)\} \\
&+\frac{(G_{12}^2 - M_2M_3 + M_1M_4)}{h^2k^2} \\
&\{\psi(i+i_0,\,j+j_0) + \psi(i+i_0,\,j-j_0) + \psi(i-i_0,\,j+j_0) + \psi(i-i_0,\,j-j_0) \\
&+4\psi(i,\,j) - 2\psi(i+i_0,\,j) - 2\psi(i,\,j+j_0) \\
&-2\psi(i,\,j-j_0) - 2\psi(i-i_0,\,j)\} \\
&+\frac{G_{12}M_4}{k^4}\{\psi(i,\,j+2j_0) + \psi(i,\,j-2j_0) \\
&+6\psi(i,\,j) - 4\psi(i,\,j+j_0) - 4\psi(i,\,j-j_0)\} = 0
\end{aligned}
\tag{10}
$$

5   Finite Element Method

The displacement model inside the element is expressed as [9]

$$u_x(x,\,y) = \alpha_1 + \alpha_2 x + \alpha_3 y$$

$$u_y(x,\,y) = \alpha_4 + \alpha_5 x + \alpha_6 y$$

$$\vec{U} = [\eta]\vec{\alpha}$$

The stress-strain relations [10] are given by

The explicit form of the stiffness matrix is [9] $\left[k^{(e)}\right] = [B]^T[D][B]t \iint_A dA.$

E_1, E_2, E_3 = Young's moduli in the 1-, 2-, and 3-directions. ν_{ij} = Poisson's ratio.

The stiffness matrix of the element in the global XYZ coordinate system is as follows [9]

$$[K^{(e)}] = [\lambda]^T [k][\lambda]$$

$$\{F\} = [K].\{U\}$$

Different components of stresses in terms of displacements are given by Deb Nath [5]

$$\sigma_{xx}(x, y) = \frac{1}{K_1 K_4 - K_3 K_2} \left[K_4 \frac{\partial u_x}{\partial x} - K_2 \frac{\partial u_y}{\partial y} \right] \tag{11}$$

$$\sigma_{yy}(x, y) = \frac{1}{K_2 K_3 - K_1 K_4} \left[K_3 \frac{\partial u_x}{\partial x} - K_1 \frac{\partial u_y}{\partial y} \right] \tag{12}$$

$$\sigma_{xy}(x, y) = G_{12} \left[\frac{\partial u_x}{\partial y} + \frac{\partial u_y}{\partial x} \right] \tag{13}$$

$$\sigma_{zz}(x, y) = \frac{E_3}{E_1 E_2 (K_1 K_4 - K_2 K_3)} \left[\begin{array}{c} (\nu_{13} K_4 E_2 - \nu_{23} K_3 E_1) \dfrac{\partial u_x}{\partial x} \\[2mm] -(\nu_{13} K_2 E_2 - \nu_{23} K_1 E_1) \dfrac{\partial u_y}{\partial y} \end{array} \right] \tag{14}$$

$$\vec{\sigma} = [D]\vec{\varepsilon} \quad \vec{\sigma} = \begin{bmatrix} \sigma_{xx} \\ \sigma_{yy} \\ \sigma_{zz} \\ \sigma_{xy} \end{bmatrix} = \begin{bmatrix} \frac{1}{E_1} & \frac{-\nu_{12}}{E_1} & \frac{-\nu_{13}}{E_1} & 0 \\ \frac{-\nu_{12}}{E_1} & \frac{1}{E_2} & \frac{-\nu_{23}}{E_2} & 0 \\ \frac{-\nu_{13}}{E_1} & \frac{-\nu_{23}}{E_2} & \frac{1}{E_2} & 0 \\ 0 & 0 & 0 & \frac{1}{2G_{12}} \end{bmatrix} \begin{bmatrix} \varepsilon_{xx} \\ \varepsilon_{yy} \\ \varepsilon_{zz} \\ \varepsilon_{xy} \end{bmatrix}$$

6   Results and Discussion

Figure 1 shows the deformed shape of a thick orthotropic plate with its original shape. The angle between fibers and x axis is 0°. Most parts of the width of the plate contract (along the x direction) which is reasonable but the loading sections along the x direction expand due to the lack of the management of the boundary conditions of the corner points as shown in Fig. 1. The dimensions of the plate along x and y axis are assumed a and b, respectively. The applied tensile stress at both ends of the plate is $S = 600$ MPa. Different displacement components are made dimensionless dividing displacement components by its dimensions. In the similar manner different stress components are made dimensionless dividing them by the applied tensile stress

S MPa. If any dimensionless stress component exceeds 1.0, that stress component would be greater than the applied stress.

Figure 2 a–d illustrate normalized different stress components σ_{xx}/S, σ_{zz}/S, σ_{yy}/S and σ_{xy}/S respectively at different sections of the plate. Except the corner points, boundary conditions of all boundaries of the plate are satisfied (see Fig. 2) because the corner points cannot be satisfied analytically and numerically due to the limitations of the methods. From Fig. 2a and b, it is observed that the loading sections ($y/b = 0$, 1) are critical as compared to other sections. Comparative studies of the displacement and stress components at some sections obtained by the analytical and FDM method as shown in Figs. 3 and 4 show that the present solutions of the thick orthotropic plate under tension are reliable. U_x, U_y are the displacement components along x and y
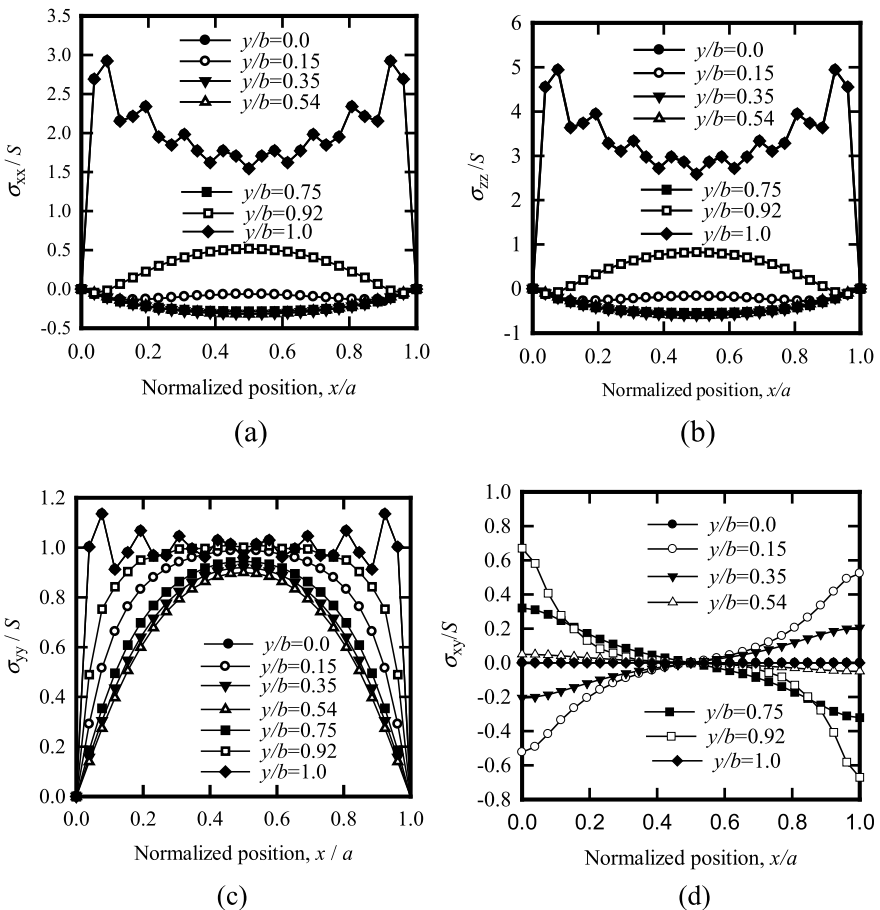
Fig. 2 Different components of normalized stresses such as **a** σ_{xx}/S, **b** σ_{zz}/S, **c** σ_{yy}/S, **d** σ_{xy}/S at different sections of the thick orthotropic plate obtained by the analytical method

(a)   (b)
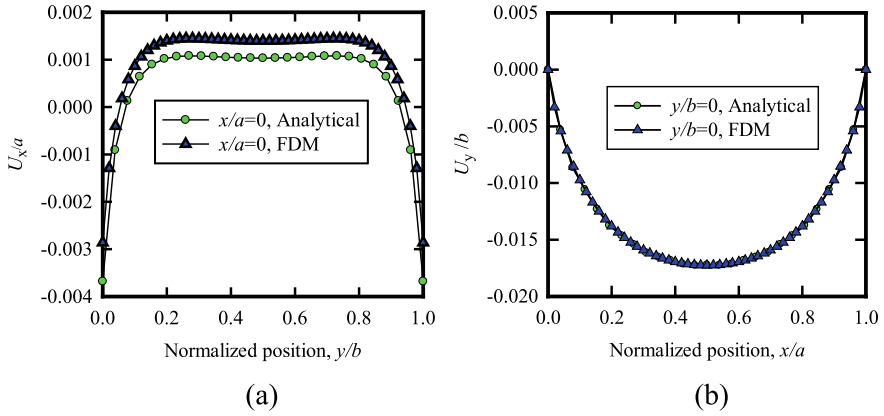
Fig. 3 Comparative study of different components of normalized displacements such as **a** U_x/a at the section $x/a = 0$, **b** U_y/b at the section $y/b = 0$ obtained by the analytical and FD methods

(a)   (b)
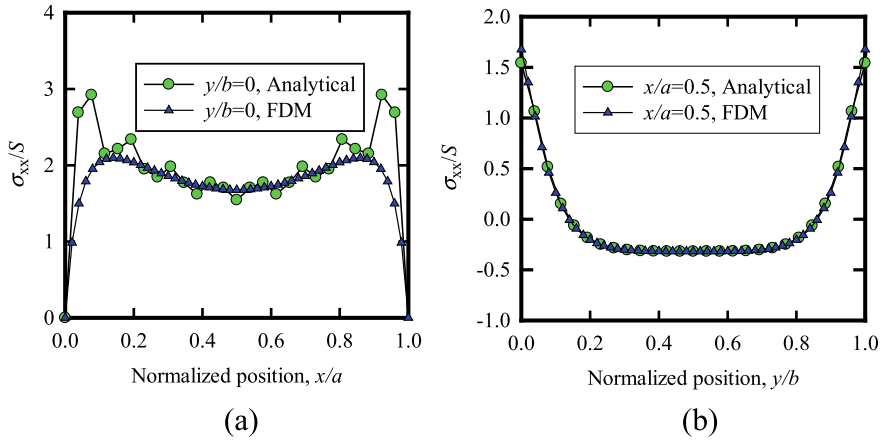
Fig. 4 Comparative study of normalized normal stress, σ_{xx}/S **a** at the section $y/b = 0$, **b** at the section $x/a = 0.5$ of the plate obtained by the analytical and FD methods

directions respectively. σ_{xx}, σ_{yy} and σ_{zz} are the normal stress components along x, y and z, directions, respectively. σ_{xy} is the shear stress component.

7   Conclusion

A thick orthotropic plate under tension is solved using the displacement potential formulations by two approaches such as analytical and FD methods. From the studies, two critical sections are identified under tension at the stressed plate. Deformed shape

with the original shape and stresses at different sections of the plate are studied using analytical approach. Comparative studies of the elastic field of the plate under tension using analytical and finite difference methods show that the solutions of the present problem are reliable and can be used for designing purposes.

References

1. Jin G, Ye T, Jia X, Gao S (2014) A general Fourier solution for the vibration analysis of composite laminated structure elements of revolution with general elastic restraints. Compos Struct 109:150–168
2. Nie GJ, Batra RC (2010) Static deformations of functionally graded polar-orthotropic cylinders with elliptical inner and circular outer surfaces. Compos Sci Technol 70:450–457
3. Calme O, Bigaud D, Jones S, Hamelin P (2006) Analytical evaluation of stress state in braided orthotropic composite cylinders under lateral compression. Compos Sci Technol 66:3040–3052
4. Zhu H, Sankar BV (2004) A combined Fourier Series-Galerkin method for the analysis of functionally graded beams. ASME J Appl Mech 71:421–424
5. Deb Nath SK (2016) Development of single function potential approach of orthotropic composite materials for the case of plane strain conditions. Mech Adv Mater Struct 23:1326–1334
6. Deb Nath SK, Afsar AM, Ahmed SR (2007) Displacement potential solution of a deep stiffened cantilever beam of orthotropic composite material. J Strain Anal Eng Design 42:529–540
7. Deb Nath SK, Reaz Ahmed S (2009) Displacement potential solution of stiffened composite struts subjected to eccentric loading. Appl Math Model 33:1761–1775
8. Xu R, Wu Y-F (2007) Two-dimensional analytical solutions of simply supported composite beams with interlayer slips. Int J Solids Struct 44:165–175
9. Rahman MI, Mahboob M, Nilufar S (2003) Finite element analysis of two dimensional elastic problems. Thesis for Bachelor of Science in Mechanical Engineering, Bangladesh University of Engineering and Technology, Dhaka, Bangladesh
10. Jones RM (1999) Mechanics of composite materials, 2nd edn
11. Alshaya A, Rowlands R (2017) Experimental stress analysis of a notched finite composite tensile plate. Compos Sci Technol 144:89–99
12. Seon G, Makeev A, Cline J, Shonkwiler B (2015) Accessing 3D shear stress-strain properties of composites using digital image correlation and finite element analysis based optimization. Compos Sci Technol 117:371–378
13. Deb Nath SK (2017) Analytical solution of mixed boundary value problems using the displacment potential approach for the case of plane stress and plane strain conditions. Int J Appl Mech Eng 22:269–291

Comparison of Papaya Cushioning Materials by Ellipsoid Evaluation Method

Mayuree Inwan, Ratiya Thuwapanichayanan [ORCID]**, and Supakit Sayasoonthorn** [ORCID]

1 Introduction

Papaya (*Carica papaya* L.) is one of the most popular tropical fruits of the world. It can be cultivated well in both tropical and subtropical regions, including Thailand, which has a suitable climate and is able to grow good quality papaya for export. However, the current export volume is not high, with 90 percent of papaya grown in Thailand used for the domestic market despite papaya expected to become an economically important fruit in the future [1]. In the process of transporting papaya from farmers to consumers, mechanical loading often causes damage to the fruit, such as bruising, abrasions, skin breaks, punctures, etc. This damage can happen at any stage of the process from harvesting and storage to transportation but especially during the retailing phase. Such damage has a direct effect on the consumer's purchasing decisions. Therefore, many researchers have studied the possibilities of preventing the damage of agricultural products. From past research, it was found that cushioning material can prevent the damage of agricultural products [2–4]. Some researchers have conducted studies on the use of agricultural waste materials such as rice straw, banana rope, sawdust, and also waste materials that can be degraded [2, 5, 6]. The cushioning materials tested in these studies were able to prevent damage of agricultural products to varying extents. Above all, the ability to prevent this damage depends on the type of application, the placement pattern and the physical properties of each type of agricultural produce and also includes the methods used for assessing bruising [7, 8]

There are several methods for assessing the damage prevention effectiveness of cushioning materials, such as a graphical representation of impact energy—bruise

M. Inwan · R. Thuwapanichayanan · S. Sayasoonthorn (✉)

Department of Farm Mechanics, Faculty of Agriculture, Kasetsart University, Bangkok 10900, Thailand

e-mail: agrspks@ku.ac.th

volume [2], a graphical representation of impact energy—bruises area [5], the use of photographs [9], as well as other assessment methods [10]. The evaluation methods used in each case are based on the physical properties of agricultural produce and the nature of the damage that appears. Therefore, the objective of this research was to compare the protective performance of papaya cushioning materials during retailing. The ability of the cushioning material was tested by assessing bruising volume through the ellipsoid method, while the bulk density and cost of the cushioning material were also assessed to select the most suitable material to prevent the mechanical damage of papaya.

2 Materials and Methods

2.1 Materials

Papaya at a weight of 0.5–1.0 kg/fruit and ripeness of P5 on the ripening index with yellow colour throughout [11], which are the most common trading conditions on the market, were used in the test. The cushioning materials selected for testing were: (1) frustum cone foam of 10 mm in diameter and 9 cm in length (Fig. 1a); (2) bead foam of 13, 18 and 25 mm in diameter (Fig. 1a); and (3) mesh foam of 5 mm in diameter (Fig. 1b).

(a)   (b)   (c)
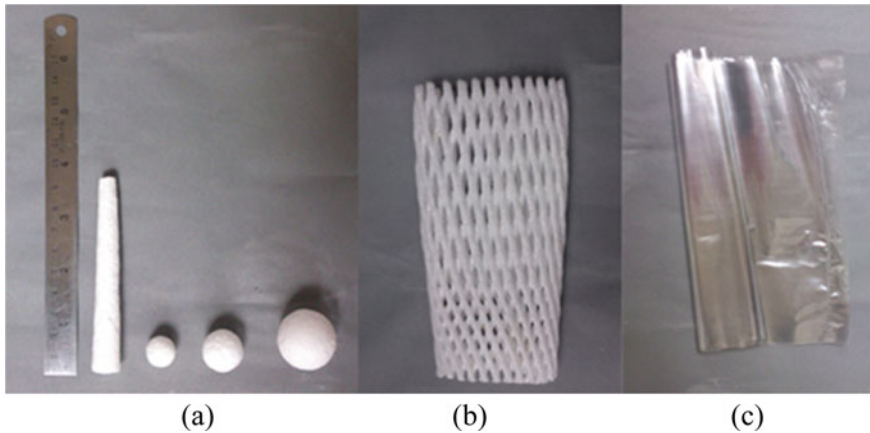
Fig. 1 Cushioning materials selected for testing

2.2 Methods

The impact test performed in this study involved a free-fall drop test of papaya in an 8 × 14 inch (width x length) clear plastic bag (Fig. 1c) with the cushioning material arranged in a single layer (Single layer) on one side only (Fig. 2) so that the papaya packaged inside could be seen on the other side.

The papaya was then released free fall in 6 experiments: (1) papaya fruit without cushioning material (Fig. 2a); (2) papaya wrapped in a 5 mm net foam (Fig. 2b); (3) papaya in a clear plastic bag packed in frustum cone foams of 10 mm in diameter, 9 cm in length, and an average weight of 14 g (Fig. 2c); (4) papaya in a clear plastic bag packed in bead foam of 13 mm in diameter and an average weight of 15 g (Fig. 2d); (5) papaya in a clear plastic bag packed in bead foam of 18 mm in diameter and an average weight of 7 g (Fig. 2e); and (6) papaya in a clear plastic bag packed
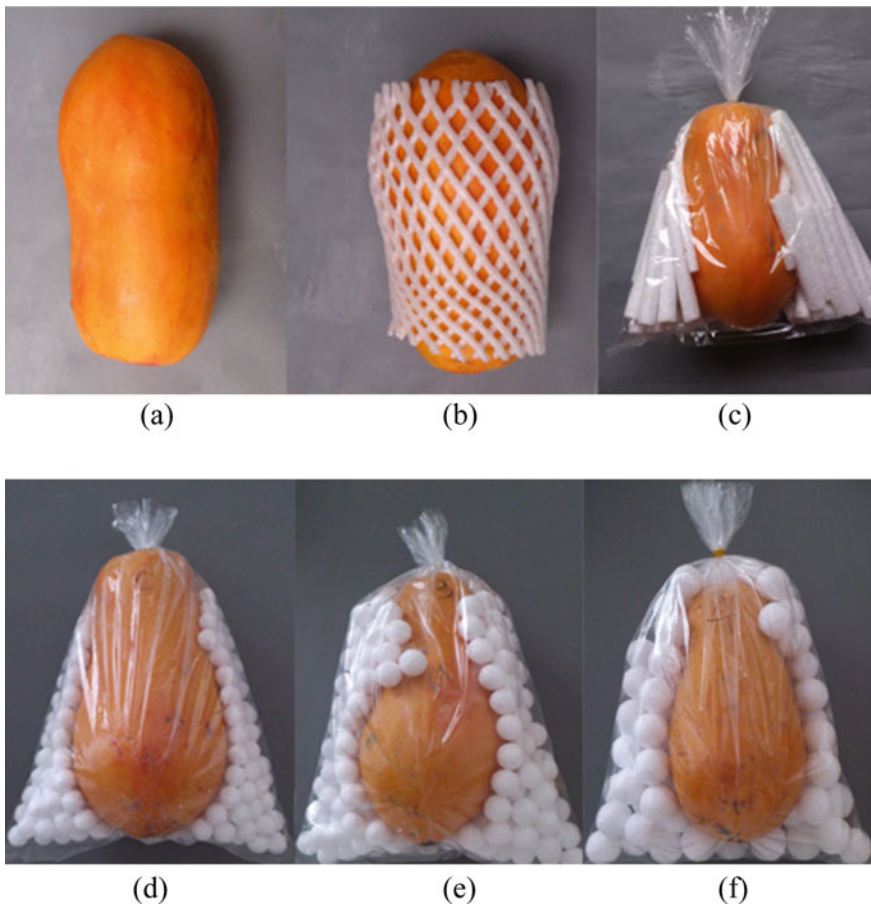
Fig. 2 Arrangement of cushioning materials to protect against mechanical damage of papaya

Fig. 3 Method of measurement for determining bruise volume by ellipsoid method [13]
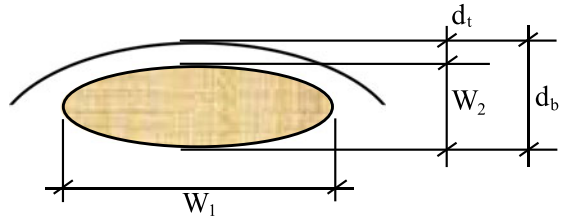
in bead foam of 25 mm in diameter and an average weight of 12 g (Fig. 2f) with three repetitions of each condition.

The free-fall drop test was performed by dropping the papaya from heights of 0.6, 0.79 and 1 m which represent the heights of selecting goods, carrying goods and displaying goods on shelves with most fruit falling from these heights at a probability of falling of 0.02 [12]. The test had to be conducted carefully to prevent rotation of the papaya when it hit the ground. If it rotated, it would cause the other side of the fruit that was not being tested to come into contact with the ground. After the test, the papaya was left at room temperature for 24 h so that any bruising could be clearly seen. In this test, the ellipsoid method was applied to determine the bruise volume [13] (Fig. 3). The bruised volume was calculated from Eq. (1).

$$BV = 4/3[(d_b - d_t)W_1 W_2/8] \tag{1}$$

when

BV = Bruise volume (mm^3)
d_b = Full depth of bruises (mm).
d_t = Depth from papaya skin to bruise (mm).
W_1 = The width of the bruise measured along the major axis (mm).
W_2 = The width of the bruise measured along the minor axis (mm)

The bulk density of the cushioning material was tested by packing it in a box with dimensions of $4 \times 7 \times 13$ cm (width $\times$ length $\times$ height) and then weighing the material to determine the weight. The bulk density can then be calculated from Eq. (2),

$$D = M/V \tag{2}$$

when

D = Bulk density (g/cm^3).
M = Mass of cushioning material (g).
V = Volume of box (cm^3).

Then the volume of the bruises of the papaya fruit was determined and a cushioning material selected using the bruise volume, bulk density of the cushioning material and the cost of cushioning material as the factors informing the decision.
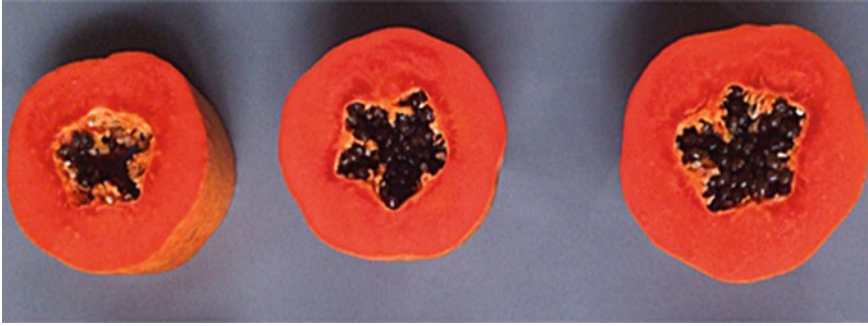
Fig. 4 Bruise volume of papaya

3   Results and Discussion

3.1   Results of Comparison of Different Types of Cushioning Materials

After the papaya was cut transversally (Fig. 4), the bruise volume was determined (Fig. 5a-c) and a graph was plotted showing the relationship between the bruise volume and the drop height of each test. The bruise volumes from all stages of the test were compared (Fig. 5d).

From Fig. 5, it can be seen that the papaya without cushioning material at drop heights of 0.6, 0.79 and 1.0 m had bruise volumes of 4.59, 7.47 and 8.62 cm^3, respectively. For the papaya wrapped in 5-mm net foam, the bruise volumes were 3.68, 5.60 and 8.49 cm^3 at drop heights of 0.6, 0.79 and 1.0 m, respectively, while no bruising was found on the papaya protected by the frustum cone foam and the bead foam of 13, 18 and 25 mm in diameter from any of the tests at the various drop heights.

The bulk density of the frustum cone foam and the bead foam of 13, 18 and 25 mm in diameter was 0.054, 0.049, 0.044 and 0.041 g/cm^3, respectively, while the cost of the cushioning material was 30, 13, 18 and 25 baht/100 pieces, respectively, and the cost of the 5-mm net foam was 65 baht/100 pieces (Table 1).

3.2   Discussion

From the test results, it was found that the bruise volume was directly proportional to the drop height (Fig. 5d). When the height was greater, the bruise volume of the papaya increased or the papaya was more damaged under all test conditions. This is because when the height is greater, the potential energy arising from the impact increased, thereby subjecting the papaya and the cushioning material to a stronger

Fig. 5 Bruise volume
(**a**–**c**) and comparison of
bruise volume of each
material (**d**)
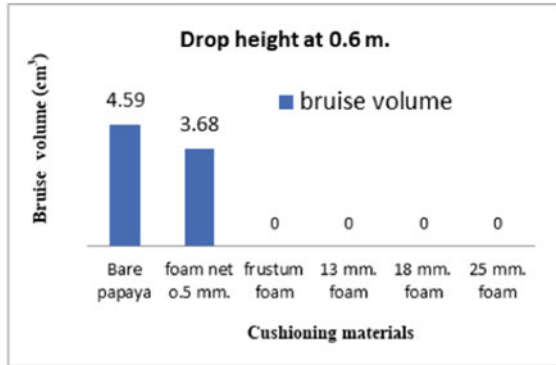
(a) 0.6 m.
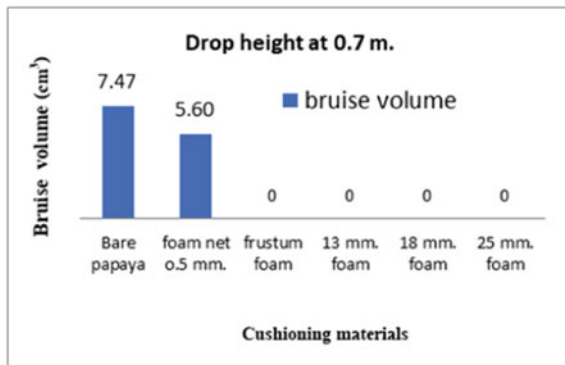
(b) 0.79 m.
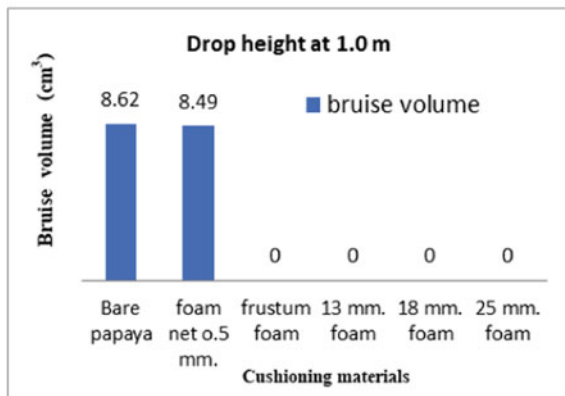
(c) 1.0 m.

Fig. 5 (continued)
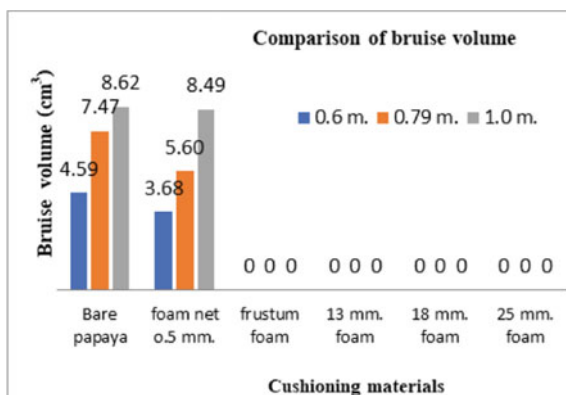
(d) Comparison of various types of material

Table 1 Bulk density and cost of each type of cushioning material

Cushioning material	Bulk density (g/cm^3)	Cost/100 pieces (THB)	Cost/Bulk density ratio (THB/g/cm^3)
Frustum cone foam	0.054[a]	30	5.56
Bead foam 13 mm in diameter	0.049[b]	13	2.65
Bead foam 18 mm in diameter	0.044[c]	18	4.10
Bead foam 25 mm in diameter	0.041[d]	28	6.83
Net foam 5 mm	–	65	-

Price Conversion: approximately 32 THB = 1 USD.

force and resulting in the bruise having a larger volume. This is consistent with the findings of previous research [3, 6]. The guidelines for selection cushioning material to prevent damage to papaya caused by impact should consider the following factors.

Comparing the ability to prevent mechanical damage to the papaya based on the bruise volumes, it was found that for the papaya protected by frustum cone foam and bead foam of 13, 18 and 25 mm in diameter, no bruises were found under all test conditions. This means that these cushioning materials are highly effective against mechanical damage to the papaya during retailing.

In addition to establishing the ability of the materials to protect against mechanical damage, it is also important to consider the bulk density factor in order to determine the quantities to be used as this will affect the cost. It is therefore necessary to select a cushioning material that can not only prevent mechanical damage well but also has a low bulk density. From testing, it was found that the lowest bulk density of the cushioning material was the bead foam with a diameter of 25 mm, followed by

bead foam with diameters of 18 and 13 mm and then frustum cone foam with bulk densities of 0.041, 0.044, 0.049, and 0.054 g/cm^3 respectively (Table 1).

For the cost factor, the cost of each type of material must be taken into account as a key factor when determining the most appropriate cushioning material. Arranged in descending order from the highest cost to the lowest, the materials are the 5-mm net foam, frustum cone foam, 25-mm bead foam, 18-mm bead foam and 13-mm bead foam with prices of 65, 30, 28, 18, and 13 THB/100 pieces respectively (Table 1).

Taking all three factors into consideration, it was found that the 13-mm bead foam was effective in preventing mechanical damage to the papaya with high bulk density when compared to the frustum cone foam, 18-mm bead foam and 25-mm bead foam at 90.74%, 89.80% and 83.78% respectively, while the material price was also relatively low compared to frustum cone foam, 18-mm bead foam and 25-mm bead foam. Considering the bulk density and the cost of the material, it was found that, in actual use, it was necessary to use large quantities of the material to prevent mechanical damage to the papaya, and the increased quantities of material, which resulted in high material cost. However, when considering the cost to bulk density ratio (THB/g/m^3) of the 13-mm diameter bead foam, it was found that it had a material cost to bulk density ratio of 2.65 THB/g/m^3, which was the lowest cost to bulk density ratio among the cushioning materials assessed in this study. This means that the cost per 1 cm^3 for the 13-mm bead foam is the lowest, although it has a relatively high bulk density compared to the other materials. For the 13-mm bead foam, even though it takes a lot of beads for it to be most effective and this results in the cost increasing, it still has a low cost compared to the other materials. Therefore, 13-mm diameter bead foam is the most appropriate cushioning material for papaya.

4   Conclusions

This study assessed the most appropriate cushioning material to protect against mechanical damage to papaya caused by free fall during the retailing phase. When considering the ability to prevent damage as measured by bruise volume, the bulk density, and the material cost of different cushioning materials, it was concluded that 13-mm bead foam was able to prevent any damage to the papaya, while it also had a total density of 0.049 g/cm^3 and a cost of 13 THB/100 pieces, making it the most suitable cushioning material for papaya during the retailing phase.

References

1. Office of Agricultural Economics Homepage. https://www.moac.go.th/moaceng-magazine-files-422991791793. Last accessed 2017/12/23
2. Brown GK, Schulte NL, Timm EJ, Armstrong PR, Marshall DE (1993) Reduce apple bruise damage. Tree Fruit Postharvest J 4(3):6–10
3. Jarimopas B, Sayasoonthorn S, Singh SP, Singh J (2007) Test method to evaluate bruising during impacts to apples and compare cushioning materials. J Testing Eval 35(3):321–326
4. Subedi GD, Gautam DM, Baral DR, Paudyal KP et al (2017) Evaluation of packaging method for transportation of apple in CFB boxes. Int J Horticulture 7(9):154–162
5. Phithayapongsakorn S, Sayasoonthorn S (2013) Comparison of apple cushioning materials by free fall drop test method. Agric Sci J 44(3)(Suppl):363–366 (in Thai)
6. Jarimopas B, Mahayosanan T, Srianek N (2004) Study of capability of net made of banana stringfor apple protection against impact. Kasetsart Eng J 17(51):9–16 (in Thai)
7. Bollen AF, Nguyen HX, Dela Rue BT (1999) Comparison of methods for estimating the bruise volume of apples. J Agric Eng Res 7(4):325–330
8. Zarifneshat S, Ghassemzadeh HR, Sadeghi M, Abbaspour-Fard MH, Ahmadi E, Javadi A, Shervani-Tabar MT (2010) Effects of impact level and fruit properties on Golden Delicious apple bruising. Am J Agric Biol Sci 5(2):114–121
9. Beyaz A, Ozturk R, Turker U (2010) Assessment of mechanical damage on apples with image analysis. J Food Agric Environ 8(3):476–480
10. Chonhenchob V, Singh SP (2004) Testing and comparison of various packages for mango distribution. J Testing Eval 32(1):69–72
11. Pereira T, Almeida PSG, Azevedo IG, Cunha M, Oliveira JG, Silva MG, Vargas H (2009) Gas diffusion in 'Golden' papaya fruit at different maturity stages. Postharvest Biol Technol 54(3):123–130
12. Rachanukroa D, Singh SP, Jarimopas B (2007) Development of sweet tamarind pod retail packaging. In: Proceedings of the international conference on agricultural, food and biological engineering & postharvest/production technology. Thai Agricultural Engineering Society. Khon Kaen, Thailand, p 230
13. Hungh YC, Prussia SE (1989) Effect of maturity and storage time on the bruise of peaches (cv. Red Globe). Trans ASAE 32(4):1368–1373

Development of Polyamide–Polysulfone Thin Film Composites with Copper–treated Zeolites as Additives for Enhanced Hydrophilicity

Sharyjel R. Cayabyab, Justine de Guzman, and Persia Ada de Yro

1 Introduction

Advanced and cost-effective technologies continue to emerge to address problems in providing clean and reliable water worldwide. Utilization of water resources such as rainwater, the large amount of wastewater generated from water systems used by different industries, and other resources from diverse bodies of water could be one of the solutions to increase water supply available for use [1–3].

At present, membrane filtration technology has been the most extensively method in water treatment. This technology employs the use of membranes which are barriers or semi-permeable materials that selectively separate species in the feed source [4–6]. Membrane technology is preferred over other water treatment technologies because of energy efficiency without thermal input, high operating performance, and cost-effectiveness with opportunity to recycle waste materials [1, 2, 7, 8]. As time passes by, the requirements for clean and reliable water became stricter, however, membrane research continues to rise to the challenge to offer better solutions and innovations for water treatment.

There are several types of pressure-driven membranes appropriate for water filtration [4, 8]. Common types are microfiltration (MF), ultrafiltration (UF), reverse osmosis (RO), and nanofiltration (NF) membranes [4–6]. Membranes are able to

S. R. Cayabyab (✉) · P. A. de Yro
Materials Science Division, Industrial Technology Development Institute, Department of Science and Technology, DOST Compound, 1631 Bicutan, Taguig City, Philippines

J. de Guzman · P. A. de Yro
School of Chemical, Biological, and Materials Engineering and Sciences, Mapúa University, 658 Muralla Street, 1002 Intramuros Manila, Philippines

School of Graduate Studies, Mapúa University, 658 Muralla Street, 1002 Intramuros Manila, Philippines

allow certain species to pass through and retain others in the feed source because of its porous structure [9, 10].

Another classification of membranes is by geometry. Membranes can be in the form of flat sheets, hollow fibers, tubules, and in spiral wound configuration [11, 12]. Additionally, membranes are grouped according to the type of material used. Membranes could be inorganic, organic/polymeric, biological, or hybrid membranes [2, 6, 8, 13]. Among these, polymeric membranes are typically used due to cost-effectiveness, ease of processability, flexibility in design, high efficiency, low energy requirement [11–13]. Most of MF, UF, RO, and NF membranes are made up of synthetic organic polymers.

Hybrid membranes are multiphase materials with improved and enhanced properties arising from each of its component [13, 14]. Hybrid membranes include mixed matrix membranes (MMM), thin film composite membranes (TFC), or thin film nanocomposites (TFN), surface located nanocomposites, etc. [13, 15]. TFCs are membranes with at least two layers of polymers [8, 16]. TFCs have an ultra-thin layer that selectively filters the species and at least one layer that acts as the support layer [16]. There are several configurations for TFCs: (1) TFCs with nanoparticles dispersed in the thin active layer, (2) TFCs with nanocomposite substrate or support layer, and (3) TFCs with nanoparticles incorporated in both the active and support layer [15, 17].

TFCs are typically fabricated using interfacial polymerization. Polymerization proceeds by reacting solutions of two highly reactive monomers dissolved in two immiscible liquids [2, 18]. The microporous support layer is initially impregnated with an aqueous solution followed by immersion in an organic solution [2, 18]. The ultra-thin polymer layer then forms at the interface of the two immiscible liquids [2, 18]. In water purification and desalination, polyamide (PA) TFCs are greatly used due to high salt rejection, excellent selectivity, relatively high permeability, applicability in a broad range of pH [2, 10, 11]. PAs are synthesized by reacting acid chlorides and polyamines [18, 19]. Among the reagents used for PA synthesis, the reaction between m-phenylenediamine (MPD) and trimesoyl chloride (TMC) has been the most successful [18]. Porous support layers for TFCs include PSf, PES, PVDF, and their sulfonated forms, polyether ketone and PAN [2].

Inorganic fillers such as zeolites can be used to impart desired properties to the membrane. Zeolites are crystalline aluminosilicates with uniformly sized pores. Zeolites have high cation-exchange ability, excellent molecular sieve properties, high permeability and selectivity, chemical resistance, and can withstand high pressure and temperature conditions, thus can be used for water desalination and purification applications [19–21]. Importantly, natural zeolites are an abundant resource and a cheap raw material. Thus, zeolites in micron and sub-micron size range are widely used as catalysts or adsorbents embedded on millimeter-sized granules. Apart from its inherent properties, zeolites can be modified with elements such as copper (Cu), silver (Ag), gold (Au), and titanium (Ti) that has outstanding antibacterial properties [22].

Natural zeolites are very abundant in the Philippines and can be turned into value-adding filler in a TFC membrane for water purification applications. This study aims

to fabricate and characterize flat sheet polyamide–polysulfone TFCs with different loadings of copper-treated zeolites using interfacial polymerization technique. The study employs a method used by Olegario, et al. in modifying zeolites using copper.

2 Methodology

2.1 Preparation of Copper-Treated Zeolite

Philippine natural zeolite (PNZ) from Saile Industries Inc. was washed and acid leached in 1.0 M hydrochloric acid (HCl) for 24 h to remove impurities. The sample was washed with deionized (DI) water several times until the pH of the supernatant became neutral. The sample was soaked in 1.0 M sodium hydroxide (NaOH) for 24 h to facilitate cationic exchange between calcium ions present in the sample with sodium ions. The sample was milled and prepared for copper loading. Fine powder sample was soaked in 25 wt% Cu solution ($CuSO_4 \bullet 5/2H_2O$, Sigma Aldrich) for another 24 h. The sample was initially dried in the oven and calcined for 6 h at 300 °C to lock the copper ions inside the cages of zeolite [22]. The sample obtained was copper-treated zeolite (CuZ).

2.2 Thin Film Composite Fabrication

Microporous PSf support layer was fabricated using phase inversion technique. PSf pellets (15 wt%) was dissolved in N-methylpyrrolidone (NMP) via vacuum mixing until homogenous casting solution was obtained. The solution was casted on a nonwoven PES fabric using an automatic casting machine (Porometer, MemCastTM). Then, it was coagulated in DI water. The support layer was stored in DI water for 16 h then dried at room temperature for 3 min prior the interfacial polymerization.

To form the PA layer, aqueous solution and organic solution were prepared using the ratios given in Table 1. The aqueous solution composed of MPD, camphorsulforic acid (CSA), triethylamine (TEA) while the organic solution composed of TMC in hexane. The support layer was immersed in the aqueous solution for 5 min, and then excess liquid was removed. The membrane was subsequently immersed in the organic solution containing CuZ for another 3 min. The resulting membrane was dried in an oven at 50 °C for further cross-linking reaction and solvent evaporation [19].

Table 1 Formulation of different solutions for the fabrication of PA-PSf TFCs with CuZ

CuZ loading (wt%)	Casting solution (wt%/10 g solution)		Aqueous solution (g/50 mL solution)			Organic solution (wt% in 100 mL hexane)
	PSf	NMP	MPD	TEA	CSA	TMC
0	15	85	1	1	2	0.1
0.1	15	85	1	1	2	0.1
0.2	15	85	1	1	2	0.1
0.5	15	85	1	1	2	0.1

2.3 Characterization of CuZ

The particle size of CuZ was measured using Dynamic Light Scattering particle size analyzer (DLS, Horiba Scientific, Nanopartica SZ-100V2). The chemical composition of PNZ and CuZ were determined using X-ray diffractomer (XRD, Shimadzu, LabX XRD-6000) with 40.0 kV voltage and 30.0 mA current. The scan range of the analysis was from 8° to 60° at 1.00 degree per minute scan rate. The surface morphology of CuZ was observed using a Scanning Electron Microscope (SEM, Hitachi, SU-3500) at 15 kV accelerating voltage. The elemental compositions of the pristine zeolite and CuZ samples were determined using Energy Dispersive Spectroscopy (EDS, Bruker, XFlash 6–60).

2.4 TFC Characterization

The surface morphology and surface features of the fabricated TFCs were observed using SEM (Hitachi, SU-3500) at 15 kV accelerating voltage. Prior SEM imaging, the TFCs were sputtered with gold using Ion Sputtering Machine (ISM, Hitachi, E-1045). The topographic features and surface roughness parameters were observed and measured, respectively, using Atomic Force Microscope (AFM, Park Systems, XE-100) with 5 μm × 5 μm scan size. The surface wetting properties were analyzed by determining the contact angles of the TFCs using a goniometer (Biolin Scientific) with water as the wetting liquid.

3 Methodology

3.1 Copper Treatment of PNZ

The impregnation of sodium-exchanged PNZ in copper salts such as $CuSO_4 \cdot 5/2H_2O$ aims to exchange sodium with copper ions [23]. The Cu-exchanged zeolite was calcined for the activation of Cu on the surfaces of zeolite and to obtain a more stabilized form of Cu as an oxide [23, 24]. The average particle size of copper-treated zeolite is in the range of 550–650 nm.

The diffractogram of sodium-exchanged PNZ and CuZ are presented in Fig. 1. Sodium-exchanged PNZ powder sample was found to have two types of zeolites, namely mordenite and clinoptilolite. Strong characteristic peaks for mordenite are located at 2θ values of 15.34°, 18.29°, 19.70°, 22.83°, 25.75°, and 27.81° with corresponding d-spacings in Å of 5.77, 4.85, 4.50, 3.98, 3.45, and 3.20 [25]. Characteristic peaks for clinoptilolite were observed at 2θ values of 9.84°, 29.80°, 31.96°, and 32.48° with corresponding d-spacings in Å of 8.98, 3.00, 2.80, and 2.75, respectively [25]. These peaks were also observed for CuZ. Thus, the structure of zeolite was preserved and not altered. CuZ has characteristic peaks that match the profile of copper (II) oxide. Peaks are found at 2θ values of 34.92°, 35.54°, and 39.04° [26]. Calcination was performed at 300 °C to remove water as well as volatile organic and inorganic molecules [23]. However, beyond this temperature, monovalent copper species, Cu+ starts to form [23]. Moreover, reaction parameters used in the experiment favor the formation of copper (II) oxide.

The surface morphology and surface features of CuZ powder sample is shown in Fig. 2. SEM images show light-colored particles embedded on larger dark-colored
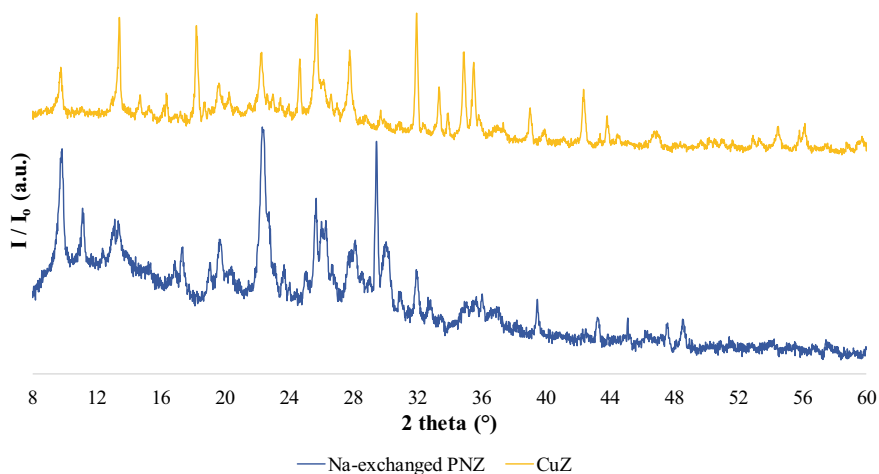
Fig. 1 XRD diffractogram of PNZ and CuZ

Fig. 2 SEM image of CuZ CuZ at 15.0 kV accelerating voltage with 10k× magnification using BSE mode
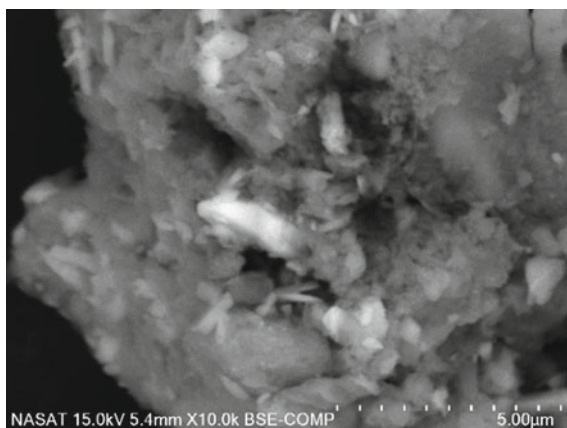
Table 2 Elemental composition of PNZ and CuZ

Element	Average mass percentage (%)	
	PNZ	CuZ
Carbon	27.18	30.44
Oxygen	36.81	29.49
Aluminum	4.35	2.21
Silicon	15.57	14.77
Copper	–	19.22
Sulfur	–	3.87
Others (i.e., Sodium, Magnesium, Calcium, Iron, etc.)	16.09	–

granules/particles. This suggests that copper was successfully synthesized on the surfaces of PNZ as light-colored particles on SEM images indicate a material with heavier atomic weight [25].

Results for elemental analysis are given in Table 2. After copper treatment of PNZ, the average mass percentage of copper increased to 19.22%. Other ions such as sodium, magnesium, calcium, and iron that were initially present in sodium-exchanged zeolite were no longer detected after copper treatment.

3.2 Thin Film Composite Membranes

The surface morphology and surface features of TFC membranes with varying CuZ loading are presented in Fig. 3. All TFCs were images at 3 kV at 5000× magnification using Secondary Electron (SE) mode. All the membranes displayed a characteristic of spots and wrinkles on the surfaces of the TFCs [21, 27–29]. Formation of the thin
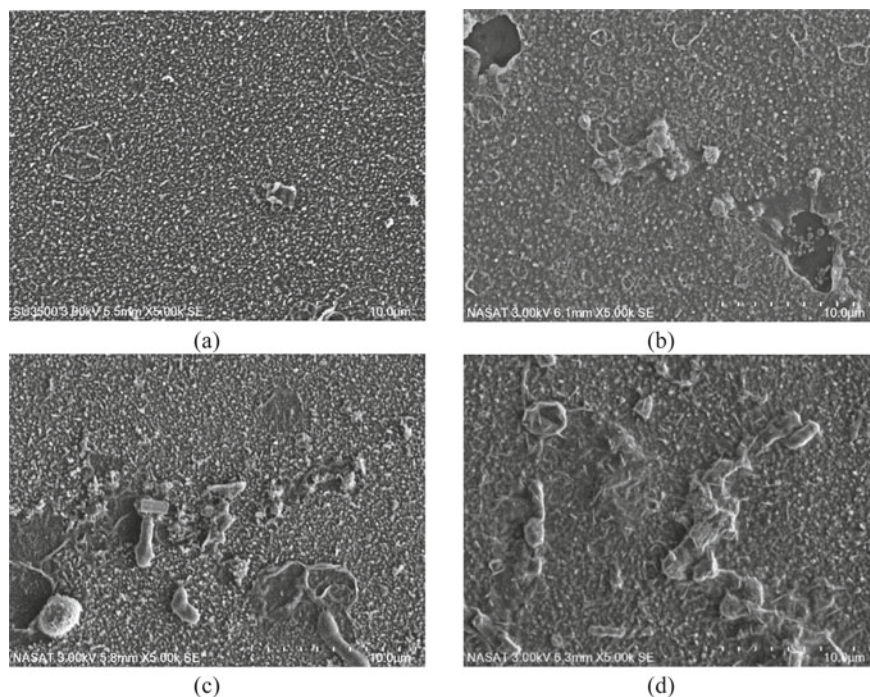
Fig. 3 SEM images of TFCs **a** PNZ, **b** 0.1 wt% CuZ, **c** 0.2 wt% CuZ, and **d** 0.5 wt% CuZ. All micrographs were imaged 3 kV accelerating voltage, 5k× magnification using SE mode

PA layers proceeds by the diffusion of pore-trapped MPD reactant on the surface of PSf into the organic solution containing TMC [29]. These structures are formed due to the differences in the diffusion coefficients of MPD and TMC as the polymerization proceeds [29]. Moreover, the chemical interaction of the reagents in the aqueous solution affects the bonding present in the solution and viscosity of the solution and consequently generating these structures [29]. It was also observed that as the CuZ loading increases, the size of spots and intensity of wrinkling increases. This suggests that addition of CuZ affects the diffusion of MPD causing coarser and bigger spots [28]. At same time, CuZ particles became more visible on the surface of the membrane due to its large particle size.

Additionally, the incorporation of CuZ enhances the miscibility between the aqueous and organic solutions. As the zeolites interact with MPD in the aqueous solution, hydration proceeds and heat is released [30] thereby affecting the miscibility and consequently, the morphology of the resulting PA thin layer [21]. CuZ particles also act as physical obstruction during diffusion and polymerization, thus the presence of irregularities on the membrane surface [28].

The plot of average surface roughness against the increasing CuZ loading is shown in Fig. 4. There is a decreasing trend in the average surface roughness of the TFCs as the CuZ loading increases. The average surface roughness (Ra) value of

Fig. 4 Plot of average surface roughness against CuZ loading
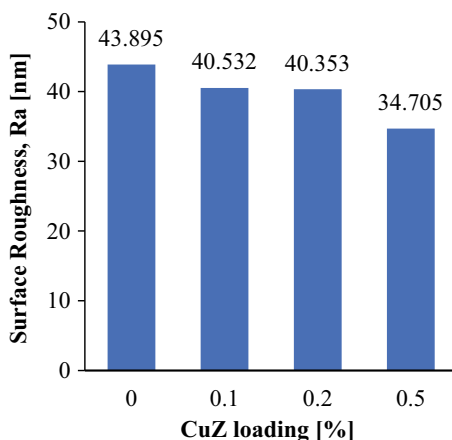
the TFCs decreases gradually from 43.895 to 34.705 nm with increasing CuZ loading in aqueous solution from zero to 0.5 wt% as seen in Fig. 4. The decreasing trend could be due to agglomeration and uneven distribution of the CuZ particles on certain areas of the top surface of the membrane; consequently, resistance to diffusion of reactants decrease the surface roughness of the membrane [28, 31]. The decrease in surface roughness can be beneficial in attaining desired membrane properties such as fouling and wetting. Most studies on the effect of roughness on fouling have indicated that a smoother surface tends to be less afflicted by fouling than a rougher surface due to lower surface area available for foulant attachment [32].

Figure 5 shows the contact angle values with increasing CuZ loading. It can be observed that as the CuZ loading increases, the water droplet decreases in size and becomes flatter. This shows the increased wetting property of the fabricated TFCs with increased amount of CuZ. Zeolites are generally hydrophilic because of the excess negative charges in its structure [21, 31, 33]. The negative charges are

Fig. 5 Plot of contact angle measurement against CuZ loading
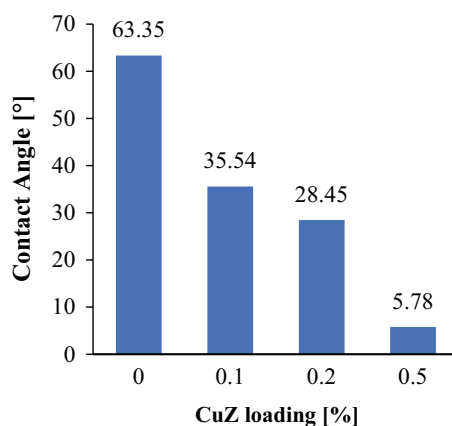
compensated by exchanged cations such as sodium, copper, iron, etc. These cations fill intracrystalline channels and cavities in the structure of the zeolite, as well as the surfaces [21]. With increased amount of CuZ, negative charges accumulate causing a large drop in contact angle and consequently enhanced hydrophilicity.

4 Conclusion and Recommendation

Philippine natural zeolite was successfully surface modified using copper to obtain the copper-treated zeolite. XRD revealed that calcination at 300 °C for 6 h produced CuZ with copper in the form of CuO. Moreover, it was found that the pristine structure of mordenite and clinoptilolite in zeolite was preserved and not altered during the modification. The average particle size of CuZ was in the range of 550–650 nm. SEM images show that copper species were found on the surface of zeolites. Moreover, EDS detected high percentage of Cu in the sample.

Polyamide–polysulfone TFCs with CuZ were successfully fabricated in this study. The effect of different loading of CuZ on the properties of PA thin film composite was analyzed using different characterization techniques. SEM revealed characteristic spots and wrinkles on all of the TFCs at different CuZ loading. With increasing CuZ loading, the spot size was increased, and the intensity of wrinkling was also increased. Increase in the spot could be affected by the diffusion of MPD and enhanced miscibility between the solutions in the presence of CuZ. AFM analysis showed the topography and surface roughness of the membranes. There is a gradual decrease in the surface roughness of the TFCs as a function of increasing CuZ. With this, wettability and anti-fouling properties of the TFCs might improve.

Contact angle measurement showed that the hydrophilicities of the TFC membranes were greatly enhanced with the increasing CuZ loading. CuZ imparted hydrophilicity in the membranes which could improve wetting and membrane performance. Although the TFC membranes with CuZ showed expected surface morphology and wetting property, it is recommended that further analysis be performed, such as performing antibacterial tests to check its antibacterial property and other characterization techniques such as uniaxial tensile test and use of cross flow filtration for other desired properties for water treatment.

References

1. Elimelech M, Phillip WA (2011) The future of seawater desalination: energy, technology, and the environment. Sci 333:712–717
2. Pendergast MTM, Hoek EMV (2011) A review of water treatment membrane nanotechnologies. Energy Environ Sci 4:1946–1971
3. Wang S, Peng Y (2010) Natural zeolites as effective adsorbents in water and wastewater treatment. Chem Eng J 156:11–24

4. Singh R (2015) Membrane technology and engineering for water purification, 2nd edn. Butterworth-Heinemann, Oxford, UK

5. Ezugbe EO, Rathilal S (2020) Membrane technologies in wastewater treatment: a review. Membr 10(89):89–117

6. Esfahani MR, Aktij SA et al (2019) Nanocomposite membranes for water separation and purification: fabrication, modification, and applications. Sep Purif Technol 21:465–499

7. Geise GM, Lee HS et al (2010) Water purification by membranes: the role of polymer science. J Polym Sci Part B: Polym Phys 48:1685–1718

8. Jhaveri JH, Murthy ZVP (2016) A comprehensive review on anti-fouling nanocomposite membranes for pressure driven membrane separation processes. Desalination 379:137–154

9. Cui ZF, Jiang Y, Field RW (2010) Fundamentals of pressure-driven membrane separation processes. Membrane technology, 1st edn. H.S. Butterworth-Heinmann, Oxford, UK, pp 1–18

10. Basilia B, Cayabyab S et al (2020) Development of nanocomposite polysulfone-nanoclay membrane with enhanced hydrophilicity. J Environ Sci Manage SI-1:29–36

11. Saleh TA, Gupta VK (2016) Nanomaterial and polymer membranes. Elsevier, An overview of membrane science and technology

12. Gupta O, Roy S (2020) Nanocomposite membranes for water and gas separation. In: Recent progress in development of nanocomposite membranes. Elsevier

13. Ladewig B, Al-Shaeli MNZ (2017) Fundamentals of membrane reactors: materials. Systems and membrane fouling, Springer, Singapore

14. Boffa V, Marino E (2017) Current trends and future developments of (bio)-membranes. In: Inorganic materials for upcoming water purification membranes, 1st edn. Elsevier

15. Yin J, Deng B (2015) Polymer-matrix nanocomposite membranes for water treatment. J Membr Sci 479:256–275

16. Fane AG, Tang CY, Wang R (2011) Membrane Technology for Water: Microfiltration, Ultrafiltration, Nanofiltration, and Reserve Osmosis. In: Treatise on Water Science. Elsevier Science, Amsterdam, US

17. Pendergast MTM, Nygaard JM et al (2010) Using nanocomposite materials technology to understand and control reverse osmosis membrane compaction. Desalination 261:255–263

18. Gohil JM, Ray A (2017) A review on semi-aromatic polyamide TFC membranes prepared by interfacial polymerization: potential for water treatment and desalination. Sep Purif Technol 181:159–182

19. Feng C, Khulbe KC et al (2015) Recent progress in zeolite/zeotype membranes. J Membr Sci Res 1:49–72

20. Ghosh AK, Hoek EMV (2009) Impacts of support membrane structure and chemistry on polyamide–polysulfone interfacial composite membranes. J Membr Sci 336:140–148

21. Jeong B-H, Hoek EMV et al (2007) Interfacial polymerization of thin film nanocomposites: a new concept for reverse osmosis membranes. J Membr Sci 294:1–7

22. Olegario-Sanches E, Tan M et al (2017) Copper-treated philippine natural zeolites for *escherichia coli* inactivation. Mater Sci Forum 890:150–154

23. Kumashiro R, Kuroda Y, Nagao M (1999) New analysis of oxidation state and coordination environment of copper ion-exchanged in zsm-5 zeolite. J Phys Chem 103:89–96

24. Snyder BER, Bols ML et al (2018) Iron and copper active sites in zeolites and their corelation to metalloenzymes. Chem Rev 118:2718–2768

25. Abd Mutalib M, Rahman MA et al (2017) Scanning electron microscopy (SEM) and energy dispersive X-ray (EDX) spectroscopy. In: Membrane characterization. Elsevier

26. Joint committee on powder diffraction standards: powder diffraction file search manual inorganic compounds. JCPDS (1976)

27. Ma N, Wei J et al (2012) Zeolite-polyamide thin film nanocomposite membranes: towards enhanced performance for forward osmosis. J Membr Sci 405–406:149–157

28. Borjigin B, Liu I et al (2020) Influence of incorporating beta zeolite nanoparticles on water permeability and ion selectivity of polyamide nanofiltration membranes. J Environ Sci 98:77–84

29. Tan Z, Chen S et al (2018) Polyamide membranes with nanoscale Turing structures for water purification. Science 360:518–521
30. Lind ML, Ghosh AK et al (2009) Influence of zeolite crystal size on zeolite-polyamide thin film nanocomposite membranes. Langmuir 25(17):10139–10145
31. Lind ML, Jeong B-H et al (2009) Effect of mobile cation on zeolite-polyamide thin film nanocomposite membranes. J Mater Res 24(5):1624–1631
32. Baig MI, Ingole PG et al (2017) Water vapor selective thin film nanocomposite membranes prepared by functionalized Silicon nanoparticles. Desalination 415:1–13
33. McDonnell AMP, Beving D et al (2005) hydrophilic and antimicrobial zeolite coatings for gravity-independent water separation. Adv Funct Mater 15(2):336–340

Dynamics and Mechanical Engineering

Numerical RANS Researches of Aerodynamics a Propeller Ring and Fuselage Interference for Thrust Increases

Vitaliy V. Gubskiy, Olga V. Pavlenko, and Albert V. Petrov

1 Introduction

Thrust of the isolated propeller was decreased in high airflow speed. But it was increased at propeller installation in a low velocity zone of a boundary layer behind a fuselage (or an engine nacelle). It is applicable for a propeller in a ring. The propeller advantages in a boundary layer are described the impulse theory. It was confirmed the results of calculations by numerical methods [1–5]. Also were confirmed of practice of use of pusher propellers and propellers in a ring on many aircraft, such as ship on an air cushion, small aircraft, and no piloted systems, including a vertical takeoff and landing aircraft. This design concept was applied not only to thrust increase, but also safety of the propeller from damages, to increase maintenance safety and to reduce noise [5–8].

For investigations of propeller in a boundary layer conditions behind a schematically fuselage, the model of an axisymmetrical body with a pusher six-bladed propeller in a rear part and with the electric drive [9] was designed and made. Also, it made for estimations of propeller thrust and aerodynamic characteristics combinations of the fuselage and the propeller. In T-102 TsAGI wind tunnel was carried out experimental researches of fuselage model with pusher propeller at the fixed rotor speed $N = 6000$ rpm, in the range of free-stream velocities $V = 0–50$ m/s, at the maximum Reynolds's number Re $= 8.3$ million. As a propulsor, the six-blade

V. V. Gubskiy (✉) · O. V. Pavlenko · A. V. Petrov
Central Aerohydrodynamic Institute (TsAGI), Zhukovsky Street, Zhukovsky, Moscow 140180, Russia
e-mail: vitaly.gubsky@tsagi.ru

A. V. Petrov
e-mail: albert.petrov@tsagi.ru

101
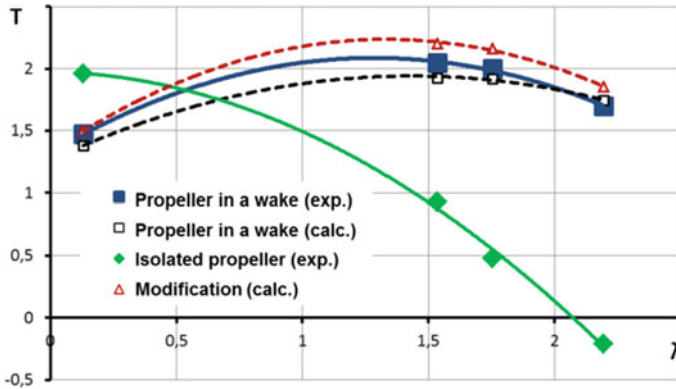
Fig. 1 Dependency between thrust of the isolated and thrusting propeller from speed of flight

propeller in diameter $D = 0.24$ m with blades made of P-107 profile was used. Pressure fields on fuselage surfaces, and also aerodynamic and thrust characteristics of a propeller was research. The analysis of experimental data [9] was shown:

- Thrust of the pulling propeller monotonically decreases up to zero in velocity increase to $V \sim 50$ m/s;
- Presence of the operating propeller, installation on a rear fuselage, increases the base drag and increasing drag of all model.
- Thrust of a propeller grows in a boundary layer with increase in flow velocity to $V \sim 40$ m/s, despite drag increase, and only then has reduction smoothly.

The increment curves of propeller thrust (T) from speed airflow are presented in Fig. 1.

The numerical studies the capability of increase in effect on the propeller thrust which was placed in a rear fuselage, in two directions was considered:

- At the expense of the base drag decrease in rear fuselage.
- At the expense of place propeller ring.

2 Numerical Researches of Various Fuselage Models with an Pusher Propeller

For increase in thrust of the pusher propeller, several versions were considered:

1. Modification of the initial rear fuselage (Fig. 2a) which conducted on based on diffuser parts the R. H. Liebeck's wing profile, with observance of an attached flow condition by the B. S. Stratford theory (Fig. 2b) [10, 11];
2. Using construction «a Propeller ring» (Fig. 2c, d).
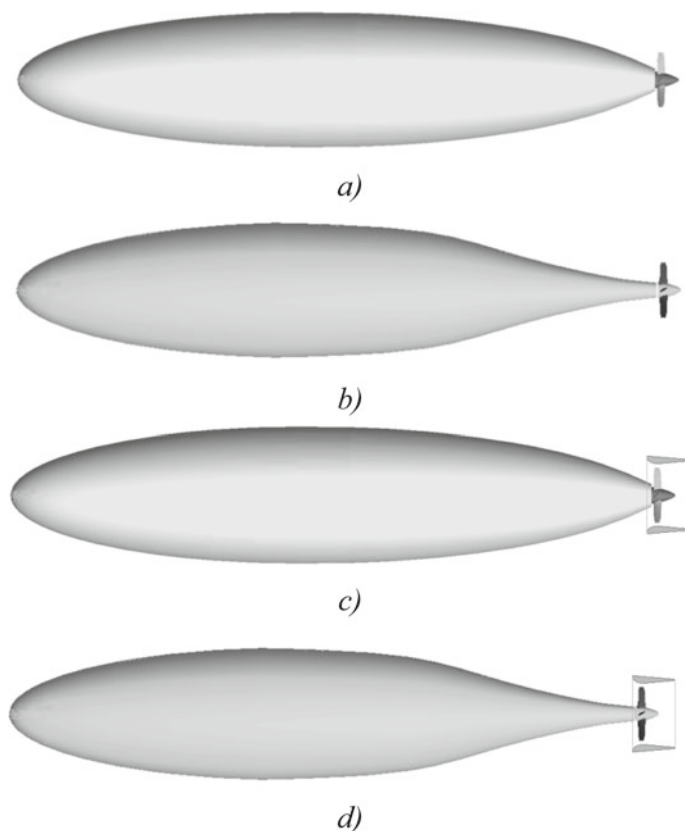
Fig. 2 Computational models: initial fuselage; a modified fuselage; an initial fuselage + propeller ring; a modified fuselage + propeller ring

Calculation of various models type at $\alpha = 0$ was performed using RANS-equations on the structured mesh containing about 17 million cells. For the simultaneous calculation of the translational motion of the fuselage and the rotation of the propeller, two computational domains were chosen: the first domain simulated the airflow onto the studied model, and the second domain—the rotational air motion simulating the rotation of the propeller.

Numerical research was shown (Fig. 3). Change only in the shape of the initial rear fuselage of Liebeck's profile [10] (without using a ring, Fig. 2a, b), diminishes base rarefaction (Fig. 4) without creating a separation and led to a slight increase in propeller thrust in the entire calculated range of flight speeds.

Total influence on thrust model from change of rear fuselage shape and ring propeller installation was shown in Fig. 5. An increment of an pusher propeller thrust owing to ring installation was determined as $\Delta T = T_{p+\text{ring}} - T_p$. It was shown that at an angle of attack $\alpha = 0$, the propeller ring thrust with the initial fuselage (Fig. 2c)
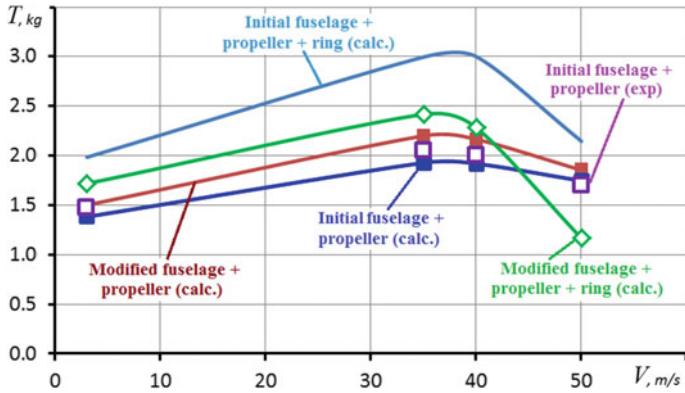
Fig. 3 Thrust of pusher propeller from airflow velocity

Fig. 4 Dependency between influence of the rear fuselage shape with propeller and distribution of pressure factor in section $z = 0$, $V = 50$ m/s
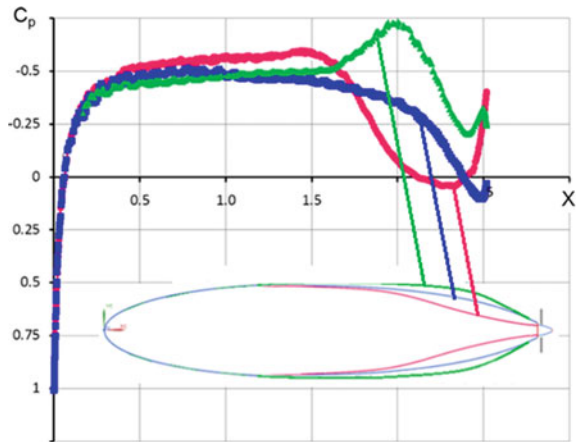
Fig. 5 Dependency between Increment of pusher propeller thrust owing to installation of a ring and airflow velocity
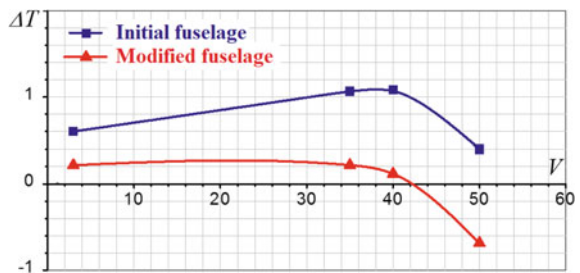
was more than thrust of the propeller ring with the modified fuselage (Fig. 2d), i.e., change of the rear fuselage shape has led to propeller ring thrust reduction.

According to numerical research, at airflow velocity $V \leq 35$ m/s, modification the rear fuselage shape to increase propeller efficiency without a ring. However, if flights with higher speeds $V \geq 40$–50 m/s the propeller thrust was diminished below level of initial fuselage.

3   The Propeller Ring and the Shape of the Fuselage Research

The analysis of the received results at $\alpha = 0$ and flow velocity $V = 35$ m/s was shown that characteristics of a propeller ring thrust were influenced by the rear fuselage shape. It was possible to change of a local angle of attack at which the flow runs on the ring (Fig. 6). On the designed model, the corner of ring profile installation was equal $\delta_r = -5°$. Corresponded to the global angle of attack of model $\alpha = 0$ the airflow near shape was streamlined and corresponded to a local angle of attack $\delta = 20°$ of the initial rear fuselage, and to an angle $\delta = 9°$ of the modified rear part.

For these boundary conditions, on the model with the initial rear shape a local angle of attack of ring profile $\alpha_r = 7°$, and for a modified rear shape $\alpha_r = -1°$. Thus, modification of the rear fuselage shape leads to reduction of the local angle of attack of the ring profile on $\Delta\alpha = 8°$ to propeller ring thrust reduction in comparison with the initial rear fuselage shape and leads. That's why this solution is not effective enough on the model with a small boundary layer.

Fig. 6 Velocity vectors in section plane XOY at $z = 0$ ($V = 35$ m/s), initial fuselage
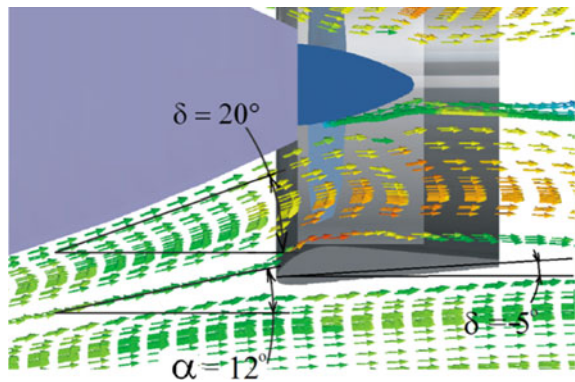
4 Aerodynamic Parameters of the Ring Profile

In the course of numerical researches of a ring profile flow and it depending on a local angle of attack in boundary layer aerodynamic characteristics of the isolated profile (in a vertical plane of symmetry) were calculated. 2D numerical calculation of the ring profile was performed at software based on RANS-equations on the structured mesh containing about 700 thousand of cells.

The calculation results of the aerodynamic characteristics of the isolated ring profile were shown in Figs. 7, 8 and 9. It was shown that the local angle of attack of a ring profile with an initial fuselage ($\alpha = 7°$) corresponds to the maximum lift-to-drag ratio of the 2D profile.

In Fig. 10, a pressure distribution on the ring profile where the angle of attack $\alpha = -5°$ was a local angle of attack of the ring profile without the fuselage was shown. Also, $\alpha = -1°$ was a local angle of attack of a ring profile with the modified fuselage shape, and $\alpha = 7°$—was a local angle of attack with the initial fuselage.

Fig. 7 The aerodynamic characteristics of a ring profile: lift coefficients and a pitch angle from an angle of attack
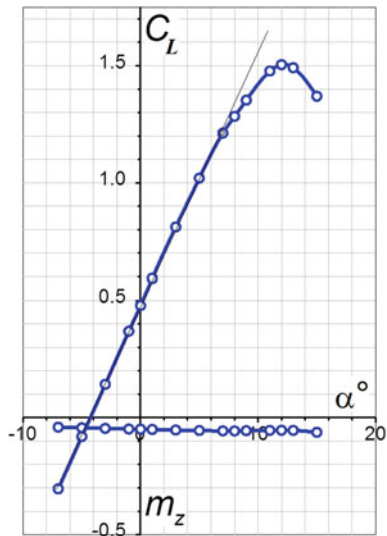
Fig. 8 The aerodynamic characteristics of a ring profile: drag coefficient from an angle of attack
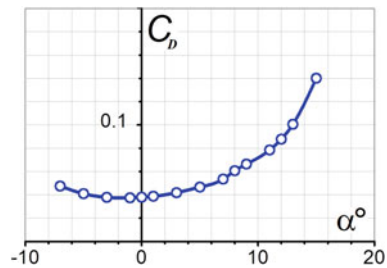
Fig. 9 The aerodynamic characteristics of a ring profile: lift-to-drag ratio from an angle of attack
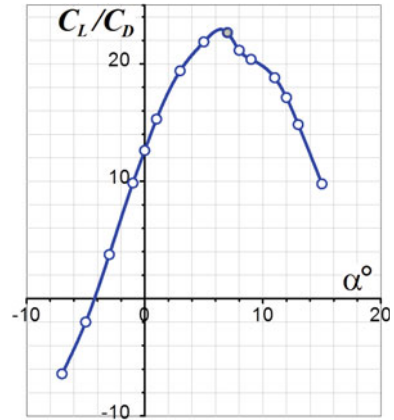
Fig. 10 Dependency between pressure distribution on a ring profile from an angle of attack
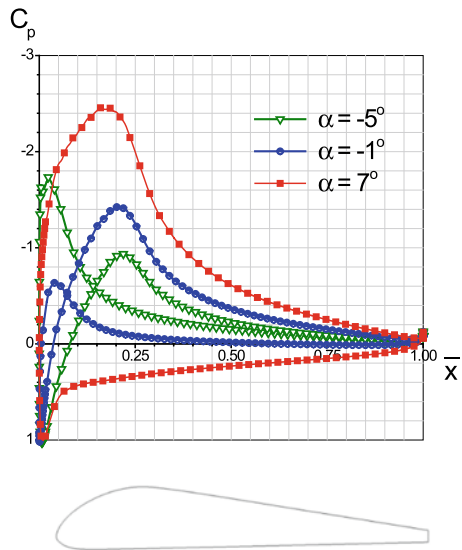
Thus the isolated profile had the greatest rarefaction on the upper surface and value of the maximum lift-to-drag ratio.

The ring placed in a boundary layer in low velocity influences (at the expense of a pressure head) to flow over the rear fuselage. Therefore angles of attack of the isolated ring and the local angles of attack of the ring in a boundary layer were interdependent. Besides aerodynamic characteristics a profile and aerodynamic characteristics a ring wing—was different. If for a 2D profile $\alpha = 7°$ corresponds to the maximum lift-to-drag ratio but for a ring, based on this 2D profile, it demands additional research.

5   Conclusion

Numerical researches of fuselage boundary layer with a pusher propeller ring at airflow velocity from $V = 0$ to $V = 50$ m/s and an angle of attack $\alpha = 0$ have shown that:

- Propeller thrust depends on a local angle of attack of a ring profile;
- The local angle of attack of a ring profile depends on the rear fuselage shape;
- The propeller ring was creating the maximum thrust at a local angle of attack of the isolated 2D profile corresponding to the maximum lift-to-drag ratio.

It was shown that the complex optimization of the profile and the angle of the ring installation also profile line of the rear fuselage shape is necessary for reaching of the greatest thrust.

References

1. Razov AA (2009) The numerical analysis of an arrangement efficiency of a propeller in a viscous layer by means of the Navier-Stokes (RANS) equations. Uchenye zapiski TsAGI XL(3):28–35
2. Vozhdaev VV, Teperin LL, Chernyshev SL (2014) Application and features of modern methods of calculation of aerodynamic performances of flight vehicles on the basis of solutions of the Navier-Stokes equations. TsAGI im. prof. Zhukovskogo NE, Trudy TsAGI, Moscow, issue 2740, 62 p
3. Ostoslavskiy IV, Matveev VR (1935) About activity of the propeller placed in a ring. TsAGI im. prof. Zhukovskogo NE, Trudy TsAGI, Moscow, issue 248, 39 p
4. Skvortsov RA, Titarev VA, Belyaev IV (2016) Numerical research of noise of a propeller ring. Akustika sredy obitaniya, pp 152–155
5. Shydakov VI, Zavalov OA (2013) Numerical modeling for parametrical study of Fenestron geometry on the basis of energy analysis. Aerospace MAI J 20(5):7–16
6. Abalakin IV, Bakhvalov PA, Bobkov VG, Kozubskaya TK, Anikin VA (2016) Numerical investigation of the aerodynamic and acoustical properties of a shrouded rotor. J Fluid Dyn 51(3):419–433
7. Ostrouhov SP (2014) Aerodynamics of propellers and propeller ring propulsors. Fizmatlit, Moscow. ISBN 978-5-9221-1531-5
8. Mojzyh EI, Zavalov OA, Smiths AB (2012) Experimental researches of aerodynamic performances of an is distant-piloted flight vehicle with a carrier system "a propeller ring". Trudy MAI 50. http://trudymai.ru/eng/published.php?ID=26557
9. Alesin VS, Gubskiy VV, Druzhinin OV, Eremin VYu, Pavlenko OV (2018) Avtomatizatsiya. Sovremennye tekhnologii 72(2):91–96
10. Liebeck RH (1986) Low Reynolds number airfoil design at the Douglas aircraft company. In: Proceedings of conference on aerodynamics at low Reynolds numbers, vol 1, paper N 7
11. Stratford BS (1959) An experimental flow with zero skin friction throughout its region of pressure rise. J Fluid Mech 5(1)

The Numerical Simulation of the Flow Feature and Fluid Force Around an In-Line Oscillating Circular Cylinder by the Vortex Method

Yoshifumi Yokoi

1 Introduction

In order to capture the flow phenomenon, it is important to investigate the aspect of flow and surrounding pressure. However, the present condition is that many studies for a "lock-in phenomenon" is informed only about the aspect of flow since pressure measurement of an unsteady flow is accompanied very much by difficulty. Development of numerical computation environment in recent years is remarkable, and is in the situation which can be simulated with enough accuracy, also in the situation of such a difficult flow in an experiment. So, it seems by performing a systematic numerical simulation also in the "lock-in phenomenon" that the elucidation of a mechanism is expectable. In an experiment, it is difficult to make an unsteady flow. However, it can perform making an equal flow field relatively comparatively simply. The unsteady flow can be expressed by placing the body which gave oscillation of the same character as unsteady flow into a steady flow. Naturally, in a numerical simulation, the unsteady flow can be made simply. In order to enable it to compare with the experimental result easily, where the body which gave oscillation is placed into a steady flow, the numerical simulation was performed by this study. If it experiments by making the oscillating frequency increase, it is known that "an alternate vortex shedding type lock-in" and "a simultaneous vortex shedding type lock-in" will occur in order in a certain oscillation frequency range [1]. Moreover, when the lock-in has not occurred, it is also observed that it will be in the state of flow without the other particular flow pattern (when the lock-in strays off). The changes mechanism of the lock-in has not been clarified yet, and the aspect of the flow when straying off from the lock-in is not clarified, either.

Y. Yokoi (✉)

National Defense Academy of Japan, 1-10-20 Hashirimizu, Yokosuka, Kanagawa, Japan

e-mail: yokoi@nda.ac.jp

In this study, the natural Karman vortex was also considered to be a kind of lock-in, and two of three lock-in states considered that it competed for an appearance opportunity, and it investigated fluid force in the case, and the relationship of flow pattern.

2 Numerical Calculation

Numerical computation was carried out using a note type personal computer (NEC LaVie LL850/L) and vortex method calculation software "UzuCrise 2D ver.1.1.3" (College Master Hands Inc., 2006). The flow field to calculate is two-dimensional non-compressing viscous fluid (water is assumed), and the test body is a circular cylinder. The cross-section of the circular cylinder is expressed by 40 vortex panels divided equally. The separating shear layer introduced into the flow from a separating point is transposed to a discrete vortex, and is introduced into the flow. And also refer to reference [2, 3] for the details of the calculation method of the vortex method.

Calculation conditions were determined to compare with a previous visualization experimental result [4]. The cylinder diameter d is 16 *mm* and the main flow velocity U is 0.04 m/s. Reynolds number Re based on the diameter of the circular cylinder and main flow velocity becomes 500. The calculation parameters are oscillating amplitude ratio $2a/d$ and oscillation frequency ratio f/f_K. Here, the oscillating amplitude ratio is a ratio of the half-amplitude a of cylinder oscillation and the circular cylinder diameter d, and the oscillation frequency ratio is a ratio of the cylinder oscillating frequency f and the Karman vortex shedding frequency f_K at the time of circular cylinder stationary. The oscillating amplitude ratio $2a/d$ is 0.0 and 0.50, respectively. Here, in the case of $2a/d = 0.0$, the circular cylinder is in the stationary state. The oscillation frequency ratio f/f_K is 15 kinds, and it is 0.2 steps from 0.2 to 3.0. All calculation was carried out to the non-dimensional time $T = 100$.

As a procedure of numerical simulation, the circular cylinder stationary case (oscillating amplitude ratio $2a/d = 0.0$) was carried out first, and it carried out by setting an amplitude ratio to $2a/d = 0.5$ next, and varying oscillating oscillation frequency ratio f/f_K based on the result in circular cylinder stationary.

3 Results and Discussions

As for the flow pattern at the time of circular cylinder stationary, formation of a Karman vortex street was seen naturally. The value of each component of the fluid force in that case was the following. The average value of drag coefficient C_{DAVE} was 1.08, the root mean square value (r.m.s.) of the amplitude of drag coefficient AC_D was 0.15, the average value of lift coefficient C_{LAVE} was 0.00, and the root mean square value (r.m.s.) of the amplitude of lift coefficient AC_L was 0.73. The Strouhal number $St (= fd/U = d/(\Delta tU) = 1/T)$ for which it determined from the oscillating period T
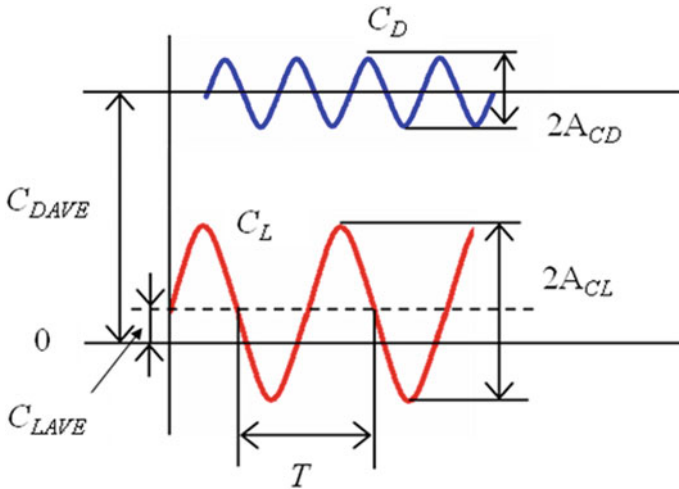
Fig. 1 The definition of the magnitude of the drag coefficient or the lift coefficient, and the definition of the oscillating period

of the lift coefficient was 0.26. In order to help an understanding of those symbols, the explanation about them is shown in Fig. 1. Although a previous experimental result [5] and good agreement were shown about fluid force, a different result was brought about the Strouhal number. About this point, since a two-dimension calculation result has the tendency which becomes high about 40 from 30% to an experimental value, it is considered to be an appropriate value on numerical computation. It seems that it is inoffensive in numerical simulation even if numerical simulation differs from an actual Strouhal number from being carried out by a frequency ratio. When the Karman vortex shedding frequency f_K at the time of circular cylinder stationary was calculated from the Strouhal number, it was 0.65 Hz.

It is one of the most interesting matters of this study to investigate influence on the fluid force by varying circular cylinder oscillation frequency. When the oscillation frequency ratio was increased, changes of the lock-in state were the following. It is in the state which the lock-in has not produced in the beginning. Secondly, it will be in the state of an alternate vortex shedding type lock-in. Then, it will be in the state of a simultaneous vortex shedding type lock-in through the state where it strayed off from the lock-in. And will be strayed off from the lock-in. An example of the time history of an instantaneously flow pattern, and circular cylinder displacement (black line in a figure) and fluid force (the blue line in the figure is the drag coefficient, and the red line is the lift coefficient) is shown in Figs. 2, 3, 4 and 5. The value of each component (the average value C_{DAVE} of the drag coefficient at the time of circular cylinder oscillation, the root mean square value (r.m.s.) AC_D of the amplitude of drag coefficient, the average value C_{LAVE} of lift coefficient, the root mean square value (r.m.s.) AC_L of the amplitude of lift coefficient) of fluid force is shown in Table 1.
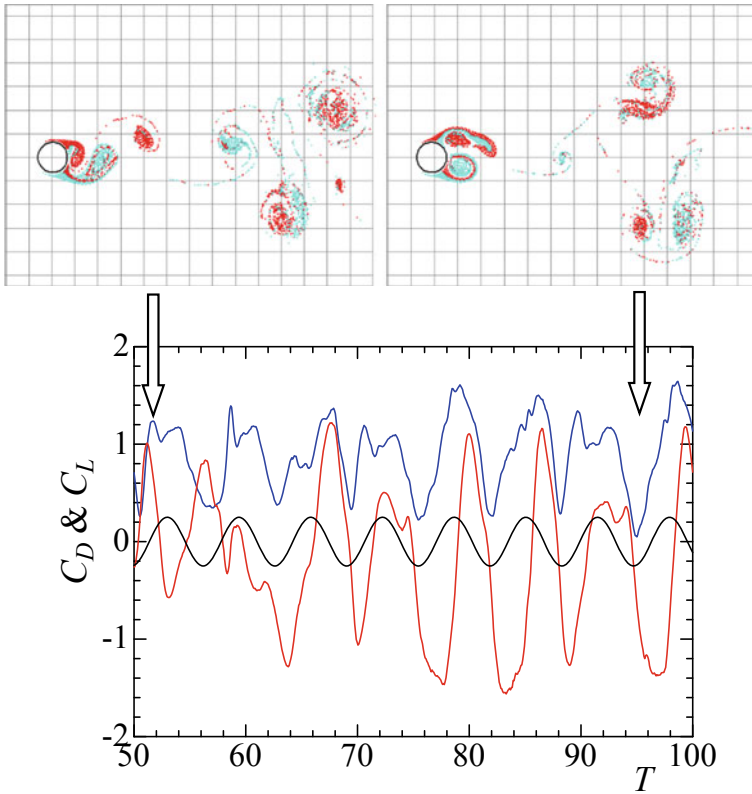
Fig. 2 The instantaneous flow features ($T = 51.48$ and $T = 95.94$) and time histories of fluid force component, $f/f_K = 0.6$
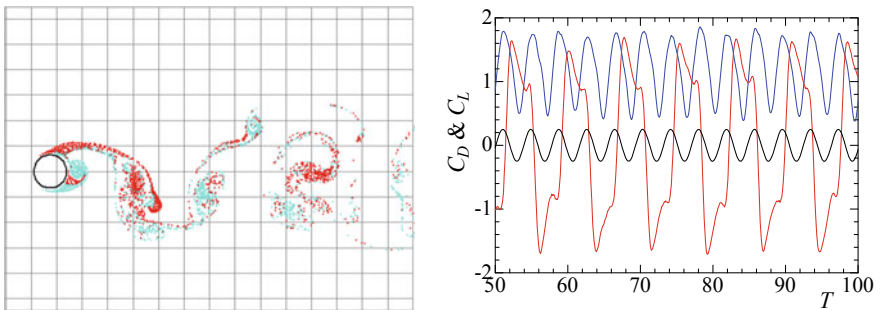
Fig. 3 The instantaneous flow feature ($T = 80.34$) and time histories of fluid force component, $f/f_K = 1.0$
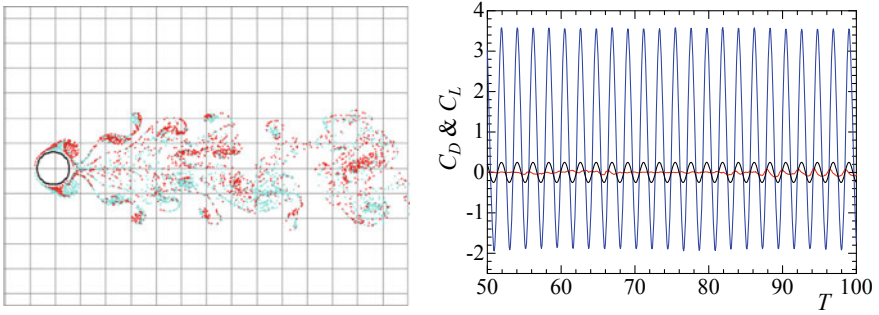
Fig. 4 The instantaneous flow feature ($T = 74.88$) and time histories of fluid force component, $f/f_K = 1.8$
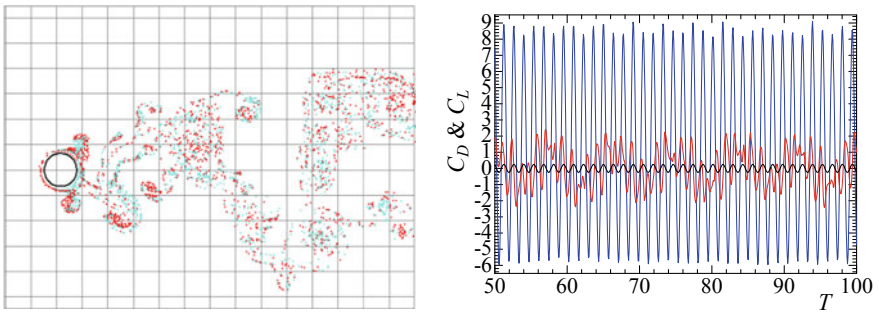
Fig. 5 The instantaneous flow feature ($T = 74.88$) and time histories of fluid force component, $f/f_K = 2.8$

Table 1 The variation of fluid force

f/f_K	C_{DAVE}	A_{CD}	C_{LAVE}	A_{CL}
0.0	1.08	0.15	0.00	0.73
0.2	1.05	0.20	0.00	0.72
0.4	1.00	0.21	0.01	0.64
0.6	0.91	0.37	-0.18	0.76
0.8	1.13	0.48	-0.01	0.93
1.0	1.20	0.45	0.05	1.13
1.2	1.19	0.70	0.08	0.95
1.4	1.32	1.00	-0.00	0.94
1.6	0.94	1.44	0.01	0.37
1.8	0.76	1.91	-0.01	0.04
2.0	0.74	2.46	-0.02	0.05
2.2	0.72	3.02	0.01	0.08
2.4	0.92	3.59	0.00	0.41
2.6	0.82	4.27	-0.01	0.19
2.8	1.30	5.02	0.04	1.20
3.0	1.38	5.85	-0.03	1.29

Figure 2 is the case where the circular cylinder oscillation frequency ratio is $f/f_K = 0.6$, and is in the state which the lock-in has not produced. It is shown by two flow patterns that the configuration and the discharge direction of the vortex shedding change with time. In the non-dimensional time $T = 51.48$, roll up of the vortex seems to change the discharge direction as a pendulum by alternation. On the other hand, in the non-dimensional time $T = 95.94$, roll up of the vortex is simultaneous and the vortex pair discharged simultaneously seems to change the discharge direction as a pendulum. If the time history of fluid force is seen, oscillation of fluid force with the regularity corresponding to cylinder movement cannot be seen. However, it can grasp that it is larger than the amplitude of drag coefficient in the amplitude of lift coefficient. Figure 3 is the case where the circular cylinder oscillation frequency ratio is $f/f_K = 1.0$, and is in the state which the alternate vortex shedding type lock-in has produced. It is shown by the flow pattern that the vortex street similar to the Karman vortex of a grand scale is formed. In the time history of fluid force, the oscillating period of the lift coefficient is a half to the cylinder oscillating period, and the oscillating period of the drag coefficient is the same. Moreover, it can grasp that it is larger than the amplitude of drag coefficient in the amplitude of lift coefficient. The regularity of oscillation of drag and lift coefficients can be seen to have become strong as compared with Fig. 2. Figure 4 is the case where a circular cylinder oscillation frequency ratio is $f/f_K = 1.8$, and is in the state which the simultaneous vortex shedding type lock-in has produced. The separating shear layer simultaneously rolled around the flow pattern forms the vortex pair from which a rotation direction differs each other by movement of the circular cylinder, and an aspect that it is discharged in the direction of down-stream is shown. In the time history of fluid force, it proves that oscillation of the drag coefficient synchronizes completely to the oscillating period of the circular cylinder. Moreover, it proves that the amplitude of the drag coefficient becomes very large. On the other hand, oscillation of the lift coefficient is lost. Figure 5 is the case where the circular cylinder oscillation frequency ratio is $f/f_K = 2.8$, and is in the state which strayed off from the lock-in. With the flow pattern, the vortex of mushroom cross-section shape is simultaneously discharged from both the sides of the circular cylinder, and the state where the surge has occurred in the wake is shown.

In the time history of fluid force, it can grasp that oscillation of the drag coefficient synchronizing to oscillation of the circular cylinder and the amplitude are also large far as compared with Fig. 4. The large oscillating amplitude of the lift coefficient of the long period which does not support circular cylinder oscillation is seen. It seems that this oscillation originates in a large surge wake. Although there is a peculiar flow pattern in an alternate vortex shedding type lock-in and a simultaneous vortex shedding type lock-in, in the state where it strayed off from the lock-in, the aspect of a complicated flow is seen everywhere in the case. In that case, it is because the "alternate vortex shedding type lock-in" or the "simultaneous vortex shedding type lock-in" will be contained in the state where "the lock-in of the natural Karman vortex" exists as foundations, in between. It is imagined that replacement of those flow patterns is dependent on the size relationship of the drag and the lift. It is dragged by circular cylinder oscillation at the high oscillation frequency side at the

time of having passed over the simultaneous vortex shedding type lock-in, and the amplitude of the drag coefficient tends to increase and the tendency for the amplitude of lift coefficient to also become large with it can read it from Table 1. The surge of this lift coefficient that became large constitutes alternate vortex formation of a circular cylinder behind, and it becomes the mechanism in which the Karman vortex of different appearance from original is formed.

4 Conclusions

A systematic numerical simulation of the flow around an oscillating circular cylinder in the direction of the flow was performed by use of vortex method. The following conclusions were obtained.

(1)   Changes of the lock-in state in the process which increases an oscillation frequency ratio were found.
(2)   Although the oscillating amplitude of the drag coefficient becomes large, the oscillating amplitude of the lift coefficient becomes small, as an oscillation frequency ratio increases.
(3)   In the size relationship of the oscillating amplitude of the lift coefficient and the drag coefficient, when the amplitude of the lift coefficient is large, it is in the alternate vortex shedding state, and when the amplitude of the drag coefficient is large, it will be in the simultaneous vortex shedding state.
(4)   When it was not in the lock-in state, it was found that it will be in the complicated flow state. It imagines because the "alternate vortex shedding type lock-in" or the "simultaneous vortex shedding type lock-in" will be intermittently contained in the state where "the lock-in of the natural Karman vortex" exists as foundations.
(5)   As future work, it is interesting to investigate the dependability of Reynolds number and to investigate the phase relationship between circular cylinder oscillation and fluid force oscillation.

References

1. Yokoi Y, Hirao K (2014) The appearance of two lock-in states in the vortex flow around an in-line forced oscillating circular cylinder. EPJ Web Conf 67(02131):1–8
2. Kamemoto K (1993) The expandability of the vortex method as a turbulent flow model (the first part: to think a basic of vortex method). Computat Fluid Dyn 2(1):20–29
3. Kuzmina KS, Marchevsky IK, Ryatina EP (2017) Exact analytical formulae for linearly distributed vortex and source sheets influence computation in 2D vortex methods. J Phys Conf Ser 918:012013-1–012013-9
4. Yokoi Y, Hirao K (2008) Vortex flow around an in-line forced oscillating circular cylinder. Trans Japan Soc Mech Eng Ser B 74(746):2099–2108

5. Korzani MG, Galindo-Torres SA, Scheuerman A, Williams DJ (2017) Parametric study on smoothed particle hydrodynamics for accurate determination of drag coefficient for a circular cylinder. Water Sci Eng 10(2):143–153

Dynamic Modeling and Dynamic Response Analysis of Annular Composite Beam Structure

Bingheng Zhu, Dengqing Cao, Youxia Li, and Tianxi Liu

1 Introduction

In recent years, artificial satellites used for earth observation, space communication, deep space exploration, etc. have been rapidly developed. At the same time, more technical requirements such as higher bandwidth and better spectrum efficiency have placed higher demands on satellite antennas. In order to meet the increasing technical requirements of remote sensing satellites, mobile communication satellites, and data relay satellites for capturing small power signals. However, due to the limitation of the volume of the rocket fairing, it is necessary to design the satellite antenna into a structure with a large stretch ratio. The large annular truss structure has the advantages of light weight, high rigidity, large diameter, easy deployment and high storage ratio, which is the ideal structure for large satellite antennas at present [1, 2]. The research on loop antennas is mainly to carry out equivalent dynamic model, inherent characteristic and dynamic response to it.

Liu [3] discretized the deformable antenna structure through the constructed hypothetical displacement field by Rayleigh–Ritz method. Combined with the Lagrange method, he established a flexible multibody dynamics model for deployable antennas. Based on the Lagrange method of multibody dynamics systems, Li [4] adopted independent Lagrange generalized coordinates to establish the deployment process of the peripheral truss deployable antenna dynamic model. Duan [5] developed a design approach for the trajectory that set up the deploying angular speed as a linear accelerated-constant-decelerated process, and then obtained the trajectory of the

B. Zhu · D. Cao (✉) · T. Liu
School of Astronautics, Harbin Institute of Technology, Harbin, People's Republic of China
e-mail: dqcao@hit.edu.cn

Y. Li
China Academy of Space Technology, Beijing, People's Republic of China

driving cable using inverse kinematics. Salehian et al. [6] used Hamilton's principle to find the governing partial differential equation of the structure. In order to accurately research the dynamic characteristics of truss structure for modular space deployable truss antenna, dynamic experiments were carried out. Based on the basic theory of dynamics and the characteristics of antenna structure, a set of dynamic experimental system was designed by Tian et al. [7], and the modal experiments under free boundary conditions were carried out by means of single-point input and multi-point output.

In this paper, loop antenna is modeling as annular composite beam structure. In order to get global modal shapes of the system, global modal method (GMM) is used. According to matching and boundary conditions, the frequency equation is obtained, thereby, getting the natural frequency and global modal shapes.

2 Dynamic Modeling for Annular Composite Beam Structure

2.1 Motion Equations of the System

As shown in the Fig. 1, the studied structure composes two parts, one part is a regular polygonal annular composite beam structure formed by multiple beams, the other part is the support beam which is perpendicular to annular beam structure. All connection points are formed by rigid connection of beams.

The floating coordinate system is established with the midpoint of beam B_i ($i = 1, 2, \cdots N + 1$) as the coordinate origin. Each beam will produce longitudinal vibration, torsional vibration and bending vibration in two directions. The longitudinal,

Fig. 1 Composite beam structure
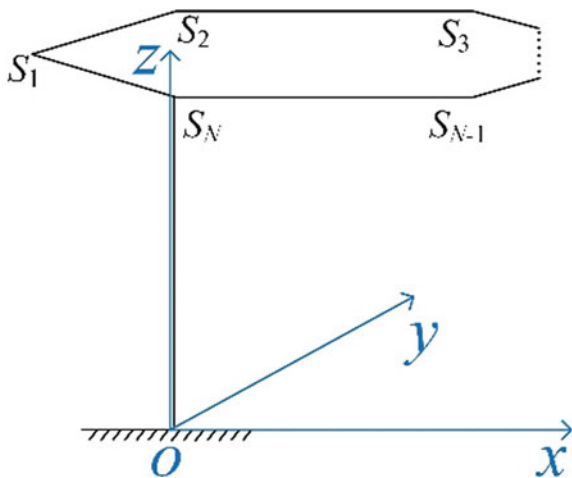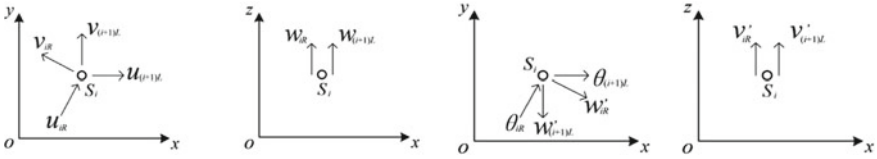
Fig. 2 Geometric matching conditions at connection point $S_i (i = 1, 2, \ldots N - 1)$

torsional and lateral displacements of the beam B_i are $u_i(x_i, t)$, $\theta_i(x_i, t)$, $v_i(x_i, t)$ and $w_i(x_i, t)$ and the governing equations of motion for beam B_i are

$$
\begin{aligned}
&E_i A_i u_i''(x_i, t) - \rho_i A_i \ddot{u}_i(x_i, t) - \xi_i \dot{u}_i(x_i, t) = 0, \\
&G_i J_i \theta_i''(x_i, t) - \rho_i J_i \ddot{\theta}_i(x_i, t) - \zeta_i \dot{\theta}_i(x_i, t) = 0, \\
&E_i I_i v_i''''(x_i, t) + \rho_i A_i \ddot{v}_i(x_i, t) + \lambda_i \dot{v}_i(x_i, t) = 0, \\
&E_i I_i w_i''''(x_i, t) + \rho_i A_i \ddot{w}_i(x_i, t) + \eta_i \dot{w}_i(x_i, t) = 0.
\end{aligned}
\tag{1}
$$

There are two kinds of connection points in the whole structure, one is formed by connection of two beams as shown in Figs. 2 and 3, and the other is formed by connection of three beams as shown in Figs. 4 and 5.
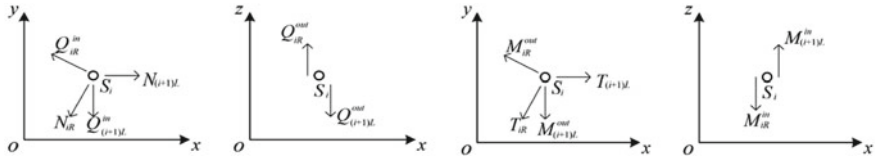
Fig. 3 Natural matching conditions at connection point $S_i (i = 1, 2, \cdots N - 1)$
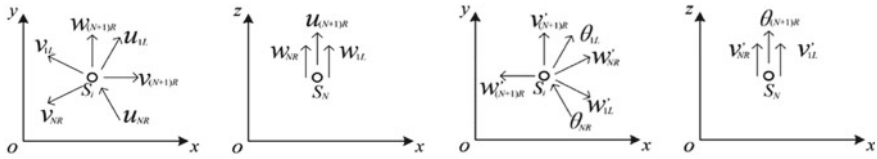
Fig. 4 Geometric matching conditions at connection point S_N
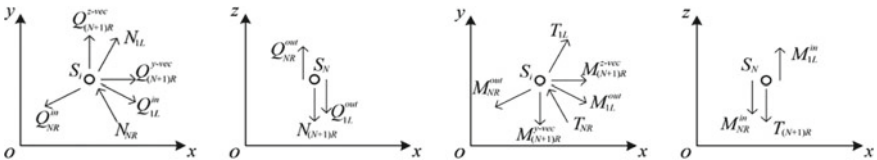
Fig. 5 Natural matching conditions at connection point S_N

The matching conditions at connection point $S_i (i = 1, 2, \ldots, N - 1)$ can be written as

$$u_i(l_i, t) \cos \alpha - v_i(l_i, t) \sin \alpha = u_{i+1}(-l_{i+1}, t),$$
$$u_i(l_i, t) \sin \alpha + v_i(l_i, t) \cos \alpha = v_{i+1}(-l_{i+1}, t),$$
$$w_i(l_i, t) = w_{i+1}(-l_{i+1}, t),$$
$$\theta_i(l_i, t) \cos \alpha + w_i'(l_i, t) \sin \alpha = \theta_{i+1}(-l_{i+1}, t),$$
$$\theta_i(l_i, t) \sin \alpha - w_i'(l_i, t) \cos \alpha = -w_{i+1}'(-l_{i+1}, t),$$
$$v_i'(l_i, t) = v_{i+1}'(-l_{i+1}, t),$$
$$E_i A_i u_i'(l_i, t) \cos \alpha + E_i I_i v_i'''(l_i, t) \sin \alpha = E_{i+1} A_{i+1} u_{i+1}'(-l_{i+1}, t),$$
$$E_i A_i u_i'(l_i, t) \sin \alpha - E_i I_i v_i'''(l_i, t) \cos \alpha = -E_{i+1} I_{i+1} v_{i+1}'''(-l_{i+1}, t),$$
$$E_i I_i w_i'''(l_i, t) = E_{i+1} I_{i+1} w_{i+1}'''(-l_{i+1}, t),$$
$$G_i J_i \theta_i'(l_i, t) \cos \alpha + E_i I_i v_i''(l_i, t) \sin \alpha = G_{i+1} J_{i+1} \theta_{i+1}'(-l_{i+1}, t),$$
$$G_i J_i \theta_i'(l_i, t) \sin \alpha + E_i I_i v_i''(l_i, t) \cos \alpha = -E_{i+1} I_{i+1} w_{i+1}''(-l_{i+1}, t),$$
$$E_i I_i v_i''(l_i, t) = E_{i+1} I_{i+1} v_{i+1}''(-l_{i+1}, t) \tag{2}$$

And the matching conditions on connection point S_N can be written as

$$u_1(-l_1, t) \cos \beta + v_1(-l_1, t) \sin \beta = w_{N+1}(l_{N+1}, t),$$
$$u_1(-l_1, t) \sin \beta - v_1(-l_1, t) \cos \beta = v_{N+1}(l_{N+1}, t),$$
$$u_N(l_N, t) \cos \beta - v_N(l_N, t) \sin \beta = w_{N+1}(l_{N+1}, t),$$
$$u_N(l_N, t) \sin \beta + v_N(l_N, t) \cos \beta = -v_{N+1}(l_{N+1}, t),$$
$$w_1(-l_1, t) = u_{N+1}(l_{N+1}, t), \quad w_N(l_N, t) = u_{N+1}(l_{N+1}, t),$$
$$\theta_1(-l_1, t) \cos \beta - w_1'(-l_1, t) \sin \beta = v_{N+1}'(l_{N+1}, t),$$
$$\theta_1(-l_1, t) \sin \beta + w_1'(-l_1, t) \cos \beta = -w_{N+1}'(l_{N+1}, t),$$
$$\theta_N(l_N, t) \cos \beta + w_N'(l_N, t) \sin \beta = v_{N+1}'(l_{N+1}, t),$$
$$\theta_N(l_N, t) \sin \beta - w_N'(l_N, t) \cos \beta = w_{N+1}'(l_{N+1}, t),$$
$$v_1'(-l_1, t) = \theta_{N+1}(l_{N+1}, t), \quad v_N'(l_N, t) = \theta_{N+1}(l_{N+1}, t),$$
$$E_1 A_1 u_1'(-l_1, t) \cos \beta - E_1 I_1 v_1'''(-l_1, t) \sin \beta - E_N A_N u_N'(l_N, t) \cos \beta$$
$$- E_N I_N v_N'''(l_N, t) \sin \beta = -E_{N+1} I_{N+1} w_{N+1}'''(l_{N+1}, t),$$
$$E_1 A_1 u_1'(-l_1, t) \sin \beta + E_1 I_1 v_1'''(-l_1, t) \cos \beta + E_N A_N u_N'(l_N, t) \sin \beta$$
$$- E_N I_N v_N'''(l_N, t) \cos \beta = -E_{N+1} I_{N+1} v_{N+1}'''(l_{N+1}, t),$$
$$E_1 I_1 w_1'''(-l_1, t) - E_N I_N w_N'''(l_N, t) = -E_{N+1} A_{N+1} u_{N+1}'(l_{N+1}, t),$$
$$G_1 J_1 \theta_1'(-l_1, t) \cos \beta - E_1 I_1 w_1''(-l_1, t) \sin \beta - G_N J_N \theta_N'(l_N, t) \cos \beta$$
$$- E_N I_N w_N''(l_N, t) \sin \beta = E_{N+1} I_{N+1} v_{N+1}''(l_{N+1}, t),$$
$$G_1 J_1 \theta_1'(-l_1, t) \sin \beta + E_1 I_1 w_1''(-l_1, t) \cos \beta + G_N J_N \theta_N'(l_N, t) \sin \beta$$
$$- E_N I_N w_N''(l_N, t) \cos \beta = -E_{N+1} I_{N+1} w_{N+1}''(l_{N+1}, t),$$

$$E_1 I_1 v_1''(-l_1, t) - E_N I_N v_N''(l_N, t) = G_{N+1} J_{N+1} \theta_{N+1}'(l_{N+1}, t) \tag{3}$$

The boundary conditions of the system are

$$u_{N+1}(-l_{N+1}, t) = 0, \; v_{N+1}(-l_{N+1}, t) = 0, \; w_{N+1}(-l_{N+1}, t) = 0,$$
$$v_{N+1}'(-l_{N+1}, t) = 0, \; w_{N+1}'(-l_{N+1}, t) = 0, \; \theta_{N+1}(-l_{N+1}, t) = 0 \tag{4}$$

2.2 Natural Frequency and Global Mode of the System

Using the method of separating variables to solve the natural frequency and global mode shapes of the system, the displacement of the system can be expressed as:

$$u_i(x_i, t) = U_i(x_i)e^{j\omega t}, \quad v_i(x_i, t) = V_i(x_i)e^{j\omega t},$$
$$w_i(x_i, t) = W_i(x_i)e^{j\omega t}, \quad \theta_i(x_i, t) = \Theta_i(x_i)e^{j\omega t} \tag{5}$$

where ω is the natural frequency of the system. Substituting Eq. (5) into Eq. (1) without damping yields

$$E_i U_i''(x_i) + \omega^2 \rho_i U_i(x_i) = 0, \quad E_i I_i V_i''''(x_i) - \omega^2 \rho_i A_i V_i(x_i) = 0,$$
$$E_i I_i W_i''''(x_i) - \omega^2 \rho_i A_i W_i(x_i) = 0, \quad G_i \Theta_i''(x_i) + \omega^2 \rho_i \Theta_i(x_i) = 0 \tag{6}$$

General solution of Eq. (6) can be written as

$$U_i(x_i) = B_i \cos(a_i x_i) + C_i \sin(a_i x_i), \quad x_i \in [-l_i, l_i]$$
$$V_i(x_i) = D_i \cos(b_i x_i) + F_i \sin(b_i x_i) + H_i \mathrm{ch}(b_i x_i)$$
$$+ K_i \mathrm{sh}(b_i x_i), \quad x_i \in [-l_i, l_i]$$
$$W_i(x_i) = L_i \cos(c_i x_i) + P_i \sin(c_i x_i) + R_i \mathrm{ch}(c_i x_i)$$
$$+ S_i \mathrm{sh}(c_i x_i), \quad x_i \in [-l_i, l_i]$$
$$\Theta_i(x_i) = X_i \cos(d_i x_i) + Y_i \sin(d_i x_i), \quad x_i \in [-l_i, l_i] \tag{7}$$

where $a_i = \omega \left(\frac{\rho_i}{E_i} \right)^{1/2}, b_i = \left(\frac{\rho_i A_i \omega^2}{E_i I_i} \right)^{1/4}, b_i = \left(\frac{\rho_i A_i \omega^2}{E_i I_i} \right)^{1/4}, d_i = \omega \left(\frac{\rho_i}{G_i} \right)^{1/2}$.

Let $\psi_i = [B_i \; C_i \; D_i \; F_i \; H_i \; K_i \; L_i \; P_i \; R_i \; S_i \; X_i \; Y_i], \; \Psi = [\psi_1 \; \psi_2 \dots \psi_{N+1}]^{\mathrm{T}}$.

Substituting generation solution Eq. (7) into the matching conditions Eq. (2), matching conditions Eq. (3) and boundary conditions Eq. (4), we have

$$\boldsymbol{H}(\omega)\Psi = 0 \tag{8}$$

where the matrix $\boldsymbol{H}(\omega) \in R^{(6N+1) \times (6N+1)}$.

2.3 Dynamic Model of the System

The discrete dynamic model is obtained by using the Galerkin truncation procedure to the continuous dynamic model according to the orthogonality of the global modal shapes of the composite structures. Taking the first nth global modal shapes, the displacements of the system can be written as

$$u_i(x_i, t) = \sum_{j=1}^{n} U_i^j(x_i)q_j(t), \quad v_i(x_i, t) = \sum_{j=1}^{n} V_i^j(x_i)q_j(t),$$

$$w_i(x_i, t) = \sum_{j=1}^{n} W_i^j(x_i)q_j(t), \quad \theta_i(x_i, t) = \sum_{j=1}^{n} \Theta_i^j(x_i)q_j(t) \tag{9}$$

where $q_j(t)$ is the jth modal coordinate. According to orthogonality of the global modes, we have

$$M_s\ddot{q}_s + C_s\dot{q}_s + K_sq_s = 0, \quad s = 1, 2, \ldots n \tag{10}$$

where C_s is the coefficient of viscous damping.

3 Typical Example of Application

Considering the annular composite beam structure as a regular hexagon annular beam with support beam. Applying a displacement excitation $w_s(t)$ in the z direction to the base O in Fig. 1. Geometrical parameters and material constants are listed in Table 1.

The dynamic equation of the system can be written as

Table 1 Geometric and material parameters of composite beam structures

Parameter	Value
Annular beam length $2l$ (m)	2
Support beam length $2l_v$ (m)	3
Annular beam section diameter d (m)	0.02
Support beam section diameter d_v (m)	0.03
Annular beam elastic modulus E (GPa)	2.06
Support beam elastic modulus E_v (GPa)	2.06
Annular beam Poisson's ratio v	0.3
Support beam Poisson's ratio v_v	0.3
Annular beam density ρ (Kg/m^3)	7850
Support beam density ρ_v (Kg/m^3)	7850

$$M_s \ddot{q}_s + C_s \dot{q}_j + K_s q_s = F_s, \quad s = 1, 2, \ldots n \tag{11}$$

where

$$F_s = - \sum_{i=1}^{N} \int_{-l_i}^{l_i} (\rho_i A_i \ddot{w}_s + \eta_i \dot{w}_s) W_i^s(x_i) \mathrm{d}x_i$$

$$- \int_{-l_{N+1}}^{l_{N+1}} (\rho_{N+1} A_{N+1} \ddot{w}_s + \xi_{N+1} \dot{w}_s) U_{N+1}^s(x_{N+1}) \mathrm{d}x_{N+1}$$

4 Numerical Results and Discussion

According to Eq. (8), the natural frequency of the system can be obtained. Natural frequency can also be obtained by finite element method. Here ANSYS software, as a tool of finite element method (FEM) is used to solve natural frequency of the system. Comparing natural frequency obtained GMM to FEM, and relative error between two methods is also calculated as shown in Table 2. Substituting first 9 frequencies to Eq. (8), the global mode shapes can be obtained, which is showed in Fig. 6.

Comparing the results obtained from GMM and FEM, it shows that the natural frequency obtained by two methods are matched very well. The relative error among the first 9 frequencies of the composite beam structure is less than 0.1%. This shows the validation of our approach.

Table 2 The first 9 frequencies of the composite beam structure ω (Hz)

Mode	GMM	FEM	RE%
1	0.371	0.371	0
2	0.372	0.372	0
3	0.763	0.762	0.13
4	0.912	0.911	0.11
5	1.559	1.558	0.06
6	2.345	2.343	0.09
7	3.059	3.057	0.07
8	3.306	3.304	0.06
9	3.984	3.981	0.08
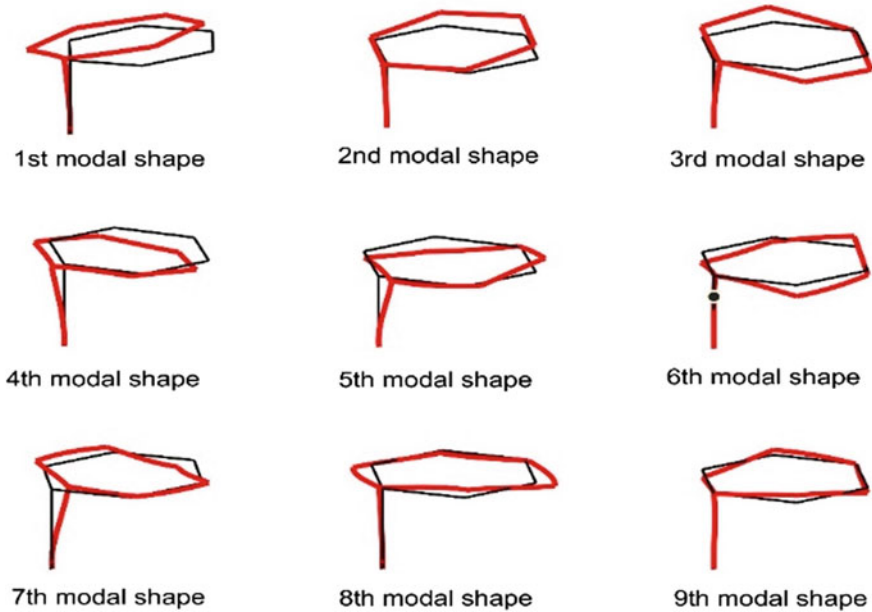
Fig. 6 The first 9-order global modal shapes

5 Conclusion

The polygonal annular beam structure is a relatively complex composite structure, and the tensile, torsional and bending motions of each beam must be considered. In this paper, the accurate natural frequencies and global mode shapes are obtained by the global modal method, which verifies the accuracy and effectiveness of the global modal method in solving complex composite beam structures. This provides a solving method for the vibration analysis of similar structures.

References

1. Siriguleng B, Zhang W, Liu T et al (2020) Vibration modal experiments and modal interactions of a large space deployable antenna with carbon fiber material and ring-truss structure. Eng Struct 207:109932
2. Guo H, Shi C, Li M et al (2018) Design and dynamic equivalent modeling of double-layer hoop deployable antenna. Int J Aerosp Eng 2018

3. Liu C, Tian Q, Hu H (2011) Dynamics of a large scale rigid–flexible multibody system composed of composite laminated plates. Multibody Syst Dyn 26(3):283–305
4. Li T, Zhang Y, Li T (2009) Deployment dynamic analysis and control of hoop truss deployable antenna. Acta Aeronaut Astronaut Sin 30(3):444–449
5. Duan B, Analysis S (2005) Optimization and control of the flexible antenna. Science Press, Beijing
6. Salehian A, Seigler TM, Inman DJ (2006) Control of the continuum model of a large flexible space structure. In: ASME international mechanical engineering congress and exposition, vol 47659, pp 561–570
7. Tian D, Liu R, Jin L et al (2019) Experimental research on dynamic characteristics of truss structure for modular space deployable truss antenna. In: International conference on intelligent robotics and applications. Springer, Cham, pp 273–282

Experimental Flow Visualization of Novel Aircraft Architectures

V. I. Chernousov, A. A. Krutov, and E. A. Pigusov

1 Introduction

The Central Aerohydrodynamic Institute (TsAGI, Russia) has researching on the novel aircraft concepts for cargo transportation [1]. Unconventional aerodynamic layouts used in these projects are not as well understood as traditional solutions, so wind tunnel tests and flow visualization are needed. This paper presents the results of experimental flow visualization studies of two unconventional aircraft layouts.

The first one—Twin-Fuselage Transport Aircraft (TFTA). The TFTA is intended for transportation of cargo weighted up to 40 tons at a distance 3000 km with speed 700–740 km/h. The obvious advantage of the twin-fuselage aircraft is a significant reduction of the maximum bending moments on wing, compared to a conventional single-fuselage aircraft [2]. As a result, with the same payload, the weight of the structure and the longitudinal dimensions of the twin-fuselage aircraft would be less than that of the single-fuselage aircraft.

The second—Heavy Cargo Aircraft with Lifting Body (HCA-LB). The HCA-LB is aimed for transportation up to 500 t of payload at the distance 6000 km with speed 450–550 km/h. It is proposed to use LNG as fuel, which will reduce emissions and improve weight efficiency of HCA-LB layout. The HCA-LB main cruise regime would be a flight in ground effect. Massive center wing with large cargo holds has low aspect ratio, which leads to unusual aerodynamics in comparison with conventional aircraft.

V. I. Chernousov · A. A. Krutov (✉) · E. A. Pigusov
Central Aerohydrodynamic Institute (TsAGI), Zhukovsky, Russian Federation
e-mail: aleksandr.krutov@tsagi.ru

E. A. Pigusov
e-mail: evgeniy.pigusov@tsagi.ru

2 Methods and Methodology

The experimental visualization studies of the novel aircraft models were carried out in the T-102 [3] and T-103 [4] low-speed wind tunnel (WT) of TsAGI test facility.

The T-102 is continuous-operation, closed layout WT with two reverse channels and an open test section designed to investigate aerodynamic characteristics of aircraft models at take-off, landing and low-speed flight. WT flow velocity is up to 55 m/s. Test section with elliptical cross-section has following dimensions: $4 \times 4 \times 2.33$ m.

The T-103 WT has a test section similar to T-102, but maximum flow velocity is 80 m/s.

Flow visualization was carried out using tuft method [5–8]. Silk tufts were attached on surface of models using thin duct tape. For TFTA model (Fig. 1) tufts were 40 mm length for fuselages and major part of wing, and 30 mm length for empennage and outer parts of wing. For HCA-LB model (Fig. 2) tufts were 50 mm length for center wing, 40 mm length for outer parts of wing and 30 mm length for empennage and nacelles.

Reference geometry parameters of the models are presented in Table 1.
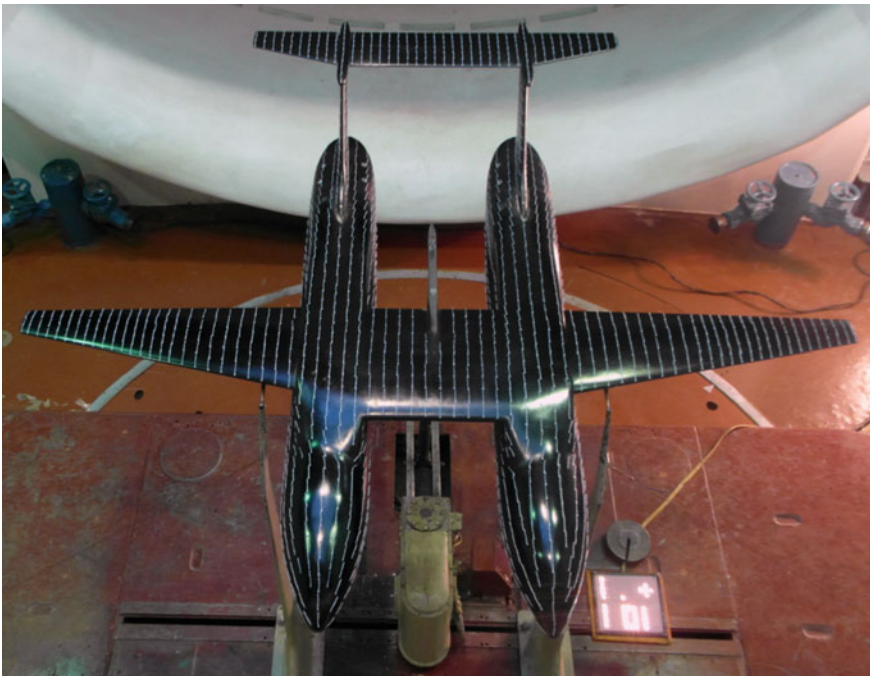
Fig. 1 The TFTA model with tufts in WT T-102

Fig. 2 The HCA-LB model with tufts in WT T-103

Table 1 Geometry parameters of the novel transport aircraft models

Parameter	TFTA	HCA-LB
Wingspan, m	2.5	2.013
Wing area, sq.m	0.66	1.275
Wing aspect ratio	9.46	3.178
Mean aerodynamic chord (MAC), m	0.306	0.796

3 Results

3.1 Twin-Fuselage Transport Aircraft

The TFTA model has a high-wing, double fuselages, double fins and single high-placed horizontal stabilizer. The TFTA model was tested in WT T-102 at flow velocity 40 m/s and the range of the angle of attack (AoA): $0 \div 17°$.

The TFTA model demonstrates the unseparated flow at cruise AoA 5° (Fig. 3). With an increase of AoA to 13°, flow separation occurs at one of the wing consoles, which is expressed in the appearance of a maximum on the lift graph. A further increase of AoA to 17° leads to flow separation on both wing consoles, while the unseparated flow on central wing is partially preserved. An asymmetrical stall on the wing console necessitates the use of slats, the simpler high-lift devices can be used on the central wing section.
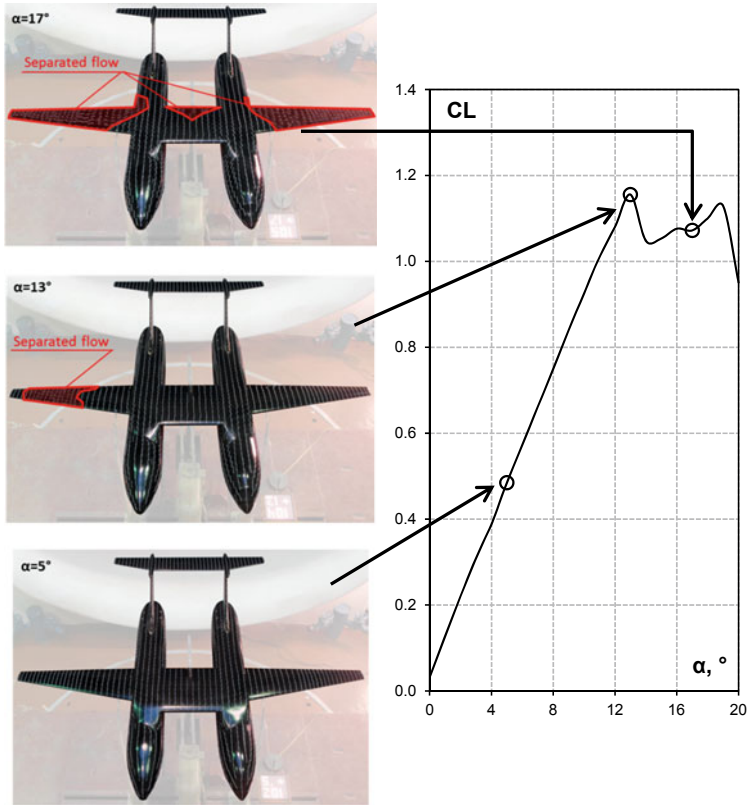
Fig. 3 The TFTA model flow visualization at different angles of attack

3.2 Heavy Cargo Aircraft with Lifting Body

The HCA-LB model is consist of large center wing with side wing consoles of smaller chord, double tail booms with fins and single high-placed horizontal stabilizer, engine nacelles are placed over the center wing. The HCA-LB model was tested in WT T-103 at flow velocity 40 m/s, the range of the AoA: $-4 \div 16°$.

Visualization of the flow around the model at different AoA (Fig. 4) shows that at high AoA flow separates on the wing consoles, which may be due to strong interference with the center section, which leads to an increase in the local inflow angle at the wing consoles.

An asymmetrical separation of the flow at an angle of attack of 12° is dangerous, because it leads to a sharp change in the roll moment (Fig. 5), asymmetric stall and spin. To eliminate this trend, vortex generators (VG) can be installed in front of the wing consoles, behind which stable vortices are formed. Figure 5 shows that the VG installation led to both a decrease in the roll moment coefficient (C_1) and a less sharp change of C_1 with an increase of AoA.
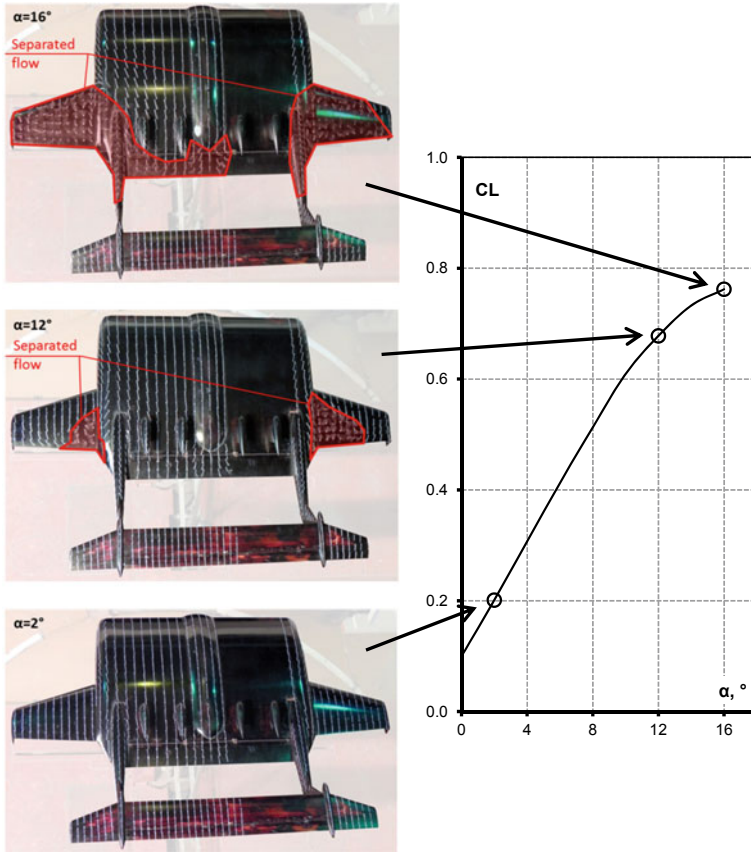
Fig. 4 The HCA-LB model flow visualization at different angles of attack

4 Conclusion

Flow visualization is an important part of experimental studies of aerodynamic configurations of novel aircraft. The flow visualization studies by the tuft method, despite the venerable age of the technology, make it possible to observe the flow pattern during the experiment and see the appearance of separation regions in the dynamics.

Consideration of the flow features of the presented novel aircraft layouts showed that the flow separation occurs on the wing consoles, which is undesirable and reduces flight safety at high angles of attack.

The results of the flow visualization studies of the considered aircraft layouts make it possible to develop solutions for improving their aerodynamic characteristics in the future.
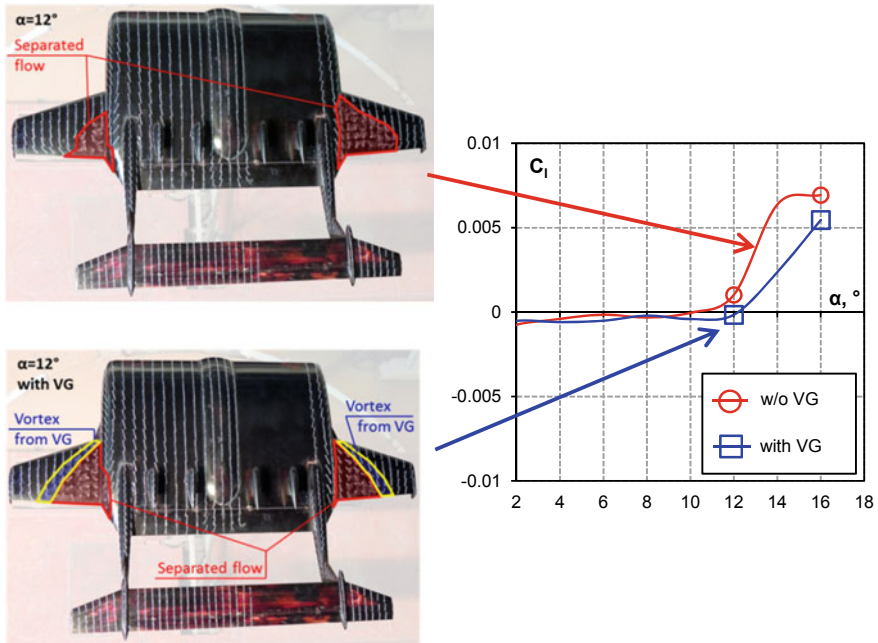
Fig. 5 Influence of the vortex generators installation on rolling behavior

References

1. Chernousov V, Krutov A, Pigusov E (2018) Containerized air freight system powered by cryo-genic fuel. In: 31st congress of the international council of the aeronautical sciences (ICAS 2018) Proceedings, Belo Horizonte, Brazil (2018). https://icas.org/ICAS_ARCHIVE/ICAS2018/data/papers/ICAS2018_0103_paper.pdf/
2. Torenbeek E (2013) Advanced aircraft—conceptual design, technology and optimisation of subsonic civil airplanes. Wiley, Chichester, pp 436
3. T-102 TsAGI wind tunnel (2020) http://www.tsagi.com/experimental_base/wind-tunnel-t-102/. Last Accessed 02 Dec 2020
4. T-103 TsAGI wind tunnel (2020). http://www.tsagi.com/experimental_base/wind-tunnel-t-103/. Last Accessed 02 Dec 2020
5. Merzkirch W (1987) Techniques of flow visualization. AGARD-AG-302
6. Skinner SN, Zare-Behtash H (2017) Semi-span wind tunnel testing without conventional peniche. Exp Fluids 58:163. https://doi.org/10.1007/s00348-017-2442-7
7. Chernousov V, Krutov A, Pigusov E (2020) Three-dimensional visualization of flow pattern near transport airplane with operating propellers in wind tunnel. J Phys: Conf Ser 1697. International Conference PhysicA.SPb/2020, Saint Petersburg, Russia. https://doi.org/10.1088/1742-6596/1697/1/012216
8. Steinfurth B, Cura C, Gehring J et al (2020) Tuft deflection velocimetry: a simple method to extract quantitative flow field information. Exp Fluids 61:146. https://doi.org/10.1007/s00348-020-02979-7

Investigation of the Movement of the Descent Vehicle in the Atmosphere of the Planet with Inflatable Braking Mechanical Devices, Taking into Account Various Perturbations at an Average Altitude of Movement

Vsevolod Koryanov, Lang Shuobin, Leo Richier, and Danhe Chen

1 Introduction

Continuous development of spacecraft missions aimed at the study of the planets of the solar system planned led to the development of unmanned spacecraft, designed to study the planet. In addition to the stages of the flight, complex maneuvers for the flight into orbit, an important stage in the implementation of the mission of spacecraft is the stage of landing of the descent vehicle while moving in the atmosphere and the moment of contact with the surface of the planet.

To successfully complete this stage, it is necessary to use special mechanical devices. These devices can provide a successful landing, unfold at a certain stage of the movement and provide the required speed reduction. It is proposed to use inflatable braking devices as such an engineering mechanical device. To simplify the problem of modeling the motion of such a descent vehicle with inflatable braking devices, the method of decomposition of the problem into separate stages of motion is used. This article is included in the cycle of scientific articles by the author [1–3]. Article [1] deals with the movement in the upper atmosphere, in article [2]—in the middle and lower atmosphere. However, the simulation was carried out only for the

V. Koryanov (✉) · L. Shuobin
Bauman Moscow State Technical University, 2-nd Baumanskaya 5, b1, Moscow 105005, Russian Federation
e-mail: vkoryanov@bmstu.ru

L. Richier
School of Aeronautics and Mechanical Engineering, ISAE-ENSMA, Chasseneuil du Poitou, France

D. Chen
School of Mechanical Engineering, Nanjing University of Science and Technology (NJUST), Nanjing, China

nominal motion case. Article [3] deals with the movement at the final stage of the movement.

In addition, the author's article [4] is devoted to the study of disturbing factors arising during descent in the atmosphere. Also in the article [5] general conclusions on the dynamics of spacecraft motion are drawn. The article [6] analyzes the use of inflatable braking devices in other areas of application—orbital servicing. This landing vehicle, considered in this article, and its prototype were described in articles [7–10]. This is landing vehicle named MetNet, and it is was one part RITD-project.

This article examines the movement at the penultimate stage of movement, taking into account various deviations of the longitudinal axis of the descent vehicle. Thus, a picture of an asymmetric flow around the descent vehicle is obtained. The main idea in this article is also the calculation of the presence of asymmetries of the descent vehicle in terms of inflatable structures due to the asymmetric displacement of the center of mass of the structure. The resulting simulation results are analyzed, and conclusions are drawn.

1.1 Theoretical Background, Modeling Hypothesis, and Preprocessing

The mathematical model is described in detail in the articles of the author [1, 2]. As already mentioned, the stages of motion in the upper atmosphere were described in [1]. The simulations were made with OpenFoam which is an efficient software for Computational Fluid Dynamic (CFD). The values of pressure and temperature are taken from the Mars climate database [11].

As we can (see Fig. 1), case 3 is supersonic so that the flow is highly compressible. So for this case, we have used the solver rhoPimpleFoam which is adapted to transient compressible flows, so adapted to our study case. If we compute the Reynolds number, we find $R_e \sim 3.10^5$ so the flow is turbulent. In the numerical resolution, we have chosen the k-epsilon model with a turbulent intensity of 1% and a characteristic length of the turbulent structure of 10 cm (an experimental study would be needed to precisely determine these values in such conditions). Because the turbulence is establishing in 3D, we have chosen a fluid domain with a small thickness equals to

Case 3: beginning of stage III
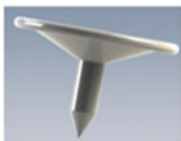
20 km   700 m/s   190 K / 90 Pa

                  Mach 3.16

Fig. 1 Case of our study and corresponding conditions

the length of the turbulent structures. During the simulation, dynamic viscosity is computed with a Sutherland law considering that the Martian atmosphere is fully composed of CO2 and for the heat capacity, we used the Janaf expression where the unknown parameters for both formulas can be easily found for CO2 in the literature. By the way, we need to specify a boundary condition for the temperature of the wall of the descent vehicle before launching the simulation. Because this parameter is unknown, we will try two temperatures of the wall (500 and 1000 K) corresponding to close values that are encountered into the shock layer as we will see. So somehow, we have proceeded on an iterative way, waiting the first results for the temperature into the shock layer to choose the temperature of the wall in the next simulations. Here were the main modeling hypothesis for the preprocessing stage of our simulations. Let's now see the results.

For case 3, we need to specify a boundary condition for the temperature of the wall of the lander vehicle. We assume that the wall is isotherm, and we will choose two temperatures (500 and 1000 K) to see the influence of this parameter on aerodynamical loads.

We used only one mesh for both cases because it is the same geometrical conditions. The mesh has to be enough refined near the lander vehicle because physical fields may vary a lot in this region.

2 Results and Analysis

Now, we will study the influence of the angle of attack on stress repartition and pressure lift and drag. We will choose three angles of attack: 0°, 10°, 15° (see Fig. 2) for the condition Twall = 1000 K. As we can see on Fig. 3, the structure of the flow is different when we choose a non-zero angle of attack. Indeed, the flow isn't symmetric anymore and repartition of stress is changed too (Fig. 4). When the angle of attack increases, repartition of stresses changes a lot mainly for the right side. We can see that the gaps between the sides in T_{px} and T_{py} repartition become less important and we totally loose the symmetry between left side and right side which makes lift increases and drag decreases as we can see in Table 1. These asymmetries can lead to some instabilities of the lander vehicle and may change his trajectory.
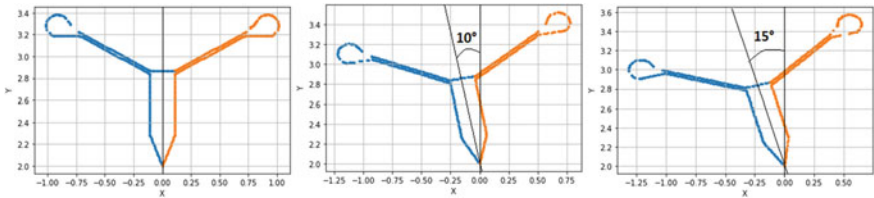
Fig. 2 Configurations of the lander vehicle for case 3
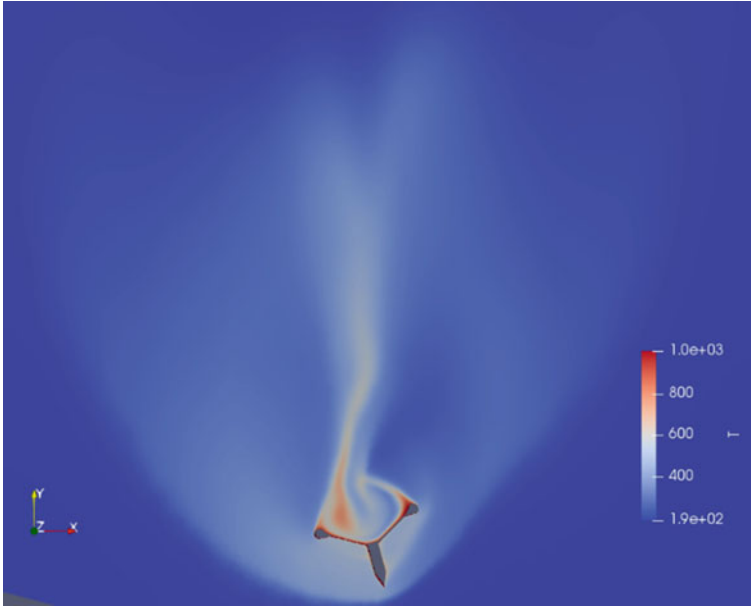
Fig. 3 Temperature field at $t = 0.015$ s for an angle of attack of 15° and a temperature of the wall of 1000 K

We must keep in mind that the top of the AIBU is not a rigid body so asymmetries in stress repartition around this part can lead to change the geometrical configuration of the lander vehicle and can lead to instability. In order to avoid this phenomenon, the descent at this stage have to be done with a low angle of attack.

In order to see the influence of asymmetries of the upper part of the AIBU, we will run two simulations for a 0° angle of attack but with an asymmetry of 5° or 10° as we can see on Fig. 5. We keep the condition $T_{wall} = 1000 K$.

Here again, we constate the loose of symmetry in pressure stress repartition (Fig. 6) which lead to increase lift (in absolute values) and decrease drag (Table 2). Lift becomes more and more negative (so along minus x axis) when the rotation of the upper part of AIBU is defined as on Fig. 5.

It is assumed that the viscous part is neglect as before when we study the influence of the angle of attack and of asymmetries.

3 Conclusions

A study of the movement of the descent vehicle with inflatable braking devices allows us to make a positive conclusion about the possibility of using inflatable technology in future.
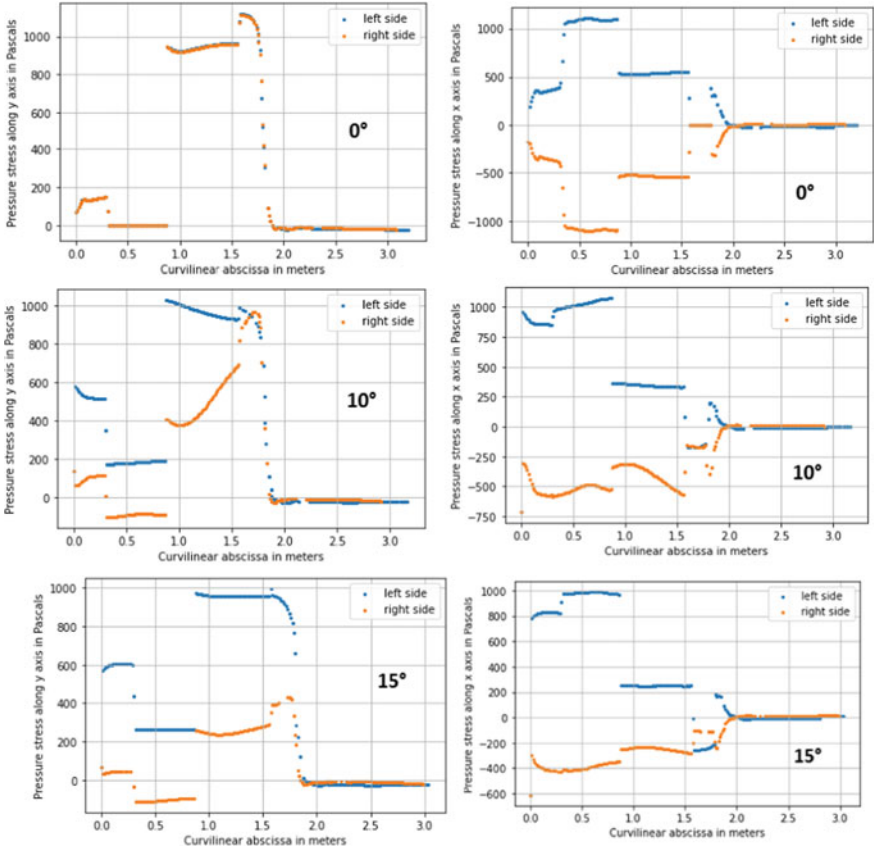
Fig. 4 Pressure stress on the lander vehicle for a temperature of the wall of 1000 K at $t = 0.015$ s (left: T_{px}, right: T_{py})

Table 1 Values of lift and drag per meter for various angles of attack and for a temperature of the wall of 1000 K at $t = 0.015$ s

Angle of attack	Lift per meter L (N/m)	Drag per meter D (N/m)
0°	4.18	1909.5
10°	270.4	1699.2
15°	383.2	1437.8
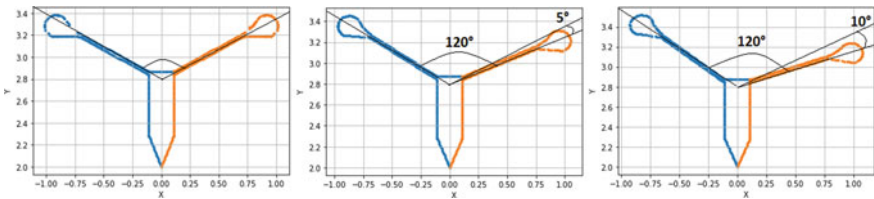
Fig. 5 Definition of the angle of asymmetry
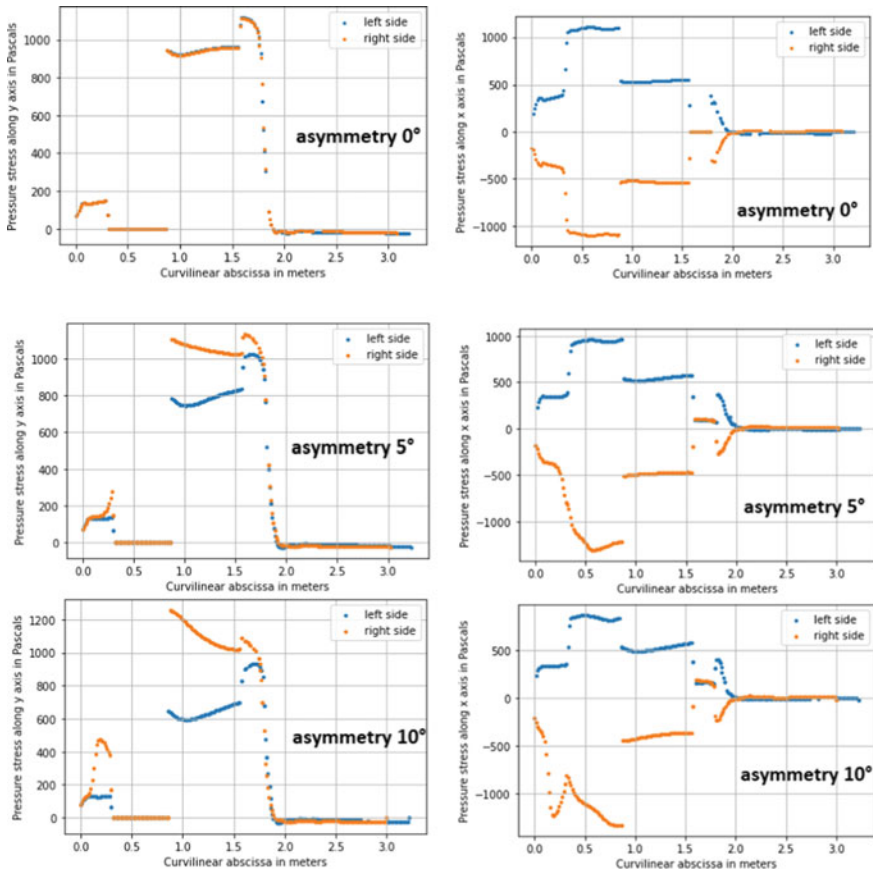
Fig. 6 Pressure stress on the lander vehicle at $t = 0.015$ s for an angle of attack of $0°$ and a temperature of the wall of 1000 K (left: T_{px}, right: T_{py})

Table 2 Values of lift and drag per meter for various angles of asymmetry, with an angle of attack of $0°$ and a temperature of the wall of 1000 K

Angle of attack	Lift per meter L (N/m)	Drag per meter D (N/m)
0°	4.18	1909.5
10°	−95	1870.8
15°	−150.4	1810.6

An order of magnitude for lift and drag per meter was found for this flight configuration.

An order of magnitude for temperature into the bow shock was found.

Limitations:

A more complete study would be needed to improve the knowledge about the behavior of turbulence for this case.

A thermal study would be needed to precisely determine the temperature of the wall (even if we have shown that it doesn't impact a lot the value of lift and drag).

References

1. Koryanov VV, Richier L, Chen D (2020) Dynamics of the landing vehicle during the entry in the high atmosphere of mars using an inflatable braking device. In: 2020 8th international conference on control, mechatronics and automation. ICCMA 2020, pp. 131–137, 9301507
2. Chen D, Richier L, Koryanov VV (2021) Dynamics of the movement of the descent vehicle in the atmosphere of Mars with the use of inflatable brakes in the lower atmosphere. J Phys: Conf Series 1786(1):012018
3. Koryanov VV, Hermosilla Heras M (2020) Research dynamic motion of a landing vehicle during the final landing stage. IOP Conf Series: Mater Sci Eng 904(1):12014
4. Koryanov V, Huanya S (2019) Analysis of emerging disturbing factors on the descent vehicle with inflatable mechanical devices during the descent stage. IOP Conf Series: Mater Sci Eng 630:012031. https://doi.org/10.1088/1757-899X/630/1/012031
5. Vsevolod K, Victor K (2018) Dynamics of angular motion of landing vehicle in martian atmosphere with allowance for small asymmetries. Int J Mech Eng Robot Res 7:385–391. https://doi.org/10.18178/ijmerr.7.4.385-391
6. Koryanov VV, Chen D, Wei X (2020) Research of using inflatable braking devices in the orbital service system application. J Phys: Conf Series 1510(1):012005
7. Harri A-M, Pellinen R, Uspensky M, Siili T, Linkin V, Lipatov A, Savijärvi H, Vorontsov V, Ivankov A (2006) Metnet atmospheric science network for Mars
8. Harri A-M, Leinonen J, Merikallio S, Paton M, Haukka H, Polkko J, Linkin V, Lipatov V, Pichkadze K, Polyakov A, Uspensky M, Vasquez L, Guerrero H, Crisp D, Haberle R, Calcutt S, Wilson C, Taylor P, Lange C, Zarnecki J (2007) MetNet : in situ observational network and orbital platform to investigate the Martian environment
9. Heilimo J, Harri A-M, Aleksashkin S, Koryanov V, Arruego I, Schmidt W, Haukka H, Finchenko V, Martynov M, Ostresko B, Ponomarenko A, Kazakovtsev V, Martin S (2015) RITD—adapting mars entry, descent and landing system for Earth
10. Marraffa L, Vennemann D, Anschuetz U, Walther S, Stelter C, Pitchkhadze K, Finchenko V (2003) RIDT—inflatable re-entry and descent technology 521. 19
11. Millour F, Forget A, Spiga M, Vals V, Zakharov L, Montabone, F, Lefèvre F, Montmessin JY, Chaufray MA, López-Valverde F, González-Galindo SR, Lewis PL, Read MC, Desjean F, Cipriani and the MCD development team. The Mars Climate Database (version 5.3)

The Use of Numerical Modeling for the Formation of Recommendations for Conducting Experiments on Ballistic Tracks

S. N. Iljukhin, V. V. Koryanov, V. O. Moskalenko, and A. G. Toporkov

1 Introduction

Perhaps the fundamental characteristic of the movement of any object is its speed relative to the selected reference frame [1]. The initial velocity characterizes the trajectory parameters and kinetic energy of a passively flying aircraft. That is why one of the most important tasks of experimental ballistics is to determine the trajectory speed of the aircraft. The solution of this problem allows us to experimentally investigate the force of air resistance to the movement of a particular type of aircraft, determine the power of the weapon under study, and obtain the value of the initial speed of the aircraft as initial data for further numerical modeling of the flight path.

To obtain objective information about the elements of a body's motion, including its velocity, measuring devices are widely used, which are located during experiments at measurement points outside of a moving body. Since the most reliable results are obtained in full-scale experiments, the most common bench installations in experimental ballistics are ballistic tracks (Fig. 1).

A ballistic track is a specially equipped shooting track that allows firing special models of aircraft or real ammunition under test or laboratory conditions, with the measurement (along with other parameters) of the speed of their movement at a number of points on the trajectory [1–4]. Structurally, a closed-type ballistic track

S. N. Iljukhin · V. V. Koryanov (✉) · V. O. Moskalenko · A. G. Toporkov
Bauman Moscow State Technical University, Moscow 105005, Russia
e-mail: vkoryanov@bmstu.ru

S. N. Iljukhin
e-mail: iljuchin.stepan@bmstu.ru

V. O. Moskalenko
e-mail: moskalenko@bmstu.ru

A. G. Toporkov
e-mail: agtoporkov@bmstu.ru

141

Fig. 1 Ballistic track of the SM-3 Department of BMSTU

is a body that restricts the working area of the experiment and ensures safety. At the beginning of this case is the launcher, and at the end—the catching device. The housing provides technological hatches for the installation of lighting, recording, or measuring equipment. Automated laboratories also include a computer system, monitoring, and synchronization devices. According to the measured values of the speed of movement of the body on a single trajectory, the value of the drag coefficient can be calculated.

Various approaches are used to measure the speed of bullets and models in laboratory conditions: a ballistic pendulum, the Doppler effect, shadow analogies. [1, 5] But the most common, effective, and affordable device for determining the speed of a flying object in bench conditions is a chronograph. As sensors in chronographs, rotating paper disks (the Stern method), special electric contact curtains, electromagnetic frames, laser, or photocells can be used. Often, the time interval between the flight of a bullet of a fixed distance can be obtained by analyzing the recording from a high-speed video camera.

However, any instruments have a certain measurement accuracy, and each method of determining the parameters of the aircraft is based on certain assumptions. If you take this into account when planning and conducting an experiment, you can increase the accuracy of obtaining the desired values. In addition, after conducting preliminary studies, you can determine the required parameters of the ballistic route for a particular experiment. For example, the length of the installation can range from 1–2 m for intra-ballistic studies to 300 m or more for large-caliber ballistic routes.

2   Methods

2.1   Mathematical Modeling of the Flight of a Small-Sized Aircraft and the Operation of a Measuring Device

To assess the impact of measuring instrument errors and the impact of the accepted assumptions, a software package was created for the primary processing of experimental data produced on ballistic installations of various levels. The function of this complex is to simulate the passive uncontrolled flight of a statically stable body (model, bullet, projectile). The software package is developed in the visual environment of C++ Builder in the C++ language.

As the base coordinate system, the normal coordinate system [1] is used, the reference point of which is located in the lower left corner of the considered route. The main assumption is that the flight of an unguided aircraft occurs in a vertical plane. The gravitational field is assumed to be plane-parallel. In the software, the method of simulating the operation of a chronograph is used to determine the speed of the aircraft.

Numerical integration of the system of equations in this package can be implemented by three methods: the Euler method, the Runge–Kutta method of the 4th order, or the Adams method of the 4th order. Each of these methods has its own advantages and disadvantages [6, 7]. By the way, the Euler method, due to its simplicity, has a high speed, but low accuracy with intensive changes in the simulated parameters. The Runge–Kutta method has a high accuracy, but due to the repeated calculation of the right-hand sides of differential equations at each step, it is characterized by low efficiency. In turn, the Adams method, which is related to multistep methods, uses the values of the function at the previous points to start integrating, although the efficiency of the Adams method is much higher than the efficiency of the Runge–Kutta method of the same order of accuracy.

The results of numerical simulation are recorded in the form of tables, on the basis of which graphical dependencies are constructed.

As an illustration of the conducted research, we will consider an experimental study of the flight of a small unguided aircraft at subsonic speeds.

3   Results

3.1   Selecting the Distance of the Ballistic Track to Determine the Drag Coefficient

As an analytical method for determining the drag coefficient C_{xa} of a passively flying object, an algorithm based on the estimation of changes in kinetic energy is used. This method is widely known and described in detail [8]. The calculated dependence
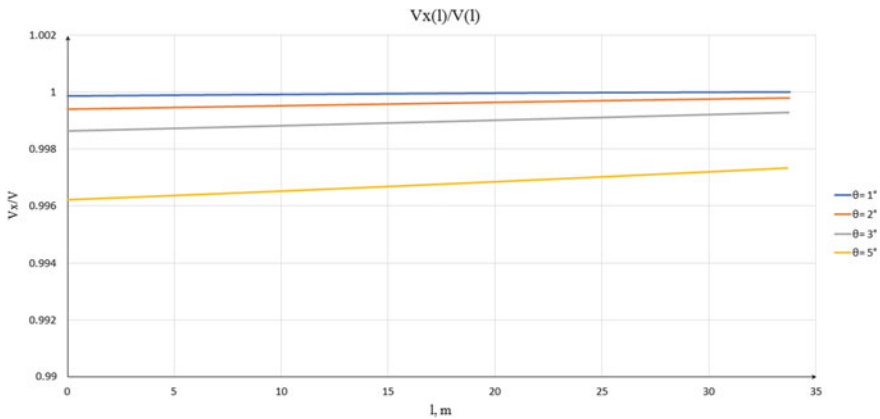
Fig. 2 Dependence of the ratio V_x / V on the distance between the measured planes l

used in the processing of experimental data is obtained on the basis of the law of change of "living" forces. To implement the main assumption of the method under consideration, shooting for determining the drag coefficient on a ballistic track is organized so that the measured section of the trajectory is horizontal to exclude the influence of gravity.

It is advisable to study the ratio of the horizontal component of the speed V_x to the value of the full speed V of the aircraft on the studied section l, since this method of determining the drag coefficient is implemented under the assumption that the studied section of the trajectory is horizontal. We study this factor for different values of the initial angle of inclination of the velocity vector to the horizontal plane θ.

Analyzing the results obtained in mathematical modeling (Fig. 2) for the example under consideration, it can be noted that when determining the drag coefficient, it is advisable to organize the launch of a small-sized aircraft at small values of the angle θ, since in this case the calculation results will be closest to the true parameters of the aircraft. At the same time, the greatest reliability of the considered assumption is achieved at a distance of more than 20 m from the beginning of the trajectory.

3.2 Evaluation of the Impact of Chronograph Accuracy on the Determination of the Drag Coefficient

It is also advisable to study the dependence of the coefficient C_{xa} obtained during the experiment on the ballistic track on the accuracy of the speed measurement. We will set the true value of $C_{xa} = 0.3$ in the software package, which will be used in flight simulation. In the simulation of the measurement and further calculation of C_{xa}, the velocity values rounded to 0.1 m/s are used. This is how the chronograph's speed measurement error is simulated.
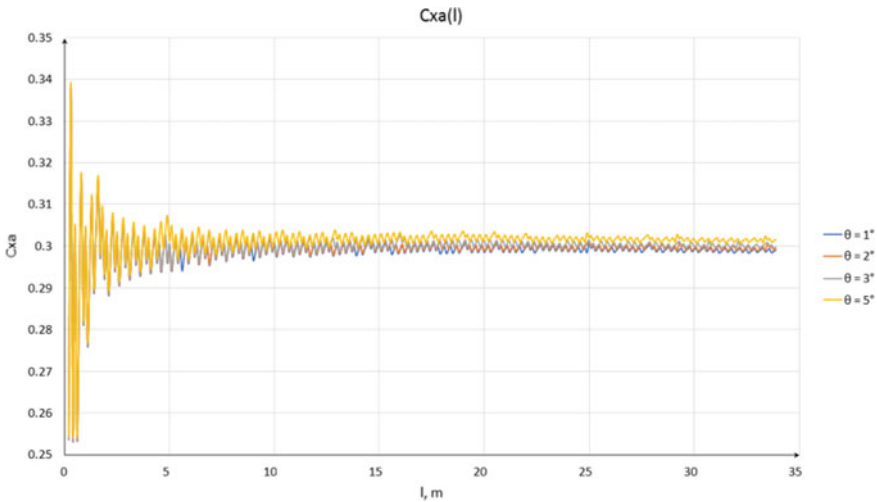
Fig. 3 The value of the measured C_{xa} as a function of l with a chronograph accuracy of 0.1

From the figure (Fig. 3), it can be seen that when determining the parameters with an accuracy of 0.1, the results obtained depend weakly on the initial angle of the throw. When the distance between the fixing planes is less than 5 m, there is a large discrepancy between C_{xa} and the true value. The value of the drag coefficient approaches the true value when the measuring area is increased. On a plot of more than 7 m, the error is less than 2%, and on a plot of more than 15 m, the error is already less than 0.5%.

3.3 Selecting the Distance of the Ballistic Track to Determine the Scattering Parameters

In addition to speed measurements and the determination of aerodynamic characteristics, the processes of collision and destruction are also widely studied in experiments on ballistic routes [9–11]. But from the point of view of ballistics, the problems of determining the scattering of hit points are also relevant [3, 12, 13]. Let's look at this in more detail. The dispersion of hit points is affected by the stability of the initial velocity, the identity of small-sized aircraft, and the parameters of weapons. Let's determine at what distance from the beginning of the trajectory it is better to study the scattering.

The figure (Fig. 4) shows the trajectory profiles for different initial velocities. The lower the initial velocity, the more the curvature of the trajectory changes and, consequently, the shorter the maximum flight range.
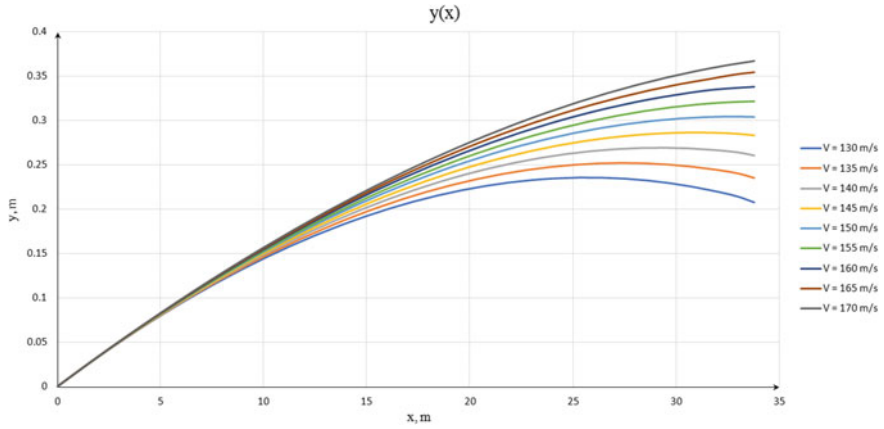
Fig. 4 Trajectory profile at different initial velocities
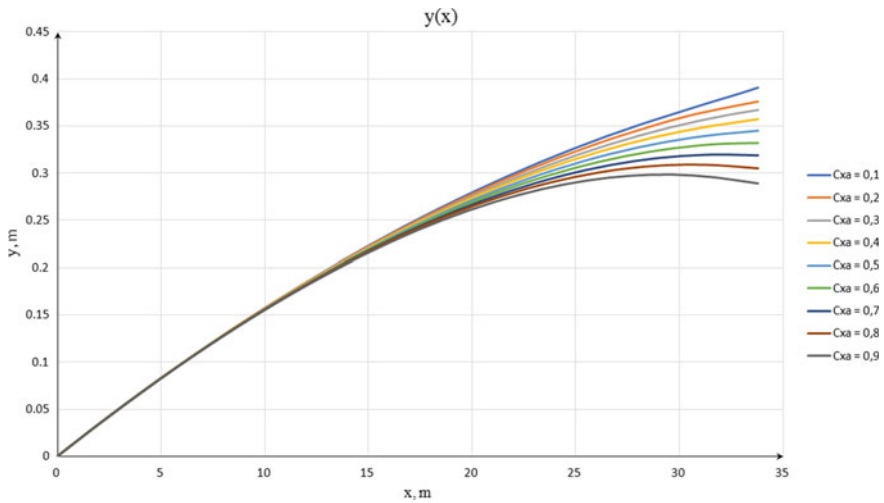
Fig. 5 Trajectory profile with different drag coefficients

When the drag coefficient varies (Fig. 5), it can be seen that the greater the C_{xa}, the more intensively the trajectory changes and the maximum flight range decreases. This is due to an increase in aerodynamic losses.

4 Conclusion

When forming the requirements for the ballistic track, it is necessary to take into account the totality of the results obtained, from which the following recommendations can be distinguished for the case of studying the flight of a small-sized aircraft at subsonic speed:

– when studying the trajectory of the aircraft for scattering, the diameter of the pipe of the ballistic route should be at least 0.4 m.
– when determining the drag coefficient, the distance between the two chronographs must be more than 7 m, and the total flight distance must be at least 15 m.
– when studying the trajectory of an aircraft for scattering the diameter of the pipe, the distance of the ballistic route should be large, preferably more than 20 m. In this case, the speed and aerodynamic shape affect the dispersion more strongly than the mass of the aircraft.

It is also worth putting forward requirements for weapons. It is necessary to strive to reduce the initial angle θ, as well as to ensure the accuracy of the positioning of the weapon, since even minor deviations θ can lead to significant errors in determining the parameters.

References

1. Lysenko LN (2018) Exterior ballistic. Moscow, BMSTU publ., p 326
2. Denny M (2011) The internal ballistics of an air gun. Phys Teacher (49):8. https://doi.org/10.1119/1.3543577
3. Iljukhin SN, Moskalenko VO, Bulavina VV (2020) Investigation of dispersion and aerodynamic drag of modified bullets at subsonic flight speeds on a ballistic track. Eng J: Sci Innov (12). https://doi.org/10.18698/2308-6033-2020-12-2039
4. Bogomolova PD (2017) Analysis of methods for conducting experimental studies with speed measurement on a ballistic track. Politechnical Student J (9). https://doi.org/10.18698/2541-8009-2017-9-160
5. Werner R, Schultz B, Frank M (2016) Influence of pellet seating on the external ballistic parameters of spring-piston air guns. Int J Legal Med 130(5):1287–1290. https://doi.org/10.1007/s00414-016-1415-3
6. Mukharlyamov RG, Beshaw AW (2013) Solving differential equations of motion for constrained mechanical systems. Discrete Continuous Models Appl Comput Sci 3:83–93
7. Khaikov VL (2018) Mathematical modeling and computer simulation of a basic problem of tube artillery external ballistics by means of the Mathcad software. Vojnoteh glas (2). https://doi.org/10.5937/vojtehg66-15328
8. Ilyukhin SN (2014) Methods for finding the drag coefficient during experimental studies on a ballistic track. Youth Scientific and Technical Bulletin, no. 1, pp 3
9. Werner R, Schultz B, Bockholdt B, Ekkernkamp A, Frank M (2017) Energy-dependent expansion of .177 caliber hollow-point air gun projectiles. Int J Legal Med 131(3):685–690. https://doi.org/10.1007/s00414-016-1528-8
10. Forrestal MJ, Warren TL, Randles PW (2014) Deceleration-displacement response for projectiles that penetrate concrete targets. In: Song B, Casem D, Kimberley J (eds) Dynamic behavior

of materials, vol 1. Conference proceedings of the society for experimental mechanics series. Springer, Cham. https://doi.org/10.1007/978-3-319-00771-7_31

11. Harshey A, Srivastava A, Yadav VK et al (2017) Analysis of glass fracture pattern made by 177″ (4.5 mm) caliber air rifle. Egypt J Forensic Sci (20):7. https://doi.org/10.1186/s41935-017-0019-5

12. Khaikov VL (2018) Single shot hit probability estimation as a result of the numerical solution of double integrals using Mathcad. Vojnoteh glas (4). https://doi.org/10.5937/vojtehg66-17433

13. Khaikov VL (2019) Assessment of the single shot hit probability as a function of the horizontal range taking into account different target types and points of aim. Vojnoteh glas (1). https://doi.org/10.5937/vojtehg67-18522

Cost Benefit of a Small-Scale Vertical Axis Wind Turbine for Residential use in Honduras

Sophia Eloise Ayestas and Alicia María Reyes Duke

1 Introduction

In recent years, the cost of electricity for residential users in Honduras has had a significant growth. Since 2016 to this year, the rate for the first 50 (kWh) consumed has had an increase of 135.19% and the rate for energy consumptions greater than 50 (kWh) has had an increase of 27.68%, making the cost of living in the country more expensive [1]. From this issue stems the interest to search for alternative energy sources for self-consumption. Solar energy is being used at a residential level, but has the disadvantage of generating electricity only during daylight unless batteries are installed, which have a high cost. The load profile of the country's households has its highest peak of consumption during the evening, for this reason, the economic benefits of investing in a wind power system that can take advantage of night-time production is being investigated. The purpose of this investigation is to determine if implementing this technology entails benefits for the residential sector under study. Information will be collected on the historical energy consumption of households located on the eastern peninsula of Puerto Cortés as well as meteorological data from the municipality's Environmental Management Unit. The energy production of the chosen wind turbine will be simulated using the software HOMER Grid, as well as the percentage of the energy demand met by the wind power system and by the national grid. The indicator Levelized Cost of Electricity (LCOE) will be used to determine if the cost of production of the proposed wind system is lower than the cost of electricity offered by the power company of Honduras, "National Electric Power Company".

S. E. Ayestas · A. M. R. Duke (✉)
Faculty of Engineering, Central American Technological University, Tegucigalpa, Honduras
e-mail: alicia.reyes@unitec.edu.hn

2   Context

The amount of small-scale wind turbines operating globally grows every year. In 2015, the number of small-scale wind turbines installed was approximately 990,000 around the world with a total installed capacity of 948 (MW). This represents an increase of 5% compared to 2014, when 944,000 units were registered. However, this number is based on the available information and even excludes large markets such as that of India, so the World Wind Energy Association (WWEA) estimates that for that year the number of units installed must have been close to one million. China is the market leader, representing 74% of installed units, followed by the United States with 16% of installed units in the world [2].

In Honduras, there is a solar-wind power generation system located in "Caratasca Lagoon", department of "Gracias a Dios", which has an installed capacity of 45 (kWp) in solar photovoltaic energy and 10 (kW) in wind energy. The wind resource is harnessed by two small-scale vertical axis wind turbines. The system is completely renewable and it is disconnected from the national power grid. This system includes inverters, combination boxes, fuse boxes, wiring, solar panels, wiring, wind turbines, and a battery bank. The hybrid system is the energy source for the U.S. naval base located in the lagoon [3, 4].

3   Methodology

The investigation has a descriptive approach that is divided into an energy demand analysis, in which the consumption of the area is analyzed and a typical residential load profile is elaborated, a technical analysis, for the choice of the wind turbine and to simulate its energy production, and a financial analysis, in which parameters such as the initial investment of the project and the operation and maintenance costs are calculated to obtain the cost benefit of the proposed system.

The main variable of the study is the cost benefit, since this is where the research problem arises. The other variables for the energy demand analysis are the savings from self-consumption, excess energy production, and energy consumed from the power grid. For the technical analysis, the independent variables are the wind resource of the area, the roughness of the terrain, the size of the wind turbine, the project lifespan, and the capacity factor of the system. For the financial analysis, the independent variables are the initial investment, O&M costs, inflation, interest rate, and loan payment.

The research hypothesis is that the cost benefit of installing a small-scale vertical axis wind turbine for residences located on the eastern peninsula of Puerto Cortés is greater than one.

This research is carried out in the eastern peninsula of the municipality of Puerto Cortés because the meteorological information comes from a station located in this

area. Since wind speed varies from one location to another, information on the historical energy consumptions was collected from the households near the station. The population of the investigation are the houses located in this area, which adds up to a total of 3,903 households. Since it is a finite population, the necessary sample to obtain a representative consumption is calculated by means of the following equation [5]:

$$n = \frac{N * Z_\alpha^2 * p * q}{d^2 * (N-1) + Z_\alpha^2 * p * q} \tag{1}$$

With a level of confidence of 95% and a precision of 3%, the historical energy consumption of at least 839 households in the area are needed.

4 Results and Analysis

4.1 Market Study

Due to the fact that the residential sector of Puerto Cortés generally has analog electric meters, information on the historical energy consumption of the households located on the eastern peninsula in the municipality of Puerto Cortés was collected in order to construct a typical load profile for the area. The historical consumptions of 3,160 houses in the area were collected in a time period from September 2016 to April 2020.

Table 1 shows the categorization of electricity consumption in the eastern peninsula of the municipality. Since consumptions below 250 (kWh), between 250–499 (kWh) and between 500–749 (kWh) are the ones with the greatest presence in the area, scenarios for monthly consumptions of 250, 500, and 750 (kWh) will be analyzed.

Using load profiles from households located in the north part of Honduras, a typical load profile was built for the country's residential sector, which is adapted for the three selected consumptions of 250, 500, and 750 (kWh) per month.

Table 1 Categorization of energy consumptions in the eastern peninsula of Puerto Cortés

Energy consumption (kWh)	Number of houses	Percentage (%)
Less than 250	2,248	71.14
250–499	710	22.47
500–749	127	4.02
750–999	35	1.11
1000–1249	16	0.50
1250–1499	14	0.44
Greater than 1500	10	0.32
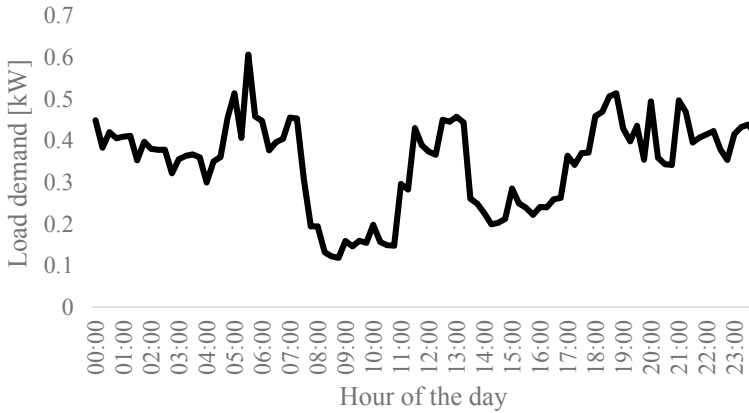
Fig. 1 Residential load profile for a monthly energy consumption of 250 kWh

In Fig. 1, the behavior of the residential load demand in the northern part of the country can be observed, which has consumption peaks at 5:30 a.m., 1:00 p.m., and 6:45 p.m. For a monthly consumption of 250 (kWh), the highest demand is 0.60 (kW). This data is entered in HOMER Grid and scenarios are simulated with consumptions of 8.33, 16.67, and 25 (kWh) per day, corresponding to a monthly consumption of 250, 500, and 750 (kWh) respectively.

4.2 Technical Analysis

The meteorological data comes from the Environmental Management Unit of Puerto Cortés. This information has one-hour intervals, with a total of 8760 data for each type of measurement, the measurements were registered between 2006 and 2014. The anemometer has an elevation of 7.0 (m).

Wind Speed. Wind speed is related to energy production because the higher the wind speed, more air mass passes through the wind turbine rotor and, therefore, more energy is generated.

In Fig. 2, the average hourly wind speeds at the height of the anemometer are shown. The hour with the highest average speed is at 8:00 p.m., with 2.80 (m/s), and the hour with the lowest average speed is at 11:00 a.m. with 1.37 (m/s). For the variation of speed with height, the logarithmic law is used, HOMER Grid offers a table of roughness coefficients depending on the type of terrain. For the research in question, a coefficient of 3.0 was used, since the area of the houses is in the center of a city.

Air Temperature. Air temperature is related to air density, as the temperature increases, the density decreases. Less air density means less air mass, so the turbine turns less and electrical energy production is reduced. According to the data obtained,
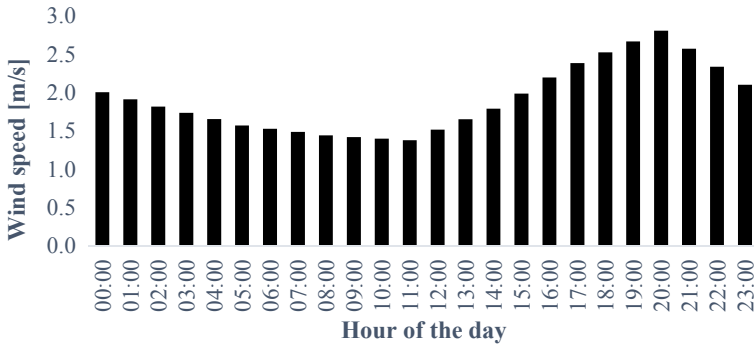
Fig. 2 Average wind speed by hour

the hour with the highest average temperature is at 5:00 p.m., with 28.23 (°C), and the hour with the lowest average temperature is at 8:00 a.m., with 23.64 (°C).

Wind Power System. To choose the wind turbine to be studied further, ten models of small wind turbines were evaluated between a power capacity of 1 (kW) and 5 (kW), both vertical and horizontal axis turbines. Turbines with low starting speeds were considered in order to get a better use out of the wind resource available.

Table 2 shows the main technical parameters of the turbines that were selected for the investigation. To calculate the energy generated from each turbine, a height of 12 (m) is considered. A height was chosen that is high enough so that the turbine is not obstructed by objects such as houses or trees and to be able to get a better use out of the wind resource, and at the same time being careful that it is not too high to avoid causing visual pollution.

Table 3 shows the results of the energy produced by the selected small wind turbines along with the calculated capacity factor. The average capacity factor for small-scale wind turbines is 17%, and this can vary within a range of 2–36%, depending on the project location [6]. The average capacity factor obtained for wind turbines in the eastern peninsula of the municipality of Puerto Cortés is 12.67%, the percentage is lower than the average mainly because the average wind speeds in the area are not very high.

A wind power system connected to the grid is composed of a wind turbine, a controller, an inverter, and a tower. Information on the total cost of these components was collected and the cost per installed power capacity of the models was calculated, which is shown in Table 4.

Figure 3 shows a comparison of the cost of the wind power system by installed capacity. It can be observed that as the installed power of the turbine decreases, the cost of the equipment tends to increase.

A decision matrix was made to choose the wind turbine model to use. For this research, a vertical axis wind turbine is preferred over a horizontal axis wind turbine because vertical axis wind turbines are more suitable for urban environments because there is more turbulence in urban areas and this type of wind turbine has the advantage

Table 2 Technical data of small wind turbines

Model	Manufacturer	Country	Axis	Blades	Power (kW)	Cut-in speed (m/s)	Cut-out speed (m/s)	Swept area (m²)	Lifespan (years)
E70PRO	Enair	Spain	HAWT	3	5	2	21	14.5	20
E30PRO	Enair	Spain	HAWT	3	3	2	20	11.34	20
HY5-AD5.6	Zhejiang Huaying	China	HAWT	3	5	3	25	24.6	20
Fortis Passaat	Fortis	Netherlands	HAWT	3	1.4	2.5	25	7.65	20
Fortis Montana	Fortis	Netherlands	HAWT	3	5	2.5	25	19.63	20
Aeolos-V 1 kW	Aeolos	Denmark	VAWT	3	1	2	15	3.2	20
Aeolos-V 3 kW	Aeolos	Denmark	VAWT	3	3	2.5	15	7.1	20
Aeolos-V 5 kW	Aeolos	Denmark	VAWT	3	5	2.5	15	22.26	20
Skyline SL-30	En-Eco	Italy	VAWT	3	3	2	16	11.2	20
UGE-4 k	Urban green energy	United Kingdom	VAWT	3	4	1.5	20	13.8	20

Table 3 Energy production of small wind turbines

Model	Power (kW)	Energy production (kWh year^{-1})	Capacity factor (%)
E70PRO	5	5,525	12.61
E30PRO	3	3,024	11.51
HY5-AD5.6	5	5,326	12.16
Fortis Passaat	1.4	1,048	8.55
Fortis Montana	5	3,743	8.55
Aeolos-V 1 kW	1	1,267	14.46
Aeolos-V 3 kW	3	4,484	17.06
Aeolos-V 5 kW	5	8,444	19.28
Skyline SL-30	3	3,074	11.70
UGE-4 k	4	3,782	10.79

Table 4 Cost per installed power capacity

Model	Power (kW)	Cost of components ($)	Cost of components per power installed ($ kW^{-1})
E70PRO	5	16,077.50	3215.50
E30PRO	3	13,110.00	4370.00
HY5-AD5.6	5	9925.00	1985.00
Fortis Passaat	1.4	6755.93	4825.67
Fortis Montana	5	18,166.95	3633.39
Aeolos-V 1 kW	1	6990.00	6990.00
Aeolos-V 3 kW	3	10,860.00	3620.00
Aeolos-V 5 kW	5	18,410.00	3682.00
Skyline SL-30	3	5428.00	1809.33
UGE-4 k	4	9864.80	2466.20

of generating electricity in any wind direction and they produce less vibrations, therefore they have a low noise emissions [7]. The cost of the equipment is a crucial factor since it represents the largest percentage of the investment, greatly affecting the cost effectiveness of the project. The capacity factor is also an important factor in determining whether the project is profitable or not. The lifespan is a factor to take into account because the longer it is, the longer the initial investment can be exploited. Finally, the quality of the wind turbine manufacturer is evaluated. Taking these factors into account, it was decided to use the 3 (kW) Skyline SL-30 wind turbine from the manufacturer En-eco for the development of the research.

Consumed Energy. In the simulations in HOMER Grid, the Skyline SL-30 turbine generated 3,074 (kWh year-1) in the urban area of Puerto Cortés. However, not all the energy produced by the system is used by the household. As mentioned
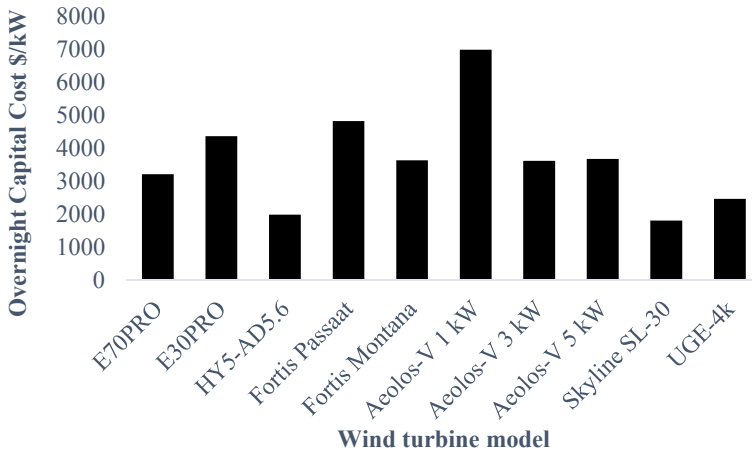
Fig. 3 Components cost comparison between turbines

Table 5 Energy used by households

Energy consumption per month (kWh)	Energy from by the wind system (%)	Energy from the grid (%)	Excess electricity (%)
250	74.0	26.0	15.9
500	46.4	53.6	3.77
750	32.4	67.6	1.56

previously, scenarios with monthly consumption of 250, 500, and 750 (kWh) were simulated.

Table 5 shows the percentage of energy consumed by the household that is supplied by the wind power system and by the national power grid according to monthly consumption. Likewise, the percentage of excess electricity production is shown, which is important to take into account to avoid an oversized system.

In Fig. 4, the production of the wind system can be seen during one day and how it manages to cover part of the load demands.

Required Ground Surface. The ground surface needed for the wind power system is a circular area with a radius of the tower height [8]. Given that the tower is set to be at 12 (m), the ground surface required by the system is 453 m^2.

4.3   Financial Analysis

A financial analysis with and without financing was carried out to determine the cost benefit (B/C) of the project. The cost benefit of the project was greater than "1" for both scenarios, however better results are obtained with financing. The benefits or
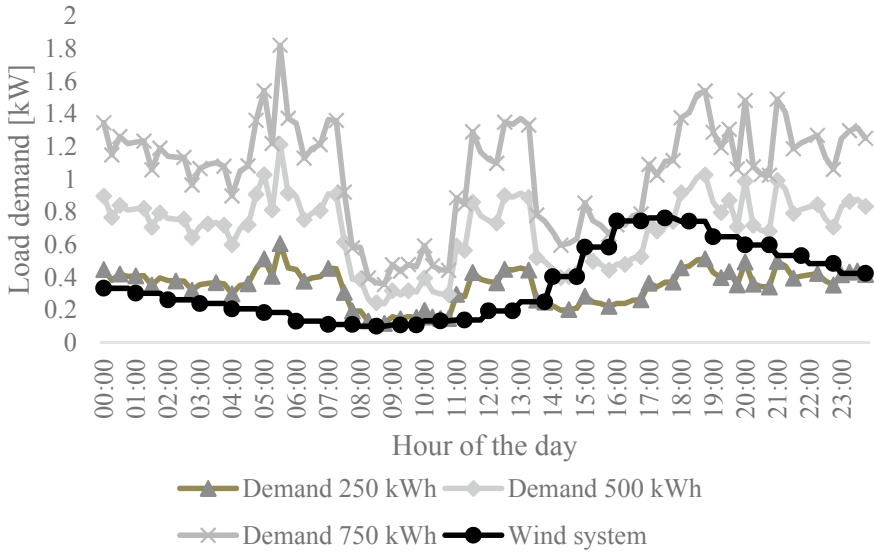
Fig. 4 Production of wind power system

income are the monetary inputs, in this case, they are the monetary savings from energy consumption that will be supplied by the wind system. To obtain the net income, expenses are deducted, which are the operation and maintenance costs and the payment of the loan. Net income over the useful life of the project is brought to the present to obtain the net present value of income (CVS). The cost of the project is the initial investment, this amount is brought to the present to obtain the net present value of costs (CVII).

The initial investment of the project includes the purchase of the equipment, the materials for the installation of the system, the labor, the transportation, the engineering expenses, and the connection to the grid. The manufacturer of the Skyline SL-30 turbine does not offer prices on the equipment, this was taken from Bortolini et al. (2014) as well as the percentage distribution of the initial investment of the project, except for transportation since it depends on the destination of the cargo [8]. The price of transportation by sea was quoted on the website of the company iContainers. The components of the system were set to be transported from the port of Genoa, Italy to the port of the municipality of Puerto Cortés.

Table 6 shows the initial investment of the project, which is a total amount of $7,145.00. For the financial analysis, the following parameters were taken into account. The percentage of excess production varies with the consumption of 250, 500, and 750 (kWh month^{-1}) as shown in Table 5.

Table 7 shows all the input parameters used to calculate the output parameters of the financial analysis of the project, such as the net present value (NPV), the internal rate of return (IRR), and the return on investment (ROI). This analysis was done using Microsoft Excel.

Table 6 Initial investment of the project

Category	Cost ($)
Wind system purchase	5428.00
Installation materials	428.53
Labor	142.84
Transportation	931.36
Engineering	71.42
Connection to the grid	142.84
Total	7145.00

Table 7 Input parameters

Installed capacity (kW)	3
Energy generated in the first year (kWh)	3074
Specific capital cost ($ kW-1)	2381.67
Dollar to lempira exchange rate	24.72
Energy rate in the first year (L kWh-1)	5.2164 [1]
Energy rate in the first year ($ kWh-1)	0.211
Annual increase in energy rate (%)	9.04%
Excess production (%)	15.9, 3.77, 1.56
Inflation (%)	1.50
O&M costs per year ($ kW-1)	108.56 [9]
Initial investment ($)	7145
Equity (%)	30
Equity ($)	2143.50
Equity interest rate (%)	7.97
Project debt (%)	70
Project debt ($)	5001.50
Loan interest rate (%)	19
Loan time (years)	5

Table 8 shows the results obtained from the analysis with financing. The LCOE of the project is higher than the rate of January 2020, which is 0.211 ($ kW^{-1}).

Table 9 shows the cost benefit of the project with financing, which is greater than 1 for the three scenarios. However, the cost benefit for a monthly consumption of 250 (kWh) is close to "1". In addition, the percentage of excess production for this consumption with the proposed wind power system is 15.9%, so it is considered that the profitability of the project is directed to monthly consumption greater than 500 (kWh).

Table 8 Output parameters with financing

Parameter	Outcome with 250 (kWh month^{-1})	Outcome with 500 (kWh month^{-1})	Outcome with 750 (kWh/month^{-1})
Payback (years)	13.33	12.12	11.93
NPV ($)	272.66	1,736.83	2,003.59
IRR (%)	8.38	10.50	10.87
ROI (%)	13	81	93
LCOE ($ kWh^{-1})	0.239	0.239	0.239

Table 9 Cost benefit of the project with financing

Parameter	Outcome with 250 (kWh month^{-1})	Outcome with 500 (kWh month^{-1})	Outcome with 750 (kWh/month^{-1})
CVS ($)	2416.16	3880.33	4147.09
CVII ($)	2143.50	2143.50	2143.50
B/C	1.13	1.81	1.93

5 Conclusions

The research hypothesis was proven by calculating the cost benefit of the implementation of a small-scale vertical axis wind turbine for residential use in the eastern peninsula of Puerto Cortés, Honduras. The B/C was greater than 1 for the considered monthly consumptions of 250, 500, and 750 (kWh), however, a consumption greater than 500 (kWh) is considered optimal due to the high percentage of excess production for lower energy consumptions. With a consumption of 500 (kWh month^{-1}) a B/C of 1.81 is obtained, indicating that the savings represent a benefit over the cost of the initial investment and the wind system with a 3 (kW) wind turbine is capable of covering 46.4% of the energy demand of the household. The LCOE of the project with financing is 0.239 ($ kWh^{-1}) and the required ground surface for the installation of the system must be at least 453 m^2. For households whose demand is mainly at night, it is convenient to implement this type generation technology since its highest production is during the evening.

References

1. CREE. Historial de tarifas (Internet) (2020). Available from: https://www.cree.gob.hn/historial-de-tarifas/
2. Pitteloud J-D, Gsänger S. Small Wind World Report (Internet) (2017). Available from: https://issuu.com/wwindea/docs/swwr2017-summary
3. Sistema híbrido solar-eólico en Caratasca, Honduras (Internet). Tecnosolar (2015). Available from: http://www.asolanosolar.com/sistemas_h%C3%ADbridos_solar

4. Award of Solicitation W912CL-14-R-0029, 50KW Hybrid Renewable System Caratasca Operation Center, Caratasca, Honduras (Internet). GovTribe (2014). Available from: https://govtribe.com/opportunity/federal-contract-opportunity/award-of-solicitation-w912cl-14-r-0029-50kw-hybrid-renewable-system-caratasca-operation-center-catarasca-honduras-w912cl14r0029#updates-table

5. Herrera Castellanos M (2011) Fórmula para cálculo de la muestra poblaciones finitas (Internet). Available from: https://investigacionpediahr.files.wordpress.com/2011/01/formula-para-cc3a1lculo-de-la-muestra-poblaciones-finitas-var-categorica.pdf

6. U.S. Department of Energy (2018) 2018 Distributed Wind Market Report (Internet). Available from: https://www.energy.gov/eere/wind/downloads/2018-distributed-wind-market-report

7. Talayero Navales A, Telmo Martínez E, Arribas de Paz L. Energía eólica (Internet). Prensas Universitarias de Zaragoza (2011). Available from: https://elibro.net/ereader/elibrodemo/44857

8. Bortolini M, Gamberi M, Graziani A, Manzini R (2014) Performance and viability analysis of small wind turbines in the European Union

9. Pantaleo A, Perellano A, Ruggiero F, Trovato M (2005) Feasibility study of off-shore wind farms: an application to Puglia region, 79

Nonlinear Dynamical Modeling and Vibration Responses of A T-Shaped Beam Structure

Shuai Chen, Dengqing Cao, Youxia Li, and Zhigang Chen

1 Introduction

A specific structure composed of multiple beams is usually used as component in large-scale flexible structures within the fields of mechanical, aeronautical and civil engineering. To acquire higher precision, reliability and stability, a nonlinear dynamical analysis of such systems is important for predicting and understanding their behavior under the effect of applied loadings.

For a multi-beam structure, due to the interaction between the components, the modal function of each beam is different from that of a single-beam structure. The dynamical model derived from the global mode functions has the advantages of lower degrees and high precision, which provides convenience for nonlinear dynamical analysis. Cao et al. established the dynamic model of the micro-electric static comb [1] and the composite flexible structure of the long-span cable-stayed bridge [2] by using the global modal method (GMM). Wei et al. used GMM to establish a spacecraft model with deployable solar panels [3] and a multi-beam structure with nonlinear hinges [4] and a nonlinear dynamic model of the L-shaped beam mass structure [5]. Then the rigid-flexible coupling motion of the spacecraft and the nonlinear effect of the flexure hinge are respectively performed. Cao et al. [6] investigated the dynamic modeling and vibration control of T-shaped beam structure.

S. Chen · D. Cao (✉)

School of Astronautics, Harbin Institute of Technology, Harbin, People's Republic of China

e-mail: dqcao@hit.edu.cn

Y. Li

China Academy of Space Technology, Beijing, People's Republic of China

Z. Chen

School of Mechanical and Electrical Engineering, Harbin Institute of Technology, Harbin, People's Republic of China

In this article, the nonlinear vibration partial differential equations of the T-shaped beam structure are established firstly. Using the method proposed in [1–6], the natural frequency and the corresponding global mode shape are worked out. Using the global mode shapes and their orthogonality relations, an explicit set of reduced-order nonlinear ordinary differential equations of motion is obtained. A typical example is given to verify the precision and effectiveness of the model by comparing the natural frequency and the global mode shape of the system obtained by the method in this paper with that obtained by the finite element method. The dynamic responses of the system with different numbers of degrees are studied. The importance of keeping nonlinear terms in matching and boundary conditions is evaluated.

2 Nonlinear Dynamic Model

As shown in Fig. 1, the T-shaped beam is fixed on a base excited by horizontal harmonics. The T-beam is composed of three lightweight inextensible beams, namely a horizontal beam and two vertical beams, considering the in-plane motion of the T-beam. The horizontal beam, the lower vertical beam and the upper vertical beam are named as Beam 1, 2 and 3, respectively. Coordinate system $o_1 x_1 y_1$ is a fixed inertial system with the origin at the left end of the Beam 1, while $o_2 x_2 y_2$ and $o_3 x_3 y_3$ are satellite inertial systems with the origins both at $(l_1, v_1(l_1, t))$. $l_i, \rho_i, E_i, I_i, A_i, u_i(x_i, t), v_i(x_i, t)$ denote the length, density, Young's modulus,
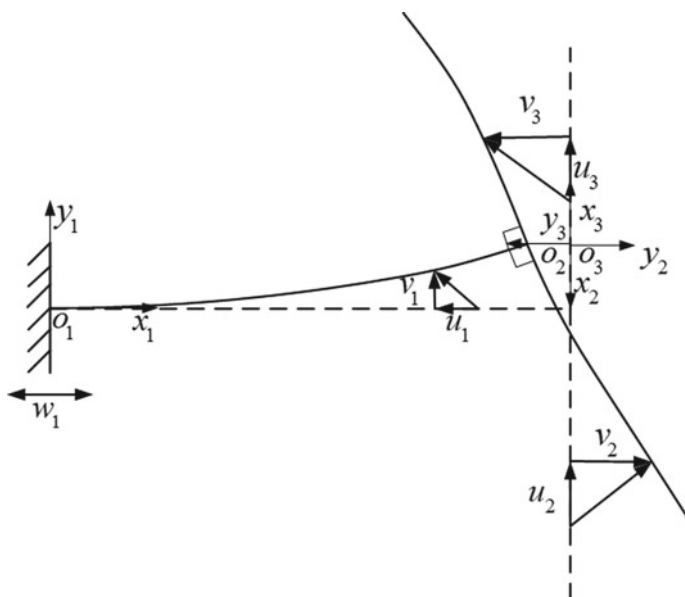
Fig. 1 Schematic of T-shaped beam structure

inertia moment, cross-sectional area, axial and lateral displacements of the i-th beam, respectively. The shear deformation and warpage of all beams can be ignored and the beams are inextensible.

The natural frequencies and the corresponding global mode functions can be obtained using the GMM developed in [6]. The transverse displacements v_i can be expressed in the following form

$$v_1 = \sum_{j=1}^{n} \varphi_{1j}(x_1)q_j(t), \; v_2 = \sum_{j=1}^{n} \varphi_{2j}(x_2)q_j(t), \; v_3 = \sum_{j=1}^{n} \varphi_{3j}(x_3)q_j(t), \quad (1)$$

where $\varphi_{1j}(x_1)$, $\varphi_{2j}(x_2)$ and $\varphi_{3j}(x_3)$ are the global mode shapes for the T-shaped beam structure, $q_j(t)$ is the generalized coordinate for the whole system.

With the nonlinear matching and boundary conditions, and orthogonality relations of the global mode functions, the ordinary differential equations of motion for the T-shaped beam structure can be obtained as

$$M_s \ddot{q}_s + K_s q_s + \sum_{j=1}^{n} \mu_s^j \dot{q}_j + \sum_{j=1}^{n} a_s^j \ddot{w}_s(t)q_j + \sum_{j,k=1}^{n} b_s^{jk} q_j \ddot{q}_k + \sum_{j,k=1}^{n} c_s^{jk} q_j q_k$$

$$+ \sum_{j,k=1}^{n} d_s^{jk} \dot{q}_j \dot{q}_k + \sum_{j,k,r=1}^{n} e_s^{jkr} q_j q_k q_r + \sum_{j,k,r=1}^{n} h_s^{jkr} \dot{q}_j \dot{q}_k q_r + \sum_{j,k,r=1}^{n} p_s^{jkr} q_j q_k \ddot{q}_r \quad (2)$$

$$= - \int_0^{l_2} \rho_2 \ddot{w}_s(t) \varphi_{2s}(x_2) dx_2 + \int_0^{l_3} \rho_3 \ddot{w}_s(t) \varphi_{3s}(x_3) dx_3, \; s = 1, 2, \cdots n.$$

where μ_s^j are damping coefficients, and $a_s^j, b_s^{jk}, c_s^{jk}, d_s^{jk}, e_s^{jk}, h_s^{jkr}, p_s^{jkr}$ are constants which can be determined by the global mode shapes. It is worth noting that the underlined terms in the parameter expression are from the nonlinear terms of matching and boundary conditions. The ordinary differential equations of motion under linear matching and boundary conditions can be obtained by ignoring the underlined terms. The ordinary differential Eq. (2) consist of geometrical and inertial nonlinear terms. The parameters in Eq. (2) are given as

$$\mu_s^j = c \sum_{i=1}^{3} \int_0^{l_i} \varphi_{ij}(x_i)\varphi_{is}(x_i) dx_i, \; a_s^j$$

$$= -\rho_1 \int_0^{l_1} \varphi_{1s}(x_1)\big[\varphi_{1j}'(x_1) + (x_1 - l_1)\varphi_{1j}''(x_1)\big] dx_1$$

$$b_s^{jk} = \rho_2 \varphi_{1k}(l_1) \int_0^{l_2} \varphi_{2s}(x_2)\big[\varphi_{2j}'(x_2) + (x_2 - l_2)\varphi_{2j}''(x_2)\big] dx_2$$

$$+ \rho_2\varphi_{1s}(l_1) \int_0^{l_2} \int_0^{x_2} \varphi'_{2k}(y)\varphi'_{2j}(y)\mathrm{d}y\mathrm{d}x_2$$

$$- \rho_3\varphi_{1k}(l_1) \int_0^{l_3} \varphi_{3s}(x_3)\big[\varphi'_{3j}(x_3) + (x_3 - l_3)\varphi''_{3j}(x_3)\big]\mathrm{d}x_3$$

$$- \rho_3\varphi_{1s}(l_1) \int_0^{l_3} \int_0^{x_3} \varphi'_{3k}(y)\varphi'_{3j}(y)\mathrm{d}y\mathrm{d}x_3$$

$$- \varphi_{2s}(0)\varphi_{1k}(l_1)\big[\rho_2 l_2\varphi'_{2j}(0) + \rho_3 l_3\varphi'_{3j}(0)\big]$$

$$c_s^{jk} = \big[E_2 I_2\varphi'''_{2j}(0) + E_3 I_3\varphi'''_{3j}(0)\big] \int_0^{l_1} \varphi_{1s}(x_1)\varphi''_{1k}(x_1)\mathrm{d}x_1$$

$$- \varphi_{1s}(l_1)\varphi'_{1k}(l_1)\big[E_2 I_2\varphi'''_{2j}(0) - E_3 I_3\varphi'''_{3j}(0)\big] - E_1 I_1\varphi_{2s}(0)\varphi'_{1j}(l_1)\varphi'''_{1k}(l_1)$$

$$d_s^{jk} = \rho_2\varphi_{1s}(l_1) \int_0^{l_2} \int_0^{x_2} \varphi'_{2k}(y)\varphi'_{2j}(y)\mathrm{d}y\mathrm{d}x_2 - \rho_3\varphi_{1s}(l_1) \int_0^{l_3} \int_0^{x_3} \varphi'_{3k}(y)\varphi'_{3j}(y)\mathrm{d}y\mathrm{d}x_3$$

and

$$e_s^{jkr} = \sum_{i=1}^{3} E_i I_i \int_0^{l_i} \varphi_{is}(x_i)\Big(\varphi'_{ir}(x_i)\big[\varphi'_{ij}(x_i)\varphi''_{ik}(x_i)\big]'\Big)' dx_i$$

$$- E_3 I_3\varphi_{2s}(0)\big[\varphi'_{3j}(0)\varphi''_{3k}(0)\varphi''_{3r}(0) + \varphi'_{3j}(0)\varphi'_{3k}(0)\varphi'''_{3r}(0)\big]$$

$$+ \big[E_1 I_1\varphi'_{1r}(l_1)\varphi'_{1j}(l_1)\varphi''_{1k}(l_1) - E_2 I_2\varphi'_{2r}(0)\varphi'_{2j}(0)\varphi''_{2k}(0)$$

$$- E_3 I_3\varphi'_{3r}(0)\varphi'_{3j}(0)\varphi''_{3k}(0)\big]\varphi'_{1s}(l_1)$$

$$- E_1 I_1\varphi_{1s}(l_1)\big[\varphi'_{1r}(l_1)\varphi''_{1j}(l_1)\varphi''_{1k}(l_1) + \varphi'_{1r}(l_1)\varphi'_{1j}(l_1)\varphi'''_{1k}(l_1)\big]$$

$$- E_2 I_2\varphi_{2s}(l_2)\big[\varphi'_{2r}(l_2)\varphi''_{2j}(l_2)\varphi''_{2k}(l_2) + \varphi'_{2r}(l_2)\varphi'_{2j}(l_2)\varphi'''_{2k}(l_2)\big]$$

$$- E_3 I_3\varphi_{3s}(l_3)\big[\varphi'_{3r}(l_3)\varphi''_{3j}(l_3)\varphi''_{3k}(l_3) + \varphi'_{3r}(l_3)\varphi'_{3j}(l_3)\varphi'''_{3k}(l_3)\big]$$

$$+ E_2 I_2\varphi_{2s}(0)\big[\varphi'_{2j}(0)\varphi''_{2k}(0)\varphi''_{2r}(0) + \varphi'_{2j}(0)\varphi'_{2k}(0)\varphi'''_{2r}(0)\big]$$

$$h_s^{jkr} = \sum_{i=1}^{3} \rho_i \int_0^{l_i} \varphi_{is}(x_i)\left(\varphi'_{ir}(x_i) \int_{l_i}^{x_i} \int_0^{\theta} \varphi'_{ij}(y)\varphi'_{ik}(y)\mathrm{d}y\mathrm{d}\theta\right)' dx_i$$

$$+ \varphi_{2s}(0)\left[-\rho_2\varphi'_{2r}(0)\int_0^{l_2}\int_0^{x_2}\varphi'_{2j}(x_2)\varphi'_{2k}(x_2)\mathrm{d}y\mathrm{d}x_2 \right.$$

$$\left. +\rho_3\varphi'_{3r}(0)\int_0^{l_3}\int_0^{x_3}\varphi'_{3j}(x_3)\varphi'_{3k}(x_3)\mathrm{d}y\mathrm{d}x_3 \right]$$

$$p_s^{jkr} = \left(-\rho_3 l_3\varphi'_{3j}(0) - \rho_2 l_2\varphi'_{2j}(0)\right)\varphi_{1r}(l_1)\int_0^{l_1}\varphi_{1s}(x_1)\varphi''_{1k}(x_1)\mathrm{d}x_1$$

$$+ \sum_{i=1}^{3}\rho_i\int_0^{l_i}\varphi_{is}(x_i)\left(\varphi'_{ik}(x_i)\int_{l_i}^{x_i}\int_0^{\theta}\varphi'_{ir}(y)\varphi'_{ij}(y)\mathrm{d}y\mathrm{d}\theta\right)'\mathrm{d}x_i$$

$$+ \varphi_{1s}(l_1)\varphi_{1r}(l_1)\varphi'_{1j}(l_1)\left[\rho_2 l_2\varphi'_{2k}(0) + \rho_3 l_3\varphi'_{3k}(0)\right]$$

$$- \rho_2\varphi_{2s}(0)\varphi'_{2j}(0)\int_0^{l_2}\int_0^{x_2}\varphi'_{2k}(x_2)\varphi'_{2r}(x_2)\mathrm{d}y\mathrm{d}x_2$$

$$+\rho_3\varphi_{2s}(0)\varphi'_{3j}(0)\int_0^{l_3}\int_0^{x_3}\varphi'_{3k}(x_3)\varphi'_{3r}(x_3)\mathrm{d}y\mathrm{d}x_3$$

3 Results and Discussion

3.1 Model Validation

A typical example of the T-shaped beam structure is given to illustrate the application procedure proposed here. Assume that the material for both beams is steel with density $\rho = 7850$ kg/m^3, Young's modulus $E = 200$ Gpa, damping ratio $c = 0.02$, Poisson's ratio $\upsilon = 0.31$. The cross sections of both beams are $b = 0.012$ m, $h = 0.002$ m. The lengths of all beams are $l_1 = 0.3$ m, $l_2 = 0.3$ m, $l_3 = 0.2$ m respectively. We use the above method to obtain the inherent characteristics of the T-shaped beam structure, including natural frequencies and global mode shapes. Table 1 shows the natural frequencies of the T-beam structure, taking the finite element calculation results from ANSYS as a reference. The maximum relative error between the natural frequency obtained by the current method and the finite element method is 0.1192%. The result shows that the method in this paper is effective and the frequency obtained by this method has higher accuracy, because there is no approximation and neglect in the mathematical derivation of this method.

Table 1 First 8 order frequency of T-shaped beam structure (Hz)

Order	GMM	FEM	Re (%)
1	5.10	5.10	0.0000
2	15.00	15.00	0.0000
3	31.76	31.76	0.0000
4	92.30	92.27	0.0325
5	117.44	117.40	0.0341
6	217.16	217.02	0.0645
7	294.02	293.67	0.1192
8	320.98	320.72	0.0811
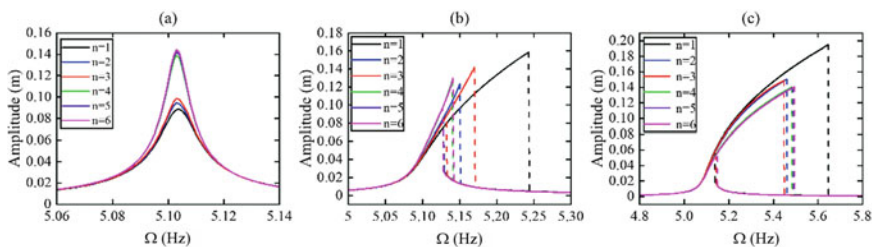
Fig. 2 Frequency responses of the system with different number of modes: **a** Linearized system, **b** Linear matching and boundary conditions, **c** Nonlinear matching and boundary conditions

3.2 Dynamic Responses

The fixed end of the T-shaped beam structure is assumed to be moving in a harmonic manner. The displacement of the moving support is assumed as $w_s(t) = w_0 \cos(2\pi\Omega t)$, where the amplitude w_0 is a constant and Ω is the frequency.

To determine the number of modes used for nonlinear vibration analysis, Fig. 2 shows the responses of the system taking different mode numbers under the sweeping frequency at the excitation amplitude $w_0 = 0.0008$ m, where the amplitude is the transverse displacement of the free end of Beam 2. Figures 2a–c represent the response of the linearized system, a nonlinear system with linear matching and boundary conditions and a nonlinear system with nonlinear matching and boundary conditions, respectively. It can be observed that in the linearized system, the resonance peaks of different modal numbers all appear at 5.1 Hz, that is equal to the first natural frequency, which illustrates that low-order frequencies play a leading role in vibration. Moreover, whether it is a linearized system, a nonlinear system under linear matching and boundary conditions or a nonlinear system with linear matching and boundary conditions, the change trend of the response value under different modal numbers is consistent. When the number of truncated modes are 4 or more, the response value has a big change, which may be due to the coupling effect between the fourth-order mode and the first-order mode. This means that the

first 4 modes should be selected for simulation in the following nonlinear vibration analysis calculations.

The force response curves of systems with linear matching and boundary conditions with different numbers of mode at the excitation frequency $\Omega = 5.12$ Hz are shown in Fig. 3a, and that of systems with linear matching and boundary conditions at the excitation frequency $\Omega = 5.2$ Hz are shown in Fig. 3b. Same jumping phenomenon can be observed. As the excitation amplitude increases, the difference in the dynamic response of the both systems with different numbers of modes becomes larger. When the vibration amplitude of the system is relatively large, more modes need to be adopted to meet the accuracy requirements. All these clearly show that the influence of higher-order modes on the dynamic response is closely related to the excitation amplitude.

The influence of different excitation amplitudes on the responses of the nonlinear system with two different conditions, including linear and nonlinear matching and boundary conditions, is shown in the Fig. 4. The curves in two pictures both show that
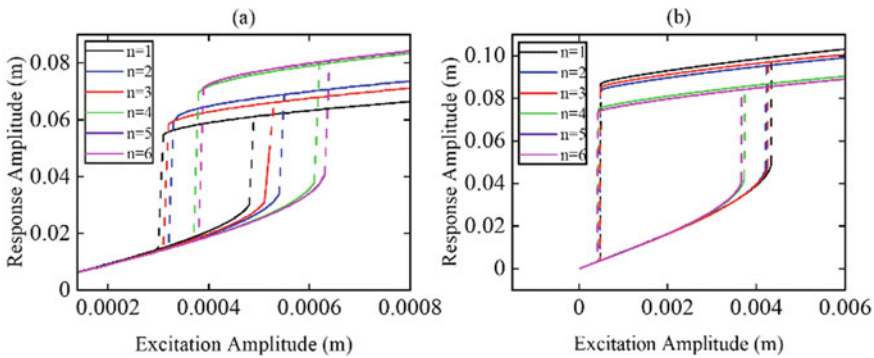
Fig. 3 Amplitude responses of different mode numbers
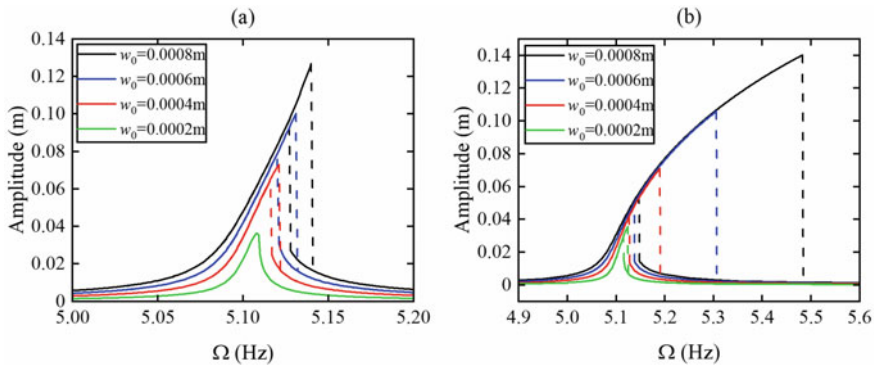
Fig. 4 Frequency responses at different excitation amplitudes: **a** Linear matching and boundary conditions, **b** Nonlinear matching and boundary conditions

the responses are positively correlated with the excitation amplitude in both systems. It can also be seen that there is a jump phenomenon in the nonlinear response.

The greater the excitation, the more obvious the jump, and the higher the corresponding jump frequency.

4 Conclusion

This article establishes the nonlinear ordinary differential motion equations describing the T-shaped beam structure and performs a series of dynamic analysis. Considering the geometric nonlinearity of the beam, and assuming that the beam is not extensible, the partial differential equations of the nonlinear motion of the T-shaped beam structure are obtained, along with their matching boundary and conditions. The validity of the proposed approach is verified by comparing the results obtained with those from FEM. The Galerkin method is used to obtain the nonlinear ordinary differential equations of motion with multi-degree-of-freedom. Based on this low-dimensional model, the following main conclusions are drawn through dynamic analysis: (1) Low-order modes dominate the dynamic analysis and the responses of the system under different mode numbers have a strong dependence on the excitation amplitude; (2) When developing the discretized governing equations of temporal modes, the nonlinear terms of the matching and boundary conditions are also worthy of our attention. Otherwise, the response of the system may change significantly.

References

1. Song M, Cao D, Zhu W (2011) Dynamic analysis of a micro-resonator driven by electrostatic combs. Commun Nonlinear Sci Numer Simul 16:3425–3442
2. Cao D, Song M, Zhu W, Tucker R, Wang C-T (2012) Modeling and analysis of the in-plane vibration of a complex cable-stayed bridge. J Sound Vib 331:5685–5714
3. Wei J, Cao D, Wang L, Huang H, Huang W (2017) Dynamic modeling and simulation for flexible spacecraft with flexible jointed solar panels. Int J Mech Sci 130:558–570
4. Wei J, Cao D, Huang H, Wang L, Huang W (2018) Dynamics of a multi-beam structure connected with nonlinear joints: modelling and simulation. Arch Appl Mech 1–16
5. Wei J, Cao D, Yang Y et al (2017) Nonlinear dynamical modeling and vibration responses of an l-shaped beam-mass structure. J Appl Nonlinear Dyn 1(1):91–104
6. Cao Y, Cao D, Huang W (2019) Dynamic modeling and vibration control for a T-shaped bending and torsion structure. Int J Mech Sci 157–158:773–786

Machinery and Control Technology

Topological Optimization of the Milling Head

Karel Raz [ID]**, Zdenek Chval** [ID]**, and Martin Stepanek**

1 Introduction

The milling technology is one of the most widely used technologies in all areas of the industry. It is essential for production of forming tools in the automotive industry and therefore is necessary to ensure maximal productivity of milling.

The aim of the performed optimization process was to improve the useful properties (increase the stiffness while maintaining the weight) of a milling head with an internal supply of coolant to the cutting point. The coolant is delivered through the beam structure. The usage of the topological optimization is a suitable tool for this task. It allows changes in the structure with respect to the specified constraints. The aim is to create a modification of the current structure with beams, which is suitable for production using the additive technology (metal 3D printer EOS M290 with DMLS technology). This progressive design of the milling head is used more often in the industry because of the optimal cooling effect [1].

2 Description of the Simulation Model

The existing design of the head is shown in the following figure. It is used as the main input for the determination of the computational model. It is a milling head with six individual cutters. Internal channels in individual beams are used for the coolant supply.

This head is manufactured from steel using the additive technology and the design is therefore considering this producing process [2] (Fig. 1).

K. Raz (✉) · Z. Chval · M. Stepanek
Regional Technological Institute, University of West Bohemia, Pilsen, Czech Republic
e-mail: kraz@rti.zcu.cz

Fig. 1 Initial design of the
milling head [2]
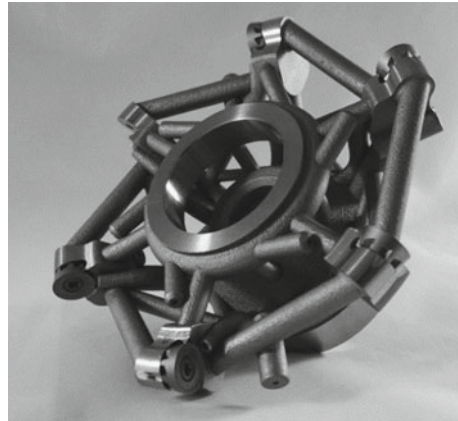
3 Loading During the Manufacturing Process

The load cases are shown in Fig. 2. These forces were applied to the input geometry, which is described further. The boundary condition of the rotational symmetry was used in the simulation model and the force was applied only to one insert [3].

The axial force caused by the screw securing the cutter to the carrier is not considered.

It is necessary to define the area of the optimization. This is shown in Fig. 3. It is a solid geometry, based on the original design, considering the internal channels. The weight of the solid input geometry ("Design Area") is 3.98 kg. The material will be removed to the target value approximately 1 kg. The rotation during operation is 300 revolutions per minute. The diameter of the milling head is 120 mm.

The cooling channels are actually loaded by the internal pressure of the coolant during the milling process. This load is negligible compared to other forces. The boundary condition of a minimum material thickness of 1 mm was applied to all surfaces of the coolant channels in order to ensure the integrity and functionality. The fixing on the surface, which is in the contact with the carrier, did the attachment of the milling [4].

F_x	600 N
F_y	810 N
F_z	650 N
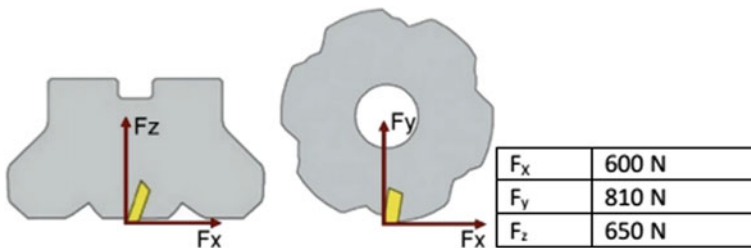
Fig. 2 Components of the loading force
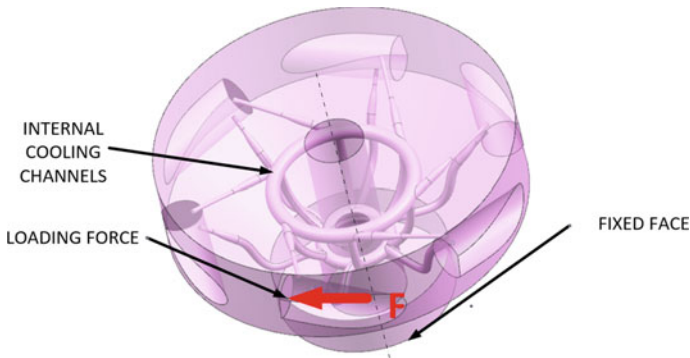
Fig. 3 Design area as input of topological optimization

The cutting force is applied to one bed of the insert using three force components as described in the table earlier. Mechanical properties of MS1 steel according to the EOS data sheet were considered. The Frustum tool (which is part of the Siemens NX CAx package in version NX 12.0.2.9) was used for the optimization [2].

4 Topological Optimization of the Structure

Results of the optimization are two selected structures, which differ by different settings of the parameter "spreading" (0–100%). This parameter controls the degree of fineness of the resulting structure. It is necessary to perform a reverse remodeling in order to analyze the stiffness. Comparing with the initial values follows. With regard to the input requirement, which is the maximum respect of the original design of cooling channels, the result is a similar bar structure as in the original solution [5, 6].

4.1 Coarse Structure

To obtain a coarse structure, the "spreading" value was set to 30%, which means that the resulting structure should be composed of larger solid elements (Fig. 4).

4.2 Fine Structure

To obtain a fine structure, the "spreading" value was set to 100%, which means that the resulting structure should be composed of beam elements (Fig. 5).
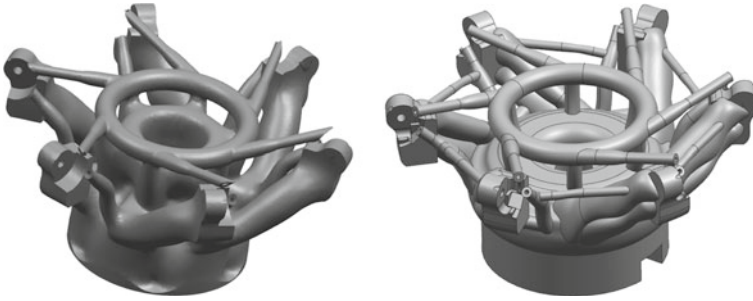
Fig. 4 Results of optimization (left), re-modeling (right)
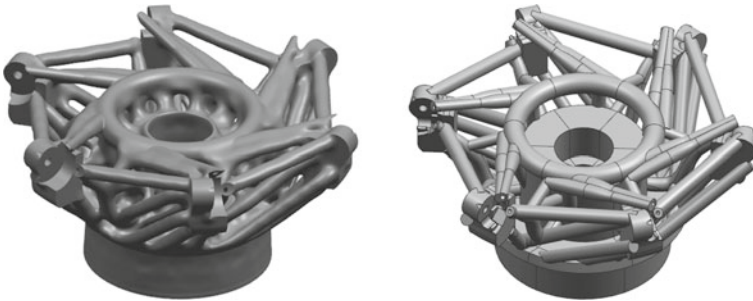
Fig. 5 Results of optimization (left), re-modeling (right)

5 Strength Evaluation

Comparative strength calculations are based on the same specification of boundary conditions as for topological optimization. A cutting force is applied to one insert and the cutter is attached by fixing the front surface at the carrier.

Comparative static calculations were performed in the FEM solver NX Nastran SOL 101-Linear Statics-Global Constraint. In order to maintain the maximum comparability of individual solutions, a uniform size and type of the tetrahedron element CTETRA10 (with a mid-node in its linear variant) was used. The global element size is 2.5 mm. The total number of elements for one task is between 150,000 and 180,000 [7].

5.1 Results of the Initial Design

This calculation was performed as a comparison for the optimized head geometries. The maximum stress is in the area of the bars. Weight of this design is 0.968 kg.
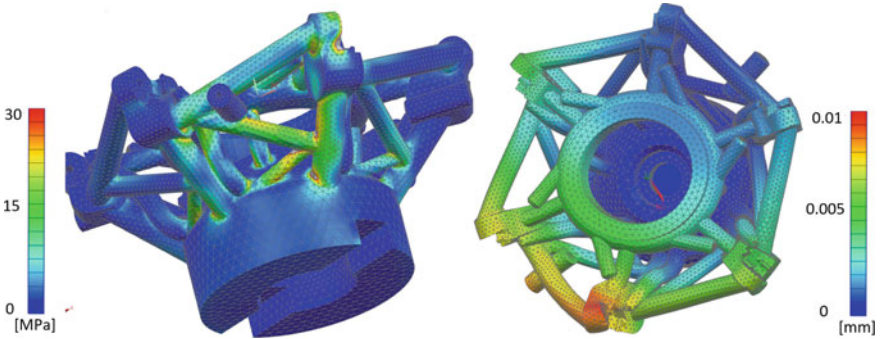
Fig. 6 Stress (left) and displacement (right) of the initial design

- Maximum displacement: 0.01 mm.
- Von-Mises stress: average value 2.7 MPa; maximum value: 97.3 MPa (Fig. 6).

5.2   Results of the Coarse Design

This geometry reached half the deformation with a weight increase of 32 g (i.e. + 3.3%) and the maximum stress value decreased by 17%. Weight of this design is 1.0 kg.

- Maximum displacement: 0.005 mm.
- Von-Mises stress: average value: 1.5 MPa; maximum value: 80.7 MPa (Fig. 7).
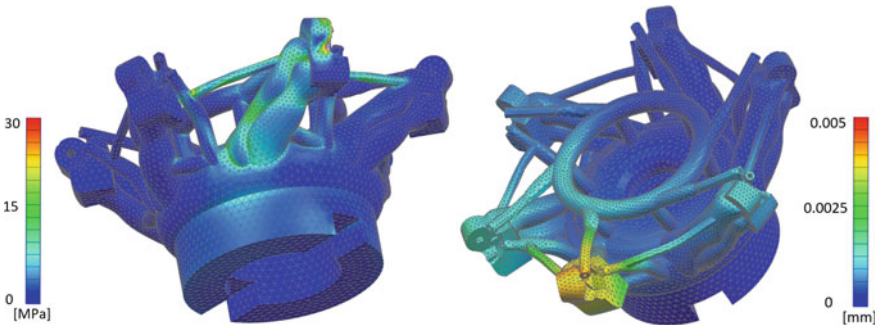
Fig. 7 Stress (left) and displacement (right) of the coarse optimized design
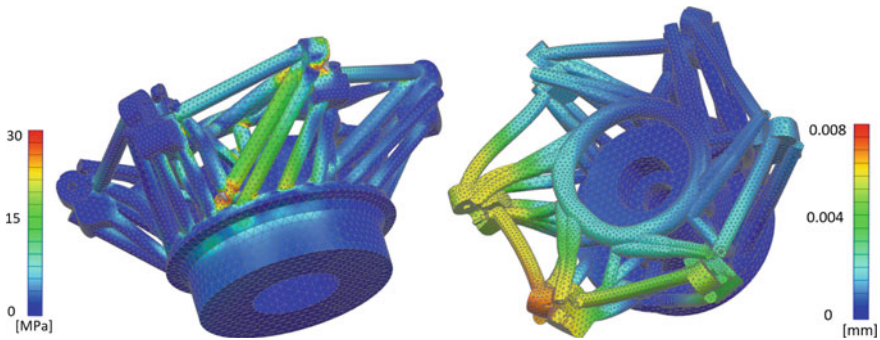
Fig. 8 Stress (left) and displacement (right) of the fine optimized design

5.3   Results of the Fine Design

The result of topological optimization in the form of a fine structure is 7.7% lighter and 20% stiffer. The stress value has changed negligibly. Weight of this design is 0.893 kg.

- Maximum displacement: 0.008 mm.
- Von-Mises stress: average value: 2.7 MPa; maximum value: 98.4 MPa (Fig. 8).

6   Conclusion

The current solution of the head can be modified and properties can be improved based on the results of topological optimization. It is possible to use two different approaches: reducing the weight while maintaining the stiffness or, increase the stiffness while maintaining the weight of the head. The report presents two selected optimization results from a total number of six different input parameter settings (only two most interesting are shown) that were made during the research. Their difference is in the value of the spreading parameter, which affects the degree of fineness of the overall structure. The subsequent production with additive technologies must be taken into account. The optimization results are presented in the form of values in Fig. 9.

It is obvious that with a minimal increase in weight is possible to increase the head stiffness by up to 50%. This research will continue with the testing of the optimized prototype of the milling head and the dynamic and thermal evaluation of the design.

	INITIAL DESIGN	OPTIMIZED COARSE STRUCTURE		OPTIMIZED FINE STRUCTURE	
	VALUE	VALUE	CHANGE [%]	VALUE	CHANGE [%]
WEIGHT [kg]	0.968	1.000	3.3	0.893	-7.7
MAXIMAL DISPLACEMENT [mm]	0.010	0.005	-50.0	0.008	-20.0
MAXIMAL STRESS [MPa]	97.300	80.700	-17.1	98.400	1.1
AVERAGE STRESS [MPa]	2.700	1.500	-44.4	2.700	0.0

Fig. 9 Results

References

1. Gibson I, Rosen D, Stucker B (2015) Additive manufacturing technologies: 3D printing, rapid prototyping, and direct digital manufacturing, 2nd edn. Springer, New York
2. Zetek M, Zetkova I (2018) New generation of the cutting tools when the AM technology is used, internet. J Adv Technol. ISSN: 0976-4860
3. Bellehumeur C, Li L, Sun Q, Gu P (2004) Modeling of bond formation between polymer filaments in the fused deposition modeling process. J Manuf Process 170–178. https://doi.org/10.1016/S1526-6125(04)70071-7
4. Ahn S-H, Montero M, Odell D, Roundy S, Wright PK (2002) Anisotropic material properties of fused deposition modeling ABS. Rapid Prototyping J 248–257. https://doi.org/10.1108/13552540210441166
5. Mulholland T, Goris S, Boxleitner J, Osswald T, Rudolph N (2018) Process-induced fiber orientation in fused filament fabrication. J Compos Sci 45. https://doi.org/10.3390/jcs2030045
6. Rodríguez JF, Thomas JP, Renaud JE (2003) Design of fused-deposition ABS components for stiffness and strength. ASME J Mech Des 125(3):545–551. https://doi.org/10.1115/1.1582499
7. Frazier WE (2014) Metal additive manufacturing: a review. J Mater Eng Perform 23:1917–1928. https://doi.org/10.1007/s11665-014-0958-z

Comparison Study of Single Valve and Sequential Valve Mode on the Effect of Steam Turbine Heat Rate

Atang Salam, Fajar Purnomo, and Wahyu Caesarendra

1 Introduction

The power business is becoming increasingly competitive and the need to reduce and manage operating costs has become considerably more important. Improvements in thermal performance can help power plant operators gain a competitive advantage by lowering operation costs and increasing plant output [1].

Optimal thermal performance levels for turbine generator units and their feed water cycles can be well achieved and maintained with ongoing programs to evaluate and assess performance. Performance monitoring activities have three objectives: (a) Thermal performance determination detection with change trends across various performance parameters; (b) Identify with the evaluation and interpretation of the exact data causing the decrease in performance; (c) Develop cost-effective solutions to fix operational and equipment problems that contribute to decreased thermal performance [1].

Electric power system raises two basic requirements on steam turbines used for power generation of electricity: one is guaranteed to meet the electricity needs of users at any time; the other is to enable the rotor to maintain in a certain speed, to ensure the stability of frequency of power grids and the safety of the steam turbine itself [2].

A. Salam (✉) · F. Purnomo
Efficiency and Performance Engineering Department, PT. Indonesia Power, Jakarta, Indonesia

F. Purnomo
e-mail: fajar.purnomo@indonesiapower.co.id

W. Caesarendra
Faculty of Integrated Technologies, Universiti Brunei Darussalam, Jalan Tungku Link, Gadong BE1410, Brunei Darussalam
e-mail: wahyu.caesarendra@ubd.edu.bn

179

The valve management program dynamically calculates data which represents control valve demand or flow as a function of the valve lift of a control valve while compensating for the pressure variation and the corrected first stage flow of coefficient [3]. For variable load of constant pressure operation unit, the rotor speed and power regulation are achieved by changing the flow of steam. Steam volume changes can be adjusted by changing the number of opened valves and controlling the inlet area of the valves [4].

It has been known for some time that the efficiency of a steam turbine power plant is degraded by the throttling losses that occur during the time when the steam spread into valves of the steam turbine are governing steam flow in the partially opened state. It is understood that any improvement in efficiency of plant performance by reduction of these throttling losses will substantially reduce fuel consumption and provide significant economic savings on the energy production process [5].

In the previous paper, several differences in the mechanism of single and sequential valve were explained and also the impact of throttling pressure main steam losses. In this research, try to see the difference between the use of the single valve method and the sequential valve method on its impact on the Turbine Heat Rate so that the plant operator can choose the right action to operate of the power plant to get a high turbine efficiency value.

2 Theoretical Background and Methods

The performance of a turbine can be identified from the value of the turbine heat rate, which is translated as the number of kilo calories of energy consumed per kWh of electrical energy when it is generated. To calculate the turbine heat rate, several ways can be used including understanding the theory of heat balance or in other words, lots of energy comes out and enters the turbine and then compares it with the energy produced by the generator [6]. Calculation of turbine cycle heat rate is formulated as:

$$TCHR = \frac{Heat_{in} - Heat_{out}}{Generator_{out}} \tag{1}$$

where TCHR (Turbine Cycle Heat Rate) is turbine heat rate (kcal/kwh); $Heat_{in}$ is heat energy that enters the turbine (kcal); $Heat_{out}$ is heat energy coming out of the turbine (kcal); and $Generator_{out}$ is electrical energy produced by a generator (kWh).

According to Eq. (1), if described by involving the components of flow steam, feed water and spray water parameters based on the heat balance, the turbine heat rate can be calculated with the following formula as:

$$THR = \frac{(M_1 \times H_1) - (M_1 + M_{mu}) \times H_f + M_2 \times (H_3 - H_2) + M_{is} \times (H_f - H_{is}) + M_{ir} \times (H_3 - H_{ir})}{P_{gg}} \tag{2}$$

where THR is turbine heat rate (kcal/kwh); M_1 is main steam flow to HP Turbine (ton/h); H_1 is enthalpy specific of main steam to HP Turbine (kJ/kg); M_{mu} is total make up water flow (ton/h); M_f is enthalpy specific of final feed water to economizer (kJ/kg); M_2 is cold reheat steam flow (ton/h); H_2 is enthalpy specific of cold reheat (kJ/kg); H_3 is enthalpy specific of hot reheat (kJ/kg); M_{is} is spray water flow to super heater (ton/h); H_{is} is enthalpy specific of spray water flow to super heater (kJ/kg); M_{ir} is spray water flow to reheater (ton/h); P_{gg} is power generator (kWh) [6].

Based on Eq. (2), it will be known how much turbine heat rate influence by the flow and enthalpy parameters of each steam to produce power.

There are two main types of regulation: (a) The qualitative regulation or throttle governing, which consists in the control of the pressure of the steam in the entrance of the turbine; (b) The quantitative regulation or nozzles governing, where the control is over the number of nozzles or stages of the turbine that receive the steam [7].

In an ideal situation with this regulation, the steam instead of enter in all the nozzles of the crown of the turbine the steam would enter only in some nozzles in all the stages. But this is not reasonable so usually it is done only in some stages. The regulation can be done controlling the power in the first stage doing a segmentation of the disc of nozzles like in the next Fig. 1.

The segmentation can be done dividing the distributing conduct in circular sectors and feeding each sector with closing and opening valves, as in the Fig. 2.

Generally single valve mode should be used during rolling to speed, synchronization, and minimum load hold period. This mode provides steam through all the control valves and nozzle space, resulting in steam flowing in a full arc of 360° into the control level bar. Thus, these parts heat up and expand more uniformly. Single valve mode should be used during the initial break-in period of operation, if possible. During this period, it is not uncommon for pressure and abnormal temperature excursions until all station controls are properly regulated and all systems are functioning properly. To ensure maximum reliability of turbine-generator units, it is usually desirable to minimize the effect of such abnormal conditions on the turbines.
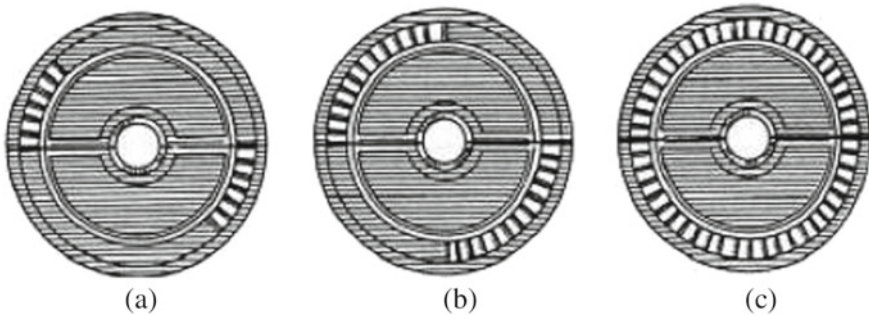
Fig. 1 Diagrams of steam turbines with different degree of admission: **a**, **b** partial admission; **c** total admission [8]
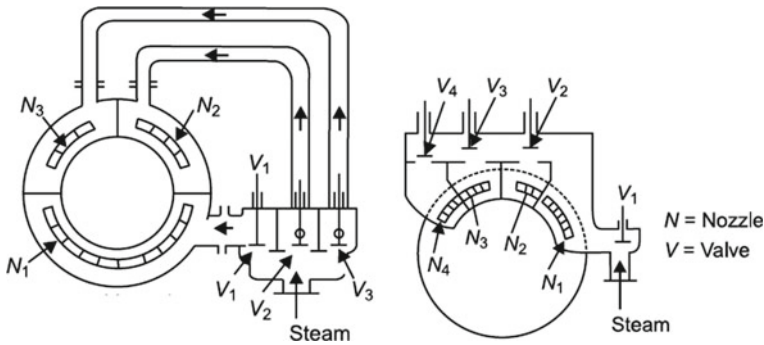
Fig. 2 Schematic of nozzle governing [9]

Operating the turbine in full arc entry mode makes the control stage a more moderate charge on a partial load than operating in partial arc entry mode. It also makes this spoon at a higher temperature, which is beneficial in terms of achieving uniformity in the distribution of mechanical loads on the turbine blades with time.

Under stable load operation, the system is switched to sequence valve control mode to reduce throttling loss caused by the influx of full arc steam and improve thermal efficiency. This sequential arrangement minimizes throttling losses (losses that occur when the valve is partially opened), and thus provides the best operating efficiency at partial loads. Depending on the mode of operation, valve management can help optimize unit efficiency and extend unit life by reducing rotor pressure through minimizing temperature differences. There may be times when sequential valve control, depending on existing throttle steam conditions, will provide better fit between the first stage steam temperature and the metal temperature and allow faster ignition [10]. Losses on the turbine consist of mechanical losses due to the friction of rotating parts or bearings, tip clearance losses due to the flow leakage through tip gap, secondary flow losses due to curved passages, and profile losses due to the blade shape, etc. [11].

3 Experimental Setup

To see the difference between the characteristics of the turbine when it is operated in single and sequential mode, it takes some testing and capturing data on Table 1 from historical Distributed Control System (DCS), then looking for the relationship and its impact on these single and sequential modes. It is necessary to collect data on flow characteristics in single valve operation mode and sequential valve operation mode, and set Digital Electro Hydraulics (DEH) load setting data recording point, Digital Electro Hydroulics (DEH) system load reference unit power, stage pressure

Table 1 Historical data DCS on single valve mode

Load (MW)	GVL1 (%)	GVR1 (%)	GVL2 (%)	GVR2 (%)
330.49	19.31	19.66	20.77	21.58
329.99	19.15	19.50	20.63	21.43
328.05	19.36	19.76	20.82	21.67
330.35	19.33	19.80	20.78	21.71
328.48	19.14	20.12	20.61	22.02
333.25	18.76	19.44	20.25	21.37
327.46	19.07	19.72	20.55	21.63
331.43	19.32	19.98	20.77	21.89
329.20	19.34	20.05	20.79	21.95
329.02	18.49	19.04	19.97	20.95
328.06	19.51	20.06	20.97	21.95
329.53	19.50	20.01	20.95	21.91
329.98	19.31	19.82	20.77	21.74
330.74	19.24	19.75	20.70	21.67
331.33	19.19	19.71	20.65	21.62
331.21	19.08	19.60	20.55	21.51
330.61	19.08	19.60	20.55	21.51
329.45	19.07	19.61	20.55	21.52
326.71	18.29	18.79	19.80	20.74

setting, main steam pressure, main steam temperature, heating temperature, GV1-GV4 opening instructions. In order to obtain valid analysis results, data filtering is carried out with the following conditions at Fig. 3.

4   Result and Discussion

According to the DCS data capture results it appears that when load demand at 300 MW load range is operated in single mode on Table 1, all valve governors respond equally according to the need for flow steam to maintain load and linear rise when load demand is high. Single valve control means that all the control valves accept a valve control signal to make the valves turn up or down at the same time, which is characterized by the throttle adjusting and full arc spread steam.

The function of valve control management is to transfer the required flow steam at every percentage of valve openings. In the operation using two different modes at the same load range there are several differences in action from the turbine valve. Based on the trending results of single valve mode, it appears that all valves receive the same control signal at a time for each load up or down change condition which

Data analysis was carried out in 2 conditions i .e. single and sequential mode

Data analysis was conducted when the load was in the range 300 MW to 500 MW with 2 minute interval

The data is analyzed when there is no soot blowing process

Discarding data that is theoretically incompatible (abnormal) with high deviation normalizations

Analysis of data with the variability method using data at different load time
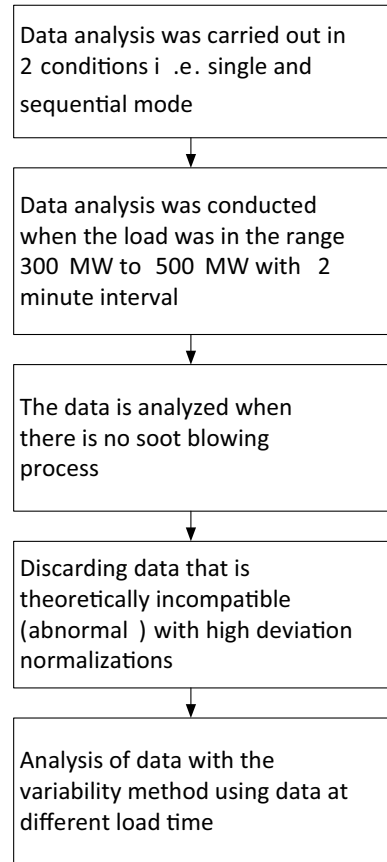
indicates the characteristic behavior of adjusting throttling for the full nozzle. The spread of heat energy on the turbine rotor in such a way will be uniform, shown with metal temperature on some parts of the turbine showing stable performance or not experiencing significant spikes.

According to Fig. 4a, when the unit operates in single mode it is evident from trending results that GVL1-2 and GVR1-2 gets a uniform open command on each valve adjusting the load change and availability of the main steam supply flow. Except valve opening fluctuations in load range 110–180 MW occurred due to changes in the calorie value of coal.

According to Table 2, when using the valve sequential mode in turbine operation in Fig. 4b, the control valve gets different up or down commands for each GV valve when the load request changes, which indicates the characteristics of adjusting nozzle in partial arc admission. However, it is different when the operation mode is changed to sequential mode when the load of 100 MW GL1-2 and GVR2 simultaneously gets the maximum full opening order (cut of command in 90%), when there is a load
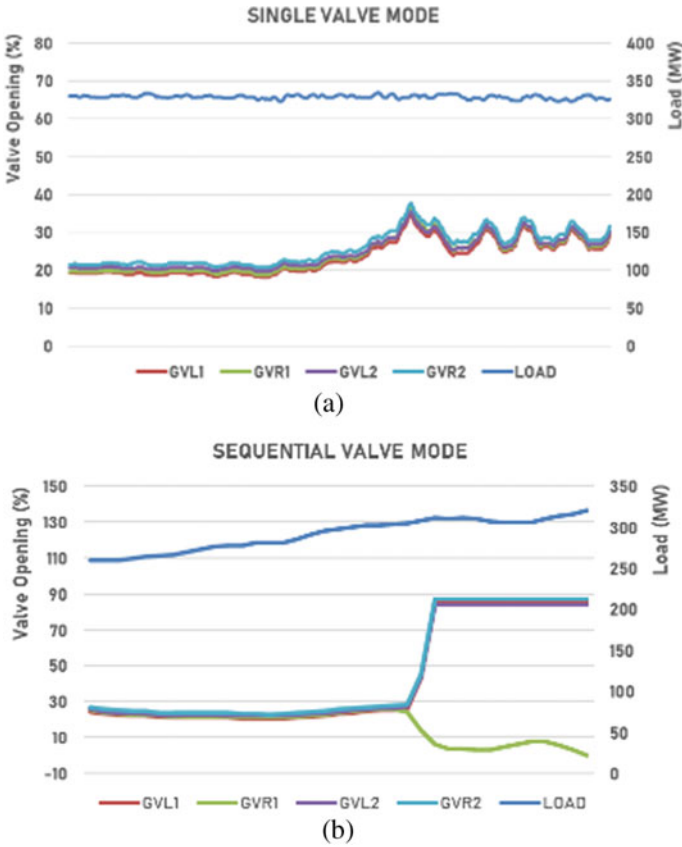
Fig. 4 Trend characteristic valve turbine **a** single mode, **b** sequential mode

increase or decrease depends on main steam flow followed by GVR1 throttling to adjust the load change.

In the characteristic curve of the turbine valve which is specific is a function of the relationship of lifting the degree of valve opening to the main steam flow required with a certain load setting. In curve characteristic steam will notice a significant difference between the operation in single mode and sequential mode as presented in Fig. 5.

When switching control valve mode regulation from single to sequential mode of Digital Electro Hydroulics System (DEHS) load reference is at 305 MW. It was noticeable that when the load increased at a stable main steam temperature at 497 °C, the need for main steam flow became reduced due to the time that 3 GV valves were ordered open to full (cut of 90%) which reduces the amount of losses. This is because when full arc admission single valve with uniformity of opening valve order for all GV indeed at the beginning of low load will make the temperature heat transfer condition uniform on each part of the turbine, only when the temperature has

Table 2 Historical data DCS on sequential valve mode

Load (MW)	GVL1 (%)	GVR1 (%)	GVL2 (%)	GVR2 (%)	Main steam flow (t/h)	Main steam press (mpa)	Main steam temp (°C)
259.72	24.47	25.19	25.71	26.93	1137.55	8.00	478.01
277.41	21.02	21.73	22.41	23.58	1181.96	8.92	487.35
302.11	24.63	25.21	25.86	26.95	1243.50	9.17	496.28
311.58	85.77	6.28	84.31	87.23	1249.85	9.38	497.74
305.76	85.78	4.80	84.30	87.23	1224.19	9.23	497.17
305.52	85.78	6.42	84.30	87.27	1227.12	9.20	497.10
306.05	85.78	7.82	84.30	87.26	1233.06	9.20	497.12
310.18	85.78	7.76	84.30	87.26	1250.46	9.34	498.35
313.75	85.78	5.84	84.30	87.29	1252.26	9.47	501.15
316.18	85.78	2.95	84.30	87.29	1252.37	9.58	502.96
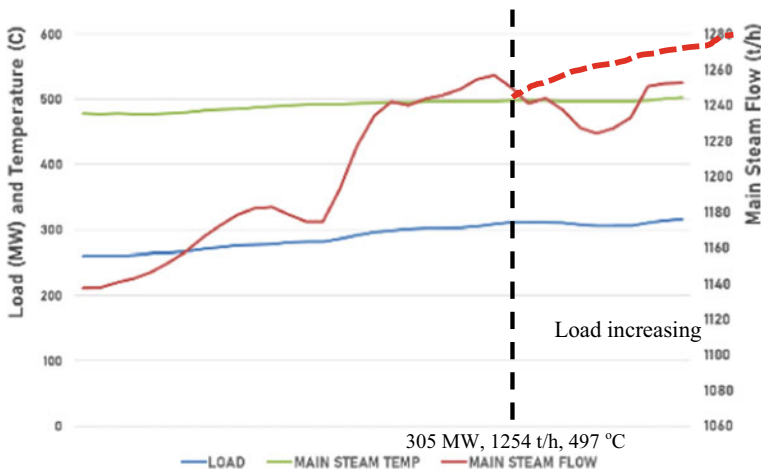
Fig. 5 Characteristic sequential valve mode in needs of flow main steam

reached a stable point then downstream pressure will be fixed in particular load. As it is known that the throttling process depends on the difference between pressures and control valves and downstream pressure. Thus when the temperature is stable then the greater the pressure difference that passes through the control valve will cause even greater energy losses due to throttling process.

With data from DCS capture historians on Table 3, in a certain time range at a load of 300–500 MW for two conditions of valve mode control and its relation to the efficiency value of the turbine.

Table 3 Turbine heat rate on single and sequential valve mode

Single mode		Sequential mode	
TCHR (kcal/kwh)	Load (MW)	TCHR (kcal/kwh)	Load (MW)
2625.59	259.72	2595.86	286.11
2540.79	305.76	2412.55	355.66
2448.46	385.62	2382.84	408.68
2364.59	402.60	2326.26	402.92
2344.64	401.07	2290.16	401.78
2362.49	398.04	2351.73	396.09
2278.97	493.82	2350.60	402.93
2254.37	496.45	2346.52	398.63
2277.74	495.40	2388.15	393.44
2283.61	500.62	2344.04	399.34
2279.04	500.15	2256.60	404.33
2284.24	496.78	2311.58	444.56
2295.10	470.95	2272.70	475.39

From the chart on Fig. 6 it is seen that the higher load then the lower the spread of data from TCHR with a stability point in the load range of 300–500 MW both in single valve mode and sequential valve mode. In terms of variability analysis by comparing the average value of 10% lowest TCHR value can be seen on Table 4.

The result average TCHR for single valve mode is at 2270.36 kcal/kwh and 2258. 45 kcal/kwh for sequential valve mode. In other words, from the chart Fig. 6 and Table 4 that in the load range of 300–500 MW, sequential mode has a better TCHR value (lower) of 11.9 kcal/kwh than single valve mode. It is more efficient to use sequential mode when the load is high caused by reduced throttling loss main steam pressure.

5 Conclussions

Efforts to reduce energy losses from the steam power plant through the valve management regulator can be seen from the throttling valve governor pattern. On the single valve mode the cylinder rotor heat expansion is uniform and the metal temperature of different steam turbine parts is in a stable condition, making the unit withstand greater load change rate. But because all of the adjustment valves are not in the fully opened state, the valves have a great throttle loss, reducing the turbine efficiency of the unit. It can be seen that when conditions are stable at high loads where uniformity of the turbine blade temperature has occurred the difference in the valve mode operation pattern can be seen significantly from the difference in throttling losses that the lowest formulation output on sequential valve mode has a more efficiency around

(a)

(b)
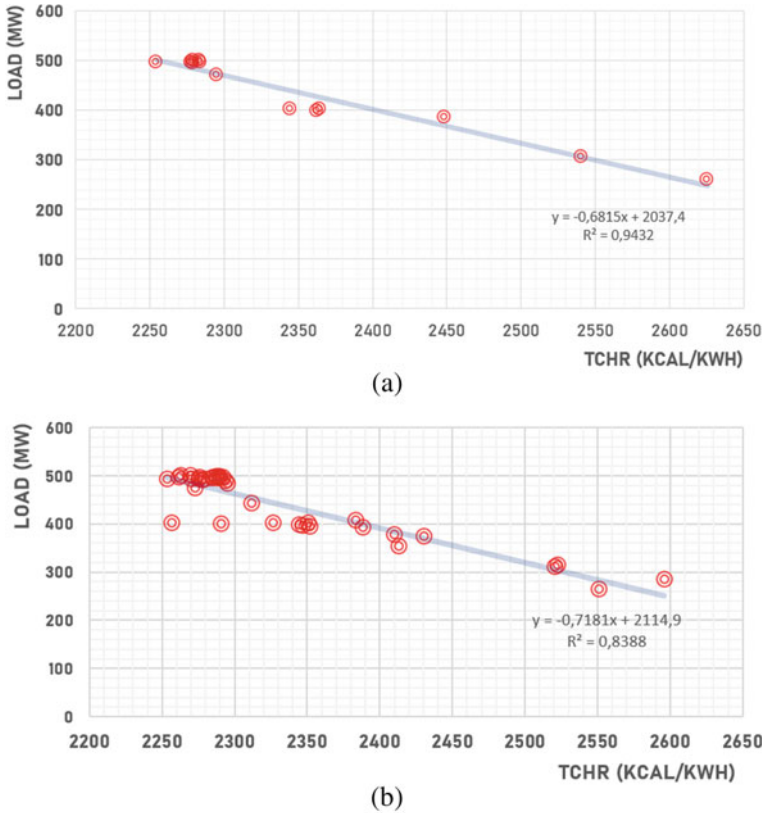
Fig. 6 TCHR variability **a** single mode, **b** sequential mode

Table 4 Difference output average TCHR on single and sequential valve

Mode valve GV	Average TCHR (kcal/kwh)	Average lowest TCHR (kcal/kwh)
Single	2,334,503,681	2,270,361,631
Sequential	2,335,793,196	2,258,45,858
Difference TCHR	1,190,305,142	

of 11.9 kcal/kwh in the 300–500 MW range than single valve mode. This happens because when conditions are stable that sequential valve can minimize throttling losses (losses that occur when the valve is partially opened), and thus provides the best operating efficiency at partial load.

References

1. Albert PG (1996) Thermal performance evaluation and assesment of steam turbine units. GE Power System, Schenectady, New York
2. Wang SX, Ge XX (2004) Digital electro hydraulic control system of steam turbine. China Electric Power Press Co, Ltd
3. Podolsky LB (Wilmington Del.), Ronnen UG (Monroeville), Lardi F (1977) System and methode for controlling turbine in the single and sequential valve modes with dynamic function generaor. O'Hara Township, Allegheny Country, both of Pa (1977)
4. Yin C, Liu J (2013) Study on valve management of DEH for steam turbine. In: The state key lab of alternate electrical power system with renewable energy sources. North China Electric Power University, Beijing, China
5. Stern LP, Johnson SJ, Binstock MH (1979) System for minimizing valve throttling losses in a steam turbine power plant. Westing House Electric Corporation, Pennysilvania
6. (1998) Procedures for routine performance tests of steam turbines. The American Society of Mechanical Engineers, ASME PTC 6S
7. Pereiro RS (2012) Analysis of different types of regulation and its efficiency in steam power cycles. Poznan University of Technology
8. University of Buenos Aires (1998) Control and governing of steam turbines, Own ed.
9. Singh O (2009) Applied thermodynamics, 3th ed.
10. Shanghai Electric Power Generation Equipment Co, Ltd, Type condensing reheat steam turbine, N600-16.67/538/538
11. Ujade D, Bhambere MB (2014) Review of structural and thermal analysis of gas turbine blade. Int J Mech Eng Rob Res 3(2):347–352

Experimental Study of Wing-Tip Vortex Core Circulation in Near-Field

Robert Stepanov and Alexander Kusyumov

1 Introduction

Wingtip vortices are the source of induced drag, which significantly affects aircraft performance. Spalart [1] and Rossow [2] published extensive literature reviews on the tip vortex formation. Tip vortices in the near-field are characterized by unsteady flow-fields inherent to initial stages of the vortex formation and evolution. Green and Acosta [3] examined unsteady vortices and their axial fluctuations in the near and far-fields. Detailed near-field turbulence measurements were presented in references [4–7].

A number of numerical and experimental studies were aimed at investigating the wingtip vortices behind full-scale aircraft wings [8]. However, the complexity of such experiments and their dependency on various atmospheric conditions including atmospheric turbulence, stratification and vertical gradients can significantly affect the evolution properties of vortices [9–16]. Shen et al. [17] examined vortex properties of full-scale aircraft using LIDAR. The results suggested that the tip vortices circulation decreases with the vortex age. Despite of a significant spread of experimental data, it was shown that there is a circulation deficit with respect to theoretical estimates, which was confirmed numerically.

In spite of an ample body of research dedicated to wingtip vortices, near-field vortex formation is still not well understood. Wingtip vortex properties depend on the distance downstream of the wing. Albano et al. [18] proposed three regions: near-field (extending up to several wing spans), where the roll-up of the vortices occurs; mid-field region (up to 200–300 wing spans), which is characterized by a

R. Stepanov (✉) · A. Kusyumov
Kazan National Research Technical University named after A.N. Tupolev—KAI, Kazan 420111, Russian Federation
e-mail: rpstepanov@kai.ru

steady condition of counter-rotating tip vortices; and the far-field region, where the vortex becomes unstable and the decay of vortex circulation is observed.

The vortex core can be defined by maximum tangential velocities within the vortex. The ability to predict the vortex core circulation is of great practical importance, with one of the reasons being the potential hazard to the following aircraft due to large rolling moments, induced by the vortex. Currently, no straightforward method exists, which would allow estimating wingtip vortex core properties in the near-field.

Winkelmann and Barlow [19] showed that the loss of lift at near-critical angles of attack is associated with "mushroom" shaped three-dimensional flow separation structures, which tend to spread from the central portion of the wing towards the wingtip region with increasing angles of attack. As such, it may indicate that near-critical angles of attack may not alter significantly the tip vortex generation process as long as the separation region on the upper surface of the wing does not spread to region of the tip vortex formation.

A number of authors [20–23] demonstrated a near-linear dependence of the wingtip vortex circulation with the wing's angle of attack (α), for various aspect ratios (AR) and downstream distances (X/c). Agibalova et al. [20] demonstrated it for a NACA 0015 wing (AR = 1; $-10° \leq \alpha \leq 10°$; $X/c = 0.5$), where the tip vortex was defined as having a constant radius for measured angles of attack. Lee [21] also observed a near-linear dependence of the vortex core circulation with the angle of attack for NACA 0012 wing at Re = 1.05×10^5 (AR = 0.87; $3° \leq \alpha \leq 10°$; $X/c = 2.5$). Greenblatt [22] obtained similar results for a NACA 0015 wing at Re = 0.5×10^6 and Re = 10^6 (AR = 4; $2° \leq \alpha \leq 12°$; $X/c = 2.2$), where the vortex was defined by applying a threshold vorticity value, which was substantially smaller than the local maximum vorticity value. Memon [23] obtained a similar result for the wingtip vortex core at Re = 2×10^5 (AR = 3; $2° \leq \alpha \leq 8°$; $X/c = 3$).

Compared to [20–23], this work examines the dependence of the vortex core circulation for different angles of attack (including near-critical angle of attack) for a wider range of downstream distances. In addition, the vortex core circulation is compared to the theoretical circulation, defined by Kutta-Joukowski theorem. This approach allows taking into account the wing's lift coefficient, which in turn depends on the angle of attack and more accurately reflects the overall configuration of the wing.

2 Experimental Setup

The experiments were conducted in T-1K wind tunnel at Kazan National Research Technical University named after A. N. Tupolev, which is a low-speed, closed circuit wind tunnel, capable of reaching up to 50 m/s wind speed, with free-stream turbulent intensity levels below 0.5%.
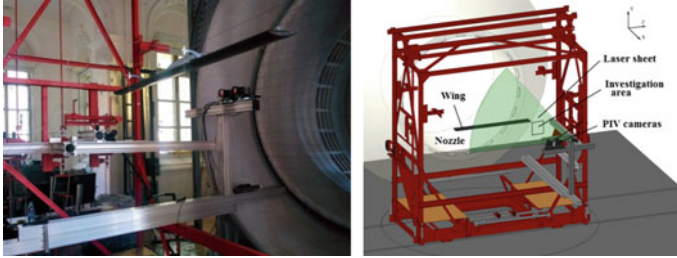
Fig. 1 A photo and 3D-model of the experimental setup at T-1K wind tunnel

A rectangular wing with an aspect ratio (AR) of 7.8 and chord length $c = 187$ mm was used. The wind speed corresponded to $V_\infty = 28$ m/s (Re $= 3.5 \times 10^5$). The wing had a modified Göttingen 387 aerofoil across its span with rounded wingtip caps.

Dantec Stereo-PIV was used for flow visualization, equipped with Nd-YaG Litron 425-10 laser with a wavelength of 532 nm. The exposure time between pulses was set to 6 ns, and the sampling frequency of obtained image pairs corresponded to 8 Hz. Olive oil was used as tracer particles with 10F03 seeding generator.

The experimental setup is shown in Fig. 1. Two FlowSenseEO-4M PIV-cameras with the resolution of 2048×2048 pixels were installed behind the wing. The first camera was positioned perpendicular to the free-stream velocity. The second camera had an offset angle of $10°$ relative to the first camera. Both cameras could be repositioned relative to the wing by sliding them along support beams, as shown in Fig. 1. Adaptive PIV algorithm was used to obtain velocity fields from raw images.

Directions of X, Y and Z axes are shown in Fig. 1. Tip vortices were investigated at different downstream distances from the trailing edge of the wing, $0.53 \le \overline{X} \le 4.22$ ($\overline{X} = X/c$) and at different angles of attack $-6° \le \alpha \le 18°$.

3 Data Analysis and Results

Wingtip vortex core was obtained from PIV velocity fields using Q-criterion, which defines a vortex as a connected region, where the Euclidian norm of the vorticity tensor Ω is greater than the rate of the strain tensor S:

$$Q = \frac{1}{2}\big(|\Omega|^2 - |S|^2\big) > 0. \tag{1}$$

The outer boundary of the core corresponded to $Q = 0$ condition. The wingtip vortex core circulation Γ_C was obtained from PIV-measurements using Stokes' theorem by integrating the velocity field V over the outer boundary l of the vortex core:

$$\Gamma_C = \oint \mathbf{V} \cdot \mathrm{d}\mathbf{l}. \tag{2}$$

Measured vortex core circulation values changed little with different downstream distances ($0.53 \leq \overline{X} \leq 4.22$) at any given angle of attack ($\alpha = \mathrm{const}$). Hence the vortex core circulation is shown in terms of average values $\Gamma_{C,\mathrm{avg}}(\alpha)$ for each angle of attack ($\alpha = \mathrm{const}$), obtained by averaging Γ_C for all measured downstream distances:

$$\Gamma_{C,\mathrm{avg}}(\alpha) = \frac{1}{N} \sum_{i=1}^{N} \Gamma_{C,i}(\alpha). \tag{3}$$

Here N represents the number of downstream distances (cross-sections) $\overline{X}$. The confidence intervals corresponded to $\pm\sigma$, where σ is the root-mean-square deviation:

$$\sigma(\alpha) = \sqrt{\frac{1}{N} \sum_{i=1}^{N} \left(\Gamma_{C,\mathrm{avg}}(\alpha) - \Gamma_{C,i}(\alpha)\right)^2}. \tag{4}$$

The theoretical bound circulation of a rectangular wing can be obtained using Kutta-Joukowski theorem:

$$\Gamma_0(\alpha) = \frac{L(\alpha)}{\rho V_\infty l} = \frac{C_L(\alpha) V_\infty c}{2}. \tag{5}$$

Here, L is the lift force of the wing, ρ is the air density; V_∞ is the free-stream velocity; c is the wing chord length; $C_L(\alpha)$ is the lift coefficient. Rectangular wings are known to have near-elliptical lift and circulation distribution along the wing span. In this work, C_L was obtained from T-1K wind tunnel balance measurements. Therefore, $\Gamma_0(\alpha)$ in (5) represents an evenly distributed average circulation value along the wing span.

The linear part of $C_L(\alpha)$ can be expressed as:

$$C_L(\alpha) = a_0(\alpha - \alpha_{L=0}). \tag{6}$$

Here, $a_0 = \frac{\mathrm{d}C_L}{\mathrm{d}\alpha}$ is the lift slope; $\alpha_{L=0} = -6.3°$ is the zero-lift angle of attack; α is an arbitrary angle of attack at the linear portion of the lift curve.

Let us define $\Gamma_{0A}(\alpha)$ as an approximate value of the bound circulation, obtained from the linear part of $C_L(\alpha)$ by substituting (6) into (5):

$$\Gamma_{0A}(\alpha) = a_0(\alpha - \alpha_{L=0}) \frac{V_\infty c}{2}. \tag{7}$$

The dependence of the average wingtip vortex core circulation $\Gamma_{C,\mathrm{avg}}(\alpha)$, obtained from PIV velocity fields, as a function of the angle of attack is shown in Fig. 2. The
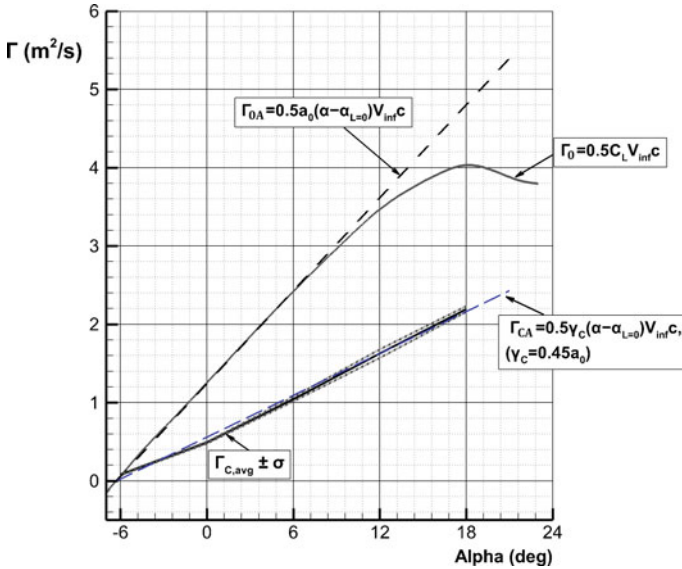
Fig. 2 The bound circulation Γ_0 compared to the experimental tip vortex core circulation $\Gamma_{C,avg}$ and the tip vortex core circulation Γ_{CA} determined by modified Kutta-Joukowski theorem

confidence intervals $\pm\sigma$ are denoted by dotted lines. Obtained results indicate that the vortex core circulation $\Gamma_C(\alpha)$ has a near-linear dependence from the angle of attack α and changes little with downstream distances $\overline{X}$ for any given angle of attack.

The theoretical circulation $\Gamma_0(\alpha)$ is also shown in Fig. 2 along with extrapolated linear relation $\Gamma_{0A}(\alpha)$. It is evident from Fig. 2, that the approximate value of the wingtip vortex core circulation $\Gamma_{CA}(\alpha)$ can be obtained by adjusting the slope of the theoretical circulation $\Gamma_{0A}(\alpha)$:

$$\Gamma_{CA}(\alpha) = k\Gamma_{0A}(\alpha) = ka_0(\alpha - \alpha_{L=0})\frac{V_\infty c}{2}. \tag{8}$$

Here, $k = 0.45$ is an empirical coefficient for the wing, considered in this work. Let us define the circulation slope of the vortex core γ_C as:

$$\gamma_C = ka_0. \tag{9}$$

Approximate values of the vortex core circulation for the range $-6° \leq \alpha \leq 18°$, including a nonlinear part of $C_L(\alpha)$, can be obtained by substituting (9) into (8):

$$\Gamma_{CA}(\alpha) = \gamma_C(\alpha - \alpha_{L=0})\frac{V_\infty c}{2}. \tag{10}$$

In other words, the vortex core circulation corresponds to 45% of theoretical bound vortex circulation, defined by Kutta-Joukowski theorem.

4   Conclusions

It has been demonstrated that the tip vortex core circulation can be estimated with good accuracy by modifying Kutta-Joukowski theorem using the vortex core circulation slope γ_C. It is shown that γ_C is proportional to the wing's lift slope a_0. Although the lift slope changes at the near-critical angles of attack, it is shown that the obtained relation can be used to estimate the wingtip vortex core circulation at near-critical angles of attack with sufficient accuracy. Future studies will be aimed at investigating the influence of various wing geometries on the circulation slope γ_C of the vortex core.

References

1. Spalart PR (1998) Airplane trailing vortices. Annu Rev Fluid Mech 30:107–138. https://doi.org/10.1146/annurev.fluid.30.1.107
2. Rossow V (1999) Lift-generated vortex wake of subsonic transport aircraft. Prog Aerosp Sci 35(6):507–660. https://doi.org/10.1016/S0376-0421(99)00006-8
3. Green S, Acosta A (1991) Unsteady flow in trailing vortices. J Fluid Mech 227:107–134. https://doi.org/10.1017/S0022112091000058
4. Phillips W, Graham J (1984) Reynolds-stress measurements in a turbulent trailing vortex. J Fluid Mech 147:353–371. https://doi.org/10.1017/S0022112084002123
5. Zilliac GG, Chow JS, Dacles-Mariani J, Bradshaw P (1993) Turbulent structure of a wingtip vortex in the near field. In: AIAA 23rd fluid dynamics, plasma dynamics, and lasers conference, 6–9 July. AIAA Paper 1993-3011. https://doi.org/10.2514/6.1993-3011
6. Dacles-Mariani J, Zilliac G, Chow J, Bradshaw P (1995) Numerical/experimental study of a wingtip vortex in the near field. AIAA J 33(9):1561–1568. https://doi.org/10.2514/3.12826
7. Chow JS, Zilliac GG, Bradshaw P (1997) Mean and turbulence measurements in the near field of a wingtip vortex. AIAA J 35(10):1561–1567. https://doi.org/10.2514/2.1
8. Chernyshev S, Gaifullin AM, Sviridenko YN (2014) Civil aircraft vortex wake. TsAGI's research activities. Prog Aerosp Sci 71:150–160. https://doi.org/10.1016/j.paerosci.2014.06.004
9. Vishinsky VV, Zamyatin AN, Sudakov GG (2006) Teoreticheskoye & eksperimentalnoye issledovaniye evolutsii vihrevogo sleda za samoletom, letyashim za samoletom, letyashim v pogranichnom sloye atmosferi. Technika vozdushnogo flota 3–4:25–38 (in Russian)
10. Tombach I (1973) Observations of atmospheric effects on vortex wake behavior. J Aircr 10:641–647. https://doi.org/10.2514/3.60276
11. Hecht AM, Bilanin AJ, Hirsh JE (1981) Turbulent trailing vortices in stratified fluids. AIAA J 19:691–698. https://doi.org/10.2514/3.50992

12. Sarpkaya T (1983) Trailing vortices in homogeneous and density-stratified media. J Fluid Mech 136:85–109. https://doi.org/10.1017/S0022112083002074
13. Sarpkaya T, Daly JJ (1987) Effect of ambient turbulence on trailing vortices. J Aircr 24:399–404. https://doi.org/10.2514/3.45459
14. Liu H-T (1992) Effects of ambient turbulence on the decay of a trailing vortex wake. J Aircr 29:255–263. https://doi.org/10.2514/3.46153
15. Robins RE, Delisi DP (1990) Numerical study of vertical shear and stratification effects on the evolution of a vortex pair. AIAA J 28(4):661–669. https://doi.org/10.2514/3.10444
16. Proctor FH (1996) Numerical simulation of wake vortices measured during the Idaho fall and Memphis field programs. In: 14th Applied aerodynamics conference, 17–20 June, pp 943–961. https://doi.org/10.2514/6.1996-2496
17. Shen S, Ding F, Han J, Lin Y-L, Pal Arya S, Proctor FH (1999) Numerical modeling studies of wake vortices: real case simulations. In: 37th AIAA aerospace sciences meeting and exhibit. January 11–14. Reno, NV (AIAA 99-0755). https://doi.org/10.2514/6.1999-755
18. Albano F, De Gregorio F, Ragni A (2003) Trailing vortex detection and quantitative evaluation of vortex characteristics by PIV technique. In: 20th International congress on instrumentation in aerospace simulation facilities. IEEE, Gottingen, Germany
19. Winkelmann AE, Barlow JB (1980) A flowfield model for a rectangular planform wing beyond stall. AIAA J 18(8):1006–1008
20. Agibalova SA, Golub VV, Moralev IA, Saveliev AS (2011) Effect of dielectric barrier discharge on wing-tip vortex formation. Tech Phys Lett 37(11):1070–1073
21. Lee T (2010) PIV study of near-field tip vortex behind perforated Gurney flaps. Exp Fluids 50(2):351–361
22. Greenblatt D (2012) Fluidic control of a wing tip vortex. AIAA J 50(2):375–386
23. Memon MO, Wabick K, Altman A, Buffo R (2014) Wingtip vortices from an exergy-based perspective. In: 52nd Aerospace sciences meeting. AIAA, Maryland

Thermal Contact Conductance Relation on Asperities Location

Ekaterina S. Golubtsova and **Mikhail V. Murashov**

1 Introduction

In the joints of rough metal solids, heat is transferred through the real contact spots formed during the deformation under the nominal pressure of the roughness protrusions, also called asperities. The total area of the real contact spots A is only a small fraction of the nominal surface area A_0. As an example, Fig. 1 shows the real contact spots on a rough copper surface with $Rz = 20\,\mu m$ at a nominal pressure $P = 25$ MPa, obtained by numerically solving the deformation problem [1]. Then the temperature field in the near-surface region of the contacting bodies changes, forming the thermal contact conduction

$$\alpha_c(\varphi) = \frac{q}{\overline{T}_2 - \overline{T}_1},$$

where q is the heat flux density, $\overline{T}_1, \overline{T}_2$ are the average temperatures over the area of the nominal lower and upper contacting surfaces, respectively, $\varphi = \frac{A}{A_0}$ is the ratio of the real contact area to the nominal area. In reality, thermal contact conductance depends on many factors, and its reliable calculation is not an easy task.

A number of models of heat transfer through a discrete contact have been developed, for example, [2–6]. However, the key problem, which is the development of a reliable method for predicting the parameters of contact heat transfer, has not yet been solved. It is not clear, in particular, whether α_c is directly proportional to φ. To answer this question, it is necessary to investigate the influence of the real contact spots location on α_c in thermal contacts. The possibility of such an influence is indicated by the results of some papers, for example, [7], where it is shown that the

E. S. Golubtsova · M. V. Murashov (✉)
Bauman Moscow State Technical University, Moscow 105005, Russia
e-mail: murashov@bmstu.ru

Fig. 1 Real contact spots on
the rough surface of copper
at nominal pressure $P =$
25 MPa [1]
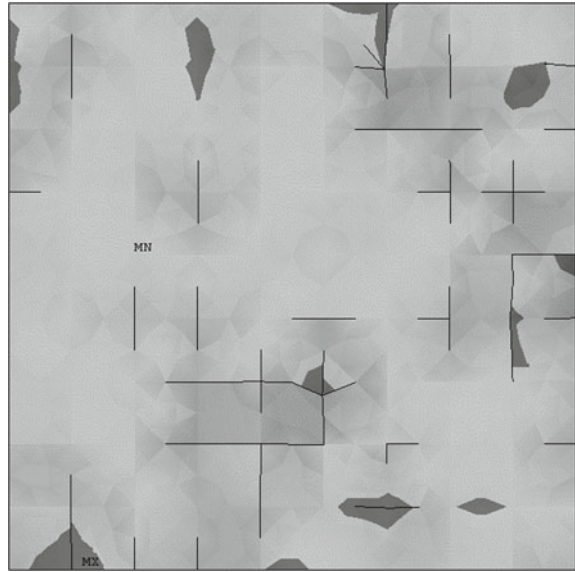
clustering of asperities and their relative position significantly affect the electrical contact conductivity.

Let's consider the models of surface roughness developed to date. There are four types of such models—multilevel, stochastic, fractal, and deterministic.

The multilevel models probably originate from the work by Archard [8], when the surface is represented by hemispherical protrusions, where smaller hemispherical protrusions of the next level are located. However, this model of the surface is academic, so it is not clear how to determine the parameters of protrusions of different levels experimentally, having a real rough surface. The development of this direction is the construction of surfaces using sinusoidal models of asperities based on the data obtained by applying the fast Fourier transform to the results of scanning a real surface [9].

Stochastic models of the contact surface are a set of geometric shapes randomly scattered on the plane. For example, in the classical work of Greenwood and Williamson [10], the roughness consists of spheres of the same radius with heights randomly distributed, for example, according to Gaussian or exponentially. A near-Gaussian distribution can also be used [11]. In [10] and further in [12], the hypothesis was adopted that as the surfaces approach, each asperity deforms, independently of the others, while in fact, during compression, the spots merge, forming complex geometric structures [13].

The use of fractal definition of surfaces in contact problems began in 1991 [14, 15]. Fractal surfaces undoubtedly have a statistical affine self-similarity of the structure, but is this sufficient for solving problems of heat transfer through a contact? In other words, does this statistical self-similarity convey those properties of the structure that have the main influence on heat transfer through the contact? After all, the

self-similarity of fractal surfaces for different roughness levels is often confirmed by comparing only the statistical distribution of the heights of the asperities, the pitch of the asperities, and the radius of curvature of their tips, as the main statistical parameters obtained from the profilometers.

Whether and to what extent thermomechanical contact models based on fractal or stochastic surface models take into account the influence of the relative position of the asperities on the thermal contact conductance is not known. This possibility appears when using deterministic surface models, where the location of the asperities on the surface is uniquely specified. Deterministic models can be built using various algorithms [16] or based on direct measurements of the sample surface [17].

In this paper, the influence of the location of the asperities on the thermal contact conductance is studied using a model two-dimensional problem of contact between two bodies. We consider representative elements of both bodies contacting each other with their flat surfaces. The contact surfaces are thermally insulated, with the exception of one or two contact spots, which different relative positions and sizes are specified for. There is no gap between the contacting surfaces. The heat conduction problem is solved by the finite element method using the ANSYS software. Such studies on spatial models are difficult due to the high computational cost and are planned for the future.

2   Formulation of the Problem

For two-dimensional analysis, two rectangular bodies N and O are considered to be in contact with a line of contact 1 mm long. Three variants of the location of the real contact spots on the contact line in the model are considered. In the first variant, the length of a single real contact spot is 0.1 mm and it is located at a distance a from the left boundary of the bodies (Fig. 2). The description of the location of the spots in the second and third variants is given in the next section. The material of both bodies is 1050 UNS A91050 aluminum with the thermal conductivity $k = 210$ W/(m K), which is not temperature dependent.

Due to scattering, reflection and refraction of thermal energy carriers at the boundary of contacting bodies, even from identical materials [2], also due to the presence of atomic roughness, thermal boundary conductance (Kapitza conductance) α_b arises in the direct contact zone. Its value is set by the TCC (Thermal Contact Conduction) parameter of the computational software (ANSYS) for contact finite elements on contact spots. As the first approximation, α_b is taken, as in [2], equal to 10^9 W/(m^2 K), which corresponds to the thermal boundary conductance for an ideal silicon contact [18]. All surfaces of bodies, with the exception of direct contact surfaces, are thermally insulated.

A medium with a constant temperature T_N acts uniformly on the top surface of body N and another medium with a constant temperature T_O acts uniformly on the bottom surface of body O. Convective heat transfer occurs between the bodies and media. Its intensity is characterized by the heat transfer coefficients h_N and h_O. Heat
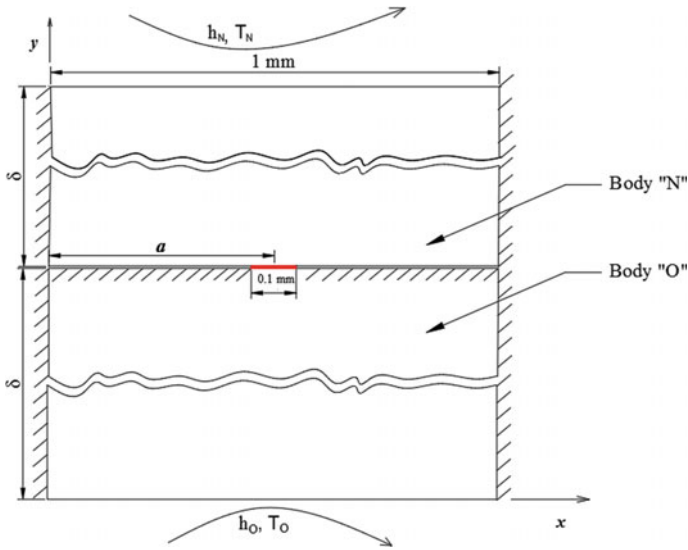
Fig. 2 The first variant for calculating heat transfer through a real contact spot

transfer conditions on the surfaces are constant in time. Heat transfer parameters at the top surface of body N are $h_N = 5000$ W/(m^2 K), $T_N = 330$ K, and at the bottom surface of body O are $h_O = 1000$ W/(m^2 K), $T_O = 273$ K. High values of the heat transfer coefficients are chosen to eliminate possible rounding errors when calculating the temperature field by the software. Radiation heat transfer is not considered.

Based on the obtained temperature field, the thermal conductance through the contact α_c can be calculated, representing the model as a sequential connection of bodies N and O and the contact itself. The thermal resistance of the model R_m will be the sum of the thermal resistance of bodies N and O R_{NO} and the thermal resistance of the contact R

$$R_m = R_{NO} + R,$$

where $R = \frac{1}{\alpha_c}$, $R_m = \frac{(T_1 - T_2)}{h_N(T_N - T_1)}$; T_1, T_2 are average temperatures on the top surface of body N and the bottom surface of body O, respectively. The temperatures are determined on the upper and lower surfaces of the bodies in order to exclude uncertainties related to the temperature differences along the contact line. Thermal resistance of bodies N and O will be equal to $R_{NO} = \frac{2\delta}{k}$, where δ is the height of each body, $\delta = 10$ mm. Then the thermal contact conductance can be calculated using the formula

$$\alpha_c = \left(\frac{T_1 - T_2}{h_N(T_N - T_1)} - \frac{2\delta}{k} \right)^{-1}.$$
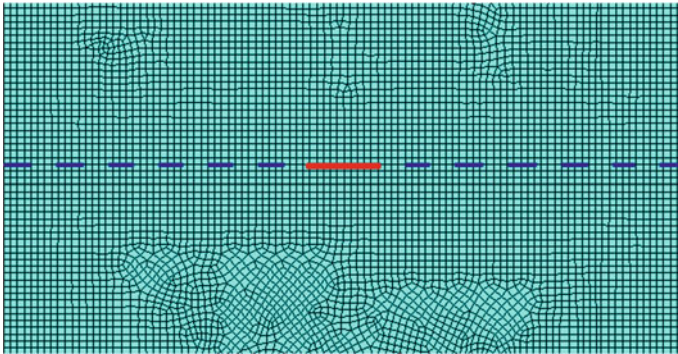
Fig. 3 Finite element mesh of the model near the contact zone (the boundary of the bodies is marked with a dotted line, the real contact spot is marked with a red bold line)

The finite element mesh of the model near the contact zone is shown in Fig. 3. The average size of the finite element was approximately 0.01 mm. The mesh includes 203,043 finite elements of the PLANE77 type. Finite elements of the TARGE169 and CONTA172 types are used for the contact spot.

3 Results

For the first variant of spots location with a single contact spot, a cycle of calculations was carried out with various values of the parameter a, characterizing the position of the real contact spot (Fig. 2). The dependence of the thermal contact conductance on the position of the real contact spot (Fig. 4) shows that the thermal contact conductance changes more than 2 times, while the real contact area is unchanged.
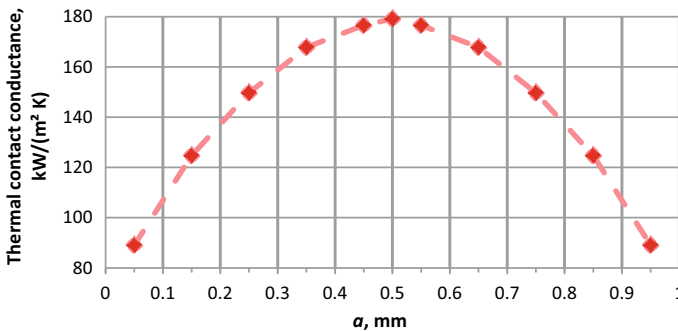
Fig. 4 Dependence of thermal contact conductance on the position of a single real contact spot along the contact line
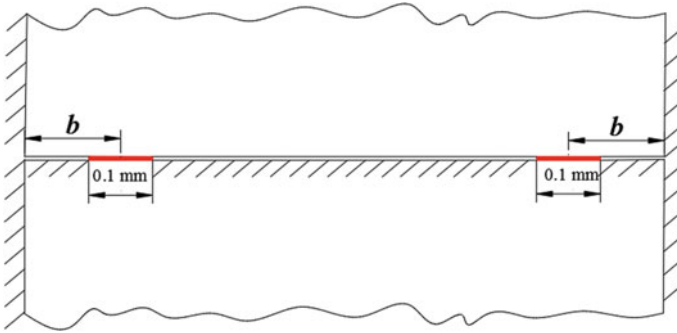
Fig. 5 The second variant with two symmetrically located real contact spots

The second variant of spots location has two equal real contact spots (0.1 mm long), located symmetrically relative to the middle of the contact line of the bodies (Fig. 5). The center of each real contact spot is spaced from the closest lateral boundary of the body at distance *b*.

The results of calculating the dependence of the thermal contact conductance on the position of the centers of the contact spots on the contact line are shown in Fig. 6. It shows that the thermal contact conductance at one 0.2 mm contact spot located in the center is equal to the conductance at two contact spots of 0.1 mm each located at the edges of the region. The minimum value of thermal contact conductance is obtained when two contact spots completely overlap in the center of the contact line. The thermal contact conductance reaches its maximum when two contact spots are located equidistant from the ends of the contact line, and from its middle.

From the comparison of the results for the first and second variants of spots location in Figs. 4 and 6, respectively, we can see that the thermal contact conductance for one spot located in the center of the contact line, with an increase in its size by 2 times from 0.1 to 0.2 mm, increases only by 50.2%, which indicates the lack of proportionality of the dependence of α_C on φ.

Fig. 6 Influence of the contact spots location on thermal contact conductance for the second variant, i.e. two symmetrically located contact spots
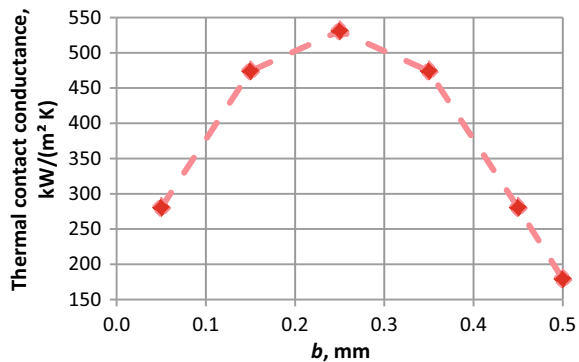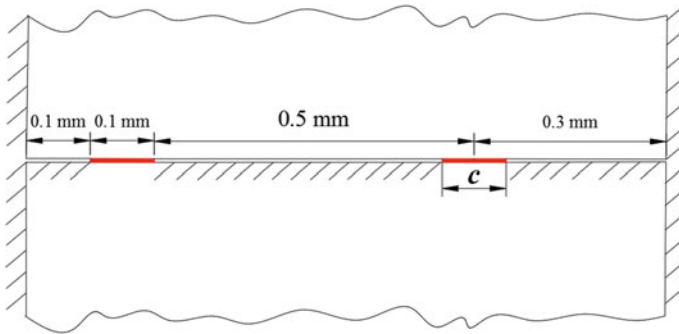
Fig. 7 The third variant of spots location where the size of the second real contact spot changes

Fig. 8 Dependence of the thermal contact conductance on the size of the second real contact spot
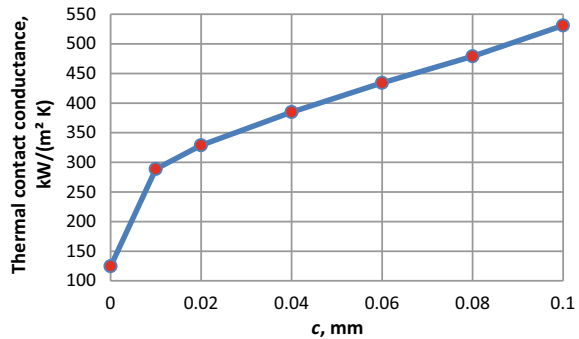
In the third variant of contact spot location, the influence of the appearance of an additional real contact spot on the thermal contact conductance is considered. The first real contact spot, 0.1 mm in size, is located 0.1 mm from the left border. The second spot, like the first, does not change its position and its center is 0.3 mm from the right border of the bodies (Fig. 7). The size of the second spot is set by the c parameter.

Figure 8 shows the dependence of the thermal contact conductance on the size of the second real contact spot for the third variant of spots location.

4 Conclusions

Thermal contact conductance significantly depends not only on the real contact area, but also on the location of the real contact spots in the nominal contact area. Moreover, the thermal contact conductance is not proportional to φ.

The calculations show that, on the one hand, for real and nominal contact areas of constant size, the thermal contact conductance changes by a factor of 2 with

relocation of the spot. On the other hand, doubling the size of a contact spot in its constant position leads to an increase in the thermal contact conductance by only 56.6%.

The relative position of the contact spots also has a significant influence. For two equal in size real contact spots with their different locations, the thermal contact conductance differs by a factor of 1.89.

The emergence of a small spot in the contact area slightly increases the real contact area, but drastically changes the thermal contact conductance. For example, the addition to the nominal contact area of the second real contact spot just 10 times smaller than the first one results in a 2.32-fold increase in thermal contact conductance.

The results obtained show that modeling the thermal contact conduction requires models that take into account the location of the real contact spots, including those with a small size. From the existing contact models, this can be done by deterministic models, since stochastic and fractal models do not take into account the location of asperities and, consequently, real contact spots.

For the future study we will explore the influence of the location of the real contact spots on a deterministic 3D-model of rough contact. Further, study will be carried out to clarify the dependence of thermal contact conduction on the size of the rough contact model.

References

1. Murashov MV, Panin SD (2010) Modeling of thermal contact conductance. In: Proceedings of the international heat transfer conference IHTC14. vol 6. Washington, DC, USA, pp 387–392. https://doi.org/10.1115/IHTC14-22616
2. Thompson MK (2007) A multi-scale iterative approach for finite element modelling of thermal contact resistance. PhD thesis. Massachusetts Institute of Technology. Cambridge, MA, USA, pp 100. https://doi.org/10.1115/MNHT2008-52385
3. Lee S, Jang YH, Kim W (2008) Effects of nanosized contact spots on thermal contact resistance. J Appl Phys 103:074308. https://doi.org/10.1063/1.2903450
4. Ciavarella M, Delfine V, Demelio G (2006) A '"re-vitalized"' Greenwood and Williamson model of elastic contact between fractal surfaces. J Mech Phys Solids 54:2569–2591. https://doi.org/10.1016/j.jmps.2006.05.006
5. Bahrami M, Yovanovich MM, Culham JR (2005) Thermal contact resistance at low contact pressure: Effect of elastic deformation. Int J Heat Mass Transf 48(16):3284–3293. https://doi.org/10.1016/j.ijheatmasstransfer.2005.02.033
6. Murashov MV (2020) Temperature field simulation of gyro unit-platform assembly accounting for thermal expansion and roughness of contact surfaces. In: Hu Z, Petoukhov S, He M (eds) Advances in artificial systems for medicine and education II. Advances in Intelligent Systems and Computing, vol 902. Springer, Cham, pp 601–616. https://doi.org/10.1007/978-3-030-12082-5_55
7. Greenwood JA (1966) Constriction resistance and the real area of contact. Br J Appl Phys 17(12):1621–1632. https://doi.org/10.1088/0508-3443/17/12/310
8. Archard JF (1957) Elastic deformation and the laws of friction. In: Proceedings of the Royal Society. Series A, mathematical and physical sciences, vol 243(1233), pp 190–205. https://doi.org/10.1098/rspa.1957.0214

9. Jackson RL, Streator JL (2006) A multi-scale model for contact between rough surfaces. Wear 261:1337–1347. https://doi.org/10.1016/j.wear.2006.03.015
10. Greenwood JA, Williamson JBP (1966) Contact of nominally flat surfaces. In: Proceedings of the Royal Society of London. Series A, mathematical and physical sciences. vol 295. pp 300–319. https://doi.org/10.1098/rspa.1966.0242
11. Zhang X et al (2004) A new method for numerical simulation of thermal contact resistance in cylindrical coordinates. Int J Heat Mass Transf 47(5):1091–1098. https://doi.org/10.1016/j.ijheatmasstransfer.2003.04.001
12. Bush AW, Gibson RD, Thomas TR (1975) The elastic contact of a rough surface. Wear 35:87–111. https://doi.org/10.1016/0043-1648(75)90145-3
13. Greenwood JA (2007) A note on Nayak's third paper. Wear 262:225–227. https://doi.org/10.1016/j.wear.2006.04.011
14. Majumdar A, Bhushan B (1991) Fractal model of elastic-plastic contact between rough surfaces. J Tribol 113(1):1–11. https://doi.org/10.1115/1.2920588
15. Borodich FM, Mosolov AB (1991) Fractal contact of solids. J Tech Phys 61:50–54
16. Murashov MV, Panin SD (2015) Numerical modelling of contact heat transfer problem with work hardened rough surfaces. Int J Heat Mass Transf 90:72–80. https://doi.org/10.1016/j.ijheatmasstransfer.2015.06.024
17. Thompson MK, Thompson JM (2010) Considerations for the incorporation of measured surfaces in finite element models. Scanning 32(4):183–198
18. Cahill DG et al (2003) Nanoscale thermal transport. J Appl Phys 93(2):793–818. https://doi.org/10.1063/1.1524305

A Modeling and Modal Analysis Method for Folded Plate

Kaiyuan Tian, Dengqing Cao, and Kaiping Yu

1 Introduction

Folded structure is more and more widely used in engineering, especially in aeronautics field. For example, solar panels of satellites, folded rudders of missiles, folded wings of airplanes, etc. When folded, the structure occupies a smaller volume, which is convenient for storage and transportation. When unfolded, the structure exhibits different dynamic properties with different angles. Many folded structures can be simplified as folded plates. The modal analysis of folded plate structure is key and difficult in the research. Guo [1–7] obtained the first several vibration modes of Z-shaped folded plate through finite element method and modal experiment, and obtained the approximate modal function, but did not get the global modal directly by numerical calculation.

Some researchers used Rayleigh–Ritz method to calculate the modal shapes of structures. Irie [8] used Rayleigh–Ritz method to obtain the modal shapes of a cantilever folded plate by numerical calculation, but he used very complex admissible functions, which were not suitable for other boundary conditions. So, it was not universal. The vibration of folded plate is three-dimensional, so the transverse vibration and in-plane vibration should be considered at the same time. Cao [9–11] and Liu [12] studied the transverse vibration modal shapes of a three-axis attitude stabilized spacecraft with solar panels. In terms of in-plane vibration, the modal shapes of a single plate were obtained by numerical calculation in references [13–15]. Comparing the natural frequencies and modal shapes of their model with that of the finite element model, the validity and accuracy of the method are demonstrated.

The difficulty of folded plate structure modeling is the treatment of boundary conditions between two plates. Therefore, this paper proposes a method to transform

K. Tian · D. Cao (✉) · K. Yu
Harbin Institute of Technology, Harbin 150001, China
e-mail: dqcao@hit.edu.cn

the linear connection between two plates into several nodes. The Rayleigh–Ritz method is used to obtain the global modes of the structure through numerical calculation. The method proposed here is valid by comparing with the natural frequencies obtained here and those from the finite element method.

2 Modeling of Folded Plate

A folded plate model is established, and the local coordinate systems (x_i, y_i, z_i) $(i = 1,2)$ are established on the two plates respectively, as shown in Fig. 1. a_1 and a_2 are the length of the two plates respectively. b is the width of the plates, h is the thickness of the plates, and θ is the angle between the two plates.

The maximum kinetic energy of the plate is:

$$T = \frac{1}{2}\rho h \sum_{i=1}^{1} \int_0^{a_i} \int_0^b \left(u^2 + v^2 + w^2\right)_i dx_i dy_i \tag{1}$$

where u_i, v_i, and w_i are the displacements in x_i, y_i, and z_i directions respectively, and ρ is the mass density.

The maximum potential energy of the plate is:

$$U = \frac{1}{2}D_1 \sum_{i=1}^{2} \int_0^{a_i} \int_0^b \left[\left(\frac{\partial u}{\partial x}\right)^2 + \left(\frac{\partial v}{\partial y}\right)^2 + 2\mu\frac{\partial u}{\partial x}\frac{\partial v}{\partial y} + \frac{1-\mu}{2}\left(\frac{\partial u}{\partial y} + \frac{\partial v}{\partial x}\right)^2\right]_i dx_i dy_i$$

$$+\frac{1}{2}D_2 \sum_{i=1}^{2} \int_0^{a_i} \int_0^b \left[\left(\frac{\partial^2 w}{\partial x^2}\right)^2 + \left(\frac{\partial^2 w}{\partial y^2}\right)^2 + 2\mu\frac{\partial^2 w}{\partial x^2}\frac{\partial^2 w}{\partial y^2} + 2(1-\mu)\left(\frac{\partial^2 w}{\partial x\partial y}\right)^2\right]_i dx_i dy_i \tag{2}$$

Fig. 1 Folded plate
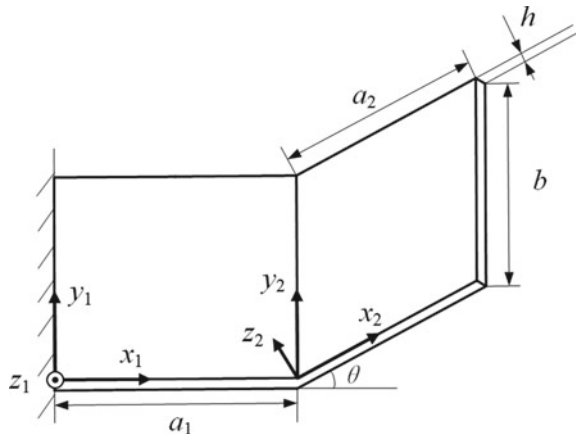
where $D_1 = Eh/(1 - \mu^2)$ and $D_2 = Eh^3/[12(1 - \mu^2)]$ are the extensional and flexural rigidities respectively, E is the modulus of elasticity.

The displacement functions can be written as follows:

$$\begin{cases} w_i(x_i, y_i, t) = W_i(x_i, y_i) \sin(\omega t) \\ u_i(x_i, y_i, t) = U_i(x_i, y_i) \sin(\omega t) \\ v_i(x_i, y_i, t) = V_i(x_i, y_i) \sin(\omega t) \end{cases} \tag{3}$$

where W, U, V are the vibration modal functions and ω is the vibration frequency. Write the modal functions as follows:

$$\begin{cases} W_i(x_i, y_i) = \sum_{m_1=1}^{m_{t1}} \sum_{n_1=1}^{n_{t1}} C_{mn}^{(i)} \varphi_{m_1}^{(i)}(x_i) \varphi_{n_1}^{(i)}(y_i), & i = 1, 2 \\ U_i(x_i, y_i) = \sum_{m_2=1}^{m_{t2}} \sum_{n_2=1}^{n_{t2}} A_{mn}^{(i)} \varphi_{m_2}^{(i)}(x_i) \varphi_{n_2}^{(i)}(y_i), & i = 1, 2 \\ V_i(x_i, y_i) = \sum_{m_3=1}^{m_{t3}} \sum_{n_3=1}^{n_{t3}} B_{mn}^{(i)} \varphi_{m_3}^{(i)}(x_i) \varphi_{n_3}^{(i)}(y_i), & i = 1, 2 \end{cases} \tag{4}$$

where m_t and n_t are the polynomial terms in x and y directions respectively. $\varphi_m(x)$ and $\varphi_n(y)$ are a group of polynomials with integral interval on $[l_1, l_2]$. They must satisfy the boundary conditions. The polynomials can be obtained as follows:

$$\psi_2(\xi) = (\xi - B_1)\psi_1(\xi)$$

$$\psi_{k+1}(\xi) = (\xi - B_k)\psi_k(\xi) - C_k\psi_{k-1}(\xi), k \geq 2$$

$$B_k = \frac{\int_{l_1}^{l_2} \xi[\psi_k(\xi)]^2 d\xi}{\int_{l_1}^{l_2} [\psi_k(\xi)]^2 d\xi} \quad C_k = \frac{\int_{l_1}^{l_2} \xi\psi_{k-1}(\xi)\psi_k(\xi)d\xi}{\int_{l_1}^{l_2} [\psi_{k-1}(\xi)]^2 d\xi} \tag{5}$$

$$\varphi_k(\xi) = \psi_k(\xi)/\sqrt{\int_{a_1}^{a_2} [\psi_k(\xi)]^2 d\xi}, \quad k = 1, 2, \cdots$$

For different boundary conditions: free-F, simply supported-S, and clamped-C, the first term is different, as shown in the Table 1.

Table 1 First term of polynomials

Boundary	$\psi_1(\xi)$
F-F	1
S–S	$(\xi\text{-}l_1)(\xi\text{-}l_2)$
C-C	$(\xi\text{-}l_1)^2(\xi\text{-}l_2)^2$
C-F	$(\xi\text{-}l_1)^2$
C-S	$(\xi\text{-}l_1)^2(\xi\text{-}l_2)$
S-F	$\xi\text{-}l_1$

Considering the boundary conditions, transform the linear connection between the two plates into p nodes whose coordinates are:

$$x_1 = a_1, x_2 = 0, \quad y_i = b(i-1)/(p-1) \tag{6}$$

The boundary conditions of connection nodes are as follows:

$$\Delta_{1i} = U_2(0, y_i)\cos\theta - W_2(0, y_i)\sin\theta - U_1(a_1, y_i) = 0$$
$$\Delta_{2i} = V_2(0, y_i) - V_1(a_1, y_i) = 0$$
$$\Delta_{3i} = U_2(0, y_i)\sin\theta + W_2(0, y_i)\cos\theta - W_1(a_1, y_i) = 0 \tag{7}$$

$$\Delta\theta_i = \left.\frac{\partial W_2}{\partial x_2}\right|_{\substack{x_2=0 \\ y_2=y_i}} - \left.\frac{\partial W_1}{\partial x_1}\right|_{\substack{x_1=a_1 \\ y_1=y_i}} = 0$$

By introducing Lagrange multipliers $\lambda_{1i}, \lambda_{2i}, \lambda_{3i}, \lambda_{4i} (i = 1, 2, ..., p)$, define

$$\prod = U - T + \lambda_{1i}\Delta_{1i} + \lambda_{2i}\Delta_{2i} + \lambda_{3i}\Delta_{3i} + \lambda_{4i}\Delta\theta_i \tag{8}$$

According to the Rayleigh–Ritz method

$$\frac{\partial \prod}{\partial C_{mn}^{(i)}} = 0, \frac{\partial \prod}{\partial A_{mn}^{(i)}} = 0, \frac{\partial \prod}{\partial B_{mn}^{(i)}} = 0$$

$$\frac{\partial \prod}{\partial \lambda_{1i}} = 0, \frac{\partial \prod}{\partial \lambda_{2i}} = 0, \frac{\partial \prod}{\partial \lambda_{3i}} = 0, \frac{\partial \prod}{\partial \lambda_{4i}} = 0 \tag{9}$$

The characteristic equation of the system can be written as

$$\left(K - \omega^2 M\right)X = 0 \tag{10}$$

The natural frequencies and modal shapes of the structure can be obtained by solving Eq. (10).

3   Results and Discussion

Select a set of variable parameters, as shown in Table 2. Then the natural frequencies are worked out and the results are discussed.

First, select three typical folded angles: 0°, 30°, and 90°. Figure 2 is the finite element model of folded plate established in ANSYS software to check the accuracy of the method. The number of terms of polynomials are: $m_{t1} = n_{t1} = m_{t2} = n_{t2} = m_{t3} = n_{t3} = r = 8$. The number of connection nodes $p = 21$.

Table 2 The value of parameters

Parameter	Value	Unit
a_1	0.2	m
a_2	0.2	m
b	0.2	m
E	2.06×10^{11}	Pa
h	0.006	m
ρ	7800	kg/m^3
μ	0.3	

(a) 0°   (b) 30°   (c) 90°
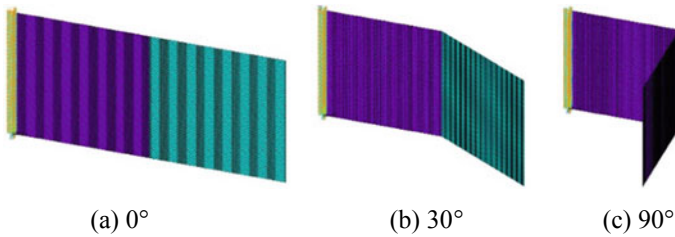
Fig. 2 Folded plate with different angles

Table 3 Natural frequencies with different angles

Order	$\theta = 0°$			$\theta = 30°$			$\theta = 90°$		
	f_1	f_2	$\triangle$ (%)	f_1	f_2	$\triangle$ (%)	f_1	f_2	$\triangle$ (%)
1	31.92	31.93	0.01	33.09	33.10	0.01	42.84	42.85	0.02
2	137.38	137.40	0.01	114.73	114.74	0.01	81.97	81.96	−0.02
3	198.94	198.96	0.01	179.68	179.71	0.02	117.26	117.30	0.03
4	447.17	447.22	0.01	332.00	332.00	0.00	280.07	279.95	−0.04
5	558.28	558.35	0.01	558.18	558.25	0.01	568.83	568.90	0.01
6	858.74	858.75	0.00	833.65	833.75	0.01	834.57	834.48	−0.01
7	864.14	864.18	0.00	941.21	941.32	0.01	836.97	837.46	0.06
8	888.55	898.62	1.13	1029.5	1029.7	0.02	987.27	987.34	0.01
9	1099.41	1099.48	0.01	1037.4	1039.8	0.23	1084.5	1083.4	−0.10
10	1178.09	1178.28	0.02	1512.4	1512.9	0.03	1531.7	1532.4	0.04

The results are shown in Table 3. f_1 represents the natural frequency (Hz) of the finite element method, f_2 represents the natural frequency of the Rayleigh–Ritz method, and $\triangle$ represents the relative error between them.

With different angles, the relative errors are all very small, which prove the method proposed here is valid.

Table 4 Natural frequencies with different r

		$r = 6$		$r = 7$		$r = 8$	
Order	f_1	f_2	△	f_2	△	f_2	△
1	33.09	33.11	0.06	33.09	0.01	33.10	0.01
2	114.73	114.73	0.00	114.78	0.05	114.74	0.01
3	179.68	179.82	0.08	179.72	0.02	179.71	0.02
4	332.00	331.65	−0.10	332.24	0.07	332.00	0.00
5	558.18	558.97	0.14	558.28	0.02	558.25	0.01
6	833.65	833.04	−0.07	834.57	0.11	833.75	0.01
7	941.21	948.81	0.81	940.27	−0.10	941.32	0.01
8	1029.5	1038.7	0.90	1029.7	0.02	1029.7	0.02
9	1037.5	1039.4	0.19	1042.6	0.49	1039.8	0.23
10	1512.4	1530.0	1.16	1507.3	−0.34	1512.9	0.03

Second, with a fixed angle of 30° and a fixed number of connection nodes $p = 21$, but with different polynomial terms r, the results are shown in Table 4.

It can be seen that the relative error will be smaller if the number of polynomial terms is bigger.

Finally, with a fixed angle of 30° and a fixed number of polynomial terms $r = 8$, but with different number p of connection nodes, the results are shown in Table 5.

It can be seen that the relative error is getting smaller if the number of connection nodes increases.

In a word, the calculation results show that this equivalent method is effective and has high accuracy. Therefore, it is reasonable to use several nodes instead of linear connection.

Table 5 Natural frequencies with different p

		$p = 7$		$p = 14$		$p = 21$	
Order	f_1	f_2	△	f_2	△	f_2	△
1	33.09	32.90	−0.58	33.04	−0.15	33.10	0.01
2	114.73	111.47	−2.84	114.10	−0.55	114.74	0.01
3	179.68	175.17	−2.51	179.43	−0.14	179.71	0.02
4	332.00	316.92	−4.54	332.03	0.01	332.00	0.00
5	558.18	558.43	0.04	557.83	−0.06	558.25	0.01
6	833.65	811.17	−2.70	822.95	−1.28	833.75	0.01
7	941.21	901.17	−4.25	939.86	−0.14	941.32	0.01
8	1029.5	993.53	−3.49	1029.5	0.00	1029.7	0.02
9	1037.5	1065.2	2.67	1031.9	−0.54	1039.8	0.23
10	1512.4	1455.1	−3.79	1460.8	−3.41	1512.9	0.03

4 Conclusion

The dynamic model of the folded plate is established by Rayleigh–Ritz method. With different folded angles, the natural frequencies can be calculated accurately by this numerical method. The results show that the linear connection between two plates can be converted into several nodes. If we want to get more accurate results, we must take more polynomial terms and more connection nodes.

Based on the modal analysis, we can get the modal shapes of the folded plate, and carry out relevant nonlinear dynamics or fluid structure coupling dynamics analysis.

References

1. Guo X, Zhang Y, Zhang W (2018) Nonlinear vibration characteristics of Z-type folded plates with internal resonance. J Vib Eng 31(02):183–197
2. Piao J, Guo X, Zhang W (2017) Nonlinear dynamics and mode analysis for a Z-type folded wings. J Dyn Control 015(001):29–38
3. Guo X, Chen L, Zhang W (2018) Aerodynamic force calculation and nonlinear dynamic analysis of Z-type morphing wings. J Dyn Control 16(5):430–439
4. Zhang Y (2018) Theoretical and experimental study on nonlinear dynamic characteristics of Z-type folded wing. Beijing University of Technology
5. Wang S, Guo X, Wang S (2020) Finite element analysis and experiment on vibration of Z-shaped morphing wing with variable section. J Dyn Control 18(6):84–89
6. Zhang Y, Guo X (2018) Modal test of Z-shaped folded plate based on LMS system. In: Proceedings of the 24th annual conference of Beijing mechanics society
7. Guo X, Zhang Y, Yan W (2020) Modal experiment of Z-shaped folding wing based on PolyMax method. Vib Test Diagnosis 196(02):118–123+212
8. Irie T (1984) Free vibration of a cantilever folded plate. J Acoust Soc Am 76(6):1743–1748
9. Cao D et al (2020) Natural frequencies and global mode functions for flexible jointed-panel structures. Am Soc Civ Eng
10. Cao Y, Cao D, He G et al (2020) Modelling and vibration analysis for the multi-plate structure connected by nonlinear hinges. J Sound Vib 492:115809
11. He G, Cao D, Cao Y et al (2020) Investigation on global analytic modes for a three-axis attitude stabilized spacecraft with jointed panels. Aerosp Sci Technolg 106:106087
12. Liu L, Cao D, Tan X (2016) Studies on global analytical mode for a three-axis attitude stabilized spacecraft by using the Rayleigh-Ritz method. Arch Appl Mech 86(12):1927–1946
13. Chen Y, Jin G, Liu Z (2014) Flexural and in-plane vibration analysis of elastically restrained thin rectangular plate with cutout using Chebyshev-Lagrangian method. Int J Mech Sci 89:264–278
14. Xing YF, Liu B (2009) Exact solutions for the free in-plane vibrations of rectangular plates. Int J Mech Sci 51(3):246–255
15. Bardell NS, Langley RS, Dunsdon JM (1996) On the free in-plane vibration of isotropic rectangular plates. J Sound Vib 191(3):459–467

Effect of Current Carrying Length in Electric Pulse Aided Deformation

A. Subrahmanyam, M. Dakaiah, Rahul Kumar Verma, and N. Venkata Reddy

1 Introduction

Electric Pulse Aided Deformation (EPAD) is gaining attention of researchers in recent years because of its ability to process high strength materials at relatively lower temperatures compared to hot working processes. Application of electric pulses during plastic deformation of a metal results in reduction of flow stress. This reduction can be due to both thermal and athermal effects. Increase in the mobility of dislocations during plastic deformation due to electron wind [1] is known as electroplastic (EP) effect [1, 2]. Note that the first paragraph of a section or subsection is not indented. The first paragraph that follows a table, figure, equation etc. does not have an indent, either.

Liu et al. [3] investigated the effect of pulsed DC current on the mechanical behaviour of TRIP 780/800 steel. Results showed that, there is a maximum instantaneous stress reduction of 285 MPa with temperature rise of 61 °C, whereas high temperature tensile tests at 115 °C showed that there is a flow stress reduction of 180 Mpa indicating the existence of EP effect. Roh et al. [4] studied the effect of

A. Subrahmanyam (✉) · M. Dakaiah · N. Venkata Reddy
Department of Mechanical and Aerospace Engineering, Indian Institute of Technology
Hyderabad, Kandi, Telangana 502285, India
e-mail: me16resch11001@iith.ac.in

M. Dakaiah
e-mail: munugalaedakaiah@iith.ac.in

N. Venkata Reddy
e-mail: nvr@mae.iith.ac.in

R. K. Verma
Research & Development, Tata Steel Limited, Jamshedpur 831001, India
e-mail: rahul.verma@tatasteel.com

applying multiple electric pulses on uniaxial tensile behaviour of Aluminium 5052-H32 alloy and concluded that electric pulses with same energy density but with different current densities caused identical stress strain behaviour (both instantaneous and permanent stress drops are same). Zhao et al. [5] studied the uniaxial tensile behaviour of Aluminium alloy AA5754 subjected to multiple electric pulses and reported that for a given energy density, the instantaneous stress drop increases with increase in the current density which indicates that current density has an independent effect on stress drop with same temperature rise.

Xie et al. [6] studied the effect of application of high frequency electric pulses on uniaxial tensile behaviour of dual phase steel DP 980. It was reported that only at 100 °C, electric current causes higher flow stress reduction compared to elevated temperature and for all other temperatures (up to 600 °C) flow stress increased due to passage of current. Magargee et al. [7] studied the electrically assisted tensile behaviour of CP titanium with and without forced air cooling conditions. They reported that flow stress reduction which was observed without forced air cooling (maximum temperature = 435 °C) is absent when forced air cooling (maximum temperature = 40 °C) was used.

From the literature, it is evident that stress reduction in EPAD is directly related to amount of joule heating [7], which in turn depends upon the current carrying length in the deformation zone. There is a need to reduce the overall joule heating in electric pulse aided tests as it is detrimental to material properties. The role of current density on instantaneous stress drop also requires further investigation as Roh et al. [4] reported that current density does not have an independent effect on stress drop but Zhao et al. [5] reported the contrary. In the present work, the effect of current carrying length on uniaxial tensile behaviour is investigated by performing single as well as multiple pulse experiments on modified tensile specimens. The role of current density on instantaneous stress drop with same temperature rise is also evaluated by conducting experiments with same energy density. Finally, the effect of applying different frequencies of electropulsing with same duty cycle on uniaxial tensile behaviour is studied.

2 Experimental Procedure and Methodology

Electrically assisted uniaxial tensile (EAT) tests are carried out on a universal tensile testing machine with a nominal strain rate of 10^{-3} s^{-1}. Material used in the experiments is a low carbon steel (C-Mn-440) in the form of a sheet with thickness of 1.02 mm. Figure 1a shows the dimensions of the standard specimen. Electric current is applied to the specimen through extensions provided in it as shown in Fig. 1b. Temperature rise in the specimen due to resistive heating is measured using single spot infrared pyrometer, which is focussed at the centre of the gauge length. A modified tensile specimen is designed with extensions to pass the electric current as shown in Fig. 1b. In the modified tensile specimen current carrying length (d) can be varied as shown in Fig. 1b. Three different current carrying lengths (d = 30 mm, 45 mm
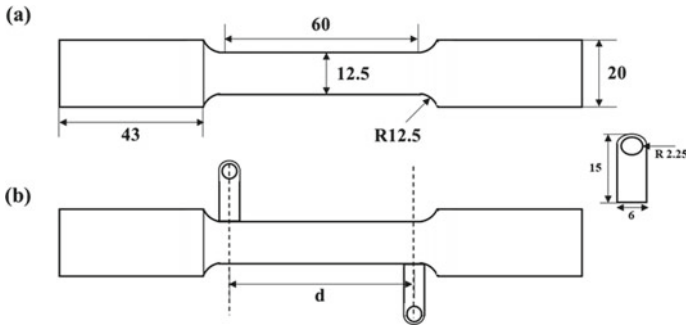
Fig. 1 Tensile specimens used in this work, **a** standard specimen, **b** modified specimen with current carrying length (d) as a variable

and 60 mm) are used in the present work. After confirming that modified specimens have same stress strain behaviour as that of the standard specimen, electric pulse aided experiments are performed.

To understand the independent effect of current density on instantaneous stress drop, three different current densities (J_0) (35.3, 27.3, 19.3 A/mm^2) and pulse durations (t_d) (2, 3.3, 6.7 s) with same energy density are used in the experiments. Current carrying length of 60 mm is kept constant in above experiments. Multiple pulse experiments are conducted at two different frequencies (f) (0.05, 0.1 Hz) with constant duty cycle (5%). Current density of 35.3 A/mm^2 is used in the above experiments.

3 Results and Discussion

The effect of added extensions to the standard specimen on tensile behaviour is studied by experiments. It is observed that, added extensions do not affect the original tensile behaviour. However, it is observed from experiments that decrease in the distance between extensions less than 30 mm has caused a shift in the failure location from centre of specimen to near fillet region. Hence, further reduction is not considered.

3.1 *Effect of Current Carrying Length*

Temperature of the specimen has increased instantaneously as soon as electric pulse is applied but the reduction in temperature is gradual. Maximum temperature reached is 190 ± 5 °C (measured at the centre of the gauge length) and it remains nearly same for all other current carrying lengths. Note that, overall joule heating is more for specimen with higher current carrying length. The effect of current carrying

Fig. 2 a Effect of current
carrying length and, **b** effect
of current density on tensile
behaviour

(a)

(b)
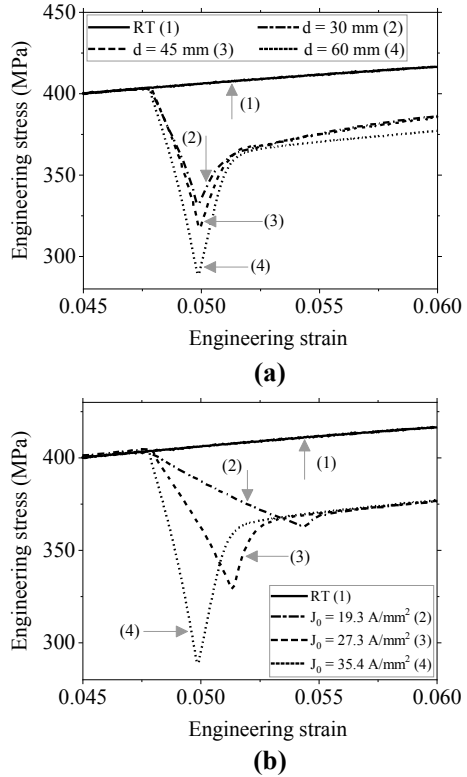
length on uniaxial tensile behaviour is shown in Fig. 2a. It is observed that with an
increase in the current carrying length from 30 to 60 mm (with $J_0 = 35.3$ A/mm^2
and $t_d = 2$ s), instantaneous stress drop increased from 70 to 122.5 Mpa. It is well
known that, joule heating increases with increase in the current carrying length hence,
higher stress reduction, even though maximum temperature at the centre of the gauge
length remains nearly same. It is also observed that temperature gradients are less
in specimen with higher current carrying length compared to specimen with lower
current carrying length. This can be attributed to internal heat generation in the current
carrying length region. This indicates that current carrying length has a significant
effect on instantaneous stress drop.

3.2 Effect of Current Density

The effect of current density with same energy density in a given time on uniaxial
tensile behaviour is shown in Fig. 2b. It is observed that with an increase in the current
density from 19.3 to 35.3 A/mm^2, instantaneous stress drop increased from 42.6 to

122.5 MPa. Maximum temperature measured during the tensile test is 190 ± 5 °C and is same for all current densities as energy supplied in a given time is constant. Hence, it can be noted that the temperature rise alone cannot determine instantaneous stress drop. In addition, current density has an independent effect on instantaneous stress drop. Further, high temperature tensile tests are carried out to understand the effect of temperature on flow stress reduction. It is observed that, stress-drop due to electric pulse is significantly higher compared to that of flow stress reduction observed in high temperature tests at similar temperatures.

3.3 Effect of Multiple Current Pulses

Results of multiple pulse experiments indicate that multiple pulses result in both instantaneous stress drop as well as permanent softening in the material. Effect of frequency at constant duty cycle (this ensures the amount of energy supplied to the system is same in a given time) on tensile behaviour and temperature rise is shown in Fig. 3a. Current density of 35.3 A/mm^2 and current carrying length of 60 mm are used in the experiments. It can be noted that the instantaneous stress drop at the time of pulse application is high for low frequency compared to that of high frequency. This can be attributed to increase in energy associated with each pulse as frequency decreases at constant duty cycle (increases the pulse duration). It is also observed that flow stress at any given time during the process is low at high frequency compared to low frequency as shown in Fig. 3a. This can be attributed to less heat dissipation time available when electric pulses are applied at high frequency with same duty cycle. Above observation indicates that use of effectiveness of applying high frequency electric pulses during metal forming processes to achieve load reduction with less temperature rise.

Figure 3b shows the variation of stress and temperature rise during tensile test with multiple pulses at different current carrying lengths. Frequency of 0.05 Hz and current density of 35.3 A/mm^2 are used in the experiments. It is observed that instantaneous stress drop is high for higher current carrying length as soon as each pulse is applied and it is due to higher joule heating. It is clear from Fig. 3b that the amount of permanent softening is more in lower current carrying length specimen. This can be attributed to the deformation zone (gauge length) because of confining the flow of current through deformation zone results in higher reduction at low temperatures. Temperature profiles (Fig. 3b) show that temperature rise after the application of first pulse is same for different current carrying lengths. However, temperature rise will not be the same after the first pulse, due to availability of more area (outside current carrying length) for heat dissipation through conduction to other regions of specimen (no internal heat generation) in lower current carrying length.

Fig. 3 **a** Effect of frequency and, **b** effect of current carrying length on tensile behaviour and temperature

(a)

(b)
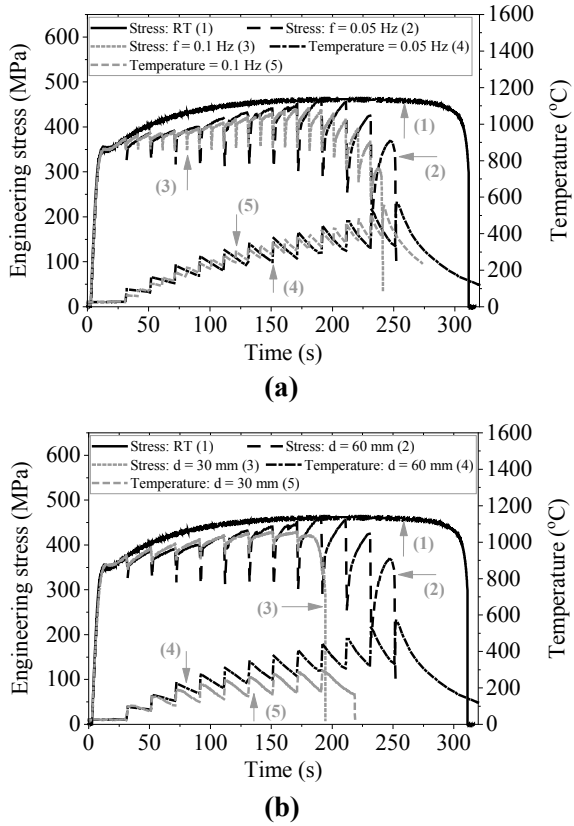
4   Conclusions

In the present study, electric pulse aided uniaxial tensile tests are carried out on modified specimens with a provision to apply electric current through constrained deformation zone to reduce the overall joule heating. Experiments show that the modified specimens have same stress strain behaviour as standard specimen. Experimental results indicate that current carrying length has a significant effect on instantaneous stress drop i.e., with an increase in the current carrying length the instantaneous stress drop increases. It is also observed that current density has an independent effect on stress drop. Multiple pulse experiments at different frequencies indicate that passing the current through deformation zone is advantageous.

References

1. Troitskii OA (1963) The effect of the anisotropy of electron and γ radiation on the deformation of zinc single crystals in the brittle state. Kokl. Akad. Nauk. SSSR, pp 148–332
2. Okazaki K (1978) A study of the electroplastic effect in metals. Scripta Metall 12:1063–1068
3. Liu X (2013) Experimental study of electro-plastic effect on advanced high strength steels. Mater Sci Eng A 582:211–218
4. Roh JH (2014) The mechanical behaviour of 5052–H32 aluminium alloys under a pulse electric current. Int J Plast 58:84–99
5. Zhao K (2016) The effect of pulse electric current on the mechanical properties and fracture behaviours of aluminium alloy AA5754. J Eng Mater Technol 138:041009–041017
6. Xie H (2015) Experimental investigation on electroplastic effect of DP980 advanced high strength steel. Mater Sci Eng A 637:23–28
7. Magargee J (2013) Characterization of flow stress for commercially pure titanium subjected to electrically assisted deformation. J Eng Mater Technol 135:041003–041010

A Preliminary Study of Shock Calibration Machine for Accelerometer Calibration

Supavee Prangphanta, Kunaphot Sukchoksirichaiporn, Patchayaporn Doungkum, Thira Jearsiripongkul, Somthana Panyadilok, Adisorn Tongkum, and Krit Jiamjiroch

1 Introduction

An accelerometer is one of the sensors that often found in a gas turbine engine of the generator as it is a very useful tool for predicting a suitable time for preventive maintenance. These sensors tend to deteriorate after use from time to time; hence, to ensure that these sensors are working accurately, they require calibrated after use for a certain amount of time [1]. It seems that most of the accelerometers are necessary to be calibrated by a vibration workbench that is often limited to a maximum of shock force at 10 g. One of the reasons why most of the sensors have only been tested under this level of shock force, even if it can stand for a higher shock level. For a shock calibration test, there are several techniques mention in ISO 16063-22:2005 [2]

Calibration: The concept of back to back technique is widely accepted for calibration for a long because this technique of connection could guaranty that both accelerometers are testing in the same condition, such as operating limits, physical, electrical characteristics and environmental. An accelerometer offers a straight charge signal in pC/g, and it may convert into acceleration by a charge amplifier [1]. Equation (1) and (2) shows the conversion between collect data voltage (V_{DAQref}) and the acceleration (a).

S. Prangphanta · K. Sukchoksirichaiporn · P. Doungkum · T. Jearsiripongkul · K. Jiamjiroch (✉)
Faculty of Engineering, Thammasat University, 99 Pahon Yo-thin RD, Klong Nung, Klong Lung, Pathumthani 12120, Thailand
e-mail: jkrit@engr.tu.ac.th

P. Doungkum
Faculty of Engineering, Pathumthani-University, Ban Klang, Mueang Pathum Thani District, Pathumthani 12000, Thailand

S. Panyadilok · A. Tongkum
Metrology and Calibration Department, Electricity Generating Authority, Sai Noi, Sai Noi District, Nonthaburi 11180, Thailand

$$a = V_{\text{ref}}/S_{\text{ref}} \tag{1}$$

and

$$V_{\text{DAQ,ref}} = G_{\text{ref}}V_{\text{ref}} \tag{2}$$

Whereas (a) represents an acceleration of the reference accelerometers, and S_{ref} is the sensitivity of the reference accelerometer. The reference sensor gives a measurable signal in volt from DAQ of the reference accelerometer ($V_{\text{DAQ,Ref}}$). This signal could converted into V_{Ref} by the ratio between $V_{\text{DAQ,Ref}}$ and gain of the reference charge amplifier (G_{ref}).

The calibration procedure begins with setting both of the accelerometers by comparing the unknown sensitivity of Sensor Under Test (SUT) with the reference sensitivity of the reference accelerometer (REF) [1, 3]. Figure 1 shows the mounting of the SUT accelerometer and REF accelerometer. Because both accelerometers are subject to the same input, it can estimate the sensitivity of the SUT by comparison with the reference sensitivity of the accelerometer as shown in the (Eq. 3)

$$S_{\text{sut}} = S_{\text{ref}}(V_{\text{sut}}/V_{\text{ref}}) \tag{3}$$

In the (Eq. 2), S_{sut} is the sensitivity of the sensor under test and voltage of the sensor under test and reference sensors refer to V_{sut} and V_{ref}, respectively. The sensitivity of the SUT is required to be systematically reported in term of measurement uncertainty and Combined Standard Uncertainty.

Guide to the expression of uncertainty in measurement (GUM) defines the measurement uncertainty as shown in the quote [4]. These measurable experiment data of the sensitivity of the SUT can report by an average of the average acceleration with $\pm$ of the type A uncertainty (u_c). This type A uncertainty can be obtained by the ratio between standard deviation (s.d.) and degree of freedom.

parameter, associated with the result of a measurement, that characterizes the dispersion of the values that could reasonably be attributed to the measurand

(Guide to the expression of uncertainty in measurement, 2020) [4]

Sensor under test (SUT)

Reference Sensor (REF)
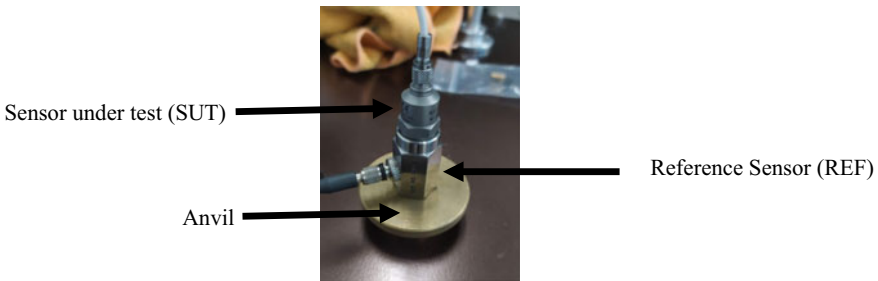
Anvil

Fig. 1 Back-to-back setting on an anvil

Shock Calibration Rig: One of the original techniques being rudimental of the shock calibration mention in BS ISO is drop-weight testing. Due to the fact that this technology has been used since the 1970s by Endevco, the drop-weight testing is still one of a few famous techniques in a shock acceleration measurement [3]. This machine can be operated by dropping a specific mass from the exact height, and then the back to back sensors that are mouthed at the base of an anvil sent the signal to the controller immediately after the weight impacted with the anvil. It seems that all of the record data at the early of development need to plot on the paper and then measure into a centimetre, and then SUT's sensitivity can obtain by (Eq. 1).

The ISO 16063-22:2005 [2] recommended many types and techniques in a shock test; however, there are not many machines suitable for achieving above 1000 g of acceleration. The result from the previous study shows that two out of those technique can offer high acceleration are Hopkinson bar testing and pneumatic exciter. These two testing apparatuses have their own benefit and drawback. Beside of the Hopkinson bar system, shock acceleration system by a pneumatic exciter is more economical and as it does not need to take a lot of space. Moreover, it is possibility to design and fabricate by the parts available in Thailand (Fig. 2).

The recent development can change the way of recording data from analogue to digital. As mentioned in the literature, to record highly dynamic data like shock response, it needs a high-speed DAQ card of at least 204.8 kS/s. And the specific control in fire-time is another extent for this kind of testing [5].

The literature gave helpful information that is DAQ speed card and fire-time [5]. Therefore, with a constant weight of anvil, frequency and fire-time, this study aims to experiment on a preliminary test on an in-house pneumatic shock calibration rig between 20 and 1000 g.

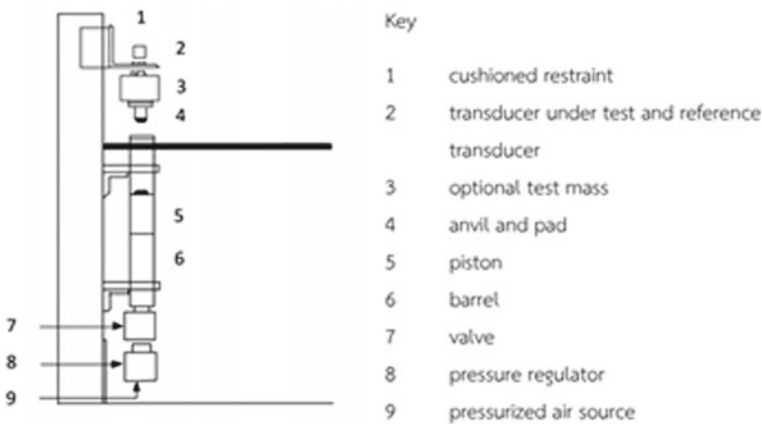| Key	
1	cushioned restraint
2	transducer under test and reference transducer
3	optional test mass
4	anvil and pad
5	piston
6	barrel
7	valve
8	pressure regulator
9	pressurized air source

Fig. 2 The calibration machine by using a pneumatic exciter [2]

2 Material and Methods

There are two main parts for this section: the development of a pneumatic exciter rig, and then all of the experiments are mentioned in Experiments.

Exciter: The main rig was developed in house based on a pneumatic exciter according to ISO 16063-22:2005 [2]. This design is accurate in a pressure control loop with an uncertainty of pressure by ±0.05 bar (Fig. 3). It expected that possible precise control in the exciter forces, this rig was designed and fabricated all of the parts with the tolerance of 0.05 mm. Lastly, because it needs to be accredited, all components have to be designed according to 16063-22:2005 [2]
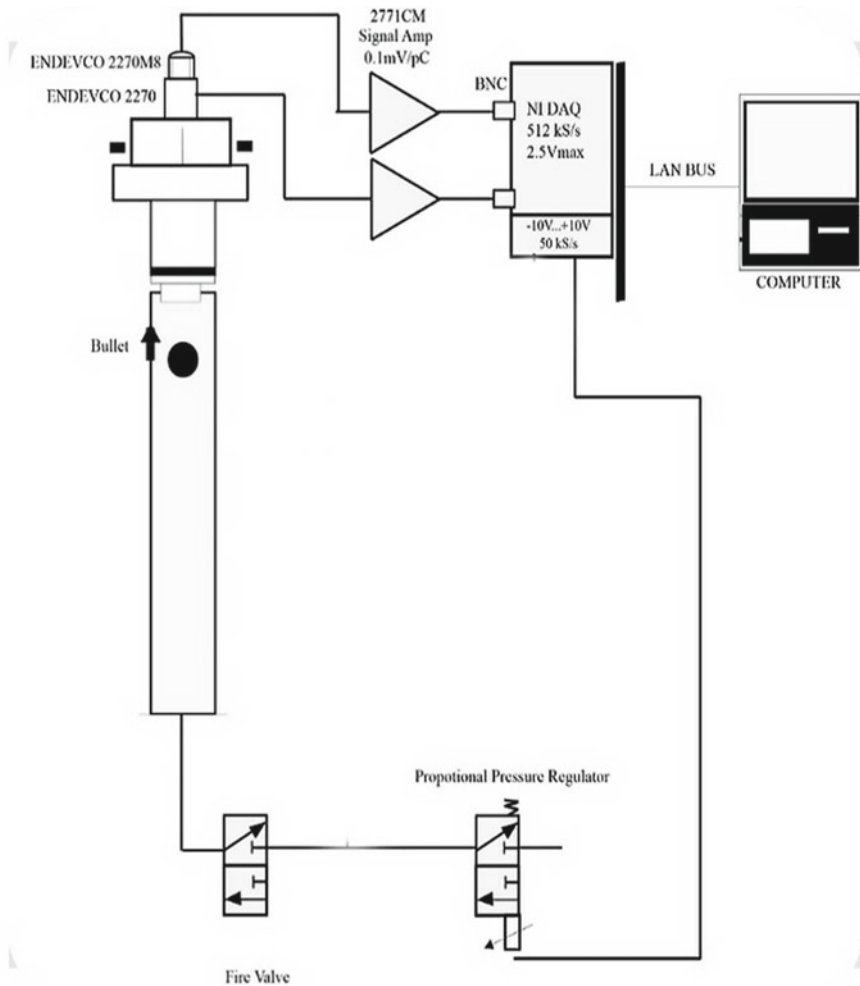

Fig. 3 Pneumatic exciter

Sensor and Controller: As all parts are new items, including the controllers and sensors, Endevco2270, Endevco2270m8 and their amplifiers are calibrated and certified by their manufacturers. With a new PXIe-controller from the National Instrument DAQ system, it has an uncertainty of 0.1%. The HMI screen developed under a LabVIEW version 2019.

Experiments: This preliminary study has experimented at 25 °C with 65% relative humidity. A 165 g stainless steel anvil with back to back of sensors was installed at the top of the barrel. The acceleration could vary depending on the pressure between 1 and 8 bar. At least expected three targets of acceleration between 20 and 1000 g obtained from the six to ten of the success shots of each condition. Signals from both sensors transferred pass through their amplifiers and converted into both acceleration and sensitivity by (Eqs. 1 and 2).

3 Results and Discussion

Figure 4 shows voltage obtained from SUT and REF sensors. It can see that signals received from 10 out of 11 shots. Both sensors gave the harmony of both signals; the sensitivity and the experiment uncertainty of SUT at 49 g are approximate 2.02pC/g ± 0.4%.

The other parameter that plays a vital role in this study is frequency response. It can be estimated at the 10 per cent of the pulse duration time. For example, Fig. 5 shows a single pulse; its duration is roughly 2.9 ms or 350 Hz.

Table 1 shows the measurable uncertainty with the sensitivity of SUT at the different acceleration level. Measurement sensitivity uncertainty of SUT is minimal at 0.1% when acceleration varies between 20 and 1000 g.
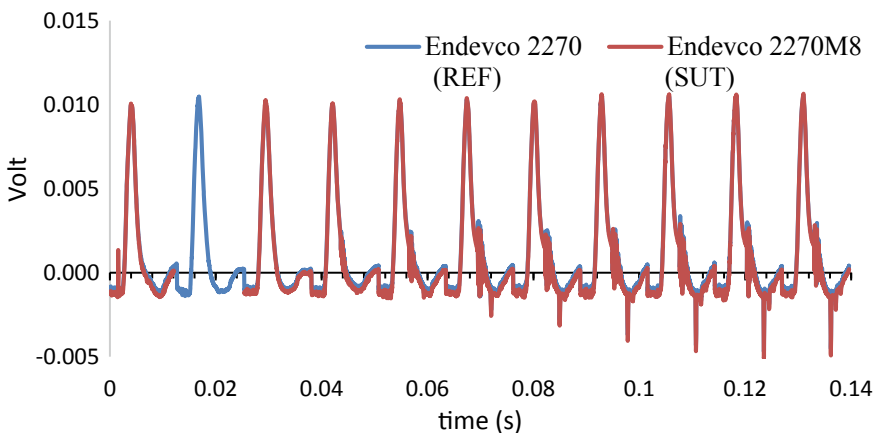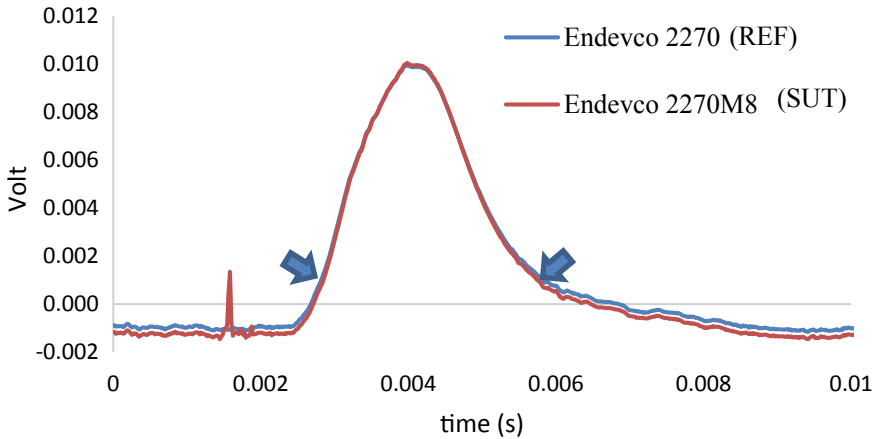

Fig. 4 Raw data of the preliminary study (10 of 11 success shots)

Fig. 5 Pulse duration time 2.9 ms or 350 Hz

Table 1 Measurement uncertainty, sensitivity and expect acceleration between 20 and 1000 g

Target acceleration	Instrument value		Measurement uncertainty (%)
	Nominal acceleration (g)	Sensitivity pC/g	
20	19.9	1.987	0.1
50	49.2	2.025	0.1
100	103.0	2.029	0.1
500	483.7	1.987	0.1
1000	948.8	2.010	0.2
Summary		2.006	0.1

Measurement uncertainty is shown as a sign of minimum deviation at 0.1%. Due to the estimated collection of certificates and calibration, both combine uncertainty and an expanded uncertainty at 95% of confidence level ($k - 2$) were used as repertoire, as shown in Table 2. Even if some more data is missing for Table 2; the most crucial information was listed and considered to calculate collect uncertainty (u_c) at 1.2% with expanding uncertainty (U) at 2.3%.

4 Conclusion

This study is a preliminary study on an in-house shock acceleration calibration rig. The experiment with a pneumatic accelerometer calibration had been done between 20 and 1000 g at a constant frequency 520 Hz; it seems that the rig was well performed by the varying input pressure between 2 and 6 bar. Shock acceleration had done with

Table 2 Expand uncertainty of a system at 95% of confidence level ($k = 2$)

Uncertainty	Symbol	Source of uncertainty	Value	Value (%)	Divisor	Ci^a	Ui^b
Reference Transducer	U_{reps}	Repeatability of Reference Transducer (V)	10^{-5}	0.1	1.0	1.0	0.1
	U_{std}	Calibration of Reference sensitivity (%)	2.2	2.2	2.0	1.0	1.1
	U_{dstd}	Drift of Reference Transducer (%)	0.2	0.20	1.732	1.0	0.115
	U_{motion}	Relative Motion of Reference Transducer (%)	0.2	0.20	1.732	1.0	0.115
	U_{trans}	Rotation/Transverse Motion of of Reference Tran	0.3	0.3	4.242	1.0	0.073
	U_{temps}	Temperature of Reference Transducer (C)	0	0	1.732	1.0	0.000
	U_{linear}	Amplitude linearity of (%)	0.1	0.1	1.732	1.0	0.057
Test Transducer	U_{repu}	Repeatability of UUC (V)	10^{-5}	0.0035	1.0	1.0	0.0035
	U_{base}	Base strain / Mounting of UUC 5000 g (g/str	1.136	0.0227	1.732	1.0	0.01312
	U_{tranu}	Rotation / Transverse Motion of of UUC (%)	0	0	1.732	1.0	0
Signal Condition	$U_{amp\text{-}linear}$	Linearity of amplifier and data	0	0	1.732	1.0	0
	$U_{cal\,CA}$	Calibration of Charge Amplifier (%)	0.2	0.2	2.0	1.0	0.1
	$U_{cr.CA}$	Relative frequency response (%)	0	0	1.732	1.0	0.000
	$U_{temp.CA}$	Temperature of Charge Amplifier (%)	0	0	1.732	1.0	0.000
Algorithm	U_{resu}	Datalogger	0.1	0.1	1.732	1.0	0.057
Evaluation	U_C	Combined Uncertainty					1.16
Test	U expand	Expanded Uncertainty		Normal ($k = 2$)			2.3

Remark Ci^a = Sensitivity Coefficient, Ui^b = Standard Uncertainty (%).

a fixed fire-time, constant frequency and the exact weight of an anvil. All of the results at the same frequency shown a measurement uncertainty at 2.006 pC/g $\pm$ 0.1%. From the initial estimate, both collect uncertainty and expand uncertainty are roughly estimated at 1.2% and 2.3%, respectively.

References

1. Sill RD. Minimizing measurement uncertainty in calibration and use of accelerometers, p 32
2. International Standard Organization (2005) Methods for the calibration of vibration and shock transducers—Part 22: shock calibration by comparison to a reference transducer, p 23
3. Endevco tech paper (1968) Comparison shock motion calibrations. In: Proceedings of the institute of environmental sciences, 9p
4. JCFGi, Metrology (2020) Guide to the expression of uncertainty in measurement in Part 6: developing and using measurement models, p 95
5. Sill RD, Kim SH (2006) Accelerometer shock sensitivity calibration using a pneumatic exciter. In: Proceedings of the 77th shock and vibration symposium, 77th shock and vibration symposium, Monterey, 11p

Failure Probability Estimation of Thermally Stable Diamond Composite Rock Cutting Tips in Underground Roadway Development

Yong Sun, Xingsheng Li, and Hua Guo

1 Introduction

The Thermally Stable Diamond Composite (TSDC) is a kind of diamond composite synthesised by high pressure and high temperature with silicon as binder [1, 2]. TSDC is superior over tungsten carbide (WC) and ordinary polycrystalline diamond (PCD) in terms of the combination of wear resistance and thermal stability which is the ability to maintain its mechanical properties at high temperature. According to [3], TSDC material is applicable when temperature is higher than 1000 °C, but PCD with cobalt as binding material is not. However, currently, there is a limitation to TSDC element size (usually less than 25 mm). The shape quality and material properties of the TSDC elements often vary considerably. More importantly, the fracture toughness of the TSDC made with the current technology is generally not as good as that of WC and PCD with metallic binder [4].

It would be ideal to increase TSDC material toughness while maintaining its high wear resistance and thermal stability. Before any breakthrough in this direction, many efforts have been made to enable existing TSDC material to be used as cutting elements in the excavation of hard rock which WC or PCD cutting elements are not able to cut [5]. An example is research on SMART*CUT picks [6], in which TSDC material is used to make the cutting tips. To optimise the applications of the TSDC cutting tips in mining and civil industries, it is necessary to understand the

Y. Sun (✉) · X. Li · H. Guo
CSIRO Mineral Resources, PO Box 883, Kenmore, QLD 4069, Australia
e-mail: Yong.Sun@csiro.au

X. Li
e-mail: Xing.Li@csiro.au

H. Guo
e-mail: Hua.Guo@csiro.au

233

failure characteristics and failure risk of the TSDC cutting tips in different cutting conditions.

Owing to the relatively low impact toughness, TSDC tips are sensitive to impact force and bending force. Unlike WC cutting tips which have a major failure mode of wear, a major failure mode of TSDC cutting tips is sudden failure, e.g. tip snapped-off from the pick body, caused by excessive bending force exerting on the tips during a rock cutting process [7]. Due to the uncertain material properties of TSDC material, randomly varied rock properties, and other uncertain factors such as machine operation, TSDC cutting tip failures during rock cutting production usually occur in a random manner. As a result, the failure risk of the TSDC cutting tips during rock cutting production should be assessed with a probabilistic method rather than a deterministic method.

To estimate the failure probability of TSDC tipped picks for optimising their applications in mining production, a probabilistic approach has been developed based on the cutting process of one drum revolution of the cutterhead of a continuous miner in 2017 [7]. In 2019, this approach was extended to estimate the TSDC cutting tip failure probability over a full cutting cycle in the underground coal mining roadway development process [8]. A full cutting cycle normally consists of a number of drum revolutions. To consider the impact of roof rock thickness on the failure probability of TSDC cutting tips at shearing-down stage which was ignored in [8], a further study was carried out in 2020 [9].

In this paper, the probabilistic approach is further extended to investigate the failure probability of the TSDC cutting tips for a given advance distance of the underground coal mining roadway development which consists of multiple cutting cycles. This capability is important to many analyses for the optimum applications of TSDC cutting tips in the mining and construction productions, such as cost–benefit analysis and what-if analysis. In addition, the tip failure probability prediction model for a full cutting cycle is improved via taking into account the impact of roof rock on the tip failure probability at the shearing-down stage. Although the failure probability model in this paper is developed based on the scenario of underground coal mining roadway development, the modelling method can also be applied to other rock cutting processes.

2   Scenario and Assumptions

The rock cutting scenario considered in this paper is the underground coal mining roadway development as illustrated in Fig. 1. An underground coal mining roadway is usually developed using a continuous miner with many cutting cycles. Figure 1 shows an example with four cutting cycles to be implemented.

In Fig. 1, a red line represents the face of the roadway after a cutting cycle. Four blue circles (solid or semi-transparent) represent the locations of the drum after the completion of the sump-in stage in four cutting cycles, respectively.
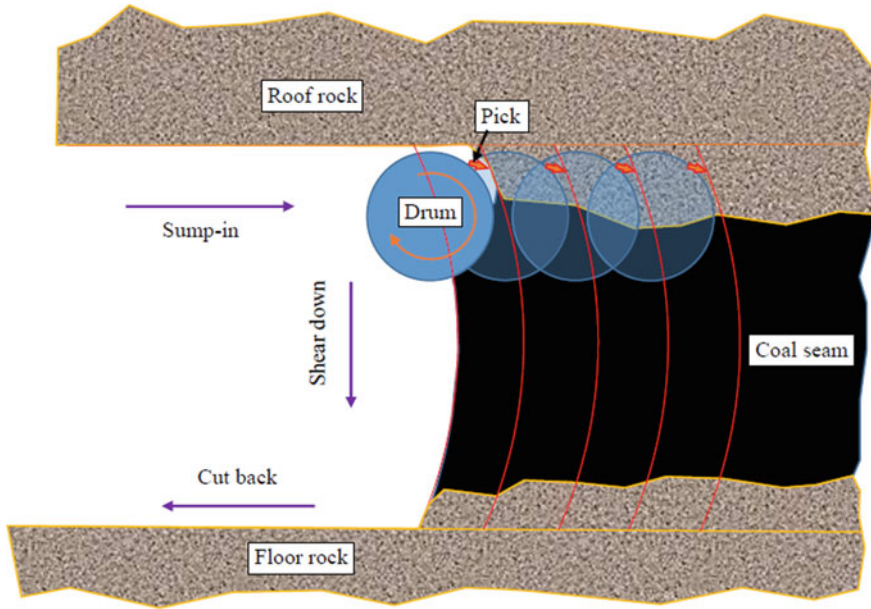
Fig. 1 Schematic diagram of underground coal mining roadway development

As mentioned in [8], a full cutting cycle in the underground coal mining roadway development typically consists of three stages: cutting into the roof rock (sump-in stage), shearing down to the floor (shearing-down stage) and cutting back to clear the floor (cutting-back stage). At the sump-in stage, the drum in the continuous miner usually cuts into the face about a half of the diameter. The cutting distance at the cutting-back stage is generally short, about 150 mm.

A drum is equipped with many cutting picks although only one pick is shown in Fig. 1. Drum cuts rock or coal through these picks. A pick installed on a drum is usually randomly selected from a batch of same picks and continues in service until it is failed. Due to many uncertain factors involved in the TSDC material manufacturing process, the formation of cutting tips and the manufacturing of picks, the strength of TSDC cutting tips varies randomly as reported in [7]. In addition, rock strength and thickness along an underground coal mining roadway usually also vary randomly.

As models developed in references [7–9] lay a foundation for the model development in this paper, the assumptions adopted for developing the relevant models in [7–9] are also adopted in this paper. In short, it is assumed that no coal exists inside rock and vice versa. The thickness of the roof and floor that are cut during the development of the roadway can be roughly described by discrete average values with corresponding probability of occurrence. Only tip sudden failure due to excessive force acting on the tip is considered, and hence the tip failures are independent of each other. Tip failures at the coal seam cutting period and at the cutting-back stage can be ignored. The probability of the tip failure in the cutting process can be

estimated as a combination of the failure probabilities of the tip used to cut a series of discrete segments of the process.

Furthermore, the following additional assumptions are made in the analysis in this paper:

Machine is well controlled. The variations of sump-in depth, drum rotational speed and drum advance speed can be ignored. The advance distance in each cutting cycle is equal to the sump-in depth of the drum in a cutting cycle. This means that the variations of the advance distances between individual cutting cycles are ignored.

Rock conditions in all cycles are the same, able to be represented using the same rock thickness distribution and strength distribution. The rationale behind this assumption is that if rock conditions in some areas are significantly different, the analysis of the failure probability can be conducted separately with different rock thickness distribution and/or strength distribution.

3 Failure Probability of Pick Tip for a Given Distance of Roadway Development

In reliability engineering, a failure probability function is often described as a function of time as demonstrated in [7–9]. While this type of description is good for modelling tip failure probability over a drum revolution or a cutting cycle, it may not be user-friendly to model tip failure probability over a long distance of the underground coal mining roadway development because of the intermittent rock cutting process during the production. To address this issue, the tip failure probability for roadway development with multiple cutting cycles is expressed as a function of advance distance of the roadway development (m).

In each cutting cycle, the roadway will be advanced for a distance of the drum's sump-in depth in a cutting cycle, which is a constant according to the above assumption. It is noted that advance distance only increases at the sump-in stage, and then remains unchanged at the shearing-down stage and cutting-back stage. However, tip failure probability can increase at both the sump-in stage and the shearing-down stage. In addition, when the tip failure probability for roadway development is under consideration, the prediction horizon usually involves tens or even hundreds of cutting cycles. In this case, the small-scale changes in the tip failure probability within a cutting cycle has little impact on the prediction accuracy (see Figs. 2 and 3). Therefore, for simplicity, the step for tip failure probability analysis over a given advance distance of the roadway development is set to the drum's sump-in depth in a cutting cycle, that is, the given advance distance is set to be an integer multiple of the drum's sump-in depth. This means that the nonlinear tip failure probability change during an individual cutting cycle is not explicitly described although it is possible to do so (e.g. see Fig. 4 in [8]). Instead, a step function is used to describe the tip failure probability change over a cutting cycle.
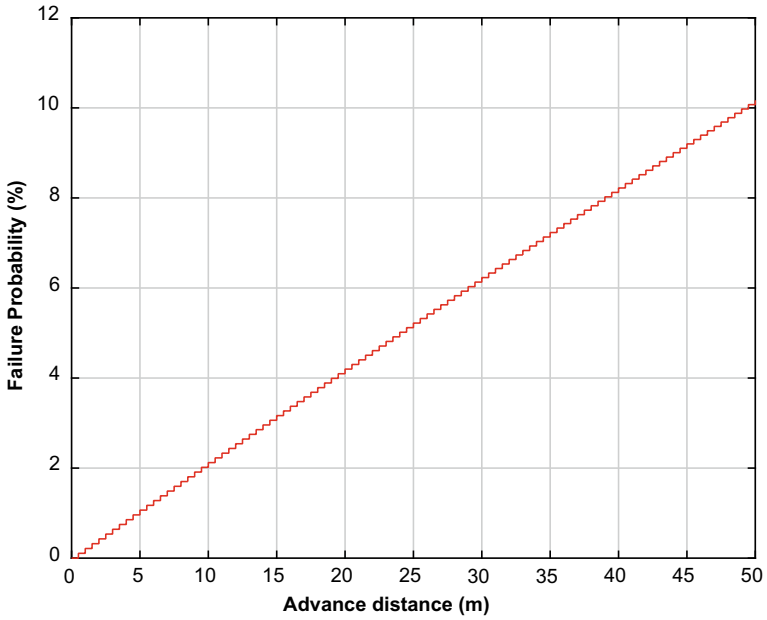
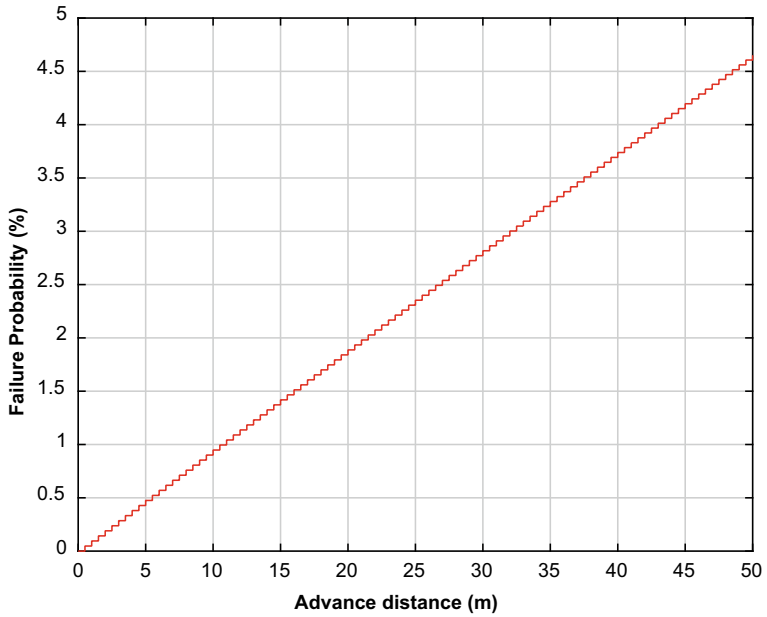**Fig. 2** TSDC tip failure probability when its allowable bending force is 9.8 kN

Fig. 3 TSDC tip failure probability when its allowable bending force is 9.9 kN

As tip failures for different cutting cycles are independent, the failure probability of a tip with allowable bending force x_a over a given advance distance consisting of n cutting cycles, $F_c(x|x_a)$, can be expressed as

$$F_c(x|x_a) = \begin{cases} 0, & 0 \le x < D_s \\ F_c(x_a), & D_s \le x < 2D_s \\ \quad \vdots & \\ 1 - [1 - F_c(x_a)]^n, & nD_s \le x < (n+1)D_s \end{cases}, \tag{1}$$

where, D_s is the roadway development advance distance per cutting cycle (mm); and $F_c(x_a)$ is the tip failure probability over a full cutting cycle.

According to [8], the failure probability of a tip over a full cutting cycle is a combination of its failure probability over sump-in stage, shearing-down stage and cutting-back stage. Therefore, with a consideration of the failure probability of the cutting tip for cutting roof rock at the shearing-down stage, $F_c(x_a)$ is given by

$$F_c(x_a) = 1 - \prod_{i=1}^{4} [1 - F_i(x_a)], \tag{2}$$

where, $F_i(x_a)$ $(i = 1, 2, 3, 4)$ are, respectively, the tip failure probability at the sump-in stage, the tip failure probability for cutting roof rock at the shearing-down stage, the tip failure probability for cutting the coal seam and floor rock at the shearing-down stage and the tip failure probability for cutting roof rock at the cutting-back stage. All $F_i(x_a)$ $(i = 1, 2, 3, 4)$ can be estimated using the corresponding models developed in [7–9].

Equation (2) implies that there is a coal seam between the roof rock and the floor rock. However, the model developed in this paper can also be applied to the scenario where there is not a coal seam between the roof rock and the floor rock (e.g. a tunnel has a complete rock face). In this case, the roof rock thickness is set to be the full height of the tunnel and the thickness of coal seam and floor is reduced to zero when using Eq. (2).

If the probability density function of the allowable forces of the cutting tips is $p(x_a)$, the failure probability of a randomly selected pick tip for advancing a distance of x m of the roadway is

$$F_c(x) = \int_{-\infty}^{\infty} F_c(x|x_a) p(x_a) dx_a. \tag{3}$$

The model developed in this paper can be used not only to estimate the tip failure probability for risk management, but also to conduct what-if analysis for pick design optimisation. A numerical study is presented in the next section to demonstrate its

application to the analysis of the influence of tip allowable bending force on the tip failure probability.

4 A Numerical Study

The parameters used in this case study are largely simulated based on the case studies presented in [7–9]. It is assumed that a set of TSDC tipped picks are installed on a 2-start continuous miner drum for developing an underground coal mining roadway with a height of 3000 mm. The drum tip-to-tip diameter, drum operational parameters, pick installation angles and rock properties are the same as those given in [7–9].

The sump-in depth in each cutting cycle is 500 mm. The moving distance of the drum centre in the shearing-down stage is approximated to 2000 mm. Both the roof rock thickness and the floor rock thickness vary along the roadway and can be represented as follows:

- The roof thickness: mean values are [950, 1200 mm], and their corresponding occurrence likelihood are [40%, 60%].
- The floor thickness: mean values are [450, 550 mm], and their corresponding occurrence likelihood are [50%, 50%].

As this case study is used to investigate the influence of tip allowable bending force on the tip failure probability, the randomness of the tip allowable bending force is not considered. Instead, two types of TSDC tips with given allowable bending forces, 9.8 and 9.9 kN, are analysed. The analysis results are shown in Figs. 2 and 3, respectively.

Both figures show that the tip failure probability increases with the increase of the advance distance. However, the increase of the failure probability of tips with an allowable bending force of 9.8 kN is much faster than that of tips with an allowable bending force of 9.9 kN. While the failure probability of the tips with an allowable bending force of 9.8 kN after advancing a distance of 50 m (equivalent to 100 cutting cycles) reaches 10.17%, the tip failure probability of the tips with an allowable bending force of 9.9 kN after advancing the same distance is only 4.65%.

The analysis results indicate that although the tip allowable bending force only increased from 9.8 to 9.9 kN, a little higher than 1%, the tip failure probability decreased by more than 50%. This means that increasing the tip allowable bending force is an effective approach to the improvement of TSDC tip reliability.

In addition, both Figs. 2 and 3 confirmed that the small-scale changes within a cutting cycle have trivial impact on the overall result of the failure probability estimation, and therefore can be ignored when the advance distance under consideration involves more than 10 full cutting cycles.

5 Conclusion

TSDC has good wear resistance and thermal stability, but its fracture toughness is relatively lower than WC and PCD. Besides, the current technology cannot make large TSDC element, and it is hard to control the element quality in terms of shape and material property. All these weaknesses of the existing TSDC may increase its failure probability when it is used to cut hard rock in the mining and construction industries.

A model to estimate the tip failure probability for a given advance distance in the underground coal mining roadway development is developed in this paper with a sole consideration of tip sudden failures due to excessive bending force acting on the tips. This model is an extension to the existing probabilistic models. In addition to estimating the tip failure probability for pick risk management, this model can be applied to optimise pick design and drum operation through what-if analysis.

A what-if case study has been presented to investigate the influences of tip allowable bending force on the tip failure probability. The results reveal that increasing the tip allowable bending force can effectively improve TSDC tip reliability. Although the presented case study focused on the investigation of the influence of tip allowable bending force, the model can be applied to study the impacts of other major factors including pick attack angle and drum operational parameters.

It is worth pointing out that the actual tip failure probability may be higher than the value estimated using the model even for TSDC tips, because only tip sudden failures due to excessive bending force acting on the tips are considered in the model and the uncertainties in some factors including DOC, angle of resultant force and drum vibration are ignored. Further studies are needed to improve the accuracy of the model by considering other failure modes and the ignored uncertainties.

References

1. Luzin V, Voronin G, Avdeev M, Boland JN (2018) Microstresses in thermally stable diamond composites made by high pressure infiltration technique. In: Materials research proceedings, vol 4. Materials Research Forum LLC., Millersville PA, USA, pp 65–70
2. Lavigne O, Luzin V, Mendez M, Malik AS, Carrasco O, Salvemini F (2019) Characterization of the residual stresses introduced by a new joining method in diamond and tungsten carbide composites. Int J Refractory Met Hard Mater 85:105051
3. Mlungwane K, Herrmann M, Sigalas I (2008) The low-pressure infiltration of diamond by silicon to form diamond–silicon carbide composites. J Eur Ceram Soc 28:321–326
4. Zhao Y, Li L, Ji H, Sun K, Li Z (2018) Effect of SiC whiskers on mechanical properties of thermally stable polycrystalline diamond prepared by HPHT sintering. Diam Relat Mater 90:54–61
5. Boland JN, Li XS, Rassool RP, Hay D (2010) Characterisation of diamond composites for tooling. J Aust Ceram Soc 46(1):1–10
6. Li XS, Sun Y (2013) Development of hard rock cutting tool with advanced diamond composites. Adv Mater Res 690–693:1831–1835
7. Sun Y, Li XS (2017) A probabilistic approach for assessing failure risk of cutting tools in underground excavation. Tunn Undergr Space Technol 70:299–308

8. Sun Y, Li XS, Guo H (2019) Failure probability prediction of thermally stable diamond composite tipped picks in the cutting cycle of underground roadway development. Appl Sci 9:1–18
9. Sun Y, Li XS, Guo H (2021) Influence of roof rock thickness on the failure probability of thermally stable diamond composite rock cutting tips. Key Eng Mater 878:98–103

Transtibial Prosthetic Socket Produced Using Additive Manufacturing

Karel Raz , **Zdenek Chval** , **and Martin Stepanek**

1 Introduction

A prosthetic socket is a critical part of whole prosthetic. It is very important to meet requirements of strength as well as comfort. The socket must be shaped adequately otherwise pain and health complication would appear [1]. Sockets are generally made manually and high requirements are laid on skills and experience of prosthetists and their big part of time participation in production process [2]. This paper is focused on the potential of an additive technology used HP Jet Fusion. It could be used for rapid design and manufacture of a prosthetic socket. The geometry and volume is reduced based on prosthetist's recommendation. The AM technology could be used for production of sockets with support of FEA simulations [3] and [4]. Some prosthetists use design software (ShapeMaker™ [Seattle Limb Systems, Poulsbo, Washington], TracerCAD™ [Polhemus, Colchester, Vermont], TT Design [Otto Bock, Minneapolis, Minnesota], OMEGA Tracer [Ohio Willow Wood, Mt. Sterling, Ohio], BioSculptor [BioSculptor Corporation, Hialeah, Florida]). This software (SW) is used for creating the socket shape and then the shape is sent to the central fabrication facilities, where positive shape of socket is manufactured. Usage of the AM would reduce requirements on an amount of manufacturing facilities owned by a prosthesist. Their design of complete socket could be sent and manufactured by company that is not mainly focused on prosthetic but just owns 3D printer. The same company owning the 3D printer could collaborate with more prosthesists and a cost is decreased. Unfortunately, low number of HP Jet Fusion printers in companies is limiting wide usage of this technology. However, due to low limit in design, AM could be potential technology for advanced socket using lattice structures for weight

K. Raz · Z. Chval · M. Stepanek (✉)

Regional Technological Institute, University of West Bohemia, Pilsen, Czech Republic

e-mail: stepanem@rti.zcu.cz

Fig. 1 Transfer of residual limb shape to CAD

reduction [5], thermoregulation, variable stiffness mentioned in article Sockets for Limb Prostheses: A Review of Existing Technologies and Open Challenges [6].

## 2 Description of Remodeling the Residual Limb in CAD

An electronic visual image of a mold of the residual limb was obtained using the scanning process. Volume of the sheet body was reduced based on a prosthetist recommendation at the distance of 40 mm below kneecap by 3% of undeform shape. A transfer of shape from the residual limb to the sheet body is shown in Fig. 1.

3 Integration of Adapter to Socket Geometry

Prosthesis socket adapter is used for connection of the socket to the other components of prosthetic and eventually for setting to required position. Adapters are connected to a socket through screws or with help of lamination. Accuracy of technology HP Jet Fusion is 200 μm and it is possible to produce threads by this technology. Adapter, which is commonly laminated in, was chosen because of that advantage. Its plastic part was integrated to socket in CAD model and a metal locking part of the adapter was screwed in after printing. Integration of the plastic part of adapter using lattice structure is shown in Fig. 2.

Two integration constructions were created. The geometry of the adapter is integrated to the socket through full volume construction in the first case. Advantage of

Fig. 2 Adapter integration
with lattice structure
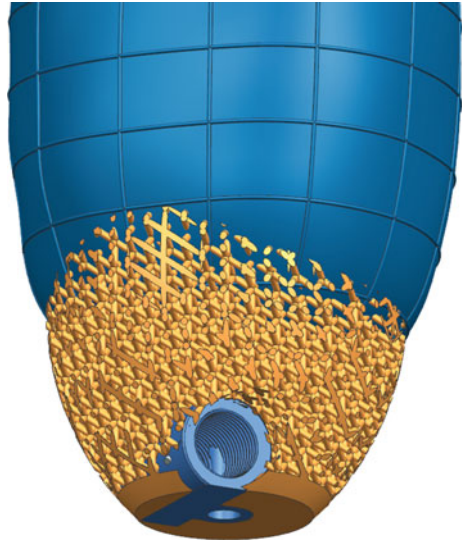
lattice structure is considered in the second construction. Both described designs are shown in Fig. 6.

Structural analysis was performed for comparison of the both designs. The deformation was compared. All DOF were fixed on the face where the socket is connected to the rest of prosthetic. Load of a quadruple of patient's weight (3400 N) was applied in socket's axis direction on whole inner surface of the socket (Fig. 3). Definition of FE model is visible in Fig. 3, where the red arrows show the load direction. Material properties of PA12 (from Siemens NX Material library) were assigned to FE model. Young's modulus was updated to 1800 MPa.

Lattice structure was replaced with full volume for the simulation of time reduction. Young's modulus of the virtual substitution material was decreased with respect to the initial Young's modulus. Value of Young's modulus of substitute material $PA12_{lattice}$ in lattice structure space was determined from a simulation of small volume of lattice structure (cube of $3 \times 3 \times 3$ cells) (Fig. 4) and also from the Eq. (1):

$$E_{\text{primitive wr}} = E * (0.5233 * w_r^2 + 0.375 * w_r) \tag{1}$$

where $E_{\text{primitive wr}}$ is Young's modulus of substituted material calculated from (1), W_r is weight ratio of full material brick and brick of lattice structure and E is Young's modulus of base material (PA12). The method for determining the average Young's modulus is described in the research paper [7].

$E_{\text{primitive wr sim}}$ is Young's modulus determined from the simulation of small volume of lattice structure and E_{used} is Young's modulus used in simulation of the socket.

Deformation of both designs was evaluated in the same reference point. The deformation of socket, using the full volume material for integration of adapter
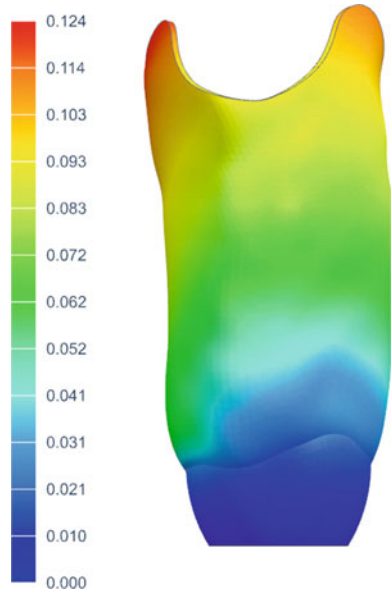
Fig. 3 Definition of FE
model
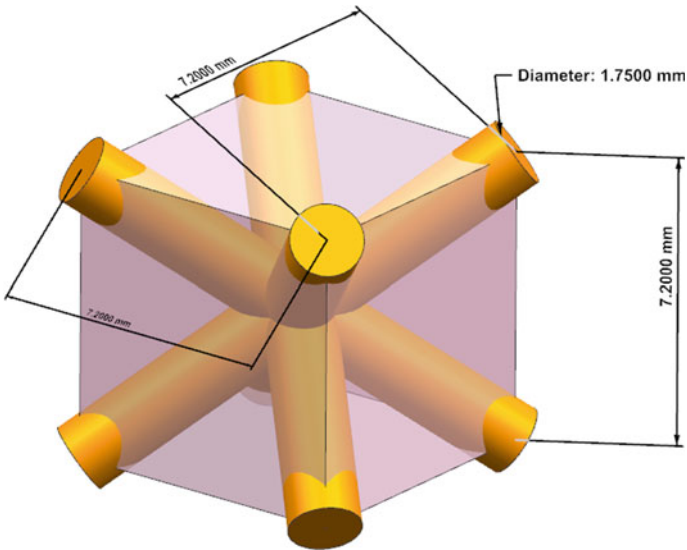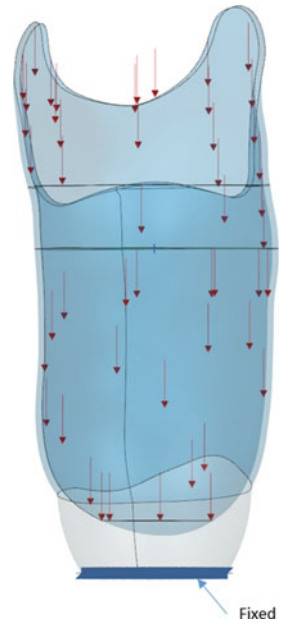
E [MPa]	w_r [-]	$E_{\text{primitive Wr}}$ [MPa]	$E_{\text{primitive sim.}}$ [MPa]	$E_{\text{used.}}$ [MPa]
1800	0.28	263	213	240

Fig. 4 Determination of young's modulus

(Fig. 5), loaded by 3400 N was 0.0812 mm. The deformation of socket using lattice structure for integration was 0.3361 mm.

Fig. 5 Deformation of full volume material construction

Fig. 6 Full volume integration (left), lattice structure integration (right)

Fig. 7 Pressure test and break of the socket

4   Produced Prosthesis Sockets

Prosthesis sockets were produced with HP Jet Fusion 4200 and made of PA12. Print time of each socket was 10 h and 25 min. Time needed for cooldown was 3 times the print time (31.5 h) and 1 h of unpacking. Production time of one socket was approx. 43 h.

Weight of prosthesis socket made of full material in the adapter space was 414 g. The weight of the socket where lattice structure was used was 343 g which is 17% weight reduction.

The socket using lattice structure was tested on Zwick/Roell Z250 (Fig. 7). Strength of the socket loaded by 3400 N was proved without break. The failure strength was 19,876 N. Configuration of the specimen in the test is shown in the next figure. Design procedure of the prosthetic socket from scanning of residual limb to ready-to-use socket is shown in Fig. 8 (Fig. 6).

5   Conclusion

A computer aided design and an additive manufacturing (AM) provide a chance for rapid production of prosthesis sockets with high accuracy and repetitiveness. Total
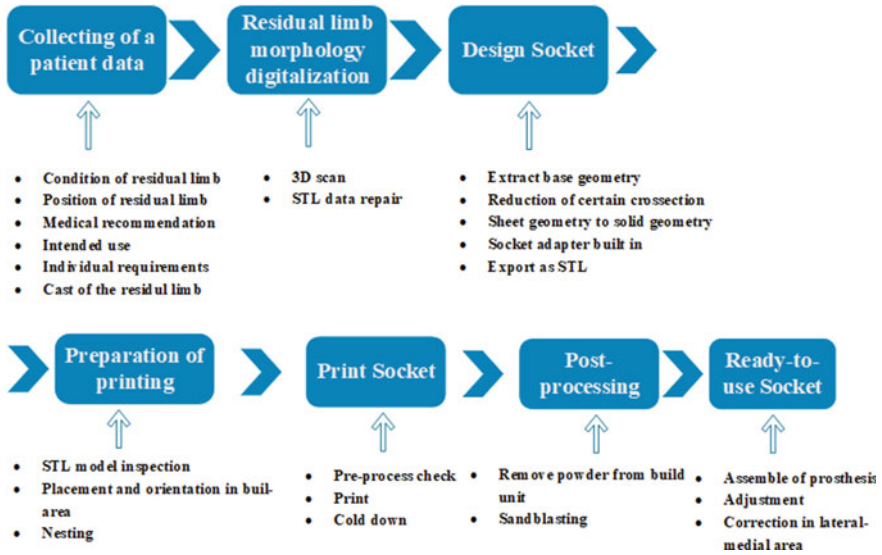
Fig. 8 Diagram of the design procedure

time from 3D scanning to ready-to-use socket took about 52 h. It is important to realize that time when a prosthetist is actively engaged into the production process is only about 7 h. The rest of time of the production is consumed by the scanning and the printing. It was possible to include an adapter into the geometry of socket. Usage of lattice structure for integration of adapter reduced socket's weight by 17%. Deformation of the socket using lattice structure (loaded by 3400 N—quadruple of patient weight) was 4.1 times larger compared to the case of full volume construction. This value is still in order of hundreds of micrometers that could be neglected. The recyclability of PA12 is an important benefit to the future.

References

1. Hsu E, Cohen SP (2013) Postamputation pain: epidemiology, mechanisms, and treatment. J Pain Res 6:121–136. https://doi.org/10.2147/JPR.S32299
2. Paterno L, Ibrahimi M, Gruppioni E et al (2018) Sockets for limb prostheses: a review of existing technologies and open challenges. IEEE Trans Biomed Eng 65:1996–2010. https://doi.org/10.1109/tbme.2017.2775100
3. Steer JW, Worsley PR, Browne M, Dickinson AS (2019) Predictive prosthetic socket design: part 1-population-based evaluation of transtibial prosthetic sockets by FEA-driven surrogate

modelling. Biomech Model Mechanobiol 19(4):1331–1346. https://doi.org/10.1007/s10237-019-01195-5. Epub 2019 June 29. PMID: 31256276; PMCID: PMC7423807

4. McGarry A, McHugh B, Buis A, Mckay G (2008) Evaluation of the effect of shape on a contemporary CAD system. Prosthet Orthot Int

5. Helou M, Kara S (2018) Design, analysis and manufacturing of lattice structures: an overview. Int J Comput Integr Manuf 31:3:243–261. https://doi.org/10.1080/0951192X.2017.1407456

6. Paternò L, Ibrahimi M, Gruppioni E, Menciassi A, Ricotti L (2018) Sockets for limb prostheses: a review of existing technologies and open challenges. IEEE Trans Biomed Eng 65(9):1996–2010. https://doi.org/10.1109/TBME.2017.2775100

7. Raz K, Chval Z, Sedlacek F (2020) Compressive strength prediction of quad-diametral lattice structures. In: Key engineering materials. Trans Tech Publications Ltd., pp 69–74